

**ADVANCEMENTS IN THE SEISMIC DESIGN OF COLD-  
FORMED STEEL STRUCTURES THROUGH THE  
INVESTIGATION OF DIAPHRAGM BEHAVIOUR AND  
THE INFLUENCE OF NON-STRUCTURAL  
COMPONENTS**

by

VIOLETTA NIKOLAIDOU



Department of Civil Engineering and Applied Mechanics

Faculty of Engineering, McGill University, Montreal

August 2018

*A thesis submitted to McGill University in partial fulfillment of the  
requirements of the degree of Doctor of Philosophy*

© Violetta Nikolaidou 2018

*Dedicated to*

*My parents, **Zachos & Efi**, and my brother, **Stefanos**,*

*for being the best family one could ever have*

*Στους γονείς μου, **Ζάχο & Έφη**, και στον αδερφό μου, **Στέφανο**,*

*γιατί είναι η καλύτερη οικογένεια που θα μπορούσε κανείς να έχει*

## ABSTRACT

Recent shake table experimental work revealed that cold-formed steel (CFS) buildings exhibit excellent structural performance under high earthquake excitations; however, the reasons behind their considerable structural capacity are still unclear. This is due to the fact that the complex nonlinear response of CFS members and their interactions in a subsystem and, subsequently, in a system level are not well defined.

Currently, in the AISI S400 North American Standard for Seismic Design of Cold-Formed Steel Structural Systems the seismic design of CFS framed structures is based on the lateral response of CFS framed shear walls and special moment frames, as the primary lateral load resisting elements. Experimental studies on the contribution of non-structural elements, such as gypsum sheathing, to the lateral response of the shear wall have revealed their potential. As such, the addition of non-structural gypsum to the shear wall component is included in the seismic design in Canada but with limitations about their applicability. In the USA, this lateral force resisting system is not specifically recognised but the benefit of gypsum is considered inherent in the system's over-strength factor. There is still great uncertainty regarding the behaviour of non-structural elements and the capacity forces they may impose on the structure. Further, the importance of the diaphragm component as part of the lateral load resisting system distributing the lateral forces to the vertical lateral load resisting elements is evident. Nonetheless, at present the AISI S400 Standard includes limited design guidelines for CFS framed diaphragms for use in the USA, while no information is available for diaphragm design in Canada. This is to be expected given the minimal pre-existing research work available on CFS framed diaphragms.

CFS joist framing sheathed with structural OSB panels is a typical diaphragm configuration

found in the floors and roofs of CFS buildings; as such, an experimental program of OSB sheathed / CFS framed diaphragm configurations was launched at McGill University and is presented in this dissertation. The aim was to provide insight on the in-plane lateral response of these subsystems when subjected to monotonic and reversed cyclic loading. Experimental results underlined the dependency of the diaphragm's lateral response on screw spacing and size. The beneficial effect of panel edge blocking was also demonstrated. Moreover, the need to update the design guidelines available in the AISI S400 Standard was highlighted by means of a comparison of design and experimental shear strength and stiffness values.

In order to explore the effect of non-structural components in a system and subsystem level, diaphragm configurations with non-structural gypsum ceiling and gypcrete flooring were tested as part of the diaphragm experimental program. The experimental results were incorporated in the floor and roof of a case-study two-storey CFS building, featuring diaphragms, shear walls and gravity walls with gypsum sheathing throughout the structure. A simplified 3D phenomenological numerical modeling approach was followed and verified using experimental data. Response history dynamic analyses results revealed the addition of gypsum sheathing and gravity walls throughout the wall-line as substantially increasing the lateral resistance of the structure. Although, the non-structural elements on the diaphragm increased its shear strength and stiffness, they had a minimal effect on the seismic response of the CFS building.

Further investigation of the influence of the diaphragm's flexibility on a CFS building was realized by means of a parametric numerical study, where three diaphragm stiffness conditions were examined; flexible, semi-rigid and rigid. Non-structural components were kept throughout the wall-line of the building as a more realistic approach. The two-storey CFS building was subjected to a design basis earthquake in the USA in the two directions and to a suite of 20

ground motions representing seismic hazard in Montreal and Vancouver, Canada, in the flexible side of the building. Modal analysis results showed that the dynamic properties of the building are directly influenced by the diaphragm flexibility. Response history analyses results revealed reduction of the wall-line storey drifts with increase of the diaphragm flexibility; the level of that reduction is dependent on the input ground motion. The rigid diaphragm assumption for the building, used in design, was able to capture adequately the shear wall forces; however, it overestimated the wall-line storey drift ratios of the CFS building.

## **RÉSUMÉ**

De récentes expériences sur table vibrante ont montré que les bâtiments avec une ossature en acier formé à froid présentent d'excellentes performances structurelles sous des excitations sismiques importantes; néanmoins, les raisons de leur capacité structurelle importante ne sont toujours pas claires. Cela est dû au fait que les réponses non-linéaires complexes des éléments en acier formé à froid et de leurs interactions dans un sous-système et, par conséquent, dans un système global, ne sont pas bien définies.

Actuellement, dans le Standard Nord-Américain AISI S400 pour la Conception parasismique des structures à ossature en acier formé à froid, cette dernière utilise la réponse latérale des murs de refend et des cadres rigides spéciaux comme principaux éléments de résistance aux charges latérales. Des études expérimentales sur la contribution d'éléments non-structuraux, comme les panneaux de gypse, à la réponse latérale des murs de refends ont révélé leur potentiel. L'ajout de panneaux de gypse non-structuraux aux murs de refends est pris en compte dans la conception parasismique du Canada mais avec des limitations sur leur application. Aux États-Unis, ce système de résistance latérale n'est pas spécifiquement reconnu mais le bénéfice des panneaux de gypse est considéré comme inclus dans le facteur d'amplification du système. Il y a encore

une grande incertitude sur le comportement des éléments non-structuraux et sur les forces capacitaires qu'elles peuvent imposer à la structure. De plus, l'importance du diaphragme comme élément du système de résistance latérale, qui transmet les charges latérales aux éléments verticaux de ce système, est évidente. Cependant, à ce jour, le Standard AISI S400 ne comprend que des recommandations limitées pour la conception des diaphragmes à ossature en acier formé à froid aux États-Unis tandis qu'aucune information n'est disponible pour la conception de ceux-ci au Canada. Cela est compréhensible étant donné le nombre restreint de travaux de recherche sur les diaphragmes à ossature en acier formé à froid.

L'ossature à poutrelles en acier formé à froid recouverte de panneaux structuraux d'OSB est une configuration courante de diaphragme utilisée pour les planchers et les toits de bâtiments en acier formé à froid ; par conséquent, un programme expérimental a été lancé à Université McGill sur ces configurations et est présenté dans ce mémoire. L'objectif était de fournir une vision de la réponse latérale en plan du sous-système lorsqu'il était soumis à un chargement monotonique et cyclique-réversible. Les résultats expérimentaux ont souligné la relation entre la réponse latérale du diaphragme et l'espacement et la taille des vis. L'effet bénéfique du blocage du bord du panneau a également été montré. De plus, le besoin de mise à jour des recommandations de conception du Standard AISI S400 a été mis en évidence grâce à la comparaison des valeurs de conception avec les valeurs expérimentales des forces de cisaillement ainsi que des rigidités.

Afin d'étudier les effets des composants non-structuraux d'un système et un sous-système, des configurations de diaphragme avec des plafonds couverts de panneaux de gypse non-structuraux et de planchers en « gypcrete » ont été testées dans le cadre du programme expérimental sur les diaphragmes. Les résultats expérimentaux ont été incorporés dans le sol et toit d'un modèle de bâtiment à deux niveaux à ossature en acier formé à froid, comprenant des diaphragmes, des

murs de refends et des murs porteurs recouverts de panneaux de gypse sur toute la structure. Un modèle numérique 3D simplifié basé sur une approche phénoménologique a été utilisé et calibré en utilisant les données expérimentales. Les résultats des analyses des réponses dynamiques ont révélé que l'ajout de panneaux de gypse et de murs porteurs le long des murs a augmenté significativement la résistance latérale de la structure. Même si les éléments non-structuraux sur le diaphragme ont augmenté sa force de cisaillement et sa rigidité, ils n'ont eu qu'un effet limité sur la réponse sismique du bâtiment à ossature en acier formé à froid.

D'autres recherches sur l'influence de la flexibilité du diaphragme sur un bâtiment à ossature en acier formé à froid ont été menées grâce à une étude numérique paramétrique dans laquelle trois conditions de rigidités ont été examinées; flexible, semi-rigide et rigide. Les composants non-structuraux ont été conservés sur les murs du bâtiment pour avoir une approche plus réaliste. Le bâtiment de deux niveaux a été soumis à un séisme de conception de base aux États-Unis dans les 2 directions et à une suite de 20 mouvements de sol représentant le risque sismique à Montréal et Vancouver (Canada), sur le côté flexible du bâtiment. Les résultats des analyses modales ont montré que les propriétés dynamiques du bâtiment sont directement influencées par la flexibilité du diaphragme. Les résultats des réponses ont montré que les déplacements des murs réduisent avec l'augmentation de la flexibilité du diaphragme; le niveau de cette réduction dépend du mouvement de sol appliqué. L'hypothèse de diaphragme rigide pour les bâtiments, utilisé en conception, a permis de déduire correctement les forces des murs de refends ; en revanche, elle surestime les ratios de déplacements des murs dans un bâtiment à ossature en acier formé à froid.

## ACKNOWLEDGEMENTS

My deepest gratitude goes to Prof. Colin A. Rogers, whom I was so fortunate to have had as an advisor throughout this stimulating adventure. Thank you for teaching me the importance of patience and perseverance. Thank you for your knowledge and support and for pushing me to go a step further in order to tackle everyday research problems. You have become a role-model for me as an academic, a mentor, an engineer and a person and you have supported and guided me more than you can imagine.

I am thankful to Prof. Dimitrios G. Lignos for his constructive feedback throughout the course of my research work. Thank you for emphasizing key points in my numerical work and for your valuable knowledge of related topics.

I would, also, like to thank my committee members and reviewers: Prof. Ghyslaine McClure, Prof. A.P.S. Selvadurai, Prof. Rola Assi, Prof. Mary Kang, Prof. Luigi Fiorino and Prof. Josephine Nalbantoglu for their time and effort in reviewing my work.

Further, I am grateful for the information and support provided by Professor Benjamin W. Schafer and Dr. Cristopher D. Moen, as well as Dr. Kara Peterman, Dr. Aritra Chatterjee, Dr. Jiazhen Leng and Dr. David A. Padilla-Liano related to the CFS-NEES Building. Thank you for your collaboration spirit and your prompt response whenever requested.

At this point, I would like to extend my heartfelt gratitude to Prof. Charis Gantes in National Technical University of Athens, who was the first to introduce me to the world of research and who supported me in pursuing my academic dreams further. Thank you for everything.

For the experimental part of this research work, my sincere appreciation goes to Patrick Latreille, David Pizzuto, Andrea Iachetta, Keith Lee, Rico Massa and Nick Adomat for your enthusiasm and hard work. John Bartczak and Dr. William Cook thank you for always finding a way.

My most heartfelt thank you goes to my research colleague and good friend Dr. Sarven Akcelyan for all our research conversations and philosophical wonderings. A special thank you is also extended to Dr. Zaid Gouleh for your kind spirit, to Dr. Andrew Komar for sharing my love for coffee, to Dr. Ahmed Elkady for always being positive, to Dr. Omar Ibrahim for your calm strength and to Sophie Lu for your positive attitude and reliability.

I would, also, like to thank for their financial support the American Iron and Steel Institute (AISI), the Canadian Sheet Steel Building Institute (CSSBI), the Natural Sciences and Engineering Research Council of Canada (NSERC), the Fonds de Recherche du Québec – Nature et Technologies (FRQNT) and the Centre d'études interuniversitaire sur les structures sous charges extremes (CEISCE). I, also, gratefully acknowledge the funding provided by McGill's Faculty of Engineering through the MEDA and the Graduate Excellence award and the scholarships offered by the Hellenic Scholarships Foundation.

I am, also, thankful to Bailey Metal Products Ltd., Simpson Strong-Tie Co. Inc., Ontario Tools and Fasteners Ltd, le Groupe Beuchesne, Maxxon Corporation, Beton Autonivelant SGI, ArcelorMittal and Construction Proco Inc. for the all the materials and tools that they provided.

A PhD can be truly challenging at times and for these times one needs extraordinary friends like Dr. Dea Van Lierop, Dr. Eleonora Tubaldi, Dr. Eleonora Botta, Dr. to be Agustin Cerani, Dr. Filippo Malandra and Liam McIntyre. Thank you for all the beautiful memories. A special thank you also goes to Dr. Dorival Jr. Martins for being everyday a constant source of positive energy. To my friends in Greece, thank you for your support and love all these years that we are apart.

Last but not least, thank you from the bottom of my heart to my amazing parents, Zachos & Efi, and my brother, Stefanos, for your unconditional love and support. I can't believe how lucky I am to have a family like this one. I cannot thank you enough; this thesis is dedicated to you.

## PREFACE & CONTRIBUTION OF AUTHORS

In accordance with the “Guidelines for Thesis Preparation”, this thesis is presented in a manuscript format. The authorships of the three articles included in this dissertation are explained below:

### Chapter 2:

Nikolaidou V., Latreille P., Rogers C. A., and Lignos D. G. (2017b). "Seismic performance characterization of wood-Sheathed and cold-formed steel framed floor and roof diaphragm structures." *Journal of Structural Engineering*, 144(2):04017215.

- ✓ The manuscript was written by Nikolaidou V. The experimental work and analytical calculations presented in the manuscript were carried out by Nikolaidou V., who led Phase 1 of the experimental program in question.
- ✓ Latreille P. assisted in the conduction of the experiments, as part of the construction team. He, also, contributed to the preparation of the results and the preliminary analytical calculations of this work.
- ✓ Rogers C. A. provided supervision and “hands-on” assistance throughout the course of the experimental program. He, also, provided feedback for the editing of this manuscript.
- ✓ Lignos D. G. provided feedback on the work and assisted in the editing of this manuscript.

### Chapter 3:

Nikolaidou V., Rogers C. A., and Lignos D. G. "Influence of non-structural components on the seismic response of cold-formed steel buildings: system & subsystem level response." (prepared for journal submission)

- ✓ The writing, the experimental work and the numerical study of this manuscript were realized by Nikolaidou V.
- ✓ Rogers C. A. supervised the research work and assisted in the experimental work and in the editing of this manuscript.
- ✓ Lignos D. G. provided feedback on the numerical work and assisted in the editing of this manuscript.

Chapter 4:

Nikolaidou V., Rogers C. A., and Lignos D. G. "Influence of diaphragm flexibility on the seismic response of cold-formed steel buildings." (prepared for journal submission)

- ✓ The numerical studies and the writing of this manuscript were conducted by Nikolaidou V.
- ✓ Rogers C. A. supervised the research work and assisted in the editing of this manuscript.
- ✓ Lignos D. G. provided feedback on the numerical work and assisted in the editing of this manuscript.

The original contributions of this dissertation are the following:

- Development of a database of shear strength and stiffness values for OSB sheathed / CFS framed floor and roof diaphragm configurations with various structural characteristics.
- Evaluation of the design guidelines for diaphragms currently available in the AISI S400 Standard (2015).
- Recommendation of a simplified phenomenological modeling approach of a 3D building model able to predict the peak seismic response of a two-storey CFS building.
- Identification of the wall-line non-structural components as substantial contributors to the lateral resistance of a two-storey CFS building compared to the diaphragm non-structural

components.

- Quantification of the influence of diaphragm flexibility on the dynamic properties and seismic response of a two-storey CFS building.
- Evaluation of the rigid diaphragm condition as a valid design assumption for accurate prediction of base shear forces and storey-drifts of a two-storey CFS building.

# TABLE OF CONTENTS

<b>Abstract .....</b>	<b>i</b>
<b>Résumé .....</b>	<b>iii</b>
<b>Acknowledgements.....</b>	<b>vi</b>
<b>Preface .....</b>	<b>viii</b>
<b>Table of contents.....</b>	<b>xi</b>
<b>List of Figures .....</b>	<b>xvi</b>
<b>List of Tables.....</b>	<b>xxv</b>

## **Chapter 1 – Introduction and Background ..... 1**

1.1 General overview .....	1
1.2 Research objectives.....	4
1.3 Scope and limitations .....	5
1.4 Thesis outline .....	7
1.5 Literature review .....	8
1.5.1 Diaphragm design provisions .....	9
1.5.2 Diaphragm and shear wall studies .....	13
1.5.2.1. Experimental work .....	13
1.5.2.2. Numerical work.....	20
1.5.3 CFS gravity framing studies .....	23
1.5.4 Non-structural gypsum sheathing and gravity walls studies.....	26
1.5.5 Diaphragm flexibility studies.....	28
1.5.6 Seismic assessment in Canada .....	37

1.5.6.1.	Design provisions .....	37
1.5.6.2.	Deaggregation data.....	40
1.5.6.3.	Ground motion databases .....	40
1.6	Summary .....	41
<b>Foreword to Chapter 2 .....</b>		<b>43</b>
<b>Chapter 2 – Structural Performance Characterization of Wood-Sheathed / Cold-Formed Steel Framed Floor and Roof Diaphragm Structures.....</b>		<b>44</b>
2.1	Abstract .....	44
2.2	Introduction.....	45
2.3	CFS framed diaphragm test program .....	48
2.4	Material properties .....	54
2.5	Diaphragm test results.....	55
2.5.1.	Roof configuration test results .....	59
2.5.2.	Floor configuration test results .....	60
2.6	Diaphragm design predictions.....	61
2.7	Conclusions .....	65
2.8	Acknowledgements .....	66
2.9	Notation.....	67
2.10	References .....	68
<b>Foreword to Chapter 3 .....</b>		<b>73</b>
<b>Chapter 3 – Influence of Non-Structural Components on the Lateral Response of Cold-Formed Steel Buildings: System &amp; Subsystem Level Response .....</b>		<b>74</b>

3.1	Abstract .....	74
3.2	Introduction .....	75
3.3	Experimental work: gypsum panels and gypcrete flooring .....	78
3.3.1.	Diaphragm specimens and test set-up.....	78
3.3.2.	Selected experimental findings on the diaphragm hysteretic behaviour .....	80
3.4	Numerical simulation of the case study CFS building.....	83
3.4.1.	Shear wall structure and connection .....	85
3.4.2.	Diaphragm.....	87
3.4.3.	Gravity framing.....	90
3.4.4.	Non-structural gypsum and gravity walls .....	91
3.5	Numerical simulation of CFS-NEES Building .....	93
3.5.1.	3D Model Verification; structural components .....	93
3.5.2.	Consideration of non-structural components .....	100
3.5.2.1	Non-structural components for the diaphragm.....	100
3.5.2.2	Non-structural components on the diaphragms & walls .....	102
3.6	Conclusions .....	106
3.7	Acknowledgements .....	107
3.8	Notation.....	108
3.9	References .....	109
	<b>Foreword to Chapter 4 .....</b>	<b>115</b>
	<b>Chapter 4 –Influence of Diaphragm Flexibility on the Seismic Response of Cold-Formed Steel Buildings .....</b>	<b>116</b>
4.1	Abstract .....	116

4.2	Introduction.....	117
4.3	Numerical model.....	121
4.4	Modal analysis: dynamic properties in z direction .....	122
4.5	Ground motion selection and scaling.....	125
4.5.1	Montreal.....	125
4.5.1.1.	Target period range .....	125
4.5.1.2.	Target response spectrum: selected ground motions for Montreal , site class C.....	126
4.5.1.3.	Scaling of selected ground motion records; Montreal, site class C .....	127
4.5.2	Vancouver .....	129
4.5.2.1.	Target response spectrum: selected ground motions for Vancouver, site class D .....	129
4.5.2.2.	Scaling of selected ground motions; Vancouver, site class D.....	130
4.6	Parametric study: Step 1 .....	131
4.6.1.	Part 1 .....	132
4.6.2.	Part 2 .....	133
4.7	Parametric study: Step 2 .....	134
4.7.1.	Montreal results .....	134
4.7.2.	Vancouver results.....	142
4.8	Conclusions.....	146
4.9	Acknowledgements.....	147
4.10	Notation.....	147
4.11	References.....	149

**Chapter 5 – Summary and Conclusions..... 154**

5.1 Overview ..... 154

5.2 Summary and conclusions ..... 154

    5.2.1 Diaphragm experimental program ..... 154

        5.2.1.1 Roof configuration ..... 155

        5.2.1.2 Floor configuration..... 156

        5.2.1.3 Design predictions..... 157

    5.2.2 Numerical modeling..... 157

        5.2.2.1 Diaphragm subsystem ..... 157

        5.2.2.2 CFS building model ..... 158

        5.2.2.3 CFS building model verification ..... 159

    5.2.3 Effect of non-structural components on the seismic response of a CFS building ..... 160

    5.2.4 Effect of diaphragm flexibility on the seismic response of a CFS building ..... 161

5.3 Original contributions ..... 163

5.4 Recommendations for future work ..... 163

**List of References ..... 166**

**Appendix A: Pinching4 parameters ..... 180**

**Appendix B: Fastener failure modes (experimental program) ..... 184**

**Appendix C: Test setup design..... 217**

**Appendix D: Supplemental material test results..... 247**

**Appendix E: Supplemental response history analysis data..... 269**

## LIST OF FIGURES

<b>Figure 1.1:</b> Example CFS framed construction; a) diaphragm and b) shear wall.....	2
<b>Figure 1.2:</b> CFS framed building; a) 3D view and, b) plan view .....	2
<b>Figure 1.3:</b> Typical CFS framed diaphragm assembly; a) structural details and, b) blocking .....	9
<b>Figure 1.4:</b> CFS-NEES Building (courtesy of Dr. Kara Peterman, University of Massachusetts Amherst) .....	18
<b>Figure 1.6:</b> Pinching4 material model in the OpenSees Platform (Lowe and Altoontash 2003).....	20
<b>Figure 2.1:</b> CFS – NEES Building; a) elevation, and b) ground floor (courtesy of Dr. Kara Peterman, University of Massachusetts Amherst) .....	47
<b>Figure 2.2:</b> CFS diaphragm test setup.....	48
<b>Figure 2.3:</b> CFS diaphragm test specimen and setup.....	49
<b>Figure 2.4:</b> Photographs of diaphragm test specimens; a) unblocked framing prior to installation of OSB sheathing, and b) completed diaphragm with roof sheathing .....	49
<b>Figure 2.5:</b> Illustration of a) CFS framing, and b) wood panel sheathing .....	51
<b>Figure 2.6:</b> Modification to the roof diaphragm configurations; full CFS frame blocking .....	51
<b>Figure 2.7:</b> CFS framing connections; a) joist-to-track connections, and b) blocking-to-joist connections .....	52
<b>Figure 2.8:</b> CUREE loading protocol for specimen 8-RB-C (blocked).....	53
<b>Figure 2.9:</b> Instrumentation of diaphragm test specimens .....	53
<b>Figure 2.10:</b> Shear force vs. rotation response for the bare CFS frame; a) 1-RF-M, and b) 2-FF-M.....	55
<b>Figure 2.11:</b> Example overall shear deformations of typical diaphragm test specimen .....	56

**Figure 2.12:** Force vs. deformation response for roof specimens; a) 3-RU-M (unblocked) & 7-RB-M (blocked), and b) 4-RU-C (unblocked) & 8-RB-C, 7-RB-M (blocked) ..... 56

**Figure 2.13:** Force vs. deformation response for floor specimens; a) 5-F#10-M & 9-F#12-M, and b) 6-F#10-C & 10-F#12-C, 9-F#12-M..... 57

**Figure 2.14:** Deformation for the roof unblocked diaphragm configurations; 3-RU-M & 4-RU-C; a) screw edge tear out, and b) lift-off of OSB panels..... 58

**Figure 2.15:** Deformation for blocked roof diaphragm configuration specimen, 7-RB-M & 8-RB-C; a) screw edge tear out, and b) post-ultimate bending action of steel framing (OSB panels removed for post-test photograph)..... 58

**Figure 2.16:** Deformation for floor diaphragm configurations with #10 screws, 5-F#10-M & 6-F#10-C; a) screw edge shear failure, b) relative displacement between panels, and c) panel edge contact effect ..... 58

**Figure 3.1:** Installation process: a) gypsum panels on underside of steel framing, and b) gypcrete on top of OSB panels ..... 80

**Figure 3.2:** Experimental results: a) RGYP and b) FCRETE ..... 81

**Figure 3.3:** Specimen failure modes; a) RGYP post-peak, separation of gypsum panels (OSB panels removed), b) RGYP: screws tilting, tearing-out or pulling-through, c) FCRETE: cracking of gypcrete and d) FCRETE: OSB panel separation and screw tear out at crack locations ..... 82

**Figure 3.4:** Numerical modeling specifics of CFS building; a) CFS-NEES Building, b) leaning columns, c) gravity framing..... 83

**Figure 3.4 (Continued):** Numerical modeling specifics of CFS building; d) diaphragm, e) gravity stud-to-bottom track connection, f) shear wall and g) holdown/chord stud connection .. 84

**Figure 3.5:** Pinching4 displacement points' calculation for the 2D shear wall model ..... 86

<b>Figure 3.6:</b> Shear wall model; subpanel approach.....	86
<b>Figure 3.7:</b> Schematic representation of the diaphragm modeling approach .....	88
<b>Figure 3.8:</b> Confinement factor application (CF); a) short direction, z and, b) long direction, x.....	89
<b>Figure 3.9:</b> Verification of summation method for shear walls and gravity walls with OSB and gypsum sheathing.....	93
<b>Figure 3.10:</b> Translational mode shapes: a) Long direction, $T_x= 0.34\text{sec}$ and b) Short direction, $T_z= 0.39\text{sec}$ .....	95
<b>Figure 3.11:</b> Wall-line storey drift ratio histories, x & z direction .....	96
<b>Figure 3.12:</b> Absolute acceleration response histories at floor level .....	97
<b>Figure 3.13:</b> Absolute acceleration response histories at roof level .....	97
<b>Figure 3.14:</b> Holdown/chord stud connection; LC3 & LC4 .....	99
<b>Figure 3.15:</b> Model 3 versus Model 1; wall-line drift ratio, x & z direction, floor & roof.....	103
<b>Figure 3.16:</b> Model 1 versus Model 2 versus Model 3; first floor storey drift ratios, z direction.....	104
<b>Figure 3.17:</b> Comparison; gypsum sheathing and gravity wall effect on shear wall.....	105
<b>Figure 3.18:</b> Model 1 versus 3; diaphragm shear distribution in both directions .....	105
<b>Figure 4.1:</b> Two-storey case study building; illustration of 3D numerical model.....	121
<b>Figure 4.2:</b> Mode shapes of the building for the three diaphragm conditions.....	123
<b>Figure 4.3:</b> Scaled response spectra of the selected ground motion records; Montreal, site class C.....	128
<b>Figure 4.4:</b> Scaled response spectra of the selected ground motion records; Vancouver, site class D.....	131

<b>Figure 4.5:</b> Response spectra of design level earthquake in the USA vs. the design response spectrum for Montreal, site class C and Vancouver, site class D .....	131
<b>Figure 4.6:</b> Flexibility of floor and roof subsystem for the 15GMs; Montreal.....	135
<b>Figure 4.7:</b> $MDD_f/ADVE$ and $MDD_r/ADVE$ ratios at ten peak amplitude time steps; Montreal .....	135
<b>Figure 4.8:</b> Base shear forces for the 15 GMs; Montreal.....	136
<b>Figure 4.9:</b> Storey drift ratios at maxFWIDR and maxRDR time; Montreal .....	139
<b>Figure 4.10:</b> Diaphragm forces at maxFWIDR and maxRDR time; Montreal.....	141
<b>Figure 4.11:</b> Base shear forces for the 5GMs, Vancouver, site class D.....	143
<b>Figure 4.12:</b> Storey drift ratios at maxFWIDR and maxRDR time; Vancouver .....	144
<b>Figure 4.13:</b> Diaphragm forces at maxFWIDR and maxRDR time; Vancouver.....	145
<b>Figure B.1:</b> General template; sheathing-to-framing screw location.....	184
<b>Figure B.2:</b> 3-RU-M-A, Screw failure modes .....	185
<b>Figure B.3:</b> 3-RU-M-B, Screw failure modes.....	186
<b>Figure B.4:</b> 3-RU-M-C, Screw failure modes.....	187
<b>Figure B.5:</b> 3-RU-M-D, Screw failure modes .....	188
<b>Figure B.6:</b> 4-RU-C-A, Screw failure modes .....	189
<b>Figure B.7:</b> 4-RU-C-B, Screw failure modes .....	190
<b>Figure B.8:</b> 4-RU-C-C, Screw failure modes .....	191
<b>Figure B.9:</b> 4-RU-C-D, Screw failure modes .....	192
<b>Figure B.10:</b> 5-F#10-M-A, Screw failure modes.....	193
<b>Figure B.11:</b> 5-F#10-M-B, Screw failure modes.....	194
<b>Figure B.12:</b> 5-F#10-M-C, Screw failure modes.....	195

<b>Figure B.13:</b> 5-F#10-M-D, Screw failure modes.....	196
<b>Figure B.14:</b> 6-F#10-C-A, Screw failure modes.....	197
<b>Figure B.15:</b> 6-F#10-C-B, Screw failure modes.....	198
<b>Figure B.16:</b> 6-F#10-C-C, Screw failure modes.....	199
<b>Figure B.17:</b> 6-F#10-C-D, Screw failure modes.....	200
<b>Figure B.18:</b> 7-RB-M-A, Screw failure modes.....	201
<b>Figure B.19:</b> 7-RB-M-B, Screw failure modes.....	202
<b>Figure B.20:</b> 7-RB-M-C, Screw failure modes.....	203
<b>Figure B.21:</b> 7-RB-M-D, Screw failure modes.....	204
<b>Figure B.22:</b> 8-RB-C-A, Screw failure modes .....	205
<b>Figure B.23:</b> 8-RB-C-B, Screw failure modes.....	206
<b>Figure B.24:</b> 8-RB-C-C, Screw failure modes.....	207
<b>Figure B.25:</b> 8-RB-C-D, Screw failure modes .....	208
<b>Figure B.28:</b> 9-F#12-M-A, Screw failure modes.....	209
<b>Figure B.29:</b> 9-F#12-M-B, Screw failure modes.....	210
<b>Figure B.30:</b> 9-F#12-M-C, Screw failure modes.....	211
<b>Figure B.31:</b> 9-F#12-M-D, Screw failure modes.....	212
<b>Figure B.32:</b> 10-F#12-C-A, Screw failure modes.....	213
<b>Figure B.33:</b> 10-F#12-C-B, Screw failure modes.....	214
<b>Figure B.34:</b> 10-F#12-C-C, Screw failure modes.....	215
<b>Figure B.35:</b> 10-F#12-C-D, Screw failure modes.....	216
<b>Figure C.1:</b> Test setup of the diaphragm experimental program (Chapter 2).....	217
<b>Figure C.2:</b> Test frame configuration .....	218

<b>Figure C.3:</b> Built-up I-shapes of fixed connection .....	237
<b>Figure C.4:</b> Rollers for the support of the distribution beam.....	238
<b>Figure C.5:</b> Test set-up plan view and reference to the related fabrication drawings .....	238
<b>Figure C.6:</b> Distribution beam plan view and reference to the related fabrication drawings ....	239
<b>Figure C.7:</b> Main beam-to-beam connections .....	239
<b>Figure C.8:</b> Double angle-to-angle connection plate (braces).....	240
<b>Figure C.9:</b> Diagonal brace angle 1 .....	240
<b>Figure C.10:</b> Diagonal brace angle 2 .....	241
<b>Figure C.11:</b> Main beam connected to actuator.....	241
<b>Figure C.12:</b> Main beam connected to built-up I-shapes in fixed connection location.....	242
<b>Figure C.13:</b> Main beam 1 connected to the uplift support for the distribution beam .....	242
<b>Figure C.14:</b> Main beam 2 connected to the uplift support for the distribution beam .....	243
<b>Figure C.15:</b> Centre main beam connected to middle roller support for the distribution beam.....	243
<b>Figure C.16:</b> Actuator-to-main beam connection .....	244
<b>Figure C.17:</b> Actuator-to-distribution beam connection.....	244
<b>Figure C.18:</b> Distribution beam .....	245
<b>Figure C.19:</b> Built-up I-shapes; fixed connection .....	245
<b>Figure C.20:</b> Beam connected to built-up I-shapes; fixed connection .....	246
<b>Figure D.1:</b> Stress-strain curve of specimen RJ - Roof – 1 .....	247
<b>Figure D.2:</b> Stress-strain curve of specimen RJ - Roof – 2 .....	247
<b>Figure D.3:</b> Stress-strain curve of specimen RJ - Roof – 3 .....	248
<b>Figure D.4:</b> Young’s modulus based on specimen RJ - Roof – 1.....	248

<b>Figure D.5:</b> Stress-strain curve of specimen RJ - Floor – 1 .....	248
<b>Figure D.6:</b> Stress-strain curve of specimen RJ - Floor – 2 .....	249
<b>Figure D.7:</b> Stress-strain curve of specimen RJ - Floor – 3 .....	249
<b>Figure D.8:</b> Young’s modulus based on specimen RJ - Floor – 1 .....	249
<b>Figure D.9:</b> Stress-strain curve of specimen J - Floor – 1 .....	250
<b>Figure D.10:</b> Young’s modulus based on specimen J - Floor – 1 .....	250
<b>Figure D.11:</b> Stress-strain curve of specimen J - Roof – 1 .....	250
<b>Figure D.12:</b> Stress-strain curve of specimen J - Roof – 2 .....	251
<b>Figure D.13:</b> Stress-strain curve of specimen J - Roof – 3 .....	251
<b>Figure D.14:</b> Young’s modulus based on specimen J - Roof – 1 .....	251
<b>Figure D.15:</b> Stress-strain curve of specimen J - Floor#12 – 1 .....	252
<b>Figure D.16:</b> Stress-strain curve of specimen J - Floor#12 – 2 .....	252
<b>Figure D.17:</b> Stress-strain curve of specimen J - Floor#12 – 3 .....	252
<b>Figure D.18:</b> Young’s modulus based on specimen J - Floor#12 – 1 .....	253
<b>Figure D.19:</b> Stress-strain curve of specimen J - Roof B – 1 .....	253
<b>Figure D.20:</b> Stress-strain curve of specimen J - Roof B – 2 .....	253
<b>Figure D.21:</b> Stress-strain curve of specimen J - Roof B – 3 .....	254
<b>Figure D.22:</b> Young’s modulus based on specimen J - Roof B – 1 .....	254
<b>Figure D.23:</b> Load - displacement curve of specimen R1// .....	257
<b>Figure D.24:</b> Load - displacement curve of specimen R2// .....	257
<b>Figure D.25:</b> Load - displacement curve of specimen R3// .....	258
<b>Figure D.26:</b> Load - displacement curve of specimen R4// .....	258
<b>Figure D.27:</b> Load - displacement curve of specimen R5// .....	258

<b>Figure D.28:</b> Load - displacement curve of specimen R6// .....	259
<b>Figure D.29:</b> Load - displacement curve of specimen R7// .....	259
<b>Figure D.30:</b> Load - displacement curve of specimen R8// .....	259
<b>Figure D.31:</b> Load - displacement curve of specimen R9// .....	260
<b>Figure D.32:</b> Load - displacement curve of specimen R10// .....	260
<b>Figure D.33:</b> Load - displacement curve of specimen R1L .....	260
<b>Figure D.34:</b> Load - displacement curve of specimen R2L .....	261
<b>Figure D.35:</b> Load - displacement curve of specimen R3L .....	261
<b>Figure D.36:</b> Load - displacement curve of specimen R4L .....	261
<b>Figure D.37:</b> Load - displacement curve of specimen R5L .....	262
<b>Figure D.38:</b> Load - displacement curve of specimen R6L .....	262
<b>Figure D.39:</b> Load - displacement curve of specimen R7L .....	262
<b>Figure D.40:</b> Load - displacement curve of specimen F1//.....	263
<b>Figure D.41:</b> Load - displacement curve of specimen F2//.....	263
<b>Figure D.42:</b> Load - displacement curve of specimen F3//.....	263
<b>Figure D.43:</b> Load - displacement curve of specimen F4//.....	264
<b>Figure D.44:</b> Load - displacement curve of specimen F5//.....	264
<b>Figure D.45:</b> Load - displacement curve of specimen F6//.....	264
<b>Figure D.46:</b> Load - displacement curve of specimen F7//.....	265
<b>Figure D.47:</b> Load - displacement curve of specimen F1L.....	265
<b>Figure D.48:</b> Load - displacement curve of specimen F2L.....	265
<b>Figure D.49:</b> Load - displacement curve of specimen F3L.....	266
<b>Figure D.50:</b> Load - displacement curve of specimen F4L.....	266

<b>Figure D.51:</b> Load - displacement curve of specimen F5L.....	266
<b>Figure D.52:</b> Load - displacement curve of specimen F6L.....	267
<b>Figure D.53:</b> Load - displacement curve of specimen F7L.....	267
<b>Figure D.54:</b> Tensile coupon tests .....	268
<b>Figure D.55:</b> Oven-dry method for moisture content measurements .....	268
<b>Figure D.56:</b> Dowel bearing strength test .....	268
<b>Figure E.1:</b> Absolute acceleration response histories at floor level in the x direction .....	269
<b>Figure E.2:</b> Absolute acceleration response histories at floor level in the z direction .....	270
<b>Figure E.3:</b> Absolute acceleration response histories at roof level in the x direction .....	270
<b>Figure E.4:</b> Absolute acceleration response histories at roof level in the z direction.....	271
<b>Figure E.5:</b> Scaled ground motions for Montreal, site class C: a) suite 1, T=0.05 to 0.2 sec, b) suite 2, T=0.2 to 0.5sec and c) suite 3, T=0.5 to 1.5sec.....	272
<b>Figure E.6:</b> Scaled ground motions for Vancouver, site class D.....	273
<b>Figure E.7:</b> Storey drift ratios at maxRWIDR and maxFDR time; Montreal, site class C.....	274
<b>Figure E.8:</b> Storey drift ratios at maxRWIDR and maxFDR time; Vancouver, site class D ....	275

## LIST OF TABLES

<b>Table 1.1:</b> Design shear strength values (Table F2.4-1, AISI S400 2015) .....	11
<b>Table 1.2:</b> Compression backbone empirical equations for local buckling failure mode.....	25
<b>Table 1.3:</b> Tension backbone analytical equations for local buckling failure mode, strength and stiffness degradation parameters, unloading and reloading parameters .....	25
<b>Table 2.1:</b> Basic floor and roof diaphragm configurations .....	50
<b>Table 2.2:</b> Specimen nomenclature .....	52
<b>Table 2.3:</b> Tensile properties of steel .....	54
<b>Table 2.4:</b> General results from the monotonic (M) and reversed cyclic (C) tests .....	59
<b>Table 2.5:</b> Design deflection values using Eq. 2.1 and 2.2 .....	64
<b>Table 2.6:</b> Nominal shear resistance values using Table F2.4-1 of AISI S400 (2015).....	65
<b>Table 3.1:</b> Diaphragm structural characteristics .....	79
<b>Table 3.2:</b> Mesh element Pinching <sup>4</sup> parameters; floor and roof.....	88
<b>Table 3.3:</b> CFS-NEES Building diaphragms: shear strength and stiffness.....	88
<b>Table 3.4:</b> Gravity framing; member capacities.....	91
<b>Table 3.5:</b> Phase 1/2a; wall-line storey drift ratios and fundamental periods.....	95
<b>Table 3.6:</b> Phase 1/2a; base shear values and floor diaphragm and overall displacement.....	96
<b>Table 3.7:</b> Description of model representations of CFS-NEES building .....	100
<b>Table 3.8:</b> Model 2; Fundamental period and wall line storey drift ratios.....	101
<b>Table 3.9:</b> Model 2; MDD, maximum displacements and base shear values .....	101
<b>Table 3.10:</b> Model 3; Fundamental period and wall-line storey drift ratios .....	102
<b>Table 3.11:</b> Model 3; MDD, maximum displacements, base shear and diaphragm shear forces .....	102

<b>Table 4.1:</b> Dynamic properties of representative building; z direction.....	123
<b>Table 4.2:</b> Deaggregation data, Montreal, site class C (Natural Resources Canada) .....	127
<b>Table 4.3:</b> Selected ground motions and scaling factors.....	128
<b>Table 4.4:</b> Selection criteria; Vancouver, site class D .....	130
<b>Table 4.5:</b> Selected ground motion records; Vancouver, site class D.....	130
<b>Table 4.6:</b> $CNP_{x&z}$ , Part 1; Wall-line storey drift ratios .....	132
<b>Table 4.7:</b> $CNP_{x&z}$ , Part 1; MDD, maximum displacements and base shear forces.....	132
<b>Table 4.8:</b> $CNP_{z&x}$ , Part 2; Wall-line storey drift ratios .....	133
<b>Table 4.9:</b> $CNP_{z&x}$ , Part 1; MDDf/r, maximum displacements and base shear forces .....	133
<b>Table 4.10:</b> Comparison of base shear values for the three flexibility systems; Montreal .....	137
<b>Table 4.11:</b> Comparison of shear force values for the three flexibility systems for each individual shear wall; Montreal .....	138
<b>Table 4.12:</b> Comparison of storey drift ratios for the three flexibility systems at maxFWIDR and maxRDR time; Montreal.....	140
<b>Table 4.13:</b> Comparison of max diaphragm forces for the three flexibility systems at floor level at maxFWIDR and roof level at maxRDR time; Montreal.....	142
<b>Table 4.14:</b> Variability of results between the three flexibility systems; Montreal .....	142
<b>Table 4.15:</b> Comparison of base shear values for the three flexibility systems; Vancouver .....	143
<b>Table 4.16:</b> Comparison of storey drift ratios for the three flexibility systems; Vancouver .....	144
<b>Table 4.17:</b> Comparison of max diaphragm forces for the three flexibility systems; Vancouver .....	145
<b>Table A.1:</b> Pinching4 parameters; diaphragm specimens .....	180
<b>Table A.2:</b> Formulas for Pinching4 parameters generation for a mesh element.....	181

<b>Table A.3:</b> Pinching4 parameters; floor & roof subsystems (No CF) .....	182
<b>Table A.4:</b> Pinching4 parameters; gravity elements (+/-) .....	183
<b>Table D.1:</b> Moisture content measurement .....	255
<b>Table D.2:</b> Moisture content measurement; extra samples .....	255
<b>Table D.3:</b> Dowel bearing strength test results .....	256

# CHAPTER 1: INTRODUCTION AND BACKGROUND

## 1.1- General overview

High-strength and light-weight cold-formed steel (CFS) members can be used as the main structural components for low-rise buildings (2 to 5 storeys). Two design methods are available for CFS members; the effective width method and the direct strength method (DSM), which was developed by Schafer (2010) at Johns Hopkins University. Both design methods are available in the AISI S100 Standard (2016) and the CSA S136 Standard (2016), among others. Typical construction practice of CFS framed buildings involves stud framing along the length of the walls and discretely or continuously braced joist framing for the floors and roof. Three CFS framing configurations between storeys are available for selection: 1) platform framing, where the wall at each storey is supported by the diaphragm (floor) of the previous storey (wall-studs interrupted); 2) balloon framing, where the wall studs are continuous throughout the height of the building and the floors are supported by the wall (wall-studs passing through the floor subsystem); and 3) ledger framing, where the wall of each storey is supported by the wall of the previous storey with the diaphragm on that level being also supported by a ledger member attached to the side of the wall. Stud and joist framing is commonly sheathed with plywood or oriented strand-board (OSB) panels to provide structural shear resistance against lateral loads (shear walls and diaphragms). Figure 1.1 illustrates a CFS framed / wood-sheathed diaphragm and shear wall, system in a typical structure. Shear walls are considered the primary component of the lateral force resisting system; however, the diaphragm's role is to distribute the lateral loads to the shear walls and ensure structural stability; as such its contribution to the lateral resistance of a CFS framed building is invaluable.

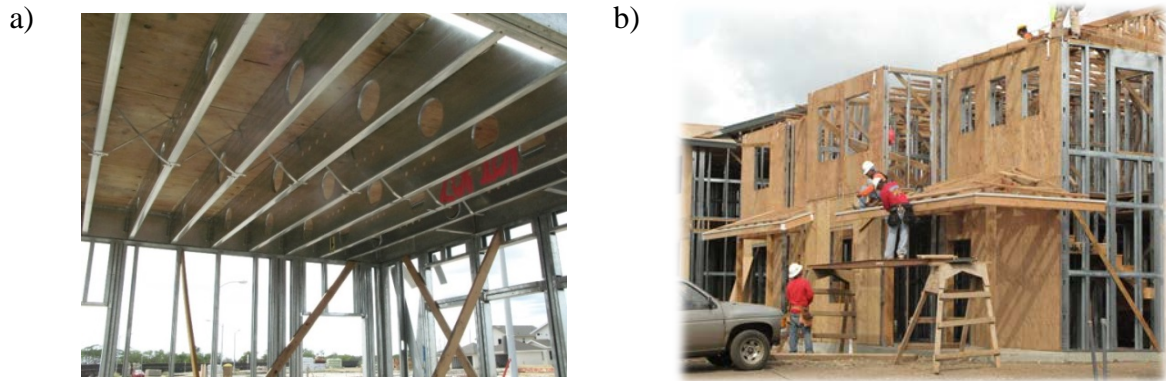


Figure 1.1: Example CFS framed construction; a) diaphragm and b) shear wall

Additional non-structural interior gypsum sheathing installed on the underside of the diaphragms (ceiling) and on the shear walls has become commonplace for purposes of fire-resistance and sound insulation. As well, other materials such as gypcrete, which is placed on the upper side of the diaphragms, can be used for additional sound insulation. Gravity framing may also be sheathed with wood panels; gravity walls are found along the perimeter of the building and bearing walls in the interior. Figure 1.2 illustrates a typical CFS framed building including non-structural components.

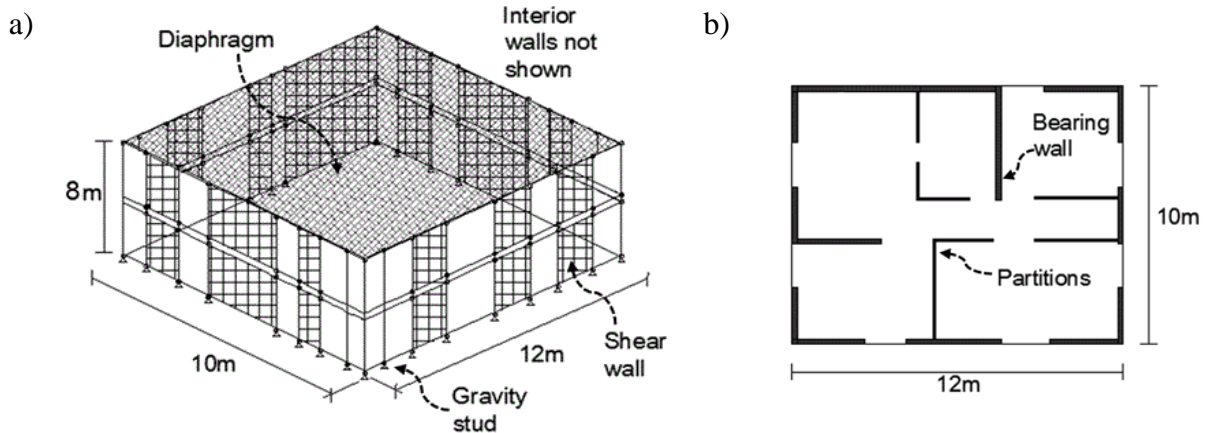


Figure 1.2: CFS framed building; a) 3D view and, b) plan view

In the last two decades there has been an increased interest in better understanding the seismic

response of CFS framed buildings, with the focus of research studies expanding from the isolated CFS stud behaviour to the CFS framed subsystem's (shear walls, diaphragms) and, eventually, the full CFS building's lateral response. The purpose is to improve the current code provisions addressing the seismic design of CFS framed structures (AISI S400 (2015) North American Standard for Seismic Design of Cold-Formed Steel Structural Systems, AISI S100 (2016) / CSA S136 (2016) North American Specification for the Design of Cold-Formed Steel Structural Members) in order to facilitate professional engineers in the construction of better, safer and more economical CFS structures. At present, the National Building Code of Canada (NBCC) (NRCC 2015) refers to the CSA S136 Standard (2016) for detailed design calculations, while this Standard in turn refers to the AISI S400 Standard (2015) for design guidelines of CFS framed systems under lateral loading. AISI S400 includes the design information for different types of lateral systems (wood sheathed shear walls, steel sheet sheathed shear walls, strap braced walls, and special moment frames), such that the response modification  $R$  coefficients in the USA as well as the equivalent  $R_d$ ,  $R_o$  seismic force modification factors in Canada listed in ASCE 7 (2016) and NBCC (NRCC 2015), respectively, can be attained. It should be noted that AISI S400 contains  $R_d$ ,  $R_o$  values for steel sheathed shear walls for Canada, which have yet to be included in the NBCC. The diaphragm's contribution to the lateral response of the structure to seismic loading is not taken into account in the design procedures found in AISI S400. A limited number of shear strength design values for specific CFS framed diaphragm configurations (LGSEA 1998) are included in the AISI S400 Standard for the USA (Table F2.4-1 (AISI 2015)) indicating that principles of mechanics must be employed for the shear strength calculation for any other type of diaphragm subsystem. Moreover, a diaphragm deflection equation (Eq. C-F2.4.3-1, Eq. 1.1 in this thesis) is available in the AISI S400 Standard (2015); however, Eq. 1.1

was procured by applying slight modifications to the deflection equation of wood framed diaphragms (Serrette and Chau 2003, see Section 1.5). For the design of wood sheathed / CFS framed diaphragms for use in Canada, no information is currently available in the AISI S400, NBCC and CSA S136 Standards. In addition, there is a lack of information regarding the effect of non-structural components on the overall lateral stiffness of the CFS structure and the additional capacity forces that they may impose on the structure. In Canada, shear walls with structural wood sheathing on one side and non-structural gypsum sheathing on the other side are included in the seismic design (AISI S400 2015). In the USA, this lateral force resisting system is not recognized; instead, the benefit from the presence of gypsum is considered inherent in the over-strength factor. The behaviour of non-structural elements and the interaction between structural and non-structural components during earthquake excitation is not well understood for CFS construction (accelerations and displacements experienced by the non-structural elements). Extensive experimental and numerical work involving multi-degree-of-freedom finite element models is necessary in order for the dynamic properties of these components and their connections to the structural elements to be established. As such, designers, oftentimes, rely on past-earthquake / post-event observations and engineering intuition for the non-structural elements' isolated design and implementation in the structure (Filiatrault and Sullivan 2014).

## **1.2- Research objectives**

The purpose of this study is to improve the knowledge on the lateral response of wood sheathed / CFS framed diaphragms to lateral loading and to investigate the influence of diaphragm flexibility on the seismic response of CFS buildings, including the effect of non-structural components. The intent is to offer guidance in the development of seismic design and detailing recommendations for CFS buildings with these diaphragm configurations that can be used in accordance with the NBCC (2015) and can be included in the AISI S400 Standard (2015).

For the purpose of this research to be achieved five main objectives were identified:

- ✓ Develop design shear strength and stiffness values for wood sheathed / CFS framed diaphragm configurations for use in Canada; characterize the diaphragm behaviour and investigate the influence of non-structural components on the diaphragm response.
- ✓ Develop a nonlinear 2D numerical model of CFS-framed diaphragms to be incorporated in 3D nonlinear models of CFS buildings adopting a simplified numerical modeling approach for the purpose of exploring the seismic response of a CFS building.
- ✓ Investigate the effect of non-structural components on the seismic response of a CFS building.
- ✓ Investigate the influence of the diaphragm's flexibility on the seismic response of a CFS building.
- ✓ Characterize the diaphragm's shear force distribution and shear force transfer to the shear walls.

### **1.3- Scope and limitations**

This study encompasses:

- A literature review on experimental and numerical studies of CFS and wood framed shear walls and diaphragms, non-structural components, the overall seismic response of CFS framed buildings, as well as other types of buildings with flexible diaphragms and the current design guidelines for seismic evaluation of structures in Canada.
- Description of a diaphragm experimental program presented in two phases including the design of a test setup to accommodate the tests and presenting results of quasi-static monotonic and reversed cyclic loading for OSB sheathed / CFS framed diaphragm configurations.
- A database of shear strength and stiffness values for OSB sheathed / CFS framed

diaphragms based on the experimental data.

- Evaluation of the design shear strength and stiffness predictions for CFS framed diaphragms currently available in the AISI S400 Standard (2015).
- Development of a 2D nonlinear numerical model created in the Open System for Earthquake Engineering Simulation (OpenSees) platform (McKenna 1997) representing OSB sheathed / CFS framed diaphragms and its calibration using the experimental data.
- Description of a simplified phenomenological modeling approach for a two-storey CFS building including shear walls, diaphragms, gravity framing and walls using the OpenSees platform.
- Experimental and nonlinear response history dynamic analyses highlighting the quantitative contribution of non-structural gypsum panels and gypcrete topping on the lateral response on a subsystem and system level.
- Modal analyses results depicting the effect of diaphragm flexibility on the dynamic properties of CFS buildings.
- Nonlinear response history analyses for three flexibility systems exploring three diaphragm stiffness conditions for a two-storey CFS building under design level earthquake ground motions.
- Characterization of the OSB sheathed / CFS framed floor's/roof's shear force distribution and evaluation of the rigid diaphragm assumption as a design approach for CFS buildings.

The work presented herein is limited to a narrow rectangular two-storey wood sheathed / CFS framed building of 7.01x15.16m size with 2.74m storey height with only perimeter shear and gravity walls (no interior walls). The diaphragm properties available are constrained to the structural and non-structural elements of the 3.66x6.1m OSB sheathed/CFS framed diaphragm

configurations tested in the Jamieson Structures Laboratory at McGill University following the cantilever testing method. Openings in the diaphragm subsystem are not considered. The earthquake ground motions employed include a design level earthquake in California, USA, following the preceding experimental study for the two-storey CFS building in question, as described in Section 1.5, as well as design level earthquake ground motions for Montreal, site class C and Vancouver, site class D, Canada.

#### **1.4- Thesis outline**

This experimental and numerical study is presented in five chapters. Following is a brief summary of the content for each chapter:

Chapter 1 contains a general overview of the topic discussed and a brief breakdown of the preceding literature that provided the foundation for this thesis, as well as recent advancements on the topic, organized in five categories:

- Diaphragm design provisions
- Diaphragm and shear wall studies
- CFS gravity framing studies
- Non-structural gypsum sheathing and gravity walls studies
- Diaphragm flexibility studies
- Seismic assessment in Canada

In Chapter 2 a presentation of the first phase of the diaphragm experimental program is provided. The chapter includes a brief description of the designed test setup and a characterization of the OSB sheathed/CFS framed diaphragm specimens' lateral response. The resulting shear strength and stiffness values of all diaphragm configurations are summarised and the equivalent design predictions available in the AISI S400 Standard (2015) are evaluated.

The focus of Chapter 3 is on the effect of non-structural components on the lateral response at a

---

system and subsystem level. In the first section of the chapter, experimental results are presented from the second phase of the diaphragm experimental program for the case of diaphragm configurations with gypsum ceiling and gypcrete topping. In the second section of the chapter, a simplified phenomenological modeling approach is described for the two-storey CFS framed building with explicit modeling of the diaphragm component, as well as the shear walls, gravity framing and gravity walls. The 3D numerical model is verified against experimental work found in Peterman (2014). Non-structural components are gradually implemented in the model, from the floor and roof to the wall-line perimeter throughout. Nonlinear response history dynamic analyses results are summarised under the Canoga Park earthquake in the two main horizontal directions (x and z) of the building.

Chapter 4 includes the results of modal and nonlinear response history dynamic analyses for three diaphragm flexibility systems under design level ground motions in Montreal, site class C and Vancouver, site class D, Canada. A preliminary study under the Canoga Park earthquake constitutes the foundation for the extensive subsequent ground motions study. The dynamic properties of the three flexibility systems are described and results in terms of base shear forces, shear wall forces, diaphragm forces, maximum diaphragm and overall displacements are explained. The importance of the input ground motion in the resulting forces and drifts is explored and the interaction between diaphragm and shear walls, as well as the diaphragm shear force distribution for the three flexibility systems is illustrated.

Chapter 5 contains a summary of the main findings of Chapters 2, 3 and 4, and offers recommendations for further experimental and numerical research.

### **1.5- Literature review**

In this section, a review is presented of previous studies related to the topics of CFS diaphragm, shear wall and building response to lateral loading. Six subsections are identified starting with

the action of the diaphragm component and its design parameters, along with the currently available design guidelines in the AISI S400 Standard (2015). The second subsection includes experimental and numerical work available on wood sheathed / CFS framed diaphragms and shear walls. The third and fourth subsections present research studies on gravity framing and non-structural components, respectively, while the fifth subsection focuses on the effect of diaphragm flexibility on the overall seismic response of buildings with various lateral force resisting systems. The literature review concludes with information available in the NBCC (2015) for the seismic assessment of structures in Canada.

### 1.5.1 Diaphragm design provisions

The floor or roof system in a structure acts as a structural diaphragm transferring the horizontal wind or earthquake forces to the vertical lateral force resisting system (LFRS) (shear walls or strap-braced walls), while ensuring stability of the structure. A diaphragm subsystem is typically comprised of framing, sheathing connected to the framing with fasteners (screws or nails) and the perimeter members (FEMA 1998), as shown in Figure 1.3a.

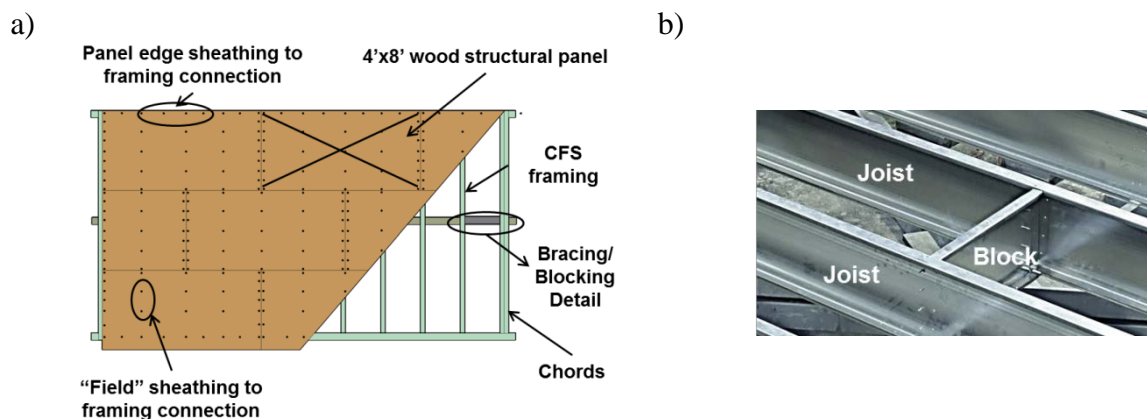


Figure 1.3: Typical CFS framed diaphragm assembly; a) structural details and, b) blocking

The diaphragm is often described as a deep, thin, wide-flanged beam, the web of which is the sheathing resisting the shear stresses, while the flanges are the perimeter edge members resisting

the flexural stresses (chords) (APA 2007). The design of a diaphragm involves the calculation of its in-plane shear stiffness and strength. A critical part to the design process is to ensure adequate shear capacity and stiffness for the diaphragm by means of designing suitable connections between the sheathing and the framing, as well as the diaphragm as a unit and the vertical LFRS elements (APA 2007). The diaphragm's contribution to resisting seismic loads in a structure depends also on its stiffness relative to the shear walls (FEMA 1998). In general, a diaphragm can be described as flexible, rigid or semi-rigid / semi-flexible. In flexible diaphragms the continuity of the chords is ignored and load is distributed based on the tributary areas of the shear walls. For rigid diaphragms, the relative stiffness of the shear walls dictates the load distribution, while for the semi-rigid case a structural analysis that takes into account the relative stiffness of the horizontal and vertical load carrying systems is required. Moreover, an important characteristic of diaphragms that influences their strength and stiffness is blocking (Figure 1.3b). In a blocked diaphragm additional supports are placed in the intermediate panel locations (simple sheet metal or CFS steel small sections) to which the panel edges are fastened (ASCE 7 2016, IBC 2015). In addition, when considering CFS framed diaphragms there is the possibility of stiffness reduction for the CFS (thin-walled) sections due to local, distortional or global buckling, that should be taken into account in the design in order for a good estimate of the diaphragm's behaviour to be made.

The AISI S400 Standard (2015) provides Table F2.4-1 (Table 1.1 in this thesis) with design shear strength values as they were developed by the analytical work of the Light Gauge Steel Engineers Association (LGSEA 1998). LGSEA provided allowable design strength values for plywood sheathed-only / CFS framed diaphragms using the National Design Specification (NDS 1991) calculation formulas for the fasteners and Tissell's and Elliot's (2004) methodology for

wood framing to calculate the diaphragm’s ultimate shear strength. Field and perimeter screw spacing was taken into account as an influential parameter in the calculation of these design shear strength values but screw size was not considered.

Table 1.1: Design shear strength values (Table F2.4-1, AISI S400 2015)

*United States and Mexico*  
Nominal Shear Strength ( $R_n$ ) for Diaphragms with Wood Sheathing<sup>1, 4</sup>  
(Pounds Per Foot)

Membrane Material	Screw Size	Thick-ness (In.)	Blocked				Unblocked	
			Screw spacing at diaphragm boundary edges and at all continuous panel edges (In.)				Screws spaced maximum of 6" on all supported edges	
			6	4	2.5	2	Load perpendicular to unblocked edges and continuous panel joints	All other configurations
			Screw spacing at all other panel edges (In.)					
6	6	4	3					
Structural I	See note 2	3/8	768	1022	1660	2045	685	510
		7/16	768	1127	1800	2255	755	565
		15/32	925	1232	1970	2465	825	615
C-D, C-C and other graded wood structural panels <sup>3</sup>	See note 2	3/8	690	920	1470	1840	615	460
		7/16	760	1015	1620	2030	680	505
		15/32	832	1110	1770	2215	740	555

1. For SI: 1" = 25.4 mm, 1 foot = 0.305 m, 1 lb = 4.45 N.
2. No. 8 screws (minimum) shall be used when framing members have a designation thickness of 54 mils or less and No. 10 screws (minimum) shall be used when framing members have a designation thickness greater than 54 mils.
3. Wood structural panels shall conform to DOC PS-1 and PS-2.
4. For wood structural panel sheathed diaphragms, tabulated  $R_n$  values shall be applicable for short-term load duration (wind or seismic loads). For other in-plane lateral loads of normal or permanent load duration as defined by the AF&PA NDS, the values in the table above for wood structural panel sheathed diaphragms shall be multiplied by 0.75 (normal) or 0.67 (permanent).

Serrette and Chau (2003) developed a mid-point deflection equation for simply supported CFS framed diaphragms by initially focusing on CFS framed shear walls. A method was proposed for the drift calculation of CFS framed shear walls with plywood, OSB or steel sheet sheathing. Gypsum sheathing was not included. The formula was based on the equivalent existing deflection equation for wood-framed shear walls, and incorporates empirical factors for the nonlinear component of the response and adjustment factors to account for the flexibility of the CFS framing shear wall configurations. Regression and interpolation analyses using shear wall test data from an experimental program were relied upon to obtain the adjustment factors. Subsequently, based on the similarities of the nonlinear response of wood-framed and CFS-

framed shear walls and of the wood-framed diaphragm and shear wall equations, Serrette and Chau proposed a second deflection equation for CFS framed diaphragms; modification factors were applied to the wood-framed diaphragm equation to account for the CFS framed diaphragm configurations. This diaphragm deflection equation is available in the AISI S400 Standard (2015) (Eq. C-F2.4.3-1) and it is Eq. 1.1 in this thesis (Eq. 1.1 is referred to as Eq. 2.2 in Chapter 2):

$$\delta = \frac{0.052vL^3}{E_s A_c b} + \frac{\omega_1 \omega_2 v L}{\rho G t_{sheathing}} + \omega_1^{\frac{5}{4}} \omega_2 (a) \left(\frac{v}{2\beta}\right)^2 + \frac{\sum_{j=1}^n \Delta_{ci} X_i}{2b} \quad (1.1)$$

, where

$A_c$  = Gross cross-sectional area of chord member ( $\text{mm}^2$ )

$b$  = Width of the shear wall/diaphragm (parallel to loading) (mm)

$E_s$  = Modulus of elasticity of steel 203,000 MPa

$G$  = Shear modulus of sheathing material (MPa)

$L$  = Diaphragm length perpendicular to direction of load (mm)

$n$  = Number of chord splices in diaphragm (considering both diaphragm chords)

$t_{sheathing}$  = Nominal panel thickness (mm)

$t_{stud}$  = Nominal framing thickness (mm)

$V$  = Total in-plane load applied to the diaphragm (N)

$v$  = Shear demand ( $V/b$ ), (N/mm)

$X_i$  = Distance between the “ $i^{\text{th}}$ ” chord-splice and the nearest support (mm)

$\alpha$  = 1 for a uniformly fastened diaphragm

$\beta$  = 2.35 for plywood and 1.91 for OSB for SI units ( $\text{N}/\text{mm}^{1.5}$ )

$\Delta_{ci}$  = Deformation value associated with “ $i^{\text{th}}$ ” chord splice (mm)

$\delta$  = Calculated in-plane deflection (mm)

$\rho$  = 1.85 for plywood and 1.05 for OSB, term for different sheathing material type

$\omega_1$  =  $s/152.4$  (for  $s$  in mm)

$\omega_2$  =  $0.838/t_{\text{stud}}$  (for  $t_{\text{stud}}$  in mm)

The terms of Eq. 1.1 express the following effects in the diaphragm lateral response: 1) the bending effect (1<sup>st</sup> term) based on the flexural capacity of chord members, 2) the shear effect (2<sup>nd</sup> term) based on shear capacity of the sheathing, 3) the inelastic effect (3<sup>rd</sup> term) using empirical factors and 4) the chord splice deformation effect due to the high tensile force applied in the chord members from lateral loading. The diaphragm design deflection equation applies for fully blocked diaphragms; a factor of 2.5 is suggested in the AISI S400 Standard (AISI 2015) for the case of unblocked diaphragms.

## **1.5.2 Diaphragm and shear wall studies**

### **1.5.2.1 Experimental work**

The only pre-existing experimental work on CFS framed diaphragms was realised in 1999 by the National Association of Home Builders Research Center (NAHBRC 1999). In this study four 3.6x7.2m diaphragm specimens were tested involving two different CFS framing thicknesses with CFS C-channel perforated joists. The specimens were unblocked with 18mm (23/32in) wood sheathing and a typical 152/305mm (6/12 in) spacing pattern of #8 sheathing screws. The maximum capacity reached was 138KN under a cyclic loading protocol consisting of two monotonic loading cycles (loading, unloading towards one direction) and pushing the diaphragm to failure. The NAHBRC also examined the individual sheathing-to-framing screw behaviour and proposed alterations to the screw slip coefficient in the existing diaphragm deflection equations for wood diaphragms provided by the American Plywood Association (Tissell and Elliott 2004, APA) in order to facilitate design predictions for CFS framed diaphragms. The importance of the individual screw shear capacity for the overall diaphragm response was

established. From 1999 there have been no other experiments involving CFS framed diaphragms until the diaphragm experimental program presented in this thesis, in Chapter 2.

Given the lack of experimental work on CFS framed diaphragms, wood framed diaphragm as well as wood and CFS framed shear wall experimental work was relied upon to gain insight as to how a CFS framed diaphragm may respond to seismic loading. One of the early studies on wood-framed shear walls and diaphragms was realized by Itani et al. (1988), where quasi-static loading and free vibration tests were performed on 2.4x2.4m plywood sheathed / wood-framed walls in order to investigate the effect of sheathing-to-framing connections and of the screw spacing; the walls were representative elements for both walls and floors of a wood-framed building. In a subsequent study, Dolan and Madsen (1992) performed 7 monotonic and 4 slow cyclic tests on wafer-board and plywood sheathed timber shear walls, including the effect of gravity loading. Richard et al. (2002) characterized the static and dynamic response of OSB sheathed timber shear walls with large openings. All studies highlighted the importance of the sheathing-to-framing connectors. Focusing on timber diaphragms, Bott (2005) tested 6 full-scale 6.1x4.9m or 3.0x12.2m diaphragms with various structural characteristics in an effort to accurately capture their stiffness and damping. Piazza et al. (2008) aimed to obtain the shear strength and stiffness of 4.0x5.0m timber framed diaphragms, commonly found in masonry buildings, including the effect of reinforcing elements; various reinforcing techniques were investigated. In a system level, shake table test results of a full-scale two storey wood framed building were presented in Christovasilis et al. (2008); the building was considered to be located in California. The building was constructed in several phases allowing for the influence of non-structural elements on the overall seismic response to become evident. More recent work involves 4.0x4.0m simply supported timber/ framed diaphragms being tested by Brignola et al.

(2012) under quasi-static reversed cyclic loading, where the importance of the diaphragm-to-wall connection was also demonstrated. Fuentes et al. (2014) tested two 2.4x7.2m timber framed diaphragms sheathed with particle panels, while Chen et al. (2014) tested 12 OSB and gypsum sheathed timber shear walls under monotonic and reversed cyclic loading. Chen's work is described further in Section 1.5.4. In addition, most recent work involves wood-framed gypsum sheathed shear walls by Lafontaine et al. (2017), where eleven 2.44x2.44m shear walls with 16mm gypsum sheathing were tested under monotonic and reversed cyclic loading.

Extensive work is available on CFS framed shear walls in a system and subsystem level; e.g. Tissel (1993), Serrette et al. (1996, 1997), Zhao (2002), Chen (2004), Landolfo et al. (2006), Branston et al. (2006), Boudreault et al. (2007), Liu et al. (2012), Yu and Li (2012), Iuorio et al. (2014), Shamim et al. (2013) and Fiorino et al. (2017), among others. In particular, Tissel (2003) tested 8 steel stud / OSB sheathed shear walls in order to provide information on the influence on the shear wall's lateral response of structural parameters such as fastener size, fastener spacing and framing thickness. Serrette et al. (1996, 1997) tested 1.2x2.4m light gauged steel framed shear walls sheathed with three types of panels, OSB, plywood and gypsum; the effect of screw spacing was explored as well.

Zhao (2002), Chen (2004), Branston et al. (2006) and Boudreault et al. (2007) were part of a major project at McGill University, which involved investigating the global response of CFS buildings as a function of the wood sheathed / CFS framed shear walls through the use of laboratory tests and numerical response history dynamic analyses. The program yielded a design analytical method for shear strength and stiffness, as well as seismic force modification factors ( $R_d$ ,  $R_o$ ) for wood sheathed / CFS framed shear walls, at present included in the NBCC and AISI S400. In the experimental part of their work the CUREE reversed cyclic loading protocol was

employed (Krawinkler et al. 2000). A total of 184 CFS framed shear walls were tested, including three specimen sizes 0.61x2.44m, 1.22x2.44m and 2.44x2.44m and five types of plywood and OSB sheathing (different thicknesses and wood material properties). In Shamim et al. (2013), further experimental testing was conducted focusing on steel sheathed CFS framed shear walls; dynamic testing of 10 1.2x2.4m shear wall configurations was realized as one of the steps in developing a design method for these lateral force resisting systems.

In the University of Naples “Federico II”, Landolfo et al. (2006) tested two prototype CFS framed buildings under monotonic and reversed cyclic loading, focusing on the nonlinear response of the 2.7x2.51m wood-sheathed shear walls. Exterior OSB and interior gypsum panels were considered as sheathing of the shear walls, while the floor was sheathed only with OSB. The cyclic protocol loading applied was developed by a previous numerical study of the authors (Della Corte et al. 2005). This work was part of a wider research project aimed to develop a performance – based seismic design procedure for OSB sheathed and gypsum sheathed shear walls (Fiorino et al. 2012). In addition, recent work of Iuorio et al. (2014) involved monotonic (loading-unloading) testing of 2 4.8x3.95m shear walls with OSB sheathing as part of building incorporating stick-built construction; auxiliary individual testing of holdowns, sheathing to framing connections and OSB panels was realised. Further, an ongoing research project at the University of Naples “Federico II” introduced a new type of construction for CFS structures using enhanced prefabricated lightweight CFS skeleton and special gypsum-based sheathing with improved seismic capabilities. In Fiorino et al. (2017) shake table test results are presented for a prototype of a 4.7x2.7m two-storey CFS building sheathed with gypsum-based panels and tested in two phases; with structural elements only and with the addition of non-structural components.

Experimental results on the lateral force resisting systems employed in the prototype two-storey CFS building in Fiorino et al. (2017) can be found in Macillo et al. (2017).

Yu and Li (2012) conducted eight monotonic and four cyclic tests on 1.22mx2.44m shear walls examining the benefits of composite steel-gypsum sheathing. The shear walls were tested under the CUREE displacement controlled loading protocol (Krawinkler et al. 2000); eight framing configurations were considered varying the chord stud, rim joist and interior stud sections and spacing. Liu et al. (2012) tested a total of 16 CFS framed shear wall configurations considering two specimen sizes, 1.22x2.74m and 2.44x2.74m. The shear wall configurations were primarily OSB sheathed except for one configuration, where only exterior gypsum panels were installed. The effect of structural details such as chord stud thickness and grade and ledger installation at the top of the wall (rim joist) as well as interior gypsum sheathing, were investigated, among others. Monotonic and the CUREE (Krawinkler et al. 2000) loading protocol, chosen for reversed cyclic loading, was applied.

On a system level, Liu et al. (2012) were part of a major research program realised at Johns Hopkins University entitled “Enabling Performance-Based Seismic Design of Multi-Story Cold-Formed Steel Structures” involving a full size two-storey CFS wood sheathed shear wall building (CFS-NEES Building) tested under earthquake loading using the Network for Earthquake Engineering Simulation (NEES) equipment site (shake table) at the State University of New York (SUNY) at Buffalo in the USA (Peterman 2014). Experimental work on the shear walls of the building was provided by Liu et al., while Peterman examined the overall seismic response to seismic loading of the building using the instrumentation data in place for the shear walls and diaphragms (Peterman et al. 2016a,b). A ledger framing construction technique was followed; a full description of the design of the CFS-NEES Building can be found in Madsen et

al. (2011). Specifically, a 7.01x15.16m two-storey CFS framed building was tested under the Canoga Park (design basis earthquake, DBE) and the Rinaldi (maximum considered earthquake, MCE) ground motions in five separate phases of construction (Figure 1.4). At each phase the ground motions were applied gradually from 16% to 100% of the full amplitude of the earthquake. The first construction phase included only the structural elements of the building (shear walls, diaphragms, gravity framing). In the subsequent phases non-structural and interior elements were gradually added (OSB sheathing throughout, interior gypsum panels, gypsum ceiling, partition walls and staircases). The final construction phase included the finishing material for the building, such as DensGlass fiberglass sheathing for moisture insulation purposes.



Figure 1.4: CFS-NEES Building (courtesy of Dr. Kara Peterman, University of Massachusetts Amherst)

The CFS-NEES Building performed beyond expectation based on the current seismic design method; however the reasons for this excellent performance are not fully understood. Shear walls showed a coupled response, indicating that the wood-sheathed gravity framing contributed greatly in the lateral resistance of the building. Exterior OSB throughout and interior gypsum had a more pronounced stiffening effect on the seismic response of the building than the DensGlass added in the last phase. The floor subsystem was found to be semi-rigid, while higher

accelerations were observed for the roof subsystem (not adequately instrumented for further information). Results from the accelerometer data available suggest that interior partition walls have sufficient length to provide coupling between the floor and the roof subsystems.

After the completion of the CFS-NEES project and the diaphragm experimental program conducted at McGill University described in this thesis, a full-scale testing of the simply supported floor assembly of the CFS-NEES Building was realized by Florig et al. (2015). The floor was tested under monotonic loading. Pin connections were constructed throughout the perimeter using slotted HSS perimeter guides. These supports allowed the chord elements to move in the loading direction and be free to bend, while the supported sides of the diaphragm (connected to shear walls) were restrained. A ledger framing connection was incorporated using CFS-stud and track members to screw in and “sandwich” on top the wood diaphragm sheathing. Further discussion of the work of Florig et al. related to the diaphragm experimental program described herein is provided in Chapter 3.

A recent study on cold-formed steel diaphragms was completed at the University of Trento in Italy that involves both experimental and numerical work. Baldassino et al. (2017) tested four full-scale CFS framed diaphragm assemblies following a cantilever testing method. Two types of joist systems were considered, truss C sections of 100mm height resulting in a diaphragm specimen size of 4.9x6m size and coupled back – to – back C sections of 200mm height resulting in a diaphragm specimen size of 4.9x4.5m. For the two systems two types of decks were explored, steel sheet with gypsum boards and steel sheet with concrete slab. The loading applied was monotonic with loading and unloading cycles without reversing the loading direction. The concrete slab led to a higher shear strength compared to the gypsum boards while the coupled

beams' higher rotational stiffness led to a higher shear resistance compared to the truss beams. Details of the numerical part of this work are presented in Section 1.5.2.2.

### 1.5.2.2 Numerical work

The CFS-NEES Building was the first full-scale experiment involving a CFS framed structure and, thus, constitutes the backbone for many numerical studies on CFS buildings. Shamim and Rogers (2013, 2015) conducted incremental dynamic analyses (IDA) of archetype CFS buildings including the CFS-NEES Building using a 3D numerical model in the OpenSees simulation platform (McKenna 1997) as part of the investigation of the seismic response of steel sheathed CFS framed shear wall subsystems. Pin ended truss elements were used to simulate the walls incorporating the uniaxial Pinching4 material model (Lowes and Altoontash 2003), calibrated using experimental data (Figure 1.6). The pinching nature of the shear wall lateral response is directly attributed to the pinching nature of the sheathing-to-framing connections response. During constant unloading (path c-b, Figure 1.6) the screw loses partial contact with the surrounding wood material; contact is regained once reloading starts in the opposite direction (path c-d, Figure 1.6).

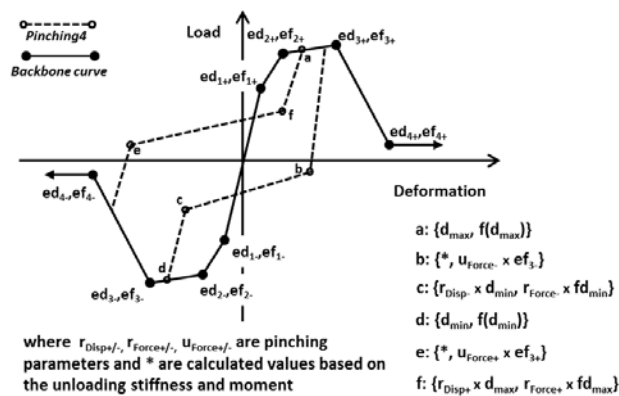


Figure 1.6: Pinching4 material model in the OpenSees Platform (Lowes and Altoontash 2003)

Leng et al. (2017) created a detailed 3D numerical model of the CFS-NEES Building incorporating most of its elements, and conducted non-linear response history analyses in order

to validate his numerical approach with the experimental data from Peterman (2014). His shear wall model followed Shamim and Rogers' numerical approach, while using Liu's experimental data to calibrate the pinching parameters of the shear wall model. It should be mentioned that in Fiorino et al. (2018) both a fastener-based finite element approach and a phenomenological approach using truss elements was used in order to simulate shear walls sheathed with gypsum-based material, related to their experimental work as mentioned in Section 1.5.2.1. Fiorino et al. (2018) mentioned that, although the finite element model requires less experimental data, the simplicity of the phenomenological model allows it to be used in whole building models and it captures accurately enough the shear wall response.

In order to ensure interaction of the shear walls with the gravity framing, Leng et al. (2017) introduced the subpanel approach, where each shear wall is represented by multiple pairs of truss elements, which are by-products of the initial pair of truss elements calibrated using the experimental data. Simple formulas are followed to acquire the material properties for the subpanels as explained in Leng's thesis (2015); Eq. 1.2 and 1.3 summarise the subpanel approach.

$$\sigma_p = \sigma_o \frac{A_o}{A_p} \frac{\cos \theta_o}{\cos \theta_p} \frac{b_p}{b_o} = \sigma_o \frac{A_o}{A_p} \frac{b_o/l_o}{b_p/l_p} \frac{b_p}{b_o} = \sigma_o \frac{A_o}{A_p} \frac{l_p}{l_o} \quad (1.2)$$

$$\varepsilon_p = \varepsilon_o \frac{l_o}{l_p} \frac{\cos \theta_p}{\cos \theta_o} \frac{h_p}{h_o} = \varepsilon_o \frac{l_o}{l_p} \frac{b_p/l_p}{b_o/l_o} \frac{h_p}{h_o} = \varepsilon_o \frac{l_o^2}{l_p^2} \frac{b_p}{b_o} \frac{h_p}{h_o} \quad (1.3)$$

, where  $\sigma_o$ ,  $\varepsilon_o$ ,  $A_o$ ,  $b_o$ ,  $h_o$ ,  $l_o$  and  $\theta_o$  are the stress, strain, truss area, width, height, length and angle of the whole panel such as  $\cos \theta_o = b_o/l_o$  (initial reference one pair of truss elements), respectively, while the same parameters with the subscript "p" are the properties of the subpanel.

The diaphragm was also included in Leng's work (2015) as a deep horizontal plane truss system following the same numerical approach as for the shear walls using shear wall material properties as no experimental data for the diaphragm were available at the time. This deep

horizontal plane truss diaphragm model concept was first introduced by Shrestha (2011) following the work of Tremblay and Rogers (2005); in this study, the RUAUMOKO software (Carr 2004) was used to simulate steel corrugated roof deck diaphragms as part of one-storey steel buildings in order to investigate their seismic response. Initially, a Stewart (1987) force vs. deformation hysteretic material model with pinching characteristics was incorporated in the deep truss diaphragm model to mimic the non-linear shear response of the diaphragm. However, the material chosen was not capable of capturing the strength degradation observed during testing. As such, Shrestha (2011) subsequently employed the deep truss numerical model in OpenSees using the Pinching4 material model, which proved to be more accurate (Figure 1.6). The results of Shrestha's study can be found in Section 1.5.5.

Another recent diaphragm simulation follows a numerical finite element approach. A detailed finite element model of the floor assembly of the CFS-NEES Building was created by Chatterjee (2016) in an effort to capture accurately the seismic response of wood sheathed CFS framed diaphragms using ABAQUS (Dassault-Systems 2013). Shell elements were used to simulate the joist, tracks and wood sheathing. Sheathing-to-framing and steel-to-steel connections were simulated using spring elements and data from the connection tests conducted at Virginia Tech, as described in his thesis. Spring elements were also used to incorporate ledger framing in his model assuming infinite in-plane and negligible out-of-plane shear wall stiffness. Using the 3D diaphragm ABAQUS model and experimental data from the diaphragm experimental program described herein, Chatterjee introduced an upper and lower limit for the monotonic non-linear response of the floor assembly in the two directions of loading. The key concept in defining those limits is the level of friction developed in the intermediate panel locations when the panels are in-contact during testing. A partial static friction force value of 0.003kN/mm was identified

and the upper and lower limit for a case of perfect friction and zero friction, respectively, between the panels was defined. Although, only the monotonic response for the floor assembly in the z direction is included in his thesis, the monotonic response in the x direction was provided directly by Chatterjee upon request and is included in this thesis in Chapter 3.

The experimental work of Baldassino et al. (2017), referred to in Section 1.5.2.1, was completed with the development of a 3D numerical model in the OpenSees platform of the whole diaphragm assembly and a 3D numerical model in ABAQUS (Dassault-Systems 2016) of the local connection of the deck to the joists. In both numerical models a finite element approach was followed, where each element is represented separately. The OpenSees diaphragm model comprised layers representing the various components of the diaphragm assembly based on the configuration modeled. The steel deck and gypsum boards were simulated separately with truss elements, while the concrete slab with the steel deck was simulated using shell elements. An intermediate layer was used as a connection to the upper final layer, where zero-length links were used. The lower layers were connected using rigid links. The nonlinear force vs. deformation response of the zero-length links was obtained from the 3D ABAQUS model of the deck to joist connection. Verification of the numerical whole model was achieved using the experimental data.

Additional information about existing numerical work of the diaphragm component for different types of buildings can be found in Section 1.5.5.

### **1.5.3 CFS gravity framing studies**

As described in Section 1.1, the capacity of a CFS beam or column is primarily dependent on the slenderness of each cross-sectional element (e.g. flange, web). Having very thin, high strength sections under compressive stresses, CFS members can deform under local, distortional or global buckling, and combinations thereof. Experimental work of beam and column CFS members is

necessary in order to obtain a better understanding of their nonlinear behaviour under loading. Padilla-Liano et al. (2014) conducted an extensive experimental program involving CFS beam and column members with various slenderness properties in order to capture all three buckling failure modes and the energy dissipation capabilities of these members. Each buckling failure mode was captured separately by testing CFS members of different lengths and thicknesses. A displacement-controlled loading protocol was adopted from FEMA 461 (2007) to accommodate the 26 axial and 24 flexural loading tests for the CFS column and beam members. The results from the axial loading tests indicated that, although the nonlinear force vs. deformation behaviour across all sections was similar, the unloading stiffness, which directly influences the hysteretic pinching exhibited by each section, was buckling mode dependent. The flexural loading tests revealed that stiffness degradation and hysteretic pinching were less pronounced for the case of local and distortional buckling compared to global buckling. The overall nonlinear response of the CFS beam members was buckling mode dependent; the CFS beam members proved able to dissipate energy even after buckling of the compressive flanges due to stress redistribution to the adjacent less damaged regions of the cross-section.

Padilla-Liano proceeded to provide Pinching4 material properties for the test specimens following two phenomenological modeling approaches; a nonlinear spring model with concentrated nonlinear axial or flexural behaviour and a nonlinear beam-column model with distributed axial or flexural behaviour (Padilla-Liano 2015). For CFS column member empirical equations were also developed to calculate the pinching parameters and backbone points of the Pinching4 material in OpenSees as a function of the local, distortional and global slenderness of the member based on the experimental data. Given the complex nonlinear behaviour of these members, the empirical equations considering all three modes are part of planned future research

because more experimental work is needed to capture fully the interaction between local, distortional and global buckling. In this thesis, only the empirical equations incorporating local buckling for column members were used (Tables 1.2 and 1.3); the corresponding tables can be found in Padilla-Liano's (2015) thesis (Table 7.3, 7.7, 7.8 and 7.9).

Table 1.2: Compression backbone empirical equations for local buckling failure mode

Load	Displacement/Strain
$\frac{P_1}{P_y} = \begin{cases} 1.0 & , \lambda_l \leq 0.689 \\ 0.760\lambda_l^{-0.737} & , \lambda_l > 0.689 \end{cases}$	$\frac{\delta_1}{\delta_y} = \frac{\varepsilon_1}{\varepsilon_y} = \begin{cases} 1.0 & , \lambda_l \leq 0.689 \\ (P_1/k_1)/\delta_y & , \lambda_l > 0.689 \end{cases}$
$\frac{P_2}{P_y} = \begin{cases} 1.0 & , \lambda_l \leq 0.776 \\ [1 - 0.15\lambda_l^{-2(0.4)}]\lambda_l^{-2(0.4)} & , \lambda_l > 0.776 \end{cases}$	$\frac{\delta_2}{\delta_y} = \frac{\varepsilon_2}{\varepsilon_y} = \begin{cases} 1.0 & , \lambda_l \leq 0.814 \\ 0.774(\lambda_l - 0.776)^{-0.078} & , \lambda_l > 0.814 \end{cases}$
$\frac{P_3}{P_y} = \begin{cases} 1.0 & , \lambda_l \leq 0.523 \\ 0.552\lambda_l^{-0.915} & , \lambda_l > 0.523 \end{cases}$	$\frac{\delta_3}{\delta_y} = \frac{\varepsilon_3}{\varepsilon_y} = \begin{cases} 2.0 & , \lambda_l \leq 0.623 \\ 1.339 + 0.345\lambda_l^{-1.371} & , \lambda_l > 0.623 \end{cases}$
$\frac{P_4}{P_y} = \begin{cases} 1.0 & , \lambda_l \leq 0.379 \\ 0.338\lambda_l^{-1.119} & , \lambda_l > 0.379 \end{cases}$	$\frac{\delta_4}{\delta_y} = \frac{\varepsilon_4}{\varepsilon_y} = \begin{cases} 6.0 & , \lambda_l \leq 0.857 \\ 5.048 + 0.491\lambda_l^{-4.287} & , \lambda_l > 0.857 \end{cases}$
	$\frac{k_1}{k_e} = \begin{cases} 1.0 & , \lambda_l \leq 1.23 \\ 1.075\lambda_l^{-0.349} & , \lambda_l > 1.23 \end{cases}$

Note: These equations can be found in Table 7.3 in Padilla-Liano (2015).

Table 1.3: Tension backbone analytical equations for local buckling failure mode, strength and stiffness degradation parameters, unloading and reloading parameters

Load	Displacement/Strain	Strength Degardation	Stiffness degradation					
$\frac{P_1}{P_y} = 1.044$	$\frac{\delta_1}{\delta_y} = \frac{\varepsilon_1}{\varepsilon_y} = 1.044$	$\beta_{2,s} = 0.427$	$\beta_{2,k} = \begin{cases} 1.0 & , \lambda_l \leq 0.377 \\ 0.669\lambda_l^{-0.412} & , \lambda_l > 0.377 \end{cases}$					
$\frac{P_2}{P_y} = 1.134$	$\frac{\delta_2}{\delta_y} = \frac{\varepsilon_2}{\varepsilon_y} = 1.404$	$\beta_{4,s} = 0.569$	$\beta_{4,k} = \begin{cases} 1.0 & , \lambda_l \leq 0.624 \\ 0.425\lambda_l^{-1.814} & , \lambda_l > 0.624 \end{cases}$					
$\frac{P_3}{P_y} = 1.172$	$\frac{\delta_3}{\delta_y} = \frac{\varepsilon_3}{\varepsilon_y} = 8.0$	<b>Unloading and reloading parameters (Figure 1.6)</b>						
		<b>Parameter</b>	<b><math>\Gamma_{Disp+}</math></b>	<b><math>\Gamma_{Force+}</math></b>	<b><math>U_{Force+}</math></b>	<b><math>\Gamma_{Disp-}</math></b>	<b><math>\Gamma_{Force-}</math></b>	<b><math>U_{Force-}</math></b>
$\frac{P_4}{P_y} = 0.872$	$\frac{\delta_4}{\delta_y} = \frac{\varepsilon_4}{\varepsilon_y} = 10.0$	<b>mean</b>	0.381	0.892	0.210	0.419	0.457	-0.022
		<b>cov</b>	0.207	0.026	0.052	0.130	0.081	-1.702

Note: These equations can be found in Tables 7.7, 7.8 and 7.9 in Padilla-Liano (2015).

The symbols in Tables 1.2 and 1.3 are as follows:  $P_i$ ,  $\delta_i$  and  $\varepsilon_i$  refer to the backbone force – deformation/strain points where  $i=1, 2, 3$  or  $4$  and to the yield force –deformation/strain points where  $i = y$ . The initial stiffness is denoted as  $k_1$  and is a function of the elastic stiffness  $k_e$ . The local buckling slenderness of the section is denoted by  $\lambda_l$ . It should be noted that the parameters suggested in Tables 1.2 and 1.3 were based on a total of 22 test results. The equations in Tables 1.2 and 1.3 follow the traditional symmetric Pinching4 material (symP4) as it is incorporated in OpenSees. Padilla-Liano suggested also an asymmetrical Pinching4 (asymP4) material due to the fact that the symP4 has the same unloading-reloading parameters for the two loading directions and, thus, does not fully reflect the observed experimental behaviour (i.e. under or over estimation of the strength degradation). However, Padilla-Liano advises for further validation of the asymP4 under different loading and boundary conditions in order for possible convergence issues associated to the new asymP4 to be identified.

#### **1.5.4 Non-structural gypsum sheathing and gravity walls studies**

The importance of including non-structural components was highlighted during the CFS-NEES experiment, as well as in other experimental work mentioned in Section 1.5.2.1; Serrette et al. (1996, 1997), Liu et al. (2012) and Chen et al. (2014). Shamim and Rogers (2015), wanting to investigate the effect of non-structural gypsum placed on shear walls on the overall building's response to seismic loading, added a 12.5mm gypsum layer in the shear walls for two simulated buildings located in Montreal and Vancouver, Canada. From the incremental dynamic analyses (Vamvatsikos and Cornell 2002) and following the FEMA P695 (2009) method, it was shown that by adding gypsum only in the shear walls of the buildings their seismic capacity was increased. An even greater increase in capacity of these buildings may be expected if non-structural components were to be placed throughout. Moreover, 25 shear walls were tested during the summer of 2014 by Lu (2015) at McGill University under reversed cyclic loading

involving shear walls and one or two layers of 15.9mm gypsum placed on both sides of a wall. The results showed that adding 2 layers of gypsum, instead of one, on both sides doubles the ultimate shear strength of the wall. Eight tests were also conducted on bearing walls with gypsum (no holdowns) revealing their lateral stiffness and capacity. The strength and stiffness of the gypsum sheathed walls with holdowns can approach the values measured for the typical CFS framed walls sheathed with structural sheathing or strapping, and hence substantially influence the overall lateral response of a building to ground motions.

Leng (2015), being part of the CFS-NEES effort, numerically simulated the two-storey building in every phase, following Shamim and Rogers' work for the shear wall and diaphragm numerical model, as described in Section 1.5.2.2, and using a fastener-based model from Buonopane et al. (2015) and Bians et al. (2015) to produce the possible nonlinear response of the sheathed gravity walls. The OpenSees CFS framed shear wall model of Buonopane et al. (2015) comprised nonlinear spring elements simulating the fasteners, and rigid diaphragm constraints simulating the sheathing. Peterman et al. (2013) conducted sheathing-to-framing connection testing and provided the experimental data for the nonlinear springs' material. Bian et al. (2015) followed the work of Buonopane et al. to create and compare numerical models of Liu's (2012) shear wall specimens. Leng developed backbone curves from the fastener-based gravity wall model with gypsum and OSB sheathing, to be used in the Pinching4 material. Given the lack of experimental data on gravity walls, Leng assumed the pinching parameters to be the same as for the shear walls. As mention in Section 1.5.2.1, Chen et al. (2014) tested twelve timber shear walls sheathed, separately with OSB or gypsum or the combination of the two, under monotonic and reversed cyclic loading. The results showed that having obtained the monotonic response of a shear wall with OSB and a shear wall with gypsum, one could combine the two and produce

accurately the monotonic response of a shear wall sheathed with both panel types, assuming there is no failure of the framing members under the increased loading.

The contribution of gypsum-sheathed partition walls and their potential for a more active engagement in the lateral resistance of light-framed buildings was demonstrated in the work of Hopkins (2013) and Swensen et al. (2016) on gypsum sheathed partition walls. Hopkins (2013) tested 20 full-scale CFS & wood framed walls with gypsum sheathing with various structural characteristics and consideration of enhancement construction techniques such as the addition of construction adhesive and the use of mechanical fasteners as sheathing-to-framing connectors, among others; increase shear strength and stiffness of the specimens was achieved. Similarly, Swensen et al. (2016) tested 1.22x1.22m CFS and wood framed walls with gypsum panels exploring various enhanced screw and adhesive sheathing-to-framing connections. In their study, the adhesive connections had the most pronounced effect on the lateral response of the partition walls by increasing the shear strength and stiffness by 2 and 3 times, respectively.

Studies on gypsum sheathing installed on CFS framed diaphragms are not available at present. However, gypsum ceiling is typically found in floor and roof configurations for purposes of fire resistance (SFA 2013).

### **1.5.5 Diaphragm flexibility studies**

The question of whether diaphragm flexibility should be considered in the analysis of buildings for seismic design has been the focus of a broad number of studies for buildings featuring either vertical bracing bents or shear walls. Further, when these lateral force resisting systems are unreinforced masonry or concrete shear walls, these structures are classified as Rigid Wall Flexible Diaphragm (RWFD) structures, indicating a considerable level of influence of the diaphragm flexibility on the overall seismic response of these structures. In the work presented in this section, researchers have focused on how the flexibility of the diaphragm may alter the

dynamic properties of the structure or lead to unexpected forces and drifts exhibited by the structure under earthquake excitations.

Knowing the dynamic properties of a structure is the first step to be able to decipher its dynamic response under lateral loads. Jain and Jennings (1985) proposed general analytical equations that can yield the dynamic properties of a single- and two-storey building with in-plane flexible diaphragms and shear walls. The basis of the analytical method is the representation of the floor as a bending beam and of the shear wall as a shear beam, thus using the well-known shear beam and bending beam equations to represent the motion of these components. Simplifications applied for the use of the method include assuming in-plane diaphragm flexibility only in one direction of the building (long, narrow buildings) and neglecting the effect of damping in the calculations. By applying the proper boundary conditions, the system of beam equations can be solved exactly providing the natural frequencies of the building. From the natural frequencies, the mode shapes and corresponding participation factors can be obtained. This method applies for buildings with long span diaphragms, allowing for their shear deformation and potential rotation to be neglected so as to treat them as simple bending beams.

Tena-Colunga and Abrams (1996) realized an analytical study on multi-storey RWFD buildings. Three case study buildings of two to eight storeys were considered with unreinforced masonry or concrete shear walls and timber floor and roof subsystems. The buildings were subjected to the Loma Prieta earthquake ground motion. Two diaphragm flexibility conditions were included in the analytical study, flexible and rigid, for purposes of comparison. The dynamic response of the buildings was studied following a multi-degree of freedom numerical model developed by the authors including foundation flexibility using rotational and translational springs. Results were presented in terms of maximum lateral accelerations, maximum lateral displacements, torsion

present in the system and periods of oscillation. Recorded acceleration data were also used when applicable. It was shown that amplification of the accelerations for diaphragms and shear walls should be expected with the increase of diaphragm flexibility, as well as considerable reduction of the torsion present in the building. The rigid diaphragm design assumption did not prove to be conservative for all cases. The fundamental period of the flexible diaphragm buildings was longer than predicted using simplified design methods.

Fleischman and Farrow (2001) examined the seismic response of narrow, long-span buildings with only perimeter lateral force resisting elements. Typically in design a rigid diaphragm assumption is followed for these buildings, although their diaphragm subsystems behave in a flexible manner. Fleischman and Farrow conducted modal and response history analyses exploring the effect of diaphragm flexibility on the seismic response of these structures including the case of inelastic diaphragm behaviour. Three-storey long-span buildings with perimeter shear walls were selected for the numerical study and subjected to the 1971 San Fernando earthquake ground motion. A level of diaphragm flexibility was identified beyond which the dynamic properties of the shear walls were modified. Specifically, the lower modes of vibration were dominated by the oscillation of the diaphragm independently of the shear walls. Thus, the shear wall vibrations were associated only with the higher modes of the building. This out-of-phase oscillation of the diaphragm subsystem can lead to unforeseeable forces and drifts; i.e. amplified mid-span drifts endangering structural stability as the gravity columns are subjected to larger lateral displacements than anticipated.

Tokoro et al. (2004) evaluated the classification criteria for a rigid or flexible diaphragm available in the Uniform Building Code (ICBO 1997). A three-storey instrumented unreinforced masonry building constructed in California was chosen for the purpose of this numerical study.

A detailed 3D finite element (FE) model was created in ETABS (CSI 1999) subjected to a number of earthquake ground motions. The diaphragm was modelled using shell elements. Diaphragm flexibility classification was based on the resulting lateral force distribution of the diaphragm to the shear walls. The study concluded that the resulting code - proposed diaphragm-to-shear wall displacement ratio value is method-dependent; dynamic loading suggested flexible floor and roof diaphragms while static loading classified the floor diaphragms as rigid. As such, considerable ambiguity exists in following the code criteria (ICBO 1997) and a more tangible diaphragm flexibility classification criterion should be developed to facilitate practical applications.

Pathak's and Charney's (2008) work involved light-frame wood buildings. A parametric numerical study was realized incorporating various plan view aspect ratios in the two horizontal directions, diaphragm flexibility values and shear walls placed in such a way as to form a symmetric and asymmetric lateral force resisting system. Three-dimensional numerical models were created in SAP2000 (CSI 2009) and two ground motion records were considered, the Imperial Valley and Northridge earthquakes. Linear orthotropic shell elements were used to construct the diaphragm model. This work highlighted the sheathing-to-framing connections as the decisive source of the resulting diaphragm flexibility irrespective of the plan view aspect ratio. Overall, it was demonstrated that the influence of diaphragm flexibility is more pronounced for torsionally asymmetric buildings, as they exhibited greater variation in the resulting seismic response when considering flexible versus rigid diaphragms.

Shrestha's (2011) diaphragm numerical model (deep horizontal truss) was presented in Section 1.5.2.2. Shrestha examined the seismic response of single-storey steel buildings with flexible CFS corrugated roof deck diaphragms by conducting non-linear dynamic analyses following two

approaches: 1) the vertical bracing system being the energy-dissipating element, while the diaphragm remains elastic and 2) the diaphragm being the main energy dissipating element. The medium (30x60x7m) and large (40x90x8m) size single-storey buildings were first designed using SAP2000 and then evaluated using dynamic analyses in OpenSees. The buildings were assumed to be located in Abbotsford, British Columbia (BC) and Montreal, Quebec (QC) in Canada and were subjected to a number of ground motion records from the work of Atkinson (2009). Results led to a revision of the fundamental period of vibration for these buildings and provided information about the performance of the eccentrically and concentrically braced structural systems. A revision of the force reduction factor,  $R_d$ , was considered to be appropriate for the case where the diaphragm was thought as the main ductile fuse element, given the shear strength degradation and inelastic demand observed in the roof deck.

Following the work of Shrestha (2011), Trudel-Languedoc et al. (2012) introduced an equivalent beam model that represents a single-storey steel building with concentrically braced frames (CBFs) connected to a flexible steel roof deck. A total of twenty continuously connected beam elements incorporated the shear and flexural stiffness properties of the diaphragm, while the rigidity of the braces was implemented in two spring elements, constituting the two supports of the beam. Lumped masses were assigned to the nodes along the length of the continuous beam element. The two structural parameters examined were the fundamental period of the building and the in-plane diaphragm to vertical bracing system lateral deformation ratio,  $\Delta_D/\Delta_B$ . Seventeen buildings were considered under modal response spectrum, linear and nonlinear response history analysis to obtain the elastic and inelastic response to loading. The buildings were assumed to be located in Vancouver, BC. The accuracy of the equivalent static force method (ESFM) was evaluated. Overall it was shown that the ESFM underestimates the

diaphragm shear force and bending moments as well as the diaphragm displacement and total drift of the buildings compared to the other types of analyses explored. Nonlinear response history dynamic analysis revealed an even greater increase of the diaphragm forces compared to the modal spectrum and linear response history dynamic analyses. The expected diaphragm shear forces at quarter length of the span and moments at mid-point increase with the increase of the fundamental period, of the diaphragm flexibility and of the seismic modification factors,  $R_d R_o$  (reduction of seismic loads). Moreover, the ductility demand on the CBFs increases for short period buildings with the increase of the diaphragm flexibility. Subsequently, Trudel-Languedoc et al. (2014) proceeded with a detailed examination of the dynamic properties of this type of building for the first and third mode of vibration. As the  $\Delta_D/\Delta_B$  increases the participation factor of the first mode decreases while of the third mode increases. As such, it was shown that for  $\Delta_D/\Delta_B$  higher than 3, less than 90% of the mass is oscillating during the first mode. Trudel-Languedoc et al. also showed that the higher shear forces observed at the quarter span locations of the diaphragm are the result of the diaphragm vibration being a combination of the first and third mode of vibration. This result renders the linear shear force distribution assumption questionable.

The research efforts of Shrestha (2011) and Trudel-Languedoc et al. (2014) led to the development of a modified approach for the determination of the period of vibration for single storey steel buildings with flexible diaphragm, discussed in Tremblay and Rogers (2017) and included in the NBCC 2015 (NRCC 2015).

Humar and Popovski (2012) investigated the influence of diaphragm flexibility on the seismic response of 33 single-storey buildings with bracing bents, as the lateral force resisting elements. The buildings were first designed in work presented by Tremblay and Stiemer (1996). The deep

beam modeling approach was employed in their work, as explained for the work of Trudel-Languedoc et al. (2012). The authors applied loading in both the short and long side of the buildings and concluded that for the majority of the buildings the diaphragms can be characterized as stiff when the loading is parallel to the long side and as flexible when the loading is parallel to the short side of the building. Through their analyses, they suggested a fundamental period equation as a function of the diaphragm's span and width. They, also, highlighted the importance of the shear deformations of the diaphragm in the overall deformation of the building and pointed out that, although period elongation leads to smaller base shear forces, inertia force redistribution in the diaphragm can lead to higher moment in the mid-span. Humar and Popovski (2013) expanded on their previous work focusing on buildings with inelastic response of the braces while the diaphragm remains elastic. They concluded that nonlinearity of the lateral force resisting elements leads to increase of the higher mode effects in the diaphragm. This led to an increase in the ductility demands on the braces with the increase of diaphragm flexibility. A method for the calculation of a force reduction factor for the design of the braces was proposed from their results. In Mortazavi and Humar (2016) the methods for the force reduction factor calculation was further refined, the amplification of in-plane forces was characterised and the response of the 33 buildings was investigated assuming now the diaphragm as the main energy dissipating element. Equations were proposed relating the ductility demand on the braces with the amplification of shear force in the quarter span and mid-span moment in the diaphragm. Additionally, for the case where the diaphragm is the energy dissipating element an alternative design method was followed following the concept of capacity design for the braces and a new force reduction factor equation was suggested. It was observed that allowing nonlinearity in the diaphragm does not significantly influence the in-plane diaphragm forces and

moments.

Koliou (2014) aimed at providing an efficient numerical tool for professional engineers to be able to conduct a large number of response history dynamic analyses of RWFD buildings in a prompt and straightforward manner. Koliou developed a 2D numerical model of a single-storey RWFD building in RUAUMOKO2D (Carr 2007) implementing the inelastic response of the roof diaphragm subsystem. An extensive diaphragm connector database was developed as a first step of this work. The resulting force vs. deformation hysteretic response of the diaphragm connectors was subsequently incorporated in an inelastic 2D diaphragm model. The resulting force vs. deformation hysteretic inelastic response of the diaphragm was, thereupon, implemented in the simplified 2D building's model using horizontal spring elements. Koliou proceeded with evaluating the seismic response of RWFD single-storey buildings under extreme earthquake excitations given the poor past performance of these structures due to unexpected excessive roof displacements. A broad number of archetype RWFD buildings were evaluated following the FEMA P695 (2009) methodology. Some of the main contributions of this work resulted in two fundamental period formulas being proposed (mechanical, semi-empirical) for these buildings and a new economical design approach exploring the concept of “forced” distributed yielding of the roof diaphragm in place of the vertical elements of the lateral force resisting system.

Nakamura et al. (2016) applied unidirectional earthquake loading to a single-storey unreinforced masonry building considering various diaphragm flexibilities and strength and stiffness eccentricity conditions. A 3D numerical model was created in RUAUMOKO (Carr. 2008), using quadrilateral membrane elements to construct the diaphragm component, and was subjected to eight ground motion records. The resulting increase or decrease in the shear wall's seismic

demands revealed a level of codependence between the system's strength and stiffness eccentricity and the flexibility exhibited by the diaphragm.

Most recently, Schafer et al. (2018) conducted a numerical study aiming to improve the seismic design of RWFD buildings comprising of tilt-up pre-cast concrete walls and steel roof deck diaphragms. A 3D numerical model was created in ABAQUS (Dassault-Systems 2014) for the purposes of evaluating the current seismic design of one of these buildings following the FEMA P695 (2009) methodology. Attempting to increase computational efficiency while successfully incorporating all nonlinear sources of the RWFD buildings, the 3D model comprised a truss system of hysteretic spring elements simulating the roof subsystem and individual elastic panels with proper thickness assigned to them simulating the concrete walls. The force vs. deformation hysteretic nonlinear response of the roof deck was captured by a preceding 3D FE model of the roof subsystem using shell element and hysteretic springs that implemented the nonlinear response of the diaphragm connectors. The RWFD building was examined under modal, pushover and incremental dynamic analysis (Vamvatsikos and Cornell 2002). Modal analysis revealed that the first mode in the two directions of loading is not able to mobilize 90% of the mass. Pushover analysis revealed a secondary resistance mechanism being activated in the roof deck after the peak load has been reached; bending of the sheet panels as well as of the joists contribute to this observed post-peak strength. Incremental dynamic analysis showed that the overall seismic design was acceptable resulting, however, in considerable damage of the roof subsystem. Reduced diaphragm shear forces compared to the base shear demands on the walls highlighted a particular trait of the seismic response of RWFD buildings, where forces are directly applied to the rigid walls and do not necessarily “pass through” the diaphragm. This characteristic of RWFD buildings was, also, observed in the building studied in this work in the

numerical results presented in Chapter 3.

## **1.5.6 Seismic assessment in Canada**

### **1.5.6.1 Design provisions**

The NBCC (NRCC 2015) defines two types of analyses to be conducted for seismic design: equivalent static force procedure and dynamic analysis, which refers to either response spectrum or response history analysis. The latter is particularly catered for structural systems featuring LFREs with nonlinear elastic (i.e. viscous dampers) or ductile inelastic (i.e. CBFs) response during earthquake loading for the seismic demands on the building to be obtained accurately. Appropriate ground motion records need to be selected as input loading for nonlinear response history dynamic analysis based on the seismic hazard probability level considered for seismic design. The NBCC provides guidelines on the selection and scaling of ground motion records for the purpose of seismic design evaluation. These design provisions have been summarised in Tremblay et al. (2015).

In order for the seismic hazard of a particular site to be properly represented a minimum number of ground motion records are selected so as to incorporate different ground motion characteristics in the analyses such as frequency, amplitude and duration. This concept aims to reduce the uncertainty and signal variability of future earthquake events for the site considered. The first step in the selection of ground motions is the definition of a target response spectrum (TRS); the response spectra of the ground motions are scaled in order to “match” the TRS. The TRS is based on the design response spectrum representing seismic hazard for the site and period range of interest. For example, for a building located in Montreal, QC the target response spectrum could be based on the uniform hazard design response spectrum (UHDRS) representing seismic hazard in Montreal for a certain probability of exceedance. In Canada, uniform hazard design response spectra (UHDRS) represent seismic hazard in various regions for a certain

probability of exceedance; the design level probability of exceedance is 2% in 50 years. The UHDRS has been recently modified in order to include the gradual amplification of the spectral acceleration (SA) in the short period range of the spectrum (Tremblay et al. 2015). Linear interpolation is allowed to be applied between the peak ground acceleration (PGA) and the corresponding SA values for the following periods: 0.05sec, 0.1sec, 0.2sec, 0.3sec and 0.5sec. This modification facilitates the selection of appropriate ground motion records for short-period structures.

The period range to be considered for the formation of the TRS is based on the modal analysis of the structure of interest. Two limits are specified: (1) the lower limit,  $T_{\min}$ , is defined as the period value of the highest mode required for 90% of the mass to be mobilized in the structure provided that it does not exceed 0.2 times the fundamental period,  $T_1$ ; and (2) the upper limit,  $T_{\max}$ , is defined as 2 times  $T_1$  provided that it does not exceed the upper bound value of 1.5sec. These limits are provided in the form of an equation in Chapter 4 (Eq. 4.1 and 4.2). These limits allow for a period range to be considered that includes all possible translational and torsional vibration modes that the structure can engage in during an earthquake excitation.

Once the period range has been established based on the dynamic properties of the structure under evaluation, deaggregation data should be acquired for the site considered indicating the magnitude (M) and fault distance (R) of earthquake events that mostly contribute to the seismic hazard per period value within the period range of interest. Through the examination of the deaggregation data period subranges are often identified with specific corresponding M-R values. The NBCC (NRCC 2015) includes three options for the definition of the TRS in order to select ground motions: (1) Method A, where the TRS is the  $M_{\text{UHDRS}}/UHDRS$  in the entire period range of interest, (2) Method B, where individual TRS are defined for each period

subrange based on the  $M_{UHDRS}/UHDRS$  and, (3) where a conditional mean spectrum (CMS) or spectra are computed instead based on the specific periods of interest according to the deaggregation data (Tremblay et al. 2015).

Regardless of the TRS method followed, several requirements need to be satisfied in selecting and scaling the ground motions records. Having selected appropriate records that satisfy the M-R values for the period subranges, the dominant earthquake source and the soil conditions for the site of interest, the shape of the ground motion spectra is checked visually so as to be in agreement with the TRS throughout the entire period range for all ground motions of all suites. The response spectrum of a ground motion should not overly exceed the TRS even at periods outside the period subrange for which the record was selected. In addition, to ensure the selection of ground motion records with response spectra closely matching the TRS over the specific period subrange, ground motion records with the minimum standard deviation of the ratio of the spectral acceleration of the TRS,  $S_{TT}$ , to the ground motion spectral acceleration,  $S_gT$ , ( $S_{TT}/S_gT$ ) may be selected. A minimum of eleven ground motions should be considered for the entire period range and its period subrange should be represented by a suite of at least five ground motion records. If possible, no more than two ground motion records should be selected per earthquake event. A linear scaling approach is, subsequently, employed per suite in two steps: (1) the first scaling factor is defined as the mean ( $S_{TT}/S_gT$ ) for each individual ground motion; and (2) the second scaling factor is thus defined so as to ensure that the geometric mean of all the ground motion spectra per suite is not below or above 10% of the TRS for the specific period subrange. The first scaling factor value is different for each ground motion while the second scaling factor is the same for all records per suite. All scaling factors must not be greater than 5 and lower than 0.2.

### **1.5.6.2 Deaggregation data**

Natural Resources Canada, a federal government organisation, provides deaggregation data for all regions in Canada based on the probabilistic seismic hazard models of Halchuk et al. (2014). For Eastern Canada the primary source of earthquake events is crustal, shallow earthquakes, while for Western Canada three dominant sources have been identified, crustal/shallow, in-slab and interface Cascadian subduction earthquake events. Given the different earthquake sources contributing to the seismic hazard in Western Canada, Goda and Atkinson (2011) highlighted the need to update the probabilistic seismic hazard models used at the time (Adams and Halchuk 2003) by employing multiple ground motion prediction equations (GMPEs) representing each earthquake type and including probabilistic data on Cascadian subduction earthquakes, among others. Goda and Atkinson developed the updated seismic hazard model as part of a research project aiming to evaluate the seismic performance of wood-framed buildings located in British Columbia. Deaggregation data are presented in Tremblay et al. (2015) based on the updated seismic hazard model of Goda and Atkinson (2011).

### **1.5.6.3 Ground motion databases**

For Eastern Canada, an extensive database of simulated ground motion records was provided by Atkinson (2009). Atkinson highlighted the lack of historical ground motion records for Eastern Canada and the advantages of generating UHDRS-compatible ground motion records, such as the ease in the selection and scaling of these signals (simple linear scaling). Records were created for 2% probability of exceedance and site classes A, B, C, D, and E based on shear-wave velocity limits in the first 30m of soil ( $V_{s30}$ ) available in the NBCC (NRCC 2015). Ground motion records of moment magnitudes,  $M$ , 6 and 7 were created resulting in 90 ground motion records per site class (45 per magnitude). All records with the corresponding spectral accelerations are provided in the Engineering Seismology Toolbox website

(www.seismotoolbox.ca). In the selection process for the ground motions, Atkinson suggests that the mean ( $S_T/T / S_gT$ ) of the selected records shall be between 0.5 and 2.0.

For Western Canada, there are a broad number of historical ground motion records available in databases such as the Pacific Earthquake Engineering Research Centre, PEER-NGA West 2 database for crustal shallow earthquakes and the Japanese K-NET and Kik-NET databases for in-slab and interface subduction earthquakes. It should be noted that to acquire accurate soil conditions for the recording stations used in the K-NET and Kik-NET databases, Boore et al. (2011) developed shear-wave velocity equations able to predict the shear wave velocity in 30m using equivalent velocity values in soil depths less than 30m. In addition,  $V_{s30}$  values are available for all K-NET stations in the electronic version of the paper by Boore et al.

## **1.6- Summary**

CFS joist framing sheathed with structural OSB panels is a typical diaphragm configuration found in the floors and roof of CFS buildings; however, only one diaphragm experimental program is available in the literature by NAHBRC (1999) considering this type of diaphragm configuration (four tests). In addition, the AISI S400 Standard (2015) offers limited design guidelines, only for the USA, for the design of diaphragms with this structural characteristics referring only to plywood sheathing and excluding the size of sheathing-to-framing connectors as a design parameter. The force versus deformation nonlinear response of the sheathing-to-framing connectors has been highlighted in the literature as the most influential parameter in the resulting shear strength and stiffness of the diaphragm. As such, there is an evident need for the design guidelines of the AISI S400 to be updated and design shear strength and stiffness values for common CFS framed OSB sheathed diaphragms to become available to professional engineers for design in Canada.

The AISI S400 Standard refers to gypsum boards as non-structural panels that are found attached to OSB sheathed CFS framed shear walls and can contribute to the lateral resistance of a CFS building. Experimental and numerical work exists in the USA, Canada and Italy on the influence of gypsum sheathing as part not only of the isolated shear wall component but also of the overall CFS building. However, no information is available on the contribution of non-structural components to the lateral response of the OSB sheathed CFS framed diaphragm component. The effect of common non-structural materials, such as gypsum and gypcrete, on the lateral response of the diaphragm needs to be identified and their impact on the overall seismic response of a CFS building investigated.

Extensive numerical work exists on the effect of diaphragm flexibility on the seismic response of buildings featuring vertical bracing bents, shear walls or tilt-up concrete walls. However, a diaphragm flexibility study is not available for the CFS framed buildings discussed herein. In addition, there is no discussion as to how the added rigidity on the walls from the non-structural elements featured in a CFS building could affect the interaction between walls and diaphragms during an earthquake excitation. As such, the influence of the diaphragm flexibility on the resulting forces and drifts of a CFS building subjected to an earthquake excitation should be explored including the effect of non-structural components.

## **Foreword to Chapter 2...**

In Chapter 2, experimental results are presented for ten OSB sheathed / CFS framed diaphragm specimens. In particular, Phase 1 of the diaphragm experimental program is presented involving 4 diaphragm configurations tested under monotonic and reverse cyclic loading. This is the first step required in developing design shear strength and stiffness values for these diaphragm configurations. The basis for the diaphragm configurations were the roof and floor subsystems of the CFS-NEES Building, as described in Chapter 1. The CFS-NEES project included shear wall testing, isolated CFS members cyclic testing and the overall shake table testing of the two-storey CFS building (Schafer et al. 2016); as such, the diaphragm experimental program presented herein is a complementary study to the CFS-NEES project providing characterisation of the diaphragm's lateral response. Based on the roof and floor configuration, the effect of various structural characteristics is explored, such as screw size and panel edge blocking.

# CHAPTER 2: SEISMIC PERFORMANCE CHARACTERIZATION OF WOOD-SHEATHED AND COLD-FORMED STEEL FRAMED FLOOR AND ROOF DIAPHRAGM STRUCTURES

Violetta Nikolaidou<sup>(1)</sup>, Patrick Latreille<sup>(2)</sup>, Dimitrios G. Lignos<sup>(3)</sup>, Colin A. Rogers<sup>(4)</sup>

## 2.1- Abstract

This paper describes a research program involving wood sheathed / cold-formed steel (CFS) framed diaphragm assemblies. The diaphragm's response to in-plane monotonic and reversed cyclic lateral loading is investigated in an effort to characterize the seismic performance of this assembly. The work presented herein focuses on the response to loading of the isolated diaphragm subsystem and serves as a complementary study to a research project involving the dynamic testing of full-scale two-story CFS framed buildings, known as the CFS – NEES project. Laboratory testing included eight 3.66 x 6.1m diaphragm specimens, i.e. four configurations, comprised of oriented strand board (OSB) sheathing screw connected to CFS C-Channel joists. The response to loading is directly related to screw pattern and size, the use of panel edge blocking, and the type of sheathing. By means of a comparison of design and experimental shear strength and stiffness values the provisions of the AISI S400 Standard were shown to be in need of improvement regarding the number of listed diaphragm configurations. Deflection predications at the design load level were considered to be reasonable.

**Keywords:** cold-formed steel; diaphragm; in-plane loading; test program; shear response

## 2.2- Introduction

A typical construction practice of cold-formed steel (CFS) structures is the stud wall system with vertical members forming the walls and sheathing installed to provide shear resistance to lateral loads (shear walls). A typical floor and roof system is comprised of discretely or continuously braced CFS joists overlaid with wood sheathing, again to provide shear resistance to lateral loads (diaphragms). The seismic design of CFS framed structures focuses mainly on the lateral response of the shear walls, as the primary component of the lateral force resisting system (LFRS), without explicitly accounting for the diaphragm's contribution to the overall seismic response of the structure. Extensive experimental and numerical work realized for the lateral response of shear walls, e.g. Dolan and Easterling 2000, Serrette et al. 2002, Branston et al. 2006, Pan and Shan 2011, Shamim et al. 2013 and Peterman et al. 2016a; 2016b, among others, provides a starting point in the effort to characterize the diaphragm behavior under in-plane loading and its contribution to the seismic response of CFS framed buildings, since little research exists for which the diaphragm response is the focal point of the work (NAHB Research center 1999, LGSEA 1998). A shear wall is effectively considered as a vertical cantilevered diaphragm (APA 2007); thus, the structural similarity between shear walls and diaphragms enables preliminary assessments of the diaphragm response through use of the shear wall studies. However, the major role of the diaphragm in distributing the lateral forces to the shear walls, the expected differences in behavior due to the presence of gravity load on the walls and the structural difference of the diaphragm's multiple sheathing panels call for an explicit characterization of its seismic response. The design provisions available for CFS framed diaphragms (AISI S400 2015, AISI S100 2016, NIST et al. 2016, CSA S136 2016) are based largely on experimental work on wood assemblies (Tissell and Elliot 2004, APA 2007);

moreover, the North American standard for the seismic design of cold-formed steel structural systems, AISI S400 2015, contains no seismic design procedure for CFS framed diaphragms for use in Canada. As such, there exists a need for this shortcoming to be addressed in order to ensure the construction of better, safer and cost-effective CFS structures.

The present design process for diaphragms is solely governed by the selection of suitable connections between the sheathing and the framing, as well as between the diaphragm and the shear walls, in order to ensure adequate shear strength and stiffness. Currently, in the AISI S400 Standard design shear strength values are provided based on analytical work by the Light Gauge Steel Engineers Association (LGSEA 1998) (Table F2.4-1, AISI S400 2015). These design values are dependent on the field and perimeter screw spacing, but not on the screw size, and are available only for a limited number of plywood sheathed / CFS framed diaphragm configurations based on the methodology included in Tissell and Elliot (2004) for wood framing. Moreover, Serrette's and Chau's (2003) work yielded a deflection equation for simply supported diaphragms, which is included in the AISI S400 Standard (Eq. C-F2.4.3-1, AISI 2015). Shear strength and stiffness values were also made available by the National Association of Home Builders Research Center (NAHBRC 1999), which carried out four monotonic tests on CFS framed / oriented strand board (OSB) sheathed diaphragms, and studied the individual sheathing-to-framing connection response. The launch of the CFS – NEES (i.e., Network for Earthquake Engineering Simulation) project in 2010 was in response to the need for advanced seismic design procedures of CFS structures. This major research project involved the dynamic testing of a full-scale two story CFS framed building (Figure 2.1), which was conducted by researchers at Johns Hopkins University (Peterman 2014). Particular emphasis was placed on the characterization of the isolated CFS framed / wood sheathed shear walls (Peterman et al. 2016a; 2016b, Liu et al.

2012), whereas the diaphragms in this structure were not specifically instrumented such that their load – deformation response could be measured; nor based on observations, were they reported to have surpassed the elastic range.

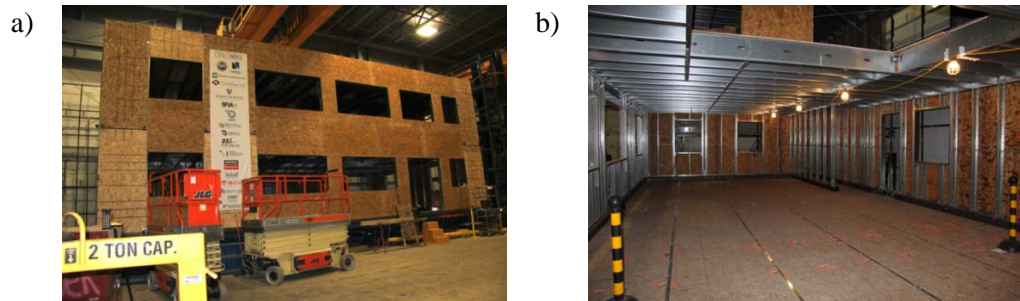


Figure 2.1: CFS – NEES Building; a) elevation, and b) ground floor (courtesy of Dr. Kara Peterman, University of Massachusetts Amherst)

The research presented herein aims to provide insight into the complex nature of the seismic response of the diaphragm subsystem. Eight OSB sheathed / CFS framed roof and floor diaphragms were tested, using either monotonic or reversed cyclic loading. The objective was to characterize the diaphragm response to in-plane loading and to obtain information for an isolated diaphragm's seismic performance to supplement the data acquired in the CFS – NEES project. To this end, the diaphragm configurations were based on the floor and roof configurations used in the CFS - NEES Building (Figure 2.1). The tests were conducted in the Jamieson Structures Laboratory at McGill University following a cantilever test method, detailed according to the provisions of the AISI S907 Standard (2013) for diaphragm testing, with the overall specimen dimensions being 3.66 m x 6.1 m (Nikolaidou et al. 2015). This paper concludes with a comparison between the measured test values and the calculated shear strength and deflection values following the AISI S400 North American Standard (2015) for the seismic design of cold-formed steel structural systems.

### 2.3- CFS framed diaphragm test program

The research program required the design and construction of a setup to accommodate the diaphragm tests (Figures 2.2 and 2.3). It consisted of a pin-connected self-reacting braced frame with wide-flange (W-shape) sections as the main beams and double angle sections as the bracing. The design aimed for the frame to remain elastic during the test and to have adequate stiffness to exhibit the minimum possible deformation, i.e. span-length / 1125. A 450 kN (tension) / 650 kN (compression) actuator, hinged at both ends, was attached to a force distribution beam, which was in turn bolted to one side of each diaphragm specimen. The support of the distribution beam comprised a roller system at three locations, which allowed it to move freely. Thus, in combination with the hinged actuator, the diaphragm specimen could also move (lengthen and shorten) perpendicular to the direction of the applied loading. The specimen was fixed along the other side to the frame. Selected photographs of the test specimen and setup are provided in Figure 2.4.

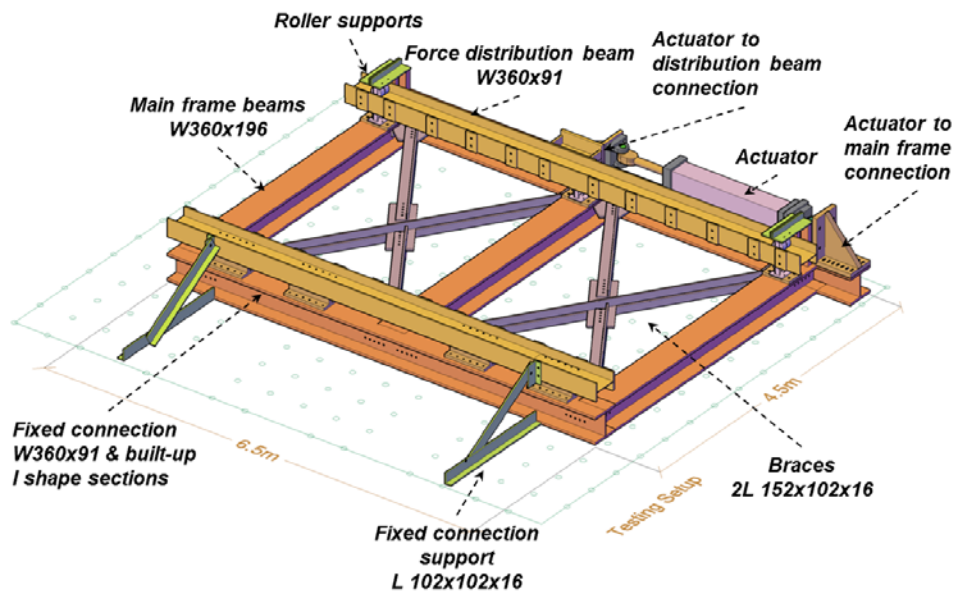


Figure 2.2: CFS diaphragm test setup

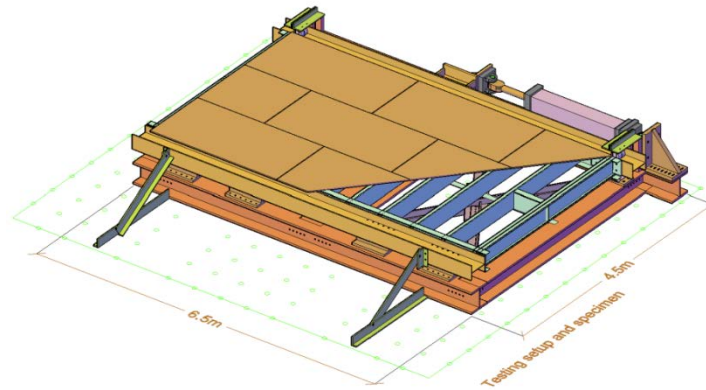


Figure 2.3: CFS diaphragm test specimen and setup

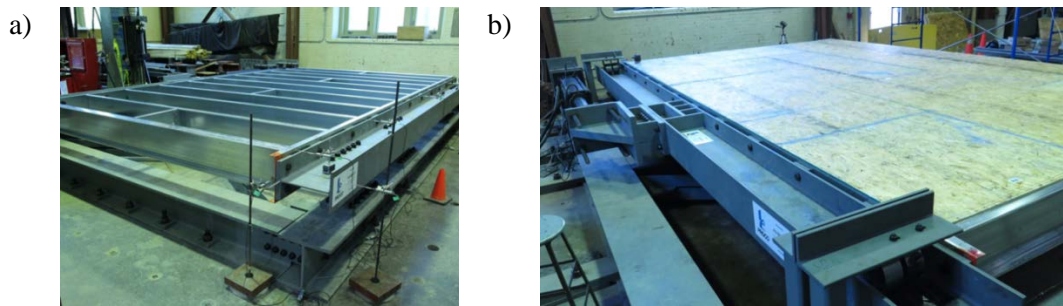


Figure 2.4: Photographs of diaphragm test specimens; a) unblocked framing prior to installation of OSB sheathing, and b) completed diaphragm with roof sheathing

The roof and floor diaphragms of the CFS - NEES Building had the following characteristics: steel thickness 1.37 mm vs. 2.46 mm, #8 vs. #10 sheathing screws and OSB panel thickness 11.1mm vs. 18.2mm with tongue and groove (T&G) edges, respectively (Table 2.1). Neither of the diaphragms included edge blocking, i.e. CFS framing under all of the OSB panel edges. Following the CFS - NEES Building design, the first two diaphragm test configurations incorporated these construction details (Figure 2.5). Subsequently, a construction parameter was altered in each configuration: i) full panel edge blocking was added to the roof configuration (full height blocking with joist sections as shown in Figure 2.6), where the full perimeter of each

OSB panel was fastened to the underlying steel framing, and ii) a larger sheathing screw size (#12) was used in the floor configuration. The objective was to investigate the effect of these two parameters on the shear strength and stiffness of the diaphragm. Monotonic and reversed cyclic loading was employed for each of the four configurations. The bare CFS framing without the sheathing was also tested under monotonic loading in order for its contribution to be accounted for separately. In total, the four diaphragm configurations, each tested with two loading protocols, and the two bare frame tests resulted in a laboratory program comprising 10 tests.

Table 2.1: Basic floor and roof diaphragm configurations

<b>Roof Diaphragm Component</b>	<b>Section (mm)</b>	<b>Length (mm)</b>
<b>Joists</b>	305S51-137M	3505
<b>Rim Joists</b>	305T51-173M	6480
<b>Web Stiffeners</b>	L 38x38x1.37	250
<b>Joist bracing</b>	305S41-137M	560
<b>Joist bracing connectors</b>	L 38x102x1.37	250
<b>Straps</b>	38x1.37	6300
<b>#8 sheathing self-drilling (152/305mm spacing)</b>	-	50
<b>#10 steel-to-steel flat head self-drilling</b>	-	20
<b>#10 steel-to-steel Hex Head Cap self-drilling</b>	-	25
<b>OSB panels (24/16 rated)</b>	2400x1200x 11	-
<b>Floor Diaphragm Component</b>	<b>Section (mm)</b>	<b>Length (mm)</b>
<b>Joists</b>	350S64-246M	3505
<b>Rim Joists</b>	350T64-246M	6480
<b>Web Stiffeners</b>	L 38x38x1.37	280
<b>Joist bracing</b>	305S51-137M	550
<b>Joist bracing connectors</b>	L 38x102x1.37	250
<b>Straps</b>	38x1.37	6300
<b>#10 sheathing self-drilling (152/305mm spacing)</b>	-	44
<b>#10 steel-to-steel flat head self-drilling</b>	-	20
<b>#10 steel-to-steel Hex Head Cap self-drilling</b>	-	25
<b>OSB panels (48/24 rated T&amp;G)</b>	2400x1200x 18	-

The material used for the fabrication of the joists and tracks was ASTM A653 (2015a) Grade 50 (i.e. nominal yield stress  $F_y = 345\text{MPa}$ ) steel. Moreover, Figure 2.5 demonstrates the following

two features of the diaphragm specimens: a double CFS joist section as a chord element to represent the presence of a wall in actual conditions (increased stiffness) and a 152.4mm sheathing extension at the fixed connection location, as per the CFS - NEES building design for ledger framing. This led to an out-to-out width of the CFS frame of 3505mm. Figure 2.7 illustrates the connections used to connect the CFS framing, while Table 2.2 includes the nomenclature followed for the specimens.

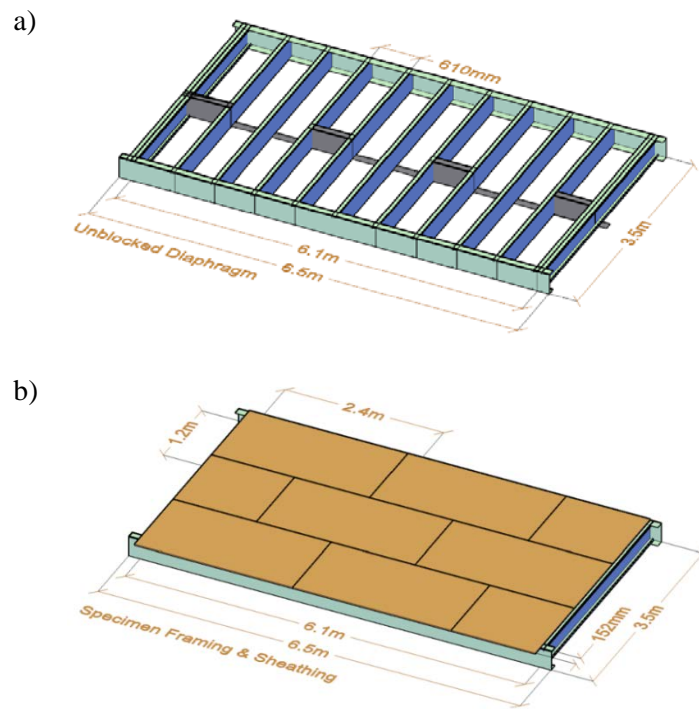


Figure 2.5: Illustration of a) CFS framing, and b) wood panel sheathing

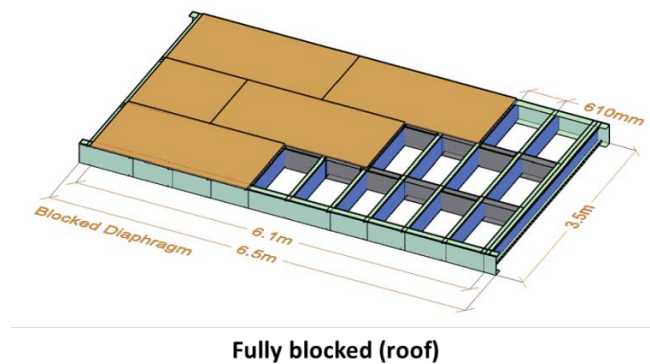


Figure 2.6: Modification to the roof diaphragm configurations; full CFS frame blocking

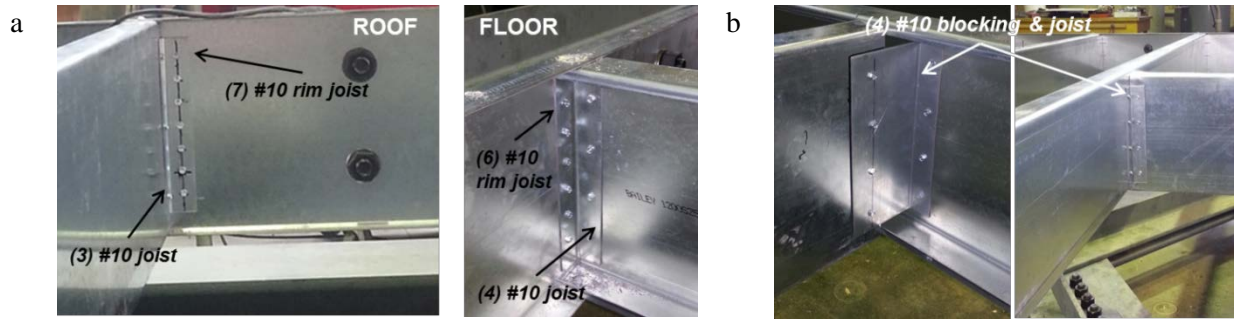


Figure 2.7: CFS framing connections; a) joist-to-track connections, and b) blocking-to-joist connections

Table 2.2: Specimen nomenclature

<b>Specimen</b>	<b>Description</b>
<b>1-RF-M</b>	Roof Bare Steel Frame Monotonic
<b>2-FF-M</b>	Floor Bare Steel Frame Monotonic
<b>3-RU-M</b>	Roof Unblocked Monotonic
<b>4-RU-C</b>	Roof Unblocked Cyclic
<b>5-F#10-M</b>	Floor #10 Screws Monotonic
<b>6-F#10-C</b>	Floor #10 Screws Cyclic
<b>7-RB-M</b>	Roof Blocked Monotonic
<b>8-RB-C</b>	Roof Blocked Cyclic
<b>9-F#12-M</b>	Floor #12 Screws Monotonic
<b>10-F#12-C</b>	Floor #12 Screws Cyclic

The CUREE displacement controlled loading protocol for ordinary ground motions (Krawinkler et al. 2000), which represents an earthquake excitation with a probability of exceedance of 10 % in 50 years, was selected for the reversed cyclic tests (i.e. Figure 2.8 depicts the loading protocol for the roof blocked specimen 8). A specific loading protocol for CFS framed diaphragms was not available; because the CUREE protocol had been extensively used for the testing of the CFS framed shear walls, relied on in the development of the AISI S400 Standard, it was decided to also use it for this study. Although seismic design input in Canada is of 2% in 50 years, the diaphragm specimens are pushed to failure, thus, capturing their full seismic performance. The effect of cumulative damage is taken into account with the repetition of multiple small deformation amplitude loading cycles followed by larger deformation amplitudes. The protocol

is based on a post peak reference displacement obtained from the monotonic test at 80% of the ultimate load. A displacement rate of 2.5mm/min for the roof and 5mm/min for the floor configuration was applied during the monotonic loading, while the cyclic loading followed a displacement rate that started with 15mm/min and increased to 60mm/min after 60mm of displacement for both the roof and floor configurations.

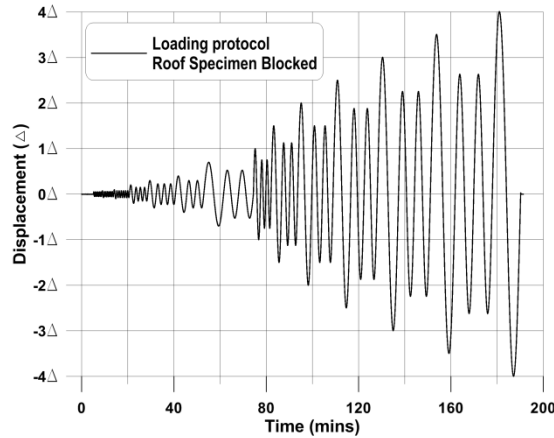


Figure 2.8: CUREE loading protocol for specimen 8-RB-C (blocked)

Regarding the instrumentation employed, lateral displacement and shear deformation as well as local in-plane displacement were captured using four string potentiometers (254 mm & 508 mm total stroke) and twelve linear variable differential transformers (LVDTs  $\pm 15$  mm stroke), as shown in Figure 2.9.

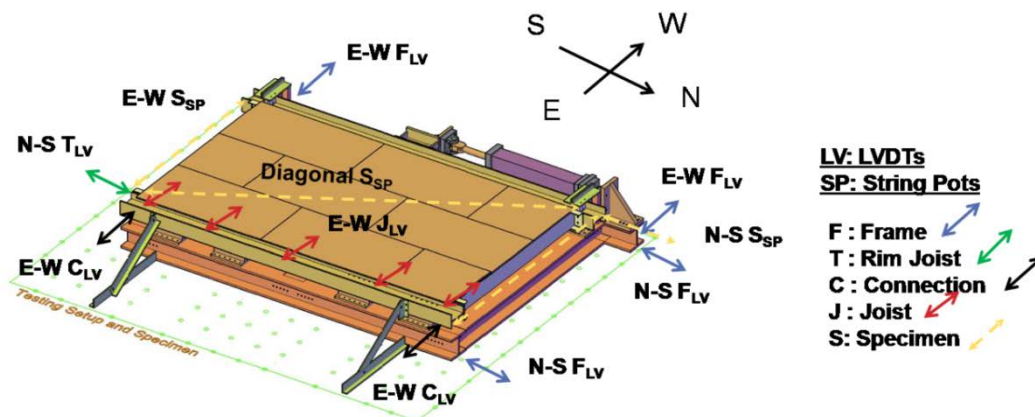


Figure 2.9: Instrumentation of diaphragm test specimens

The diaphragm response was also captured by the internal LVDT and load cell of the actuator. Vishay Model 5100B scanners and the Vishay System 5000 StrainSmart software were used to record the measured data.

#### 2.4- Material properties

Tensile coupon tests and moisture content measurements were conducted for the steel and wood material used in the experiments, respectively (Appendix D, Sections D.1 and D.2). The tensile coupon tests were based on the ASTM A370 Standard (2016) while the secondary oven-drying method of the ASTM D4442 Standard Method B (2015) was employed for the moisture content measurements. Coupons (50mm gauge length) were extracted from the CFS sections considering the different steel thicknesses (roof rim joist, roof joist, floor rim joist, floor joist). An average value was obtained for each tensile material property from three coupons for each case. Strain gauges and an extensometer were utilized to measure Young’s modulus and elongation values. The nominal yield stress and tensile strength of the ASTM A653 Grade 50 steel was 345MPa and 450MPa, respectively. Table 2.3 summarises the results from the tensile coupon tests.

Table 2.3: Tensile properties of steel

Specimens	E (MPa)	F <sub>y</sub> (MPa)	ε <sub>y</sub> (mm/mm)	F <sub>u</sub> (MPa)	ε <sub>u</sub> (mm/mm)	F <sub>u</sub> /F <sub>y</sub>	Elongation (%)	No
<b>RJ - Roof</b>	188595	387	0.0040	466	0.1717	1.20	27.5	3
<b>RJ - Floor</b>	224149	398	0.0028	474	0.1822	1.19	31.8	3
<b>J - Roof</b>	189049	391	0.0037	471	0.1959	1.20	28.7	3
<b>J - Floor</b>	210854	394	0.0036	462	0.1695	1.17	29.3	1
<b>J - Roof B</b>	200568	385	0.0015	466	0.0673	1.21	14.8	3
<b>J - Floor #12</b>	202097	410	0.0018	477	0.0858	1.16	14.6	3

Note: RJ = Rim Joist, J = Joist, B = Blocked, #12 = size #12 sheathing screws

Sharp yielding behavior was observed for all the coupon specimens with increased yield stress values expected due to the fabrication process of cold-formed steel (cold work of forming). For the moisture content measurements, samples from the OSB panels were placed for 24 hours in a constant oven temperature of 103°C in order for the oven - dry mass to be obtained (ASTM

D4442 2015, Method B). Three round specimens per panel (76.2mm in diameter) were extracted from selected panels immediately after testing and their weight was measured. Low moisture content in the range of 4% to 5% was obtained, as expected due to the fabrication process of the OSB panels.

## 2.5- Diaphragm Test Results

The hysteretic and monotonic shear force vs. deformation response was obtained for all diaphragm configurations, starting with the monotonic testing of the bare CFS frame without the sheathing. A maximum displacement of 45mm was targeted for the bare CFS framing loading to ensure that the specimen would remain in the elastic range. These tests revealed that the shear strength and stiffness contribution of the bare CFS frame is negligible, as indicated in Figure 2.10. A photograph showing the typical overall shear deformations of a wood sheathed / CFS framed diaphragm is provided in Figure 2.11; in this case Test 10-F #12-C.

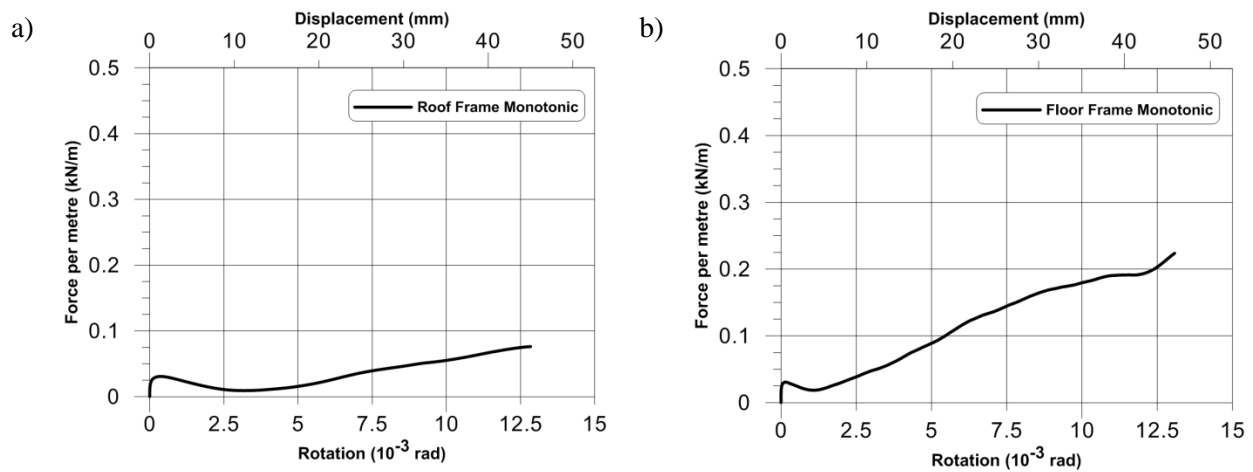


Figure 2.10: Shear force vs. rotation response for the bare CFS frame; a) 1-RF-M, and b) 2-FF-M

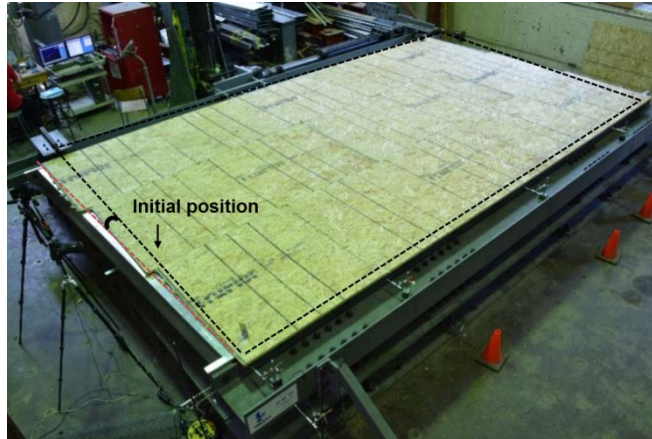


Figure 2.11: Example overall shear deformations of typical diaphragm test specimen

Subsequently, the monotonic results for specimens 3-RU-M, 7-RB-M, 5-F#10-M and 9-F#12-M are presented in Figures 2.12a and 2.13a in the form of a comparison between shear force vs. rotation response curves. Figure 2.12b includes the blocked vs. unblocked roof diaphragm configuration reversed cyclic results (8-RB-C versus 4-RU-C) while Figure 2.13b contains a comparison of the floor with #12 sheathing screws vs. the floor with #10 screws (10-F#12-C versus 6-F#10-C), respectively.

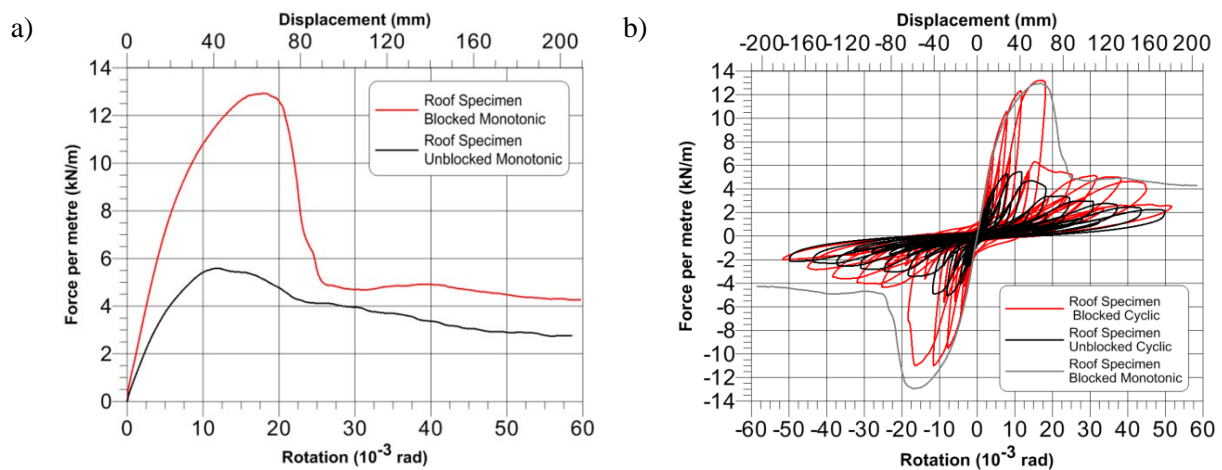


Figure 2.12: Force vs. deformation response for roof specimens; a) 3-RU-M (unblocked) & 7-RB-M (blocked), and b) 4-RU-C (unblocked) & 8-RB-C, 7-RB-M (blocked)

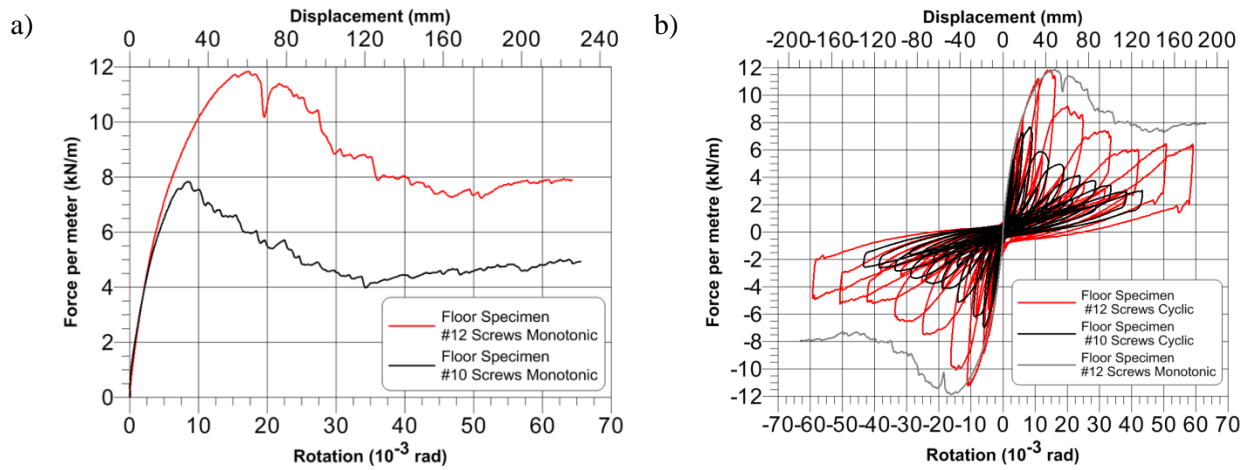


Figure 2.13: Force vs. deformation response for floor specimens; a) 5-F#10-M & 9-F#12-M, and b) 6-F#10-C & 10-F#12-C, 9-F#12-M

Referring to Figures 2.12b and 2.13b, the equivalent monotonic curve is superimposed for specimens 7 and 9, respectively. It is shown that there is no difference between the diaphragm's monotonic and the cyclic response up to the ultimate shear strength level; for positive displacements/rotations as expected the post peak cyclic curve deteriorates more quickly due to the cumulative damage of the repeated displacement cycles. This cumulative damage also results in the lower resistance attained for the negative displacement cycles.

The damage to the specimens, a result of the in-plane shear loading, is illustrated in Figures 2.14, 2.15 and 2.16. Table 2.4 summarises the corresponding data for all the tests. Details of the behavior exhibited by the specimens are provided in the following paragraphs. It should also be mentioned that the displacement shown in the graphs was obtained from the string potentiometer (N-S  $S_{SP}$ , Figure 2.9) recording the displacement of the specimen in the north-south direction. The rotation was obtained by dividing this displacement with the end members' length, 3505mm.

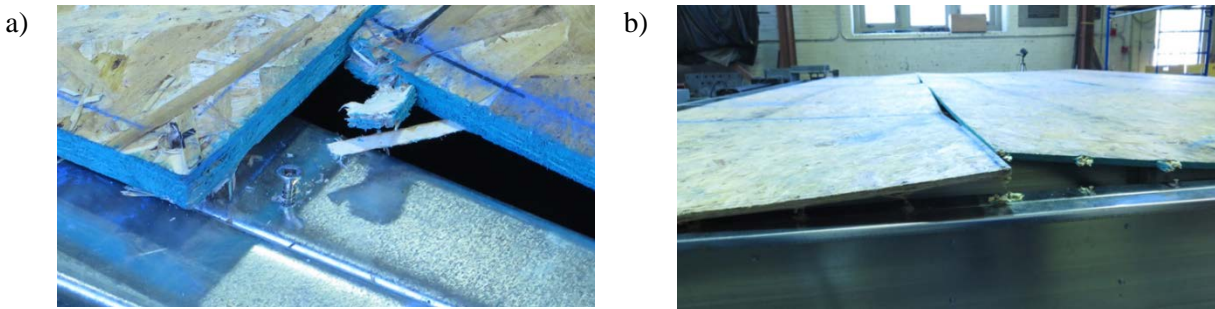


Figure 2.14: Deformation for the roof unblocked diaphragm configurations; 3-RU-M & 4-RU-C;

a) screw edge tear out, and b) lift-off of OSB panels

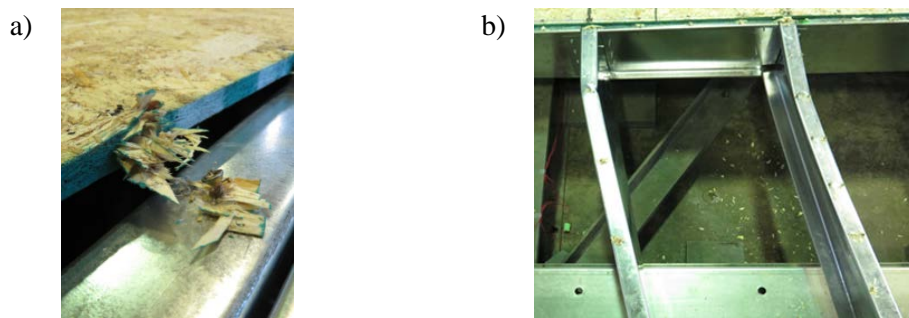


Figure 2.15: Deformation for blocked roof diaphragm configuration specimen, 7-RB-M & 8-RB-

C; a) screw edge tear out, and b) post-ultimate bending action of steel framing (OSB panels

removed for post-test photograph)

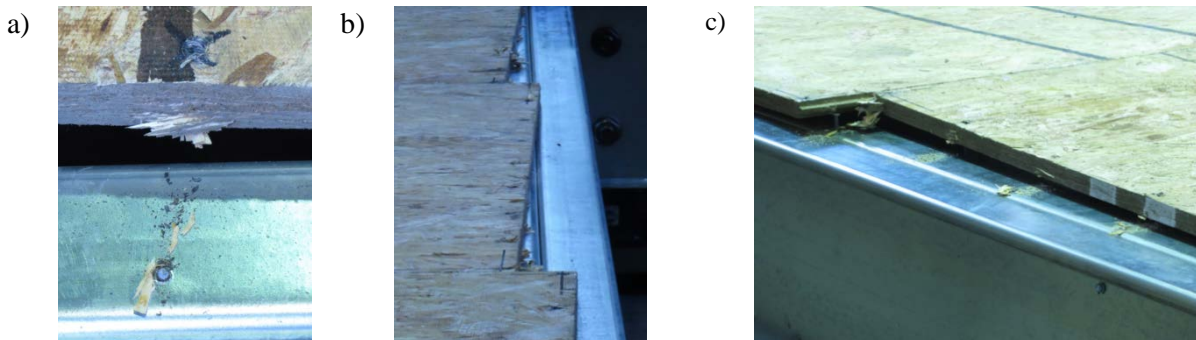


Figure 2.16: Deformation for floor diaphragm configurations with #10 screws, 5-F#10-M

& 6-F#10-C; a) screw edge shear failure, b) relative displacement between panels, and c)

panel edge contact effect

Table 2.4: General results from the monotonic (M) and reversed cyclic (C) tests

Specimens	$S_u$ (kN/m)	$\Delta_{net,o.4u}$ (mm)	$\Delta_{net,u}$ (mm)	$\theta_{net,u}$ (rad x $10^{-3}$ )	Rigidity, K (kN/mm)
<b>3-RU-M</b>	5.6	9	41.5	11.8	1.53
<b>5-F#10-M</b>	7.9	6.1	30	8.6	3.15
<b>7-RB-M</b>	13	12	62.1	17.7	2.64
<b>9-F#12-M</b>	11.8	9.4	60.7	17.3	3.07
<b>4-RU-C</b>	5.5/-5.1	7.5/-6.9	41.2/-30.6	11.8/-8.7	1.79/1.81
<b>6-F#10-C</b>	7.6/-7.1	5.8/-6.7	30.8/-23.4	8.8/-6.7	3.18/2.57
<b>8-RB-C</b>	13/-10.7	13.1/-11.1	65.5/-45	18.7/-12.8	2.48/2.34
<b>10-F#12-C</b>	11.8/-11	8.8/-9.1	57.1/-40.7	16.3/-11.6	3.29/2.93

### 2.5.1 Roof Configuration Test Results

The failure modes observed during the testing of specimens 3-RU-M and 4-RU-C were the screws tearing out or pulling through the wood after wood bearing had occurred (Figure 2.14a). Tilting of the screws was present as a desirable ductile deformation mode. Damage concentrated mostly in the middle row of the panels, where fewer screws were used (unblocked diaphragm, 304mm screw spacing). Toward the end of the test lift-off of the OSB panels was triggered in the intermediate panel locations along their edges where the sheathing was no longer attached to the framing, as illustrated in Figure 2.14b.

Adding panel edge blocking to the roof diaphragm configuration (specimens 7-RB-M, 8-RB-C) had a profound effect on the diaphragm response (Figure 2.12). This configuration yielded a 130% increase in maximum shear strength and a 70% increase in shear stiffness compared to the unblocked case (Table 4). The blocked roof diaphragm configuration exhibited the highest shear strength and stiffness overall in this experimental program even though the OSB was thinner and the sheathing screws smaller than for the floor configuration; thus, the benefit of attaching the full perimeter of each OSB panel to the underlying CFS framing was demonstrated. In this case similar failure modes to the unblocked case (Figure 2.15a) were observed (tear-out and pull-

through) accompanied by sheared fasteners mostly in areas where the fasteners penetrated two layers of steel (joist-to-rim joist connection locations). After the peak load was reached, the damage concentrated in the sheathing screw connections along the fixed edge of the test setup (Figure 2.15b). Due to the 152mm extension of the OSB in that location, as explained earlier, a shorter width panel was connected to the steel framing; thus, fewer screws were used, which potentially led to the concentration of sheathing connection failures. Ultimately, the sheathing connections in these edge panels failed, resulting in a transfer of force through the underlying steel framing by means of bending action (cantilever moment frame action of the steel framing in that location since there was no more diaphragm action, Figure 2.15b). This bending action of the steel framing is the cause of the constant level of the shear force after approximately 25 mrad rotation indicated in the response curves in Figure 2.12a and b.

### **2.5.2 Floor Configuration Test Results**

During the testing of specimens 5-F#10-M and 6-F#10-C a steeper decline of the shear strength vs. deformation curve (Figure 2.13) was observed compared to specimen 3-RU-M and 4-RU-C, attributed to the fact that the #10 sheathing screws were primarily failing in shear or remaining vertical while the wood sheathing was tearing out. This sheathing screw behavior suggested that the #10 screws (5-F#10-M, 6-F#10-C, Figure 2.16a) used thus far for this type of floor configuration were not appropriate based on the sheathing and steel thickness if a more ductile failure mode were desired. Moreover, at approximately 35mrad (Figure 2.13a and b) most of the screws in the interface of the panel rows and field had failed leading to the CFS framing underneath taking most of the load. The load increasing and then stabilizing during these final excursions showed that contact/bearing action along the edges of the intermediate panels provided additional resistance, taking also into account the T&G characteristic of the OSB

panels, which prevented lift-off of panels even though the panel edges were not blocked. A finite element model of the floor diaphragm specimen (5-F#10-M and 6-F#10-C) described in Chatterjee (2016) revealed that the level of static friction force developed during testing in the intermediate panel locations was 0.003kN/mm, which provides a minimum level of contact force being present of 0.0075kN/mm, assuming an average coefficient of friction for a wood-to-wood surface of 0.4 (Giancoli 2009). Further, the T&G panels facilitated the construction process (walking on top of the diaphragm) and, thus, would be a useful improvement for the design of the roof diaphragm. The floor configuration, comprised of greater thickness steel and sheathing, was expected to return higher shear strength and stiffness values compared to the roof configuration, as presented in Table 4. Figure 2.16 illustrates the failure mode and panel edge contact effect for the 5-F#10-M and 6-F#10-C specimens described herein.

The larger screw size (#12 vs. #10) for the floor configuration (9-F#12-M & 10-F#12-C) resulted in an overall increase of 50% in shear strength (Table 4). Screw tilting was present before shearing or pulling out of the steel due to shear and tensile forces developing between the CFS framing and OSB panels. Several joist flanges were distorted due to these applied uplift forces of the panels. Although there was an evident increase in strength due to the #12 sheathing screws, based on Figure 13, the overall force vs. deformation response was similar in shape for the two diaphragms, but the observed response of the sheathing connection seemed to be more ductile since shear fracture of the screws did not take place in the 9-F#12-M and C specimens.

## **2.6- Diaphragm Design Predictions**

The AISI S400 Standard (2015) provides a diaphragm deflection equation for simply supported span-lengths (Eq. C-F2.4.3-1) and a shear wall deflection equation (E1.4.1.4-1). Given the cantilever approach utilised in the test, it was deemed appropriate for the shear wall deflection

equation to be used in order to acquire design deflection values for the diaphragm configurations. Ultimately, it was revealed that both equations provide similar results, given the appropriate assumptions, and are presented in this paper (Eq. 2.1 for cantilever shear wall and Eq. 2.2 for simply supported diaphragm in this paper, respectively; see notation list, Section 2.9). Design deflection values were acquired for the design shear strength level following both the Canadian and US code; a resistance factor  $\phi$  of 0.6 for Load and Resistance Factor Design (60% of strength) and a safety factor  $\Omega$  of 2.5 for Allowable Strength Design (40% of strength) was considered, respectively (AISI S400 2015). Equations 1 and 2 translate into the following components of the diaphragm/shear wall response (AISI S400 (2015)): i) linear elastic bending (1<sup>st</sup> term), ii) linear elastic shear deformation (2<sup>nd</sup> term), iii) nonlinear empirical component (3<sup>rd</sup> term), and iv) overturning anchorage/ chord splice deformation.

$$\delta = \frac{2vh^3}{3E_s A_c b} + \frac{\omega_1 \omega_2 v h}{\rho G t_{sheathing}} + \omega_1^{\frac{5}{4}} \omega_2 \omega_3 \omega_4 \left(\frac{v}{\beta}\right)^2 + \frac{h}{b} \delta_v \quad (2.1)$$

$$\delta = \frac{0.052vL^3}{E_s A_c b} + \frac{\omega_1 \omega_2 v L}{\rho G t_{sheathing}} + \omega_1^{\frac{5}{4}} \omega_2 (a) \left(\frac{v}{2\beta}\right)^2 + \frac{\sum_{j=1}^n A_{ci} X_i}{2b} \quad (2.2)$$

Equation 2.1: The shear wall deflection equation refers to the deflection of a blocked CFS framed/wood sheathed shear wall. The  $\delta_v$  variable referring to the anchorage deformation was obtained using the data of the string potentiometer in the E-W direction (E-W S<sub>SP</sub>, Figure 2.9), which provided the chord member deformation, since no anchorage details were included in the diaphragm specimens.

Equation 2.2: The diaphragm deflection equation refers to the deflection of a blocked CFS framed/wood sheathed simply supported diaphragm. As such, the total shear load applied was assumed to be 2V and the total length of the diaphragm  $L = 2*3505 = 7010\text{mm}$ , since the

deflection obtained for a cantilever under point load  $P$  is equal to the one obtained by a simply supported beam at mid-span with double the cantilever length and under a load  $2P$ . The  $\Delta_{ci}$  variable referring to the chord splice deformation was obtained using the data of the string potentiometer in the E-W direction (E-W  $S_{SP}$ , Figure 2.8), as for Eq. 2.1. The splice was assumed to be in the middle of the chord; thus,  $X_i = 3505\text{mm}$ . It should be noted that the shear modulus values employed in the calculations (i.e.  $G = 1317 \text{ N/mm}^2$  for the roof specimens) were obtained from TECO's document entitled Design Capacities for Oriented Strand Board (TECO 2008). Further, an amplification factor of 2.5 is suggested for the diaphragm deflection equation (Eq. C-F2.4.3-1 AISI S400 (2015)) when the diaphragm is unblocked. Such factor does not exist for the shear wall deflection (E1.4.1.4-1 AISI S400 (2015)) equation since a shear wall is always blocked. However, since both equations yield similar results and refer to a diaphragm in this paper the 2.5 factor is applied to both.

Table 2.5 provides the results for Eq. 2.1 and 2.2 compared to the observed values from testing corresponding to the design level of 40% and 60% of the shear strength. It is shown that Eq. 2.1 and 2.2 provide similar results and that in almost all the cases the error between calculated and observed data is close to 20% or lower. Further, looking at the error percentages of Table 2.5 and the force vs. deformation curves of Figures 2.12 and 2.13, it can be observed that the error is reduced when the level of force considered for calculation corresponds to the near linear part of the curve, which indicates that Eq. 2.1 and 2.2 can confidently be used to calculate deflection at the design shear strength level but may not produce as accurate results for the peak shear strength level. Included in Table 2.5 is the relative error of calculated displacements with respect to measurements. It should be noted that a different process was followed compared to the one presented in Nikolaidou et al. 2017, in which the focus was to compare the deflection design

values at the ultimate shear strength level with an equivalent elastic displacement,  $\delta_{\text{elastic}}$ , provided by the experimental data at ultimate assuming elastic response of the diaphragm. This effort led to this updated process were only the design level shear strength was considered and appropriate assumptions were made for both deflection equations leading to more reasonable results.

Table 2.5: Design deflection values using Eq. 2.1 and 2.2

<b>Deflection At 40% Strength</b>	<b>3-RU-M &amp; 4-RU-C</b>	<b>5-F#10-M &amp; 6-F#10-C</b>	<b>7-RB-M &amp; 8-RB-C</b>	<b>9-F#12-M &amp; 10- F#12-C</b>
$\delta_{\text{Observed}} \text{ (mm)}$	8.18	5.61	10.6	7.82
$\delta_{\text{Calculated}} \text{ (mm)},$ <b>Eq. 2.1</b>	8.46	4.68	8.67	9.59
<b>% Error</b>	3.4	16.6	18.2	22.7
$\delta_{\text{Calculated}} \text{ (mm)},$ <b>Eq. 2.2</b>	8.59	4.52	8.06	8.83
<b>% Error</b>	5.1	19.4	23.9	12.9
<b>Deflection At 60% Strength</b>	<b>3-RU-M &amp; 4-RU-C</b>	<b>5-F#10-M &amp; 6-F#10-C</b>	<b>7-RB-M &amp; 8-RB-C</b>	<b>9-F#12-M &amp; 10- F#12-C</b>
$\delta_{\text{Observed}} \text{ (mm)}$	13.52	9.61	17.4	15.32
$\delta_{\text{Calculated}} \text{ (mm)},$ <b>Eq. 2.1</b>	13.72	10.54	14.4	17.32
<b>% Error</b>	1.5	9.7	17.2	13
$\delta_{\text{Calculated}} \text{ (mm)},$ <b>Eq. 2.2</b>	13.48	9.81	12.53	15.03
<b>% Error</b>	0.3	2.1	28	1.9

Table 2.6 lists the nominal shear resistance values,  $V_{\text{AISI}}$ , as obtained from Table F2.4-1 of the AISI S400 Standard (2015) to be used in design and the measured shear resistance values,  $V_{\text{TEST}}$ , provided from the tests for each diaphragm configuration presented herein. Table F2.4-1 refers only to plywood sheathing and does not account for the effect of the sheathing screw size; thus, meaningful design predictions cannot be made for the specific tested diaphragm specimens. Nonetheless, these are the only design shear strength values available at present in the AISI S400

Standard (2015) for the tests included in this paper; thus, based on Table 2.6, the Standard over-predicts the shear strength of specimens 3&4 and under-predicts that of specimens 9&10.

Table 2.6: Nominal shear resistance values using Table F2.4-1 of AISI S400 (2015)

<b>Shear Resistance</b>	<b>3-RU-M &amp; 4-RU-C</b>	<b>5-F#10-M &amp; 6-F#10-C</b>	<b>7-RB-M &amp; 8-RB-C</b>	<b>9-F#12-M &amp; 10-F#12-C</b>
<b>V<sub>AISI</sub> (kN/m)</b>	7.37	8.10	11.10	8.10
<b>V<sub>TEST</sub> (kN/m)</b>	5.6	7.9	13	11.8

## 2.7- Conclusions

A total of ten CFS framed / OSB sheathed diaphragm tests were completed in the experimental program described in this paper. The research focused on four main diaphragm configurations, for which various parameters were altered, such as the steel section and the OSB thickness, the screw size and the use of panel edge blocking. The objective was to characterize the in-plane force vs. deformation response of the CFS framed / wood sheathed diaphragm under monotonic and reversed cyclic loading. The main findings are summarised as follows:

- ✓ As tested, the CFS floor and roof framing without the sheathing does not contribute to the shear strength and stiffness of the diaphragm
- ✓ Panel edge blocking substantially increases the diaphragm shear strength and stiffness, with values of 130% and 70% obtained, respectively, for the roof configuration.
- ✓ Changing the sheathing screw size from #10 to #12 for panels having a thickness of 18mm does not have a measurable effect on the shape of the overall diaphragm load vs. displacement response despite the fact that it leads to a somewhat more ductile sheathing-to-framing screw connection behavior. It does cause, however, a considerable increase in the diaphragm shear strength (50%).

- ✓ T&G sheathing panels improve both the construction process and the performance of the diaphragm. As such, their further implementation also for roof diaphragms should be considered.
- ✓ In an effort to obtain design shear and deflection values the AISI S400 Standard (2015) was employed. The design deflection values calculated using the shear wall and diaphragm deflection equations (Eq. 2.1 and 2.2 in this paper) of the AISI S400 Standard (2015) were in close proximity with the experimental values for the design level shear strength of the specimens. However, regarding design shear strength values, the AISI S400 Standard (2015) at present does not include values for the case of OSB panels, and the size of the screws is not considered as an influential parameter in the design shear strength calculations. As such, relevant design shear strength values could not be obtained.

Additional experimental and numerical work is required in order for complete information about the CFS framed diaphragm response to be available to professional engineers. Studies should focus on varying parameters, such as screw spacing, panel type and diaphragm span length, as well as implementing non-structural components, such as gypsum panels.

## **2.8- Acknowledgements**

The authors would like to thank the American Iron and Steel Institute (AISI) for financially supporting this research project. Additional support was obtained from the Canadian Sheet Steel Building Institute (CSSBI) and the Natural Sciences and Engineering Research Council of Canada (NSERC). A special thank you is also extended to Bailey Metal Products Ltd., Simpson Strong-Tie Co. Inc., Ontario Tools and Fasteners Ltd, ArcelorMittal and Constructions Proco Inc. for the materials and tools that were provided.

## 2.9- Notation

The following symbols are used in this paper:

- $A_c$  = Gross cross-sectional area of chord member ( $\text{mm}^2$ )
- $b$  = Width of the shear wall/diaphragm (parallel to loading) (mm)
- $E_s$  = Modulus of elasticity of steel 203,000 MPa
- $G$  = Shear modulus of sheathing material (MPa)
- $h$  = Wall height (mm)
- $K$  = Rigidity of diaphragm specimen calculated at 40% shear strength (kN/mm)
- $L$  = Diaphragm length perpendicular to direction of load (mm)
- $n$  = Number of chord splices in diaphragm (considering both diaphragm chords)
- $s$  = Maximum fastener spacing at panel edges (mm)
- $S_u$  = Shear strength of diaphragm specimen (kN/m)
- $t_{\text{sheathing}}$  = Nominal panel thickness (mm)
- $t_{\text{stud}}$  = Nominal framing thickness (mm)
- $V$  = Total in-plane load applied to the diaphragm (N)
- $v$  = Shear demand ( $V/b$ ), (N/mm)
- $X_i$  = Distance between the “ $i^{\text{th}}$ ” chord-splice and the nearest support (mm)
- $\alpha$  = 1 for a uniformly fastened diaphragm
- $\beta$  = 2.35 for plywood and 1.91 for OSB for SI units ( $\text{N}/\text{mm}^{1.5}$ )
- $\Delta_{ci}$  = Deformation value associated with “ $i^{\text{th}}$ ” chord splice (mm)
- $\Delta_{\text{net},0.4u}$  = Displacement value of diaphragm specimen at 40% shear strength (mm)
- $\Delta_{\text{net},u}$  = Displacement value of diaphragm specimen at ultimate shear strength (mm)
- $\delta$  = Calculated in-plane deflection (mm)
- $\delta_v$  = Vertical deformation of anchorage / attachment details (mm)

$\theta_{\text{net,u}}$  = Rotation of diaphragm specimen at ultimate strength,  $\Delta_{\text{net,u}} / 3505\text{mm}$  (rad x  $10^{-3}$ )

$\rho$  = 1.85 for plywood and 1.05 for OSB, term for different sheathing material type

$\omega_1$  =  $s/152.4$  (for  $s$  in mm)

$\omega_2$  =  $0.838/t_{\text{stud}}$  (for  $t_{\text{stud}}$  in mm)

$\omega_3$  =  $\sqrt{(h/b)/2}$

$\omega_4$  = 1 for wood with structural panels

## 2.10- References

AISI S100 (2016). "North American specification for the design of cold-formed steel structural members." *American Iron and Steel Institute*, Washington, DC.

AISI S400 (2015). "North American standard for seismic design of cold-formed steel structural systems." *American Iron and Steel Institute*, Washington DC.

AISI S907 (2013). "Test standard for cantilever test method for cold-formed steel diaphragms." *American Iron and Steel Institute*, Washington, DC.

APA (2007). "*Diaphragms and shear walls*." Design/Construction Guide Form No. L350A, The Engineered Wood Association.

ASTM A370 (2016). "Standard test methods and definitions for mechanical testing of steel products.", *American Society for Testing and Materials*, West Conshohocken, PA.

ASTM A653 (2015a). "Standard specification for steel sheet, zinc-coated (galvanized) or zinc-iron alloy-coated (galvannealed) by the hot-dip process.", *American Society for Testing and Materials*, West Conshohocken, PA.

- ASTM D4442 (2015). "Standard test methods for direct moisture content measurement of wood and wood base materials.", *American Society for Testing and Materials*, West Conshohocken, PA.
- Branston A. E., Boudreault F. A., Chen C. Y., and Rogers C. A. (2006). "Light-gauge steel-frame wood structural panel shear wall design method." *Canadian Journal of Civil Engineering*; (33(7)), 872-889.
- Chatterjee A. (2016). "Structural system reliability with application to light steel-framed buildings." PhD Thesis, Virginia Polytechnic Institute and State University, Blacksburg, Virginia.
- CSA S136 (2016). "North American specification for the design of cold-formed steel structural members.", *Canadian Standards Association*, Rexdale, Canada.
- CSI (Computers and Structures, Inc). (2009). "Linear and non-linear static and dynamic analysis and design of three-dimensional structures basic analysis reference manual." SAP2000 V.14, Berkeley, CA.
- Dolan J. D. and Easterling W. S. (2000). "Monotonic and cyclic tests of light-frame shear walls with various aspect ratios and tie-down restraints." *Report No. TE-2000-001*, Virginia Polytechnic Institute and State University, Blacksburg, VA.
- Giancoli, D. (2009). "Physics for Scientists and Engineers with Modern Physics," Pearson Education, Inc, 4th Edition.
- Krawinkler H., Parisi F., Ibarra L., Ayoub A., and Medina R. (2000). "Development of a testing protocol for wood frame structures." *Report W-02 covering Task 1.3.2*, CUREE/Caltech

- Woodframe Project. Consortium of Universities for Research in Earthquake Engineering (CUREE), Richmond, CA.
- LGSEA (1998). "Lateral load resisting elements: Diaphragm design values." *Tech Note 558b-1*, Light Gauge Steel Engineers Association, Washington, DC.
- Liu P., Peterman K. D., Yu C., and Schafer B. W. (2012). "Cold-formed steel shear walls in ledger-framed buildings." *Annual Stability Conference*, Conference location, Grapevine, TX.
- NAHB Research center (1999). "Innovative residential floor construction: Horizontal diaphragm values for cold-formed steel framing." *U.S. Department of Housing and Urban Development*, Upper Marlboro, MD.
- Nikolaidou V., Latreille P., Rogers C. A., and Lignos D. G. (2015). "Characterization of CFS framed diaphragm behavior." *Report CM – 432*, American Iron and Steel Institute, Washington, DC.
- Nikolaidou V., Latreille P., Rogers C. A., and Lignos D. G. (2017). "Characterization of cold-formed steel framed/wood-sheathed floor and roof diaphragm structures." *16th World Conference on Earthquake Engineering*, Conference location, 452.
- NIST, Madsen R. L., Castle T. A., and Schafer B. W. (2016). "Seismic design of cold-formed steel lateral load resisting systems: A guide for practicing engineers." *GCR 16-917-38*, Applied Technology Council and the Consortium of Universities for Research in Earthquake Engineering for the National Institute of Standards and Technology, NEHRP Seismic Design Technical Brief No. 12, Gaithersburg, MD.

- Pan C. L. and Shan M. Y. (2011). "Monotonic shear tests of cold-formed steel wall frames with sheathing." *Thin-Walled Structures*, 49(2), 363-370.
- Peterman K. D. (2014). "Behavior of full-scale cold-formed steel buildings under seismic excitations." *PhD thesis*, Johns Hopkins University, Baltimore, MD.
- Peterman K. D., Stehman M. J., Madsen R. L., Buonopane S. G., Nakata N., and Schafer B. W. (2016a). "Experimental seismic response of a full-scale cold-formed steel-framed building. I: System-level response." *ASCE Journal of Structural Engineering*, 142(12): 04016127.
- Peterman K. D., Stehman M. J., Madsen R. L., Buonopane S. G., Nakata N., and Schafer B. W. (2016b). "Experimental seismic response of a full-scale cold-formed steel-framed building. II: Subsystem-level response." *ASCE Journal of Structural Engineering*, 142(12): 04016128.
- Serrette R. L. and Chau K. (2003). "Estimating the response of cold-formed steel-frame shear walls." Santa Clara University, Department of Civil Engineering. Santa Clara. CA.
- Serrette R. L., Morgan K. A., and Sorhouet M. A. (2002). "Performance of cold-formed steel-framed shear walls: Alternative configurations." *Report No. LGSRG-06-02*, Santa Clara University, Department of Civil Engineering, Santa Clara, CA.
- Shamim I., DaBreo J., and Rogers C. A. (2013). "Dynamic testing of single-and double-story steel-sheathed cold-formed steel-framed shear walls." *Journal of Structural Engineering*, 139(5), 807-817.

TECO (2008). "TECHTIP. Design capacities for oriented strand board."  
<[www.pfsteco.com/techtips/pdf/tt\\_osbdesigncapacities](http://www.pfsteco.com/techtips/pdf/tt_osbdesigncapacities)>.

Tissell J. R. and Elliot J. R. (2004). "Plywood diaphragms." *Research Report 138*, American Plywood Association (APA), Tacoma, WA.

## **Foreword to Chapter 3...**

The first part of Chapter 3 presents experimental results for diaphragm configurations with non-structural components following the same testing method as described in Chapter 2. In particular, these diaphragm configurations with non-structural components are part of Phase 2 of the diaphragm experimental program. Phase 2 also included diaphragm configurations with various structural characteristics, such as strap-blocking and an altered direction of the joist framing, among others, and can be found in detail in the thesis of Latreille (2016). The diaphragm experimental results in Chapter 3 are subsequently incorporated in the diaphragm component model of a 3D building model in order to investigate the effect of non-structural components on the seismic response of a two-storey case study CFS building. The 3D building model features diaphragms, shear walls and gravity walls. Response history dynamic analyses results are presented in two steps: a) results for the case where non-structural components are only present on the diaphragm subsystems of the building and b) results where non-structural components are placed throughout the diaphragms and walls of the building. Chapter 3 serves as a link between the experimental work presented in Chapter 2 and the numerical work presented in Chapter 4.

# CHAPTER 3: INFLUENCE OF NON-STRUCTURAL COMPONENTS ON THE SEISMIC RESPONSE OF COLD - FORMED STEEL BUILDINGS: SYSTEM & SUBSYSTEM LEVEL RESPONSE

Violetta NIKOLAIDOU<sup>1</sup>, Colin A. ROGERS<sup>2</sup>, Dimitrios G. LIGNOS<sup>3</sup>

## 3.1- Abstract

This study comprises an investigation of the influence of non-structural components on the lateral response of the diaphragm subsystem, and, subsequently, on the overall seismic response of a cold-formed steel (CFS) framed building. The experimental results for two diaphragm configurations with gypsum ceiling and gypcrete flooring were utilized with the chosen two-storey case study CFS building, incorporating diaphragms, shear walls and gravity walls with gypsum sheathing found throughout the structure. Through nonlinear response history analyses it is shown that, although non-structural components on the diaphragm increase its shear strength and stiffness, it is the addition of gypsum sheathing and gravity walls throughout the wall-line of the building that led to an overall stiffer seismic response. It was found that the gravity walls are the dominant lateral load resisting elements.

**Keywords:** cold-formed steel buildings, non-structural components, gypsum panels, gravity walls, diaphragms

### 3.2- Introduction

Over the last decade, numerous multi-university research projects have focused on the seismic response of cold-formed steel (CFS) framed buildings aiming to better understand their complex nature in order to improve their seismic design provisions, e.g. Fiorino et al. (2017), Macillo et al. (2017), Yu and Li (2012), Iuorio et al. (2014), Peterman et al. (2016a,b), Leng et al. (2017), Padilla-Liano et al. (2014), Florig et al. (2015), Chatterjee (2016), and Nikolaidou et al. (2017). The CFS-NEES (Network for Earthquake Engineering Simulation) building (Peterman et al. 2016a,b) was the first full-scale shake table experiment featuring a two-storey 7.01x15.16m CFS framed building. This building was tested in various construction phases, with exterior oriented strand board (OSB) and interior gypsum sheathing added throughout. The CFS-NEES building, tested under various levels of earthquake loading, provided valuable experimental data that facilitated the calibration of numerical models used to simulate CFS building under ground motion excitation (Leng et al. 2017). This work suggested that the non-structural components can greatly contribute to the lateral load resistance and stiffness of a CFS building in addition to its structural components.

Gypsum sheathing is a common non-structural element installed throughout a CFS building providing fire resistance and sound proofing for shear walls, diaphragms and gravity walls. Gravity walls could be considered as non-structural elements for the resistance of lateral loads, as this is not their role in the building. Available studies highlighting the contribution of the gypsum are found in the work of Christovasilis et al. (2008) and Chen et al. (2014) on timber framed shear walls, among others. Work on gypsum sheathed CFS or wood framed partition walls is also available by Hopkins (2013) and Swensen et al. (2016). Further, Buonopane et al. (2015) developed a fastener-based model in OpenSees (McKenna 1997) able to predict the

nonlinear response of CFS framed shear walls using experimental connection data from Peterman et al. (2013). Bian et al. (2015) used this fastener-based model to simulate a wall system including both shear walls and gravity walls with and without OSB and gypsum sheathing. They showed the increase in shear strength and stiffness of the shear wall due to the added gypsum sheathing, as well as the ability of the gravity wall to carry up to half of the imposed lateral load. Chen et al. (2014) tested timber framed shear walls with gypsum and OSB sheathing, highlighting the difference and lateral contribution of these two materials, and showing that the nonlinear response of a shear wall with both OSB and gypsum can be obtained by summing the individual responses of two walls, one with gypsum and one with OSB sheathing, separately. Lu (2015) tested 25 shear walls and discovered that two layers of 15.9mm gypsum placed on both sides of a CFS framed shear wall double its shear strength. Focusing on bearing walls (no holdowns), Lu's eight wall specimens revealed substantial lateral stiffness and capacity. Examining the influence of the non-structural gypsum in a system level, Shamim and Rogers (2015) demonstrated through numerical simulations an increase in the collapse capacity of two buildings, in Vancouver and Montreal, Canada, through the means of incremental dynamic analyses after adding gypsum sheathing on the shear walls. Peterman et al. (2016a) recorded the gradual increase in lateral stiffness of the CFS-NEES building with the addition of exterior OSB and interior gypsum throughout. Peterman, also, explained that gravity elements can be perceived as part of the lateral force resisting system in CFS buildings.

The aforementioned studies highlight the strong influence of non-structural components on the lateral response of a CFS building and the need to clearly quantify their contribution. The current North American building codes and CFS related design standards (AISI S400 North American Standard for Seismic Design of Cold-Formed Steel Structural Systems (2015) & AISI S100

(2016) / CSA S136 (2016) North American Specification for the Design of Cold-Formed Steel Structural Members) take into account the contribution of non-structural gypsum sheathing to the lateral response of wood-sheathed shear walls for seismic design in Canada restricting their applicability. In the USA, the benefit of gypsum on the shear wall's lateral response is recognised as inherent in the system's over-strength factor. To the authors knowledge there are no prior related studies on CFS framed diaphragms with non-structural components; as such, information is lacking on the diaphragm's contribution to the overall lateral resistance of a CFS building. Research on wood sheathed / CFS framed diaphragms has been limited (Chatterjee 2016, Florig et al. 2015, Latreille 2016 and Chapter 2 of this dissertation). In particular, Chatterjee created a 3-Dimensional (3D) finite element ABAQUS model of the floor system of the CFS-NEES building and provided its monotonic nonlinear response in the two directions up to the floor's ultimate shear strength. Concentrated plasticity spring elements were used for the sheathing-to-framing and rim joist-to-wall stud connections based on experimental data from Moen et al. (2016). Florig et al. tested the full-scale simply supported floor system of the CFS-NEES building and provided its nonlinear monotonic response up to the peak load, assuming loading perpendicular to the long dimension of the diaphragm. Nikolaidou et al. (2017) and Latreille (2016) conducted full scale experiments on nine 3.66m x 6.1m OSB sheathed/CFS framed diaphragm configurations (16 diaphragm specimens) tested under monotonic and reversed cyclic loading. The first phase of the program contained an examination of the effect of blocking and screw size on the diaphragm's nonlinear response to lateral load; the second phase included an investigation of joist orientation, strap blocking, smaller screw spacing and non-structural components, such as gypsum ceiling and gypcrete flooring. Gypcrete flooring is often used for sound insulation purposes, and also improves the fire resistance rating.

Herein is presented: (1) experimental results for the case of the isolated diaphragm subsystem with non-structural gypsum ceiling and gypcrete flooring; and (2) nonlinear response history analyses results for the CFS-NEES building, chosen as the case study building. A simplified modeling approach is followed based on the work of Leng et al. (2017) including shear walls, gravity walls and the diaphragm component. The floor and roof subsystems are simulated using the experimental data of the Phase 1 & 2 diaphragm test program at McGill University (Chapter 2, Latreille 2016). The contribution of the interior gypsum and gravity walls to the lateral response of the building is quantified in terms of fundamental period, base shear distribution and general shear wall behaviour.

### **3.3- Experimental work: gypsum panels and gypcrete flooring**

Selected results for the two diaphragm configurations with non-structural components of the diaphragm experimental program Phase 2 conducted at McGill University are summarised in this section.

#### **3.3.1 Diaphragm specimens and test set-up**

The diaphragm specimens were 3.66x6.1m OSB sheathed and CFS framed based on the floor and roof diaphragm subsystems of the CFS-NEES building; the diaphragm experimental program was supplementary to the NEES project in order to provide information on the particular isolated diaphragm response. The cantilever approach was followed (AISI S907 2013) and a 4.5x6.5m test set-up was designed. These dimensions were also chosen so as to accommodate the spacing restrictions of the Jamieson Structures Laboratory at McGill University; a detailed description can be found in Chapter 2.

Table 3.1 provides the structural details of the two diaphragm specimens in question. The nomenclature is as follows: Number – Specimen Description – Type of Loading; i.e. 14-RGYP-

M refers to the 14<sup>th</sup> specimen of the diaphragm experimental program, RGYG refers to the roof configuration with the gypsum ceiling and M refers to monotonic loading. As such, FCRETE refers to the floor configuration with the gypcrete flooring and C to reversed cyclic loading.

Table 3.1: Diaphragm structural characteristics

<b>14-RGYG-M, 15-RGYG-C: Roof Diaphragm with 16mm gypsum panels ceiling/Unblocked*</b>	<b>Section (mm) ASTM A653 (2015) Grade 50 steel</b>	<b>Length (mm)</b>
<b>Joists</b>	305S51-137M	3505
<b>Rim Joists</b>	305T51-173M	6480
<b>Web Stiffeners</b>	L 38x38x1.37	250
<b>Joist bracing</b>	305S41-137M	560
<b>Joist bracing connectors</b>	L 38x102x1.37	250
<b>Straps</b>	38x1.37	6300
<b>#8 sheathing self-drilling (152/305mm spacing)</b>	-	50
<b>#10 steel-to-steel flat head self-drilling</b>	-	20
<b>#10 steel-to-steel Hex Head Cap self-drilling</b>	-	25
<b>OSB panels (24/16 rated)</b>	2438x1219x11	-
<b>One layer, Type X, gypsum panels</b>	2400x1200x16	-
<b>#6 Type S, drywall screws (305mm spacing)</b>	-	32
<b>16-FCRETE-M: Floor Diaphragm with 19mm gypcrete topping/Unblocked*</b>	<b>Section (mm) ASTM A653 (2015) Grade 50 steel</b>	<b>Length (mm)</b>
<b>Joists</b>	350S64-246M	3505
<b>Rim Joists</b>	350T64-246M	6480
<b>Web Stiffeners</b>	L 38x38x1.37	280
<b>Joist bracing</b>	305S51-137M	550
<b>Joist bracing connectors</b>	L 38x102x1.37	250
<b>Straps</b>	38x1.37	6300
<b>#12 sheathing self-drilling (152/305mm spacing)</b>	-	44
<b>#10 steel-to-steel flat head self-drilling</b>	-	20
<b>#10 steel-to-steel Hex Head Cap self-drilling</b>	-	25
<b>OSB panels (48/24 rated T&amp;G)</b>	2438x1219x18	-
<b>19mm GYP-CRETE2000@/3.2K (Maxxon 2016)</b>	-	-

Note: \*Unblocked: Fewer screws in the intermediate panel locations ; no steel underneath to attach all OSB panel edges

The FCRETE was tested under monotonic loading only while RGYG was, also, tested under reversed cyclic loading. The reversed cyclic loading was chosen to be the CUREE displacement controlled loading protocol for ordinary ground motions (Krawinkler et al. 2000). The RGYG configuration was the first to be tested of the two. From Phase 1 it was shown that up to its peak response the diaphragm specimens behaved similarly under both types of loading. Therefore, for

Phase 2 it was decided to conduct more monotonic tests. However, since non-structural components had not been included in Phase 1, for RGYB both types of loading were employed. Further details regarding the testing program can be found in Chapter 2. The gypsum panels were installed on the underside of the CFS-framing. Figure 3.1a shows the diaphragm specimen being raised using a crane to facilitate access to install the gypsum ceiling panels. Joint compound and tape were applied at the intermediate gypsum locations and screw locations that allowed reinforcement of the gypsum sheathing-to-framing connections.

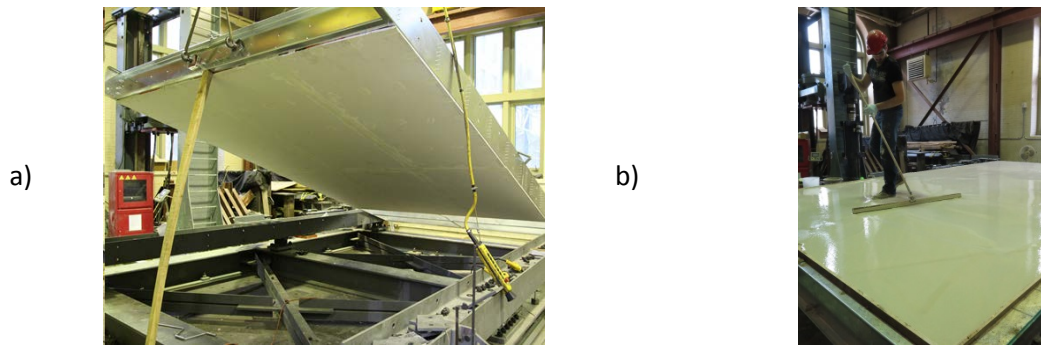


Figure 3.1: Installation process: a) gypsum panels on underside of steel framing, and b) gypcrete on top of OSB panels

Installing the gypcrete flooring had several steps. First, a 25mm high plywood perimeter was put in place in order to ensure uniform height of the gypcrete flooring. Then a powder floor primer had to be added using a handheld roller to ensure adequate bonding between the gypcrete and OSB panels. The gypcrete mixture was prepared on site and was poured evenly across the floor surface. The gypcrete was allowed to cure for 28 days before testing. Detailed information can be found in Latreille (2016).

### 3.3.2 Selected experimental findings on the diaphragm hysteretic behaviour

Shear force versus rotation relations are plotted for the same diaphragm configurations with and without non-structural components. Figure 3.2a demonstrates the shear response under reversed

cyclic and monotonic lateral loading for the RGYP versus the 4-RU-C specimen (see Chapter 2, Section 2.3). Figure 3.2b includes the FCRETE and 9-F#12-M shear response curves, respectively. These figures clearly show the increase in shear strength and stiffness, as a direct result of the non-structural components. In particular, the gypsum panels result in a 60% increase in shear strength and an over 100% increase in shear stiffness. Referring to Figure 3.2a both the monotonic and cyclic responses are shown. For both loading types there are practically no differences up to the peak response. In the post-peak range more pronounced strength degradation is observed under cyclic loading due to the inelastic cumulative damage effects compared to that seen under monotonic loading. During testing, the RGYP specimen experienced sporadic failure of the drywall gypsum-to-framing connection screws causing a drop in shear strength prior to reaching the peak load. Figure 3.3a shows the gypsum panels disconnected from the framing after most of the drywall screw connections have failed. Typical failure modes of the OSB sheathing-to-framing connection screws were observed in the post-peak response such as screw tear-out or pull-through concentrated in the weakened intermediate panels locations for an unblocked configuration (Figure 3.3b).

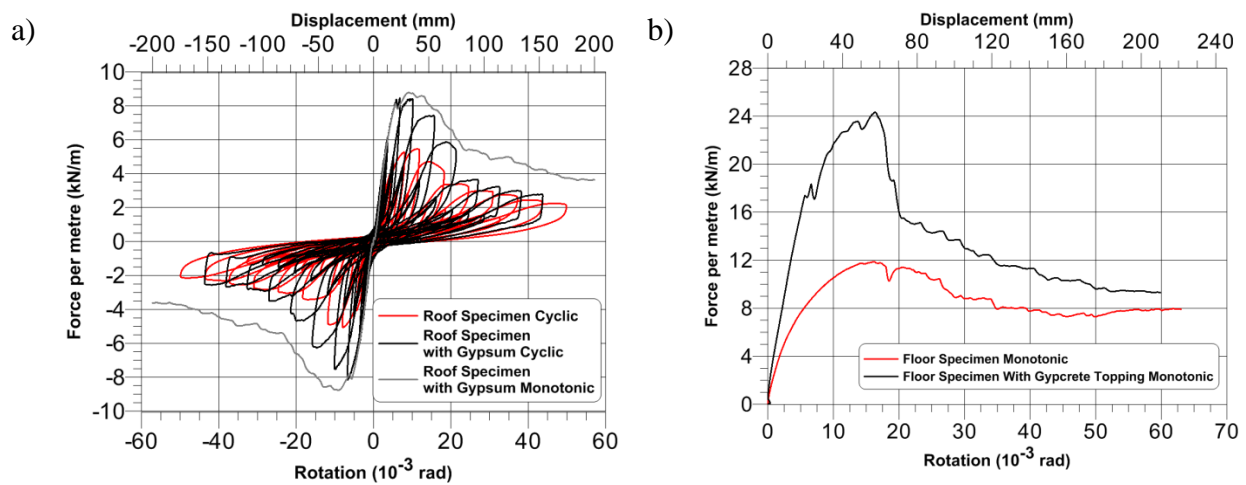


Figure 3.2: Experimental results: a) RGYP and b) FCRETE

The gypcrete's lateral contribution translates to over a 100% increase in shear strength and stiffness for the FCRETE specimen, as illustrated in Figure 3.2b. This increase in lateral resistance of the floor system is directly attributed to the bonding of the gypcrete flooring with the OSB panels. This composite material restrained the sheathing-to-framing connection screws from tilting, which increased the connection resistance. This is consistent with other test observations (Hopkins 2013 and Swensen et al. 2016). As a result, tear out or wood bearing was the primary mode of connection failure. During testing, the tension field created from the lateral loading led to cracking of the gypcrete at locations perpendicular to the tensile forces (Figure 3.3c); crack propagation eventually resulted in the panels separating at these locations (Figure 3.3d). After testing, the gypcrete surface had to be crushed using a jackhammer to separate the two materials. It should be noted that no difference was observed in the overall post-peak behaviour of the roof and floor configuration after adding gypsum or gypcrete, respectively.

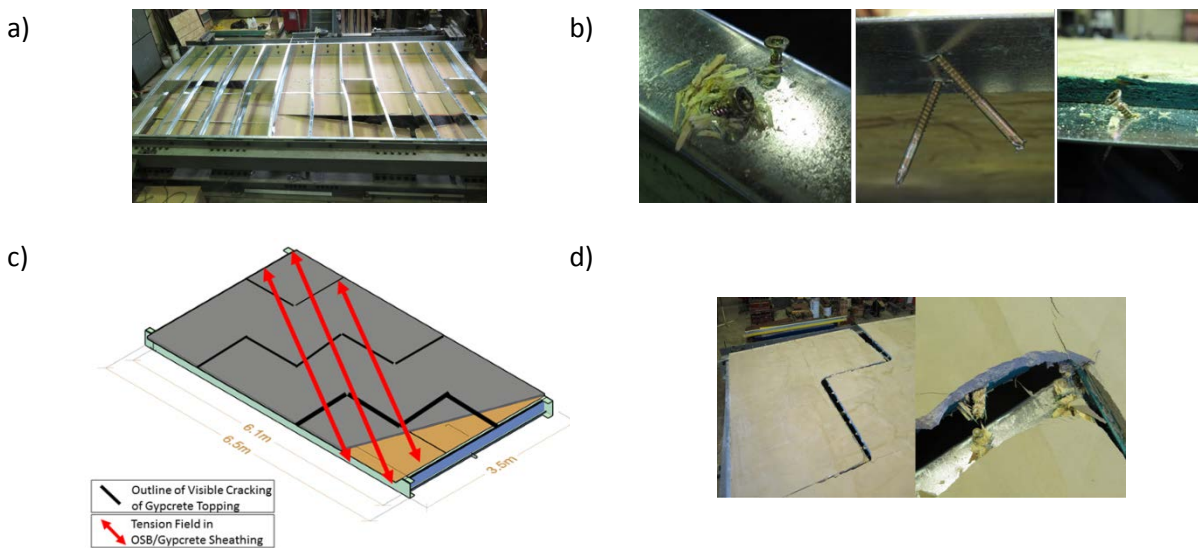


Figure 3.3: Specimen failure modes; a) RGYP post-peak, separation of gypsum panels (OSB panels removed), b) RGYP: screws tilting, tearing-out or pulling-through, c) FCRETE: cracking of gypcrete and d) FCRETE: OSB panel separation and screw tear out at crack locations

### 3.4- Numerical simulation of the case study CFS building

The CFS-NEES building is a 7.01mx15.16m two-storey structure with 2.74m storey height.

Figure 3.4 illustrates the modeling approach followed in OpenSees Version 2.4.5 (McKenna 1997) for all the structural and non-structural elements, which is described in detail in the following sections.

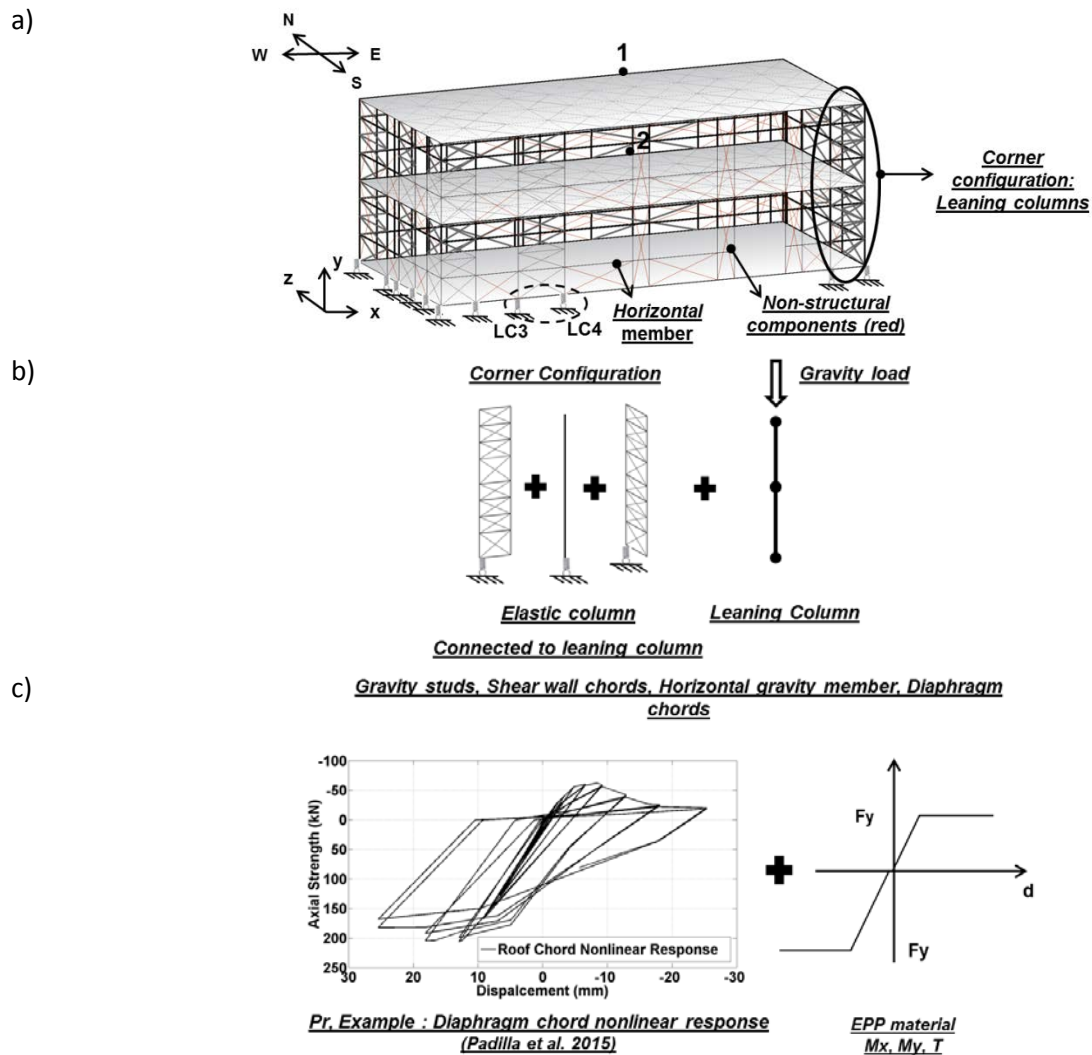
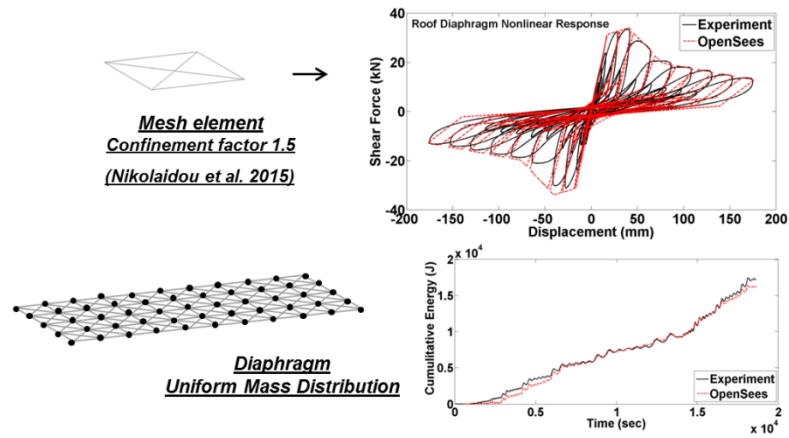
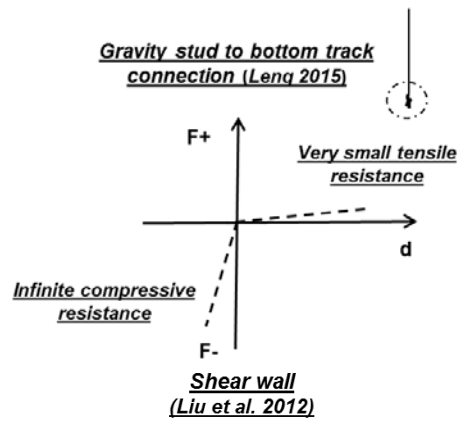


Figure 3.4: Numerical modeling specifics of CFS building; a) CFS-NEES building, b) leaning columns, c) gravity framing

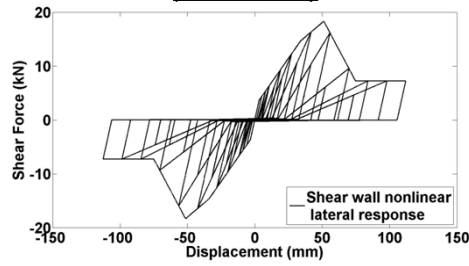
d)



e)



f)



g)

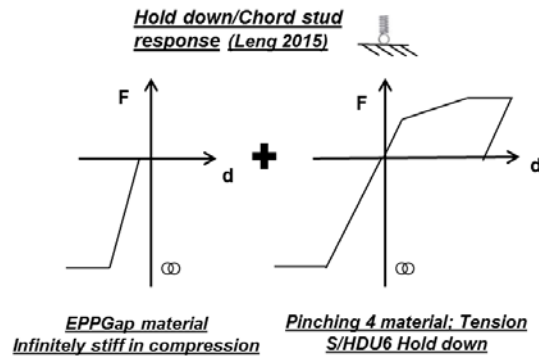


Figure 3.4 (Continued): Numerical modeling specifics of CFS building; d) diaphragm, e) gravity stud-to-bottom track connection, f) shear wall and g) holddown/chord stud connection

### 3.4.1. Shear wall structure and connection

The basis for the simulation of the shear wall elements lies in the work of Shamim and Rogers (2013), who used a pair of truss elements and the Pinching4 material (Lowe and Altoontash 2003) in OpenSees to create a 2D shear wall model. The 2D shear wall model was demonstrated to be capable of reproducing the nonlinear response of the shear wall once the Pinching4 parameters were calibrated to shear wall component test data. Leng et al. (2017) employed the same shear wall model, and calibrated the pinching parameters using the experimental data of Liu et al. (2012), who tested shear wall configurations with the same sheathing, dimensions and structural characteristics as the shear walls of the CFS-NEES building. Tests 4 and 14 by Liu et al. (1.24m x 2.674m and 2.44m x 2.74m, respectively) were used for the material model of the CFS-NESS Building shear walls. The Pinching4 backbone points for one pair of shear wall truss elements were  $(0.2\delta, 0.2V)$ ,  $(0.8\delta, 0.8V)$ ,  $(\delta, V)$  and  $(1.534\delta, 0.395V)$ , with unloading and reloading parameters  $rDisp= 0.33$ ,  $rForce= 0.02$  and  $uForce= 0.0$  (as suggested in Leng 2015). For the intermediate shear wall widths an average shear resistance value from tests 4 and 14 was assumed ( $v = 14.8$  kN/m). In this work, the Pinching4 displacement points were calculated using linear interpolation. The shear wall deflection equation (Eq. E1.4.1.4-1), as provided in the AISI S400 Standard (AISI 2015), was also used to validate the linear interpolation approach, and to calculate the displacement points for the 3.82m wide shear wall (outside the width range of the tests by Liu et al. (2012)). Figure 3.5 shows the trend of the displacement values at the peak response versus the width-to-height,  $b/h$ , shear wall ratios as calculated using the deflection equation compared to a linear trend and the test data using linear interpolation. It should be noted that the maximum difference between the linear interpolation test data and the deflection equation values was 27%.

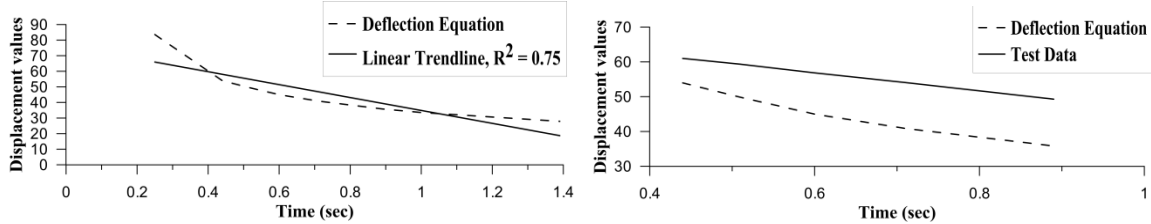


Figure 3.5: Pinching4 displacement points' calculation for the 2D shear wall model

In Figure 3.4f, a displacement-controlled loading protocol is applied to a single-story shear wall using the calibrated Pinching4 backbone points and pinching parameters based on Leng (2015) and Liu et al. (2012) in order to demonstrate the shear wall's nonlinear lateral response. Further, Leng et al. (2017) introduced the subpanel approach allowing any given shear wall model to be constructed with more than one pair of truss elements/subpanels. The subpanel approach enabled the force-transfer between shear walls and gravity framing, and allowed for the creation of shear wall models with openings (windows), i.e. partial height wall segments. The shear walls in the work presented herein were modelled using four pairs of truss elements, as shown in Figure 3.4a. This approach also worked well for the addition of non-structural elements (Section 3.4.4). Figure 3.6 shows the nonlinear force-deformation response of a shear wall simulated with one pair of truss elements, compared to that of the same shear wall using four pairs of truss elements, when the model is pushed to failure.

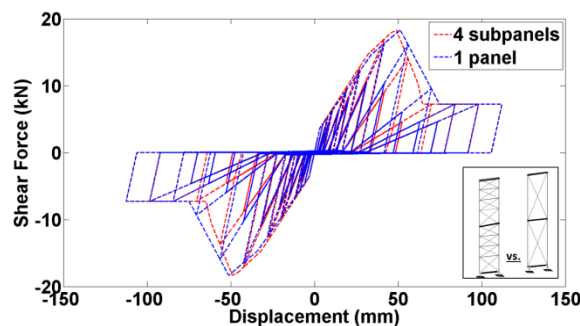


Figure 3.6: Shear wall model; subpanel approach

The 80% post-peak strength is commonly used to define the failure point for a shear wall, where

the drift ratio should not exceed the limit of 2.5% (AISI S400 2015). In Figure 3.6, the two curves are in agreement, thus verifying the subpanel approach. The Pinching4 component model simulated the response up to approximately 100mm indicating collapse of the shear wall after that point. This is consistent with the experimental data ( $\approx 4\%$  drift) by Liu et al. (2012).

During testing of the CFS-NEES building, the shear wall connection to the bottom track of the building consisted of a holdown device, which was instrumented to measuring the tensile force for each shear wall chord stud, and an actual pin-connection of the chord stud to the track section. This was realised in OpenSees using a pair of parallel zerolength spring elements (Leng et al. 2017), each of which was represented by a uniaxial component model (Figure 3.4g). The holdown/spring element was simulated with the Pinching4 model assuming the same compressive and tensile stiffness using information from the holdown's manufacturer ( $F_y = 43.5\text{kN}$ ,  $F_u = 66.75\text{kN}$ ,  $\delta_y = 5.94\text{mm}$ ,  $\delta_u = 10.51\text{mm}$  for a Simpson S/HDU6 holdown (Simpson Strong-Tie Company Inc. 2017)). The pin/spring element behaviour was idealized as a gap element having an elastic - perfectly plastic response with infinite compressive stiffness. The simultaneous use of the two parallel springs led to the realistic function of the chord stud connection working as a holdown for the tensile forces and as a pin for the compressive forces.

### **3.4.2. Diaphragm**

The basis for the diaphragm simulation is found in the work of Shrestha (2011). The roof and floor diaphragms in this thesis are simulated as deep horizontal plane trusses with twoNodelink elements instead of truss elements (Figure 3.4d, force-deformation hysteretic response and corresponding cumulative energy), which were calibrated directly from the force-displacement experimental data of the diaphragm experimental program (Chapter 2).. This allowed for an efficient way to incorporate the Pinching4 backbone points in terms of force-displacement in the

twoNodelink elements. The hysteretic energy dissipated per loading cycle by the 2D diaphragm model was “matched” to the corresponding experimental one (Section 3.3). Figure 3.4d shows the 3D diaphragm model while Figure 3.7 shows the process of the modeling approach, where half of the roof and floor was simulated initially using a mesh element (Table 3.2) in order to obtain their shear strength and stiffness (Table 3.3).

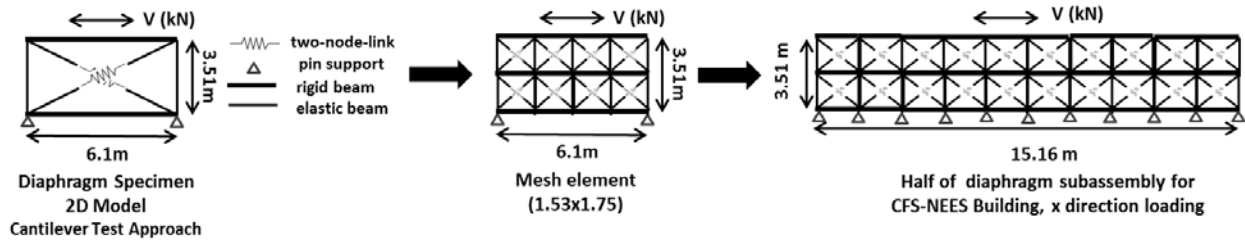


Figure 3.7: Schematic representation of the diaphragm modeling approach

Table 3.2: Mesh element Pinching4 parameters; floor and roof

Material parameters	Floor	Roof
$\pm P$ (kN)	8.4, 8.9, 6.4, 3.4	6, 6.6, 3.9, 2.2
$\pm \delta$ (mm)	4.1, 9.5, 15.6, 49.4	5.3, 13.3, 25.0, 66.3
$\pm rDisp$	0.85	0.85
$\pm rForce$	0.40	0.40
$\pm uForce$	-0.20	-0.20
<b>gk</b>	0.9 0.9 1.2 1.2 0.85	0.9 0.9 1.2 1.2 0.85
<b>gf</b>	0.01 0.05 0.1 0.1	0.01 0.05 0.1 0.1
<b>gd</b>	0.90	0.90
<b>gd</b>	0.2 0.2 2.0 2.0 0.03	0.2 0.2 2.0 2.0 0.03
<b>gE</b>	4.6	4.6

Note: The parameters' definition can be found in Lowes and Altoontash (2003)

Table 3.3: CFS-NEES building diaphragms: shear strength and stiffness

Subsystems	Floor	Roof
$v_{x,z}$ (kN/m)	7.3	5.2
$k_x$ (kN/mm)	17.8	7.6
$k_z$ (kN/mm)	3.5	1.7

Note: The symbols' definition is provided in Section 3.8.

A comparison with the results of Chatterjee (2016) and Florig et al. (2015) showed that the diaphragm stiffness values obtained for the floor subsystem through the diaphragm experimental program were lower than the those reported from both mentioned studies. In particular, Chatterjee proposed an upper and lower limit of the floor’s nonlinear response based on the level of friction developed between the sheathing panels during testing; the diaphragm stiffness in Table 3.2 in this thesis is lower than the lower limit case. This was attributed to the fact that the connection of the diaphragm to the wall stud was not included in the test setup of the diaphragm experimental program at McGill University, while it was part of both the works of Chatterjee and Florig et al. As such, it was decided to implement the wall stiffness effect by applying a confinement factor (CF) of 1.5 to the experimental diaphragm stiffness value. The factor was calculated by matching the lower bound monotonic response of the floor subsystem to the lower bound value proposed by Chatterjee (Figure 3.8). This conservative value was used for the building modeling described herein; further study is recommended in order to incorporate the stiffening effect of the surrounding walls on the diaphragm into a numerical model.

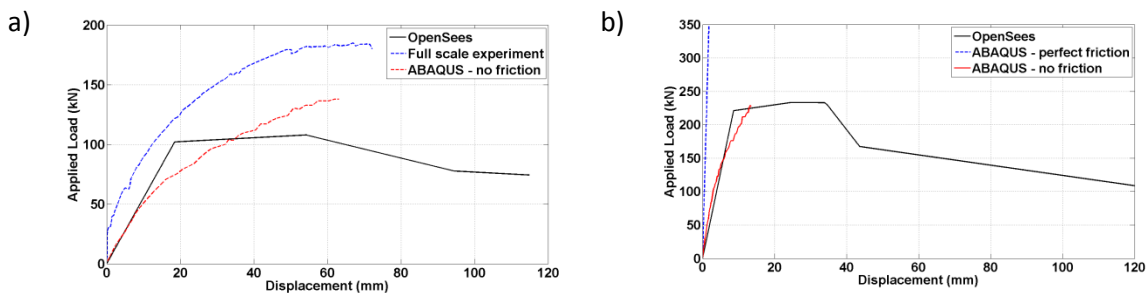


Figure 3.8: Confinement factor application (CF); a) short direction, z and, b) long direction, x

It should be noted that dowel bearing strength test (ASTM D5764-97a 2013) was conducted for the floor and roof wood panels to measure the compressive strength of the wood; this test was conducted in order to examine whether the increased stiffness recorded during Florig’s et al. test

was also due to stronger wood panels used in their test. However, the resulting average bearing

strength for the floor subsystem was 35.66MPa with a coefficient of variation of 0.18 (Appendix D); this result is comparable with the wood properties of the full-scale floor test (Florig et al. 2015,  $\mu = 36.6\text{MPa}$ ,  $\text{cov} = 0.21$ ).

### **3.4.3. Gravity framing**

The gravity framing in a CFS building comprises a vast number of stud and track members throughout the structure. Given the aim of the study is to investigate through numerical modeling the response of the building under lateral loads, a simplified approach was explored where for the gravity framing double sections were assigned to the gravity stud elements so as to reduce by half their number in the simulation. The gravity framing was explicitly modeled so as to consider its contribution to the lateral response by providing lateral resistance and energy dissipation, as is the case in a CFS building (Leng 2015, Peterman 2014). Leaning columns were considered in the four corners of the building in order to account for destabilizing effects (the equivalent leaning column concept). As such, gravity load was applied to the shear walls based on their tributary area and on the leaning columns, as shown in Figure 3.4b. The mass was uniformly distributed in the floor and roof subsystems, as shown in Figure 3.4d; the mass values were obtained from Peterman (2014).

The gravity studs, shear wall and diaphragm chords, rim joists and horizontal members (Figure 3.4c) were simulated as distributed plasticity nonlinear beam-column elements combining a Pinching4 material for the axial strength and an elastic perfectly plastic material for the flexural strength and torsional stiffness (Figure 3.4c). The section aggregator was featured in OpenSees to combine the uniaxial material properties. Padilla-Liano's et al. (2014) is the first experimental work on CFS column and beam members aimed at fully characterising the nonlinear response of these members by exploring the three influential buckling failure modes; local, distortional and

global buckling. Based on his experimental results, in his thesis Padilla-Liano provided empirical expressions to calculate the Pinching4 backbone points as a function of the local buckling slenderness of a column member (Tables 7.3, 7.7, 7.8 and 7.9 in Padilla-Liano’s thesis (2015)). The direct strength method (AISI S100 2016, Schafer 2010) was relied upon for the calculation of the member buckling slenderness values and capacities, as shown in Table 3.4.

Table 3.4: Gravity framing; member capacities

<b>Member Capacities</b>	<b>Double 600s162-54</b>	<b>Double 600s162-33</b>	<b>1200t200-97</b>	<b>1200s250-97</b>	<b>1200t200-68</b>	<b>1200s200-54</b>	<b>600t150-54</b>
<b>P+ (kN)</b>	293.5	113.3	363.9	461.8	294.5	248.5	133.0
<b>P- (kN)</b>	-133.3	-42.1	-135.2	-190.7	-82.2	-65.5	-51.7
<b>M<sub>x</sub>(kNm)</b>	8.2	3.1	15.0	28.1	11.7	10.4	3.4
<b>M<sub>y</sub>(kNm)</b>	±1.8	±0.7	1.2/-1.3	2.6/-3.2	0.8/-1.2	1.0/-1.9	±0.4

Note: symbol definitions are provided in Section 3.8.

The gravity stud connection to the bottom track of the structure was idealized as a zero-length element. A multilinear component model comprising an infinite compressive stiffness and negligible tensile stiffness, as shown in Figure 4e (Leng et al. 2017) was assigned to the zero-length element. All members were considered braced against global buckling modes. The sections were the following: 600s162-54/33 floor/roof gravity studs, double 600s162-54 shear wall chord members, 1200s200-54 roof joists, 1200t200-68 roof rim joists, 1200s250-97 floor joists, 1200t200-97 floor rim joists and 600t150-54 horizontal members (Peterman 2014).

#### 3.4.4. Non-structural gypsum and gravity walls

Pinching4 truss elements were relied upon to add interior gypsum and exterior OSB throughout the wall-line of the structure, as the next step of the numerical work. For the shear walls, Liu’s tests 3 and 13 (Liu et al. 2012) were used to provide the nonlinear response of shear wall specimens with both OSB and gypsum sheathing. For the gravity walls, Leng (2015) used a

fastener-based model created for CFS framed shear walls by Buonopane et al. (2015) to produce the nonlinear response, since no experimental data are available for gravity walls with OSB and gypsum sheathing at present. Leng used the Pinching4 model separately for a gravity wall with gypsum sheathing and one with OSB sheathing (two V- $\delta$ , shear strength – displacement curves with the same pinching parameters as for shear walls). However, in this thesis, to avoid adding double the number of truss elements in the model, a combined nonlinear response was calculated for the gravity walls by summing the two separate nonlinear responses provided by Leng. As such, one pair of truss elements was used for each gravity wall to represent both the OSB and the gypsum sheathing. Chen et al. (2014) in their work on timber shear walls showed the validity of the summation method. In order to verify further this method a 2D shear wall and a 2D gravity wall model was created. The shear wall model was first evaluated under reversed cyclic loading using one pair of truss elements (OPTE) with the model calibrated using Liu’s test 13, which included both OSB and gypsum. Subsequently, the shear wall model was evaluated using two coincident pairs of truss elements (TCPTE); one pair based on Liu’s test 12 (only OSB) and one based on Liu’s test 16 (only gypsum). In Figure 3.9a, it can be seen that the two nonlinear force-displacement responses are in agreement with the TCPTE model slightly overestimating the lateral response. Subsequently, an OPTE gravity wall model incorporating the calculated combined nonlinear response was compared to the equivalent TCPTE model incorporating separately Leng’s V- $\delta$  curves. In Figure 3.9b, it is shown that both modeling approaches produce a similar nonlinear response, with the lateral response from the TCPTE model being more conservative. The subpanel approach was applied for the different dimensions of gravity walls throughout the building. It should be noted that fixed connections were assumed for the 3D building model throughout for purposes of computational efficiency and practicality. This

assumption overestimates the in-reality semi-rigid connections' stiffness; however, further experimental work is necessary in that front, the rigid connections allow for bending of the chord studs which is expected and, based on the results, it is the truss/twoNodelink elements of the components that work primarily in receiving the shear force.

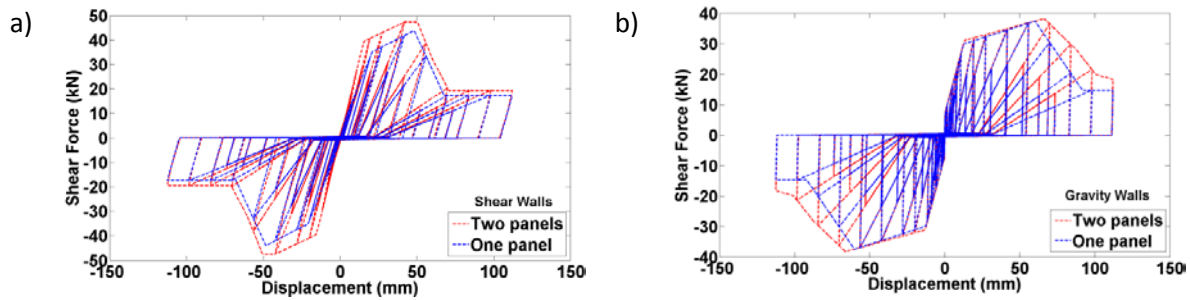


Figure 3.9: Verification of summation method for shear walls and gravity walls with OSB and gypsum sheathing

### 3.5- Numerical simulation: CFS-NEES building

#### 3.5.1. 3D Model Verification; structural components

The numerical modeling approach followed for the CFS-NEES building with the explicit simulation of its floor and roof subsystems was verified by conducting nonlinear response history analysis, subjecting the 3D model to the Canoga Park ground motion record (CNP, x, y and z components) from the 1994 Northridge earthquake and comparing the results with the experimental data, as provided by Peterman (2014) for Phase 1/2a. The CNP earthquake was applied to the building during the shake table testing representing a design basis earthquake (10% probability of exceedance in 50 years) in urban Southern California. To compare the experimental results with the simulated ones, the 3D model of the CFS-NEES building was subjected to the achieved shake table motion (Peterman 2014). The 3D model considered geometric nonlinearities with the P-Delta transformation. Viscous damping was simulated with the Rayleigh damping model using a 5% damping ratio in the first two natural frequencies.

Three-dimensional white noise tests of the CFS-NEES building in Phase 1 and 2a, with amplitude defined by peak ground acceleration (PGA) of 0.05g to 0.1g, resulted in a 4% damping ratio for the Phase1/2a building with the acceptable error of +/- 1% expected for experimentally obtained damping values (Peterman 2014). However, as the construction of the CFS-NEES building progressed, i.e. non-structural components were added, a damping ratio as high as 8% was indicated by the white noise tests. In particular, for Phase 2c (addition of exterior OSB and interior gypsum) a damping ratio of 5% to 8% was obtained in the x direction, with a corresponding value of 8% to 10% in the z direction. However, in the 3D CFS building models presented herein, the 5% damping value was chosen for the following reasons: a) the white noise tests in Phase 2c were conducted after 44% of the CNP had been applied in the structure (even with no damage observed) and b) the NEHRP (the National Earthquake Hazards Reduction Program) / FEMA P-750 recommended damping value is 5% (Building Seismic Safety Council (2009)). The seismic mass considered in the model was 18.9kNsec<sup>2</sup>/m and 13.4kNsec<sup>2</sup>/m at the floor and roof levels, respectively (Peterman 2014). The stiffness proportional part of the damping matrix was obtained from all elements considering the current stiffness matrix.

Figure 3.10 illustrates the first two mode shapes with the corresponding fundamental periods of vibration in the two directions. Peterman (2014) provides information about the first mode of vibration in the long (x) direction of the building for Phases 1 and 2a; the mode is primarily translational with some participation from the short (z) direction as well (torsion). However, although for Phase 1 and 2a the structural configuration of the building is the same, the first mode shape of the building for Phase 2a does not exhibit much torsion. The first mode shape of the 3D building model in the x direction (Figure 3.10a) agrees with the first mode shape in the x direction as provided for the CFS-NEES building for Phase 2a ( $T_x=0.32\text{sec}$  and  $T_z=0.36\text{sec}$ ).

The second mode shape of the building is the fundamental translational mode in the short ( $z$ ) direction (Figure 3.10b); small deflection of the roof subsystem is observed with respect to the corner nodes, while for the floor subsystem it is negligible.

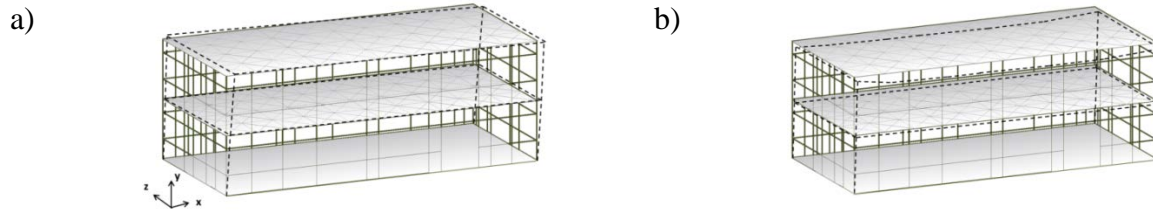


Figure 3.10: Translational mode shapes: a) Long direction,  $T_x = 0.34\text{sec}$  and b) Short direction,  $T_z = 0.39\text{sec}$

The fundamental periods provided in Figure 3.10, although elongated, are in close proximity (up to 8% difference) to the experimental ones (Table 3.5). In Tables 3.5 and 3.6 the building's seismic response is quantified in terms of wall-line drift ratios, maximum diaphragm deflection in the  $z$  direction ( $MDD_{fz}$ ), as defined by ASCE 7-16 (ASCE 2016), and maximum overall displacement ( $\text{Disp}_{f\max}$ ) of the floor subsystem, base shear values and fundamental periods recorded in both directions. Wall-line storey drift ratios were calculated based on the average displacement of two corner nodes in each direction ( $u$  for  $x$  direction and  $v$  for  $z$  direction). Referring to Table 3.6, the base shear forces are calculated, first, based on the shear wall contribution ( $V_x^{\text{sw}}, V_z^{\text{sw}}$ ). The total base shear forces were also quantified including the gravity framing contribution ( $V_x^{\text{tot}}, V_z^{\text{tot}}$ ). The Method 1 base shear forces from Peterman (2014) used to compare to the numerical values obtained from the 3D OpenSees model.

Table 3.5: Phase 1/2a; wall-line storey drift ratios and fundamental periods

Phase $\mathbf{1, CNP_{x,y,z}}$	$\Delta_{u1}/h(\%)$	$\Delta_{u2}/h(\%)$	$\Delta_{v1}/h(\%)$	$\Delta_{v2}/h(\%)$	$\mathbf{T_x}$	$\mathbf{T_z}$
<b>Model</b>	1.54	1.22	0.75	0.51	0.34	0.39
<b>Test</b>	1.18	0.81	0.85	0.56	0.32	0.36

Note: The symbols' definition is provided in Section 3.8.

Table 3.6: Phase 1/2a; base shear values and floor diaphragm and overall displacement

<b>Phase 1, <math>CNP_{x,y,z}</math></b>	<b><math>V_x^{sw}</math> (kN)</b>	<b><math>V_x^{tot}</math> (kN)</b>	<b><math>V_z^{sw}</math> (kN)</b>	<b><math>V_z^{tot}</math> (kN)</b>	<b>Disp<sub>fmax</sub> (mm)</b>	<b>MDD<sub>fz</sub> (mm)</b>
<b>Model</b>	96.3	154.1	65.9	109.6	28.2	7.5
<b>Test</b>	84.4*	-	79.1*	-	28	3.5

Note: The symbols' definition is provided in Section 3.8.

The results in Tables 3.5 and 3.6 demonstrate that the simplified numerical model, although more flexible, can adequately predict the peak seismic response of the building. In consideration of the total base shear values, the gravity studs were shown to contribute to resisting the lateral loads on an average of 40% in both directions. Further, the model yields a higher MDD<sub>fz</sub> by 4mm; although, this suggests a difference in the relative wall-diaphragm stiffness in the model compared to the actual building, practically this difference is small. Figure 3.11 illustrates the computed storey drift ratio response histories of the wall-line in both directions versus the measured dynamic response. The storey drift ratios of the 3D building model in the z direction are in good agreement with the experimental data; in the x direction the model over-predicts the storey drift ratios at the roof level, which suggests that the shear walls or diaphragms in the x direction can be modestly less stiff in the actual building.

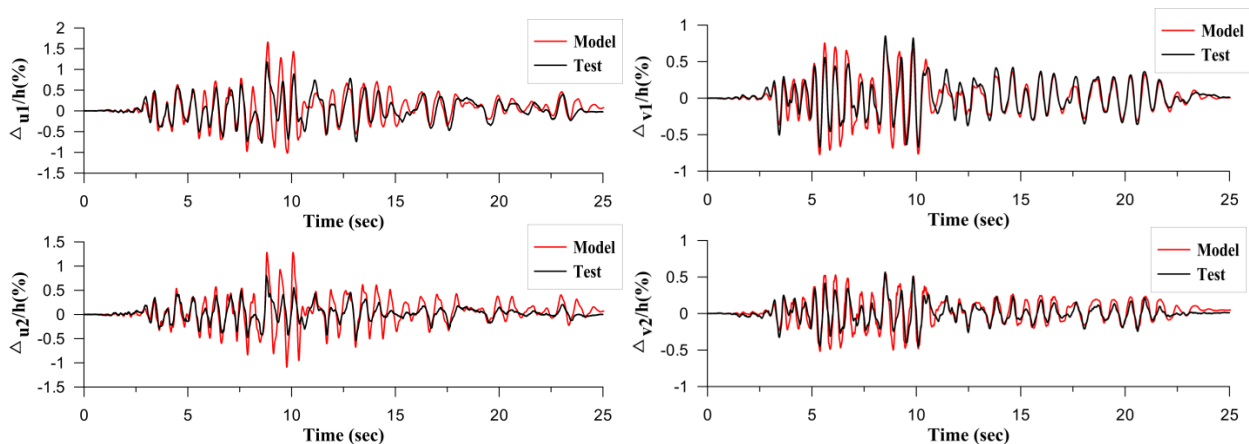


Figure 3.11: Wall-line storey drift ratio histories, x & z direction

Figures 3.12 and 3.13 illustrate the absolute acceleration histories at the four corners in the x and

z direction for the first floor and roof, respectively. The south-east (SE) and north-west corners are presented indicatively for purposes of comparison. All the data can be found in Appendix E. It is shown that in the x direction the absolute accelerations for the floor and roof are at the same level or lower, while in the z direction they are amplified compared to the experimental values. These results were to be expected given the wall-line storey drift results explained in Figure 3.11.

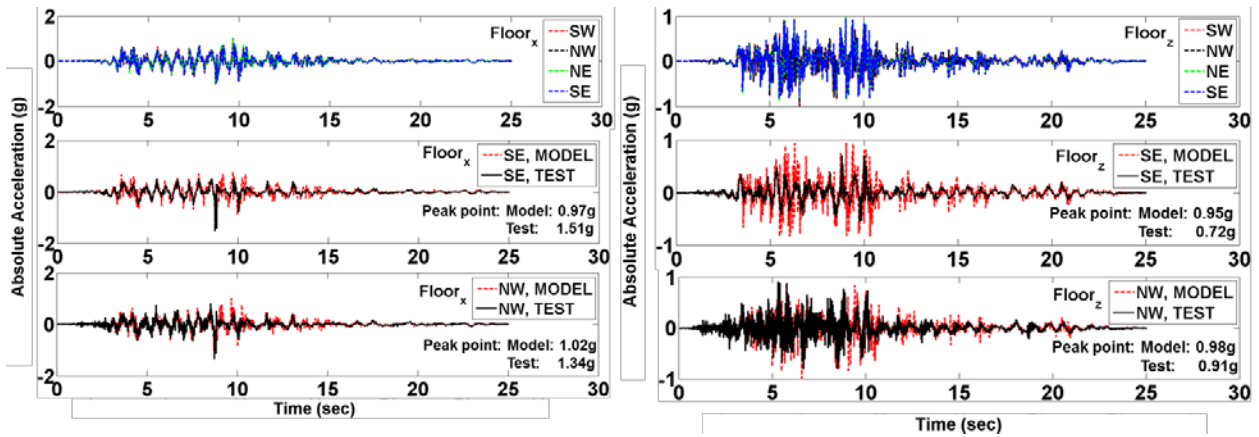


Figure 3.12: Absolute acceleration response histories at floor level

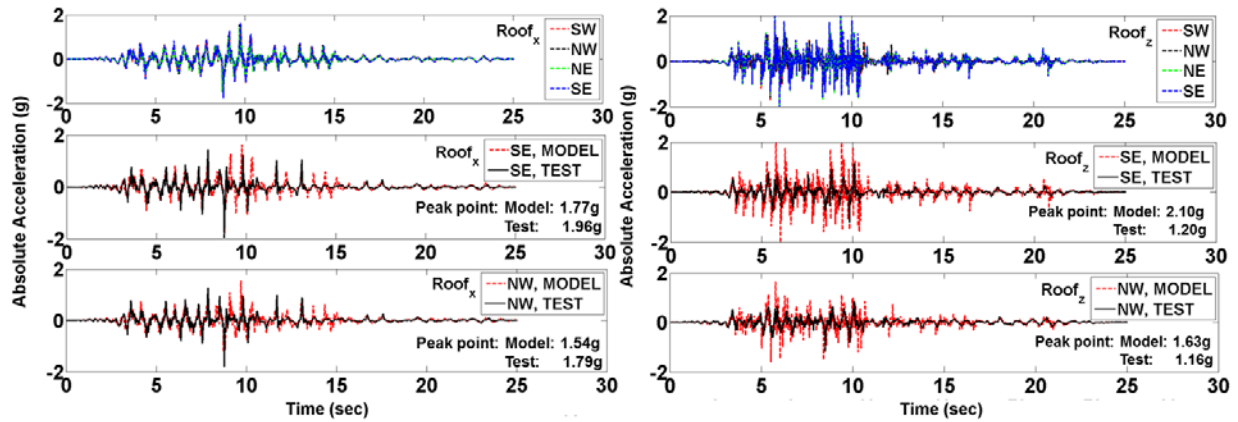


Figure 3.13: Absolute acceleration response histories at roof level

Focusing at the peak absolute acceleration values, the results are in close proximity to the experimental data, with the exception of the values for the roof level in the z direction. For the

roof level in the z direction, in particular, although the results suggest that the shear walls might be stiffer than in reality, another possible explanation is that the roof subsystem has been simulated as more flexible than in reality. Depending on the level of flexibility, amplified accelerations can be present at the roof level for both the shear walls and the diaphragm (Tena-Colunga and Abrams 1996). As such, including the stiffening effect of the shear walls in the diaphragm properties (Section 3.4.2) could lead to better approximation of the peak absolute accelerations at the roof level. In addition, absolute acceleration graphs revealed a higher frequency of the 3D model compared to the CFS-NEES building, which was not as evident from the wall-line storey drift response histories. In general, the deviations observed in the results of the 3D building model compared to the CFS-NEES building could be attributed to the potential variability in the numerous structural properties implement in the model based on isolated experimental work. In addition, for the mass distribution, to achieve the seismic design weight of the CFS-NEES building, concrete blocks were added in certain locations throughout the floor and roof (Peterman 2014). As such, the uniform mass distribution chosen for the 3D building model did not match perfectly the conditions of the CFS-NEES building, in particular, but was chosen as a general assumption for the modeling of CFS buildings overall.

The 3D building model serves as an efficient tool able to capture the overall seismic response of a CFS building and to provide insight into the influence of non-structural elements on the building's overall seismic behaviour. At a local level, comparing the holdown/chord stud connection response to that recorded during testing in various locations, it was shown that the numerical model did not capture the intended behavior of the holdown. This was attributed to the rigid foundation assumed in the model. An effort to improve the holdown / chord stud connection response included allowing the foundation to bend, following a trial and error

approach for its flexibility, in the direction of the gravity loading. However, convergence issues were caused by the vertical component of the ground motion being included in the analysis. By applying only the two-horizontal components of the CNP ground motion while allowing the foundation to bend a more realistic response of the holddown connection was obtained; as shown in Figure 3.14 indicatively for one of the shear walls in the south wall-line (LC3 and LC4, Figure 3.4a) of the building (the negative values indicate tensile force in the holddown, while the positive values represent the compressive force of the shear wall chord stud).

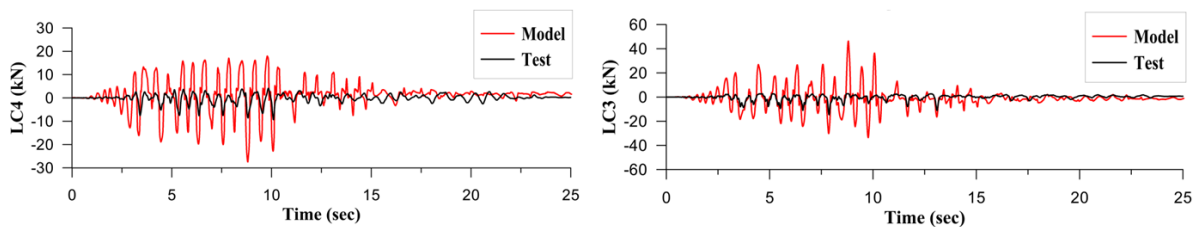


Figure 3.14: Holddown/chord stud connection; LC3 & LC4

However, the forces recorded from the model were exaggerated compared to the test data; the explicit modeling of the foundation flexibility with an appropriate damping ratio would be able to produce recorded forces in the model in closer proximity to the experimental ones; this is related, also to the potential rocking motion exhibited by the building during the shake table test, which is not included in the model. Further, the continuous connections assumed between floors, a simplification due to the lack of data for the actual stiffness of the connection in question (Leng 2015), constitutes an additional reason for the holddown / chord stud connection response provide by the 3D building model. Further work focusing on modeling explicitly the foundation and the connection between storey levels would improve the holddown / chord stud connection response. Following the above observations for the holddown / chord stud connection response and the influence of the vertical ground motion component, it was decided that for the scope of this

research work, only the two principal horizontal directions would be considered for the subsequent nonlinear response history analyses. This decision was based on the fact that the storey-based engineering demand parameters of the CFS building subjected only to the horizontal components (x and z direction), as shown in Section 3.5.2.1 & 3.5.2.2., were in close proximity to the ones presented in Tables 3.5 and 3.6 (x, z and y component results) and the corresponding experimental data.

### 3.5.2. Consideration of non-structural components

In this section, non-structural components are incorporated in the model, installed on the diaphragms and walls of the structure. Table 3.7 includes the corresponding nomenclature.

Table 3.7: Description of model representations of CFS-NEES building

<b>Model Nomenclature</b>	<b>Structural elements</b>	<b>Gypsum ceiling &amp; gypcrete flooring</b>	<b>Interior gypsum &amp; exterior OSB sheathing throughout</b>
<b>Model 1</b>	✓		
<b>Model 2</b>	✓	✓	
<b>Model 3</b>	✓	✓	✓

Note: All models are subjected to the x and z components of the CNP (100%) ground motions.

The influence of non-structural components on the seismic response of the case study CFS building is quantified by conducting response history analyses under the x and z CNP components.

#### 3.5.2.1 Consideration of non-structural components on the diaphragm

Non-structural gypcrete flooring and gypsum ceiling were incorporated in the 3D model for the floor and roof subsystems, respectively (Model 2). An elastic stiffness,  $k$ , was inserted in the twoNodelink elements;  $k_z = 6.05\text{kN/mm}$  and  $2.94\text{kN/mm}$  for the floor with gypcrete and the roof with gypsum, respectively, using the experimental data from Section 3.3 and the 2D diaphragm model explained in Section 3.4.2. It should be noted that the initial floor system for Model 1 was

installed with #10 sheathing screws while the floor system with gypcrete incorporated for Model 2 comprised of #12 sheathing screws, as per the experiment described in Section 3.3 (Table 3.1). However, Nikolaidou et al. (2017) found that the screw size primarily influences the shear strength and not the shear stiffness of the diaphragm; this assumption is adopted here after. Tables 3.8 and 3.9 present the Phase 1 diaphragm test results compared to those obtained from Model 1. The dynamic properties and storey-based engineering demand parameters (base shear forces, storey drift ratios) of the building are not practically influenced by the non-structural elements on the diaphragm; however, they have an effect on the diaphragm response and, primarily the roof subsystem.

Table 3.8: Model 2; Fundamental period and wall line storey drift ratios

<b>Building</b>	$\Delta_{u1}/h(\%)$	$\Delta_{u2}/h(\%)$	$\Delta_{v1}/h(\%)$	$\Delta_{v2}/h(\%)$	$T_x(\text{sec})$	$T_z(\text{sec})$
<b>Model 1</b>	1.66	1.28	0.80	0.54	0.35	0.39
<b>Model 2</b>	1.71	1.17	0.87	0.68	0.34	0.38
<b>Comp (%)</b>	3	9	9	26	3	3

Note: Symbol definitions are provided in Section 3.8.

Table 3.9: Model 2; MDD, maximum displacements and base shear values

<b>Building</b>	$MDD_{fz}$ (mm)	$Disp_{fmax}$ (mm)	$MDD_{rz}$ (mm)	$Disp_{rmax}$ (mm)	$V_x^{tot}$ (kN)	$V_z^{tot}$ (kN)
<b>Model 1</b>	6.9	29.2	39.4	50.7	144.1	109.4
<b>Model 2</b>	5.2	28.7	11.1	27.4	145	116.1
<b>Comp (%)</b>	25	2	72	46	0.6	6

Note: Symbol definitions are provided in Section 3.8.

The roof subsystem for Model 1 exhibited a more flexible behaviour than the floor subsystem; a fact indicated in Peterman (2014) by the increased relative accelerations observed in the mid-span of the roof subsystem compared to the floor mid-span. Adding the gypsum ceiling in Model 2 resulted in a 72% decrease of the  $MDD_{rz}$  and a 46% reduction of the maximum relative displacement at roof level in the z direction ( $Disp_{rmax}$ ). The additional shear stiffness from the

gypcrete for the almost rigid floor subsystem caused a 26% reduction of the  $MDD_{fz}$ .

### 3.5.2.2 Consideration of non-structural components on the diaphragms & walls

In addition to the gypsum and gypcrete on the diaphragm, gravity walls and gypsum sheathing were added throughout the wall-line of the building as described in Section 3.4.4 (Model 3). Tables 3.10 and 3.11 summarise the storey-based engineering demand parameters for the purpose of comparing Model 1 versus Model 3. Figure 3.15 includes a comparison of the wall-line storey drift ratios in the x and z direction, respectively, for Models 1 and 3. It is shown that the gypsum sheathing and gravity walls increased the overall stiffness of the structure, more prominently in the x direction, with an average decrease of 66% of the wall-line storey drift ratios in the x and 45% in the z direction, respectively. Fundamental periods were reduced by an average of 35%. The overall base shear was increased in both directions (Table 3.11); 80% in the x and 21% in the z direction.

Table 3.10: Model 3; Fundamental period and wall-line storey drift ratios.

<b>Building</b>	$\Delta_{u1}/h(\%)$	$\Delta_{u2}/h(\%)$	$\Delta_{v1}/h(\%)$	$\Delta_{v2}/h(\%)$	$T_x(\text{sec})$	$T_z(\text{sec})$
<b>Model 1</b>	1.66	1.28	0.80	0.54	0.35	0.39
<b>Model 3</b>	0.68	0.34	0.45	0.29	0.20	0.29
<b>Comp (%)</b>	59	73	44	46	43	26

Note: Symbol definitions are provided in Section 3.8.

Table 3.11: Model 3; MDD, maximum displacements, base shear and diaphragm shear forces

<b>Building</b>	$MDD_{fz}$ (mm)	$Disp_{fmax}$ (mm)	$MDD_{rz}$ (mm)	$Disp_{rmax}$ (mm)	$V_x^{tot}$ (kN)	$V_z^{tot}$ (kN)	$V_{dx}^{tot}$ (kN)	$V_{dz}^{tot}$ (kN)
<b>Model 1</b>	6.9	29.2	39.4	50.7	144.1	109.4	102.4	90.9
<b>Model 3</b>	5	17.2	10	16.8	259.7	132.1	154.5	114.7
<b>Comp (%)</b>	28	41	75	67	80	21	51	26

Note: Symbol definitions are provided in Section 3.8.

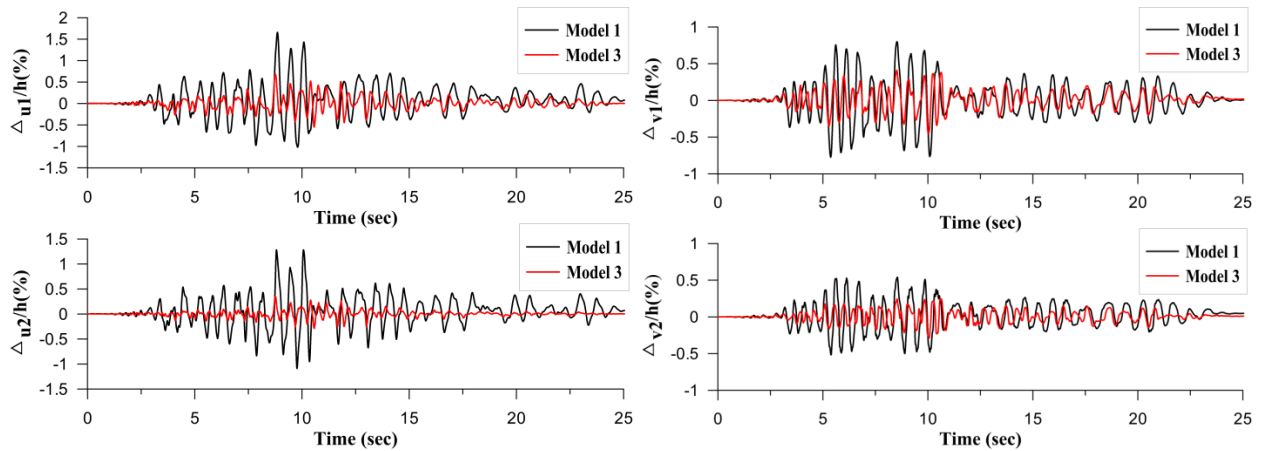


Figure 3.15: Model 3 versus Model 1; wall-line drift ratio, x & z direction, floor & roof

It should be noted that, although in Model 1 and 2 the shear walls were the main lateral force resisting elements, in Model 3 it was the gravity walls that attained the dominant lateral load-resisting role, with up to 75% contribution in receiving the base shear forces accompanied by an average 24% reduction of the shear wall forces. The tributary area of the gravity walls with sheathing was almost twice that of the shear walls in the South and North elevations in the x direction. The decrease of the  $MDD_{fz}$  and  $MDD_{rz}$  is primarily attributed to the non-structural components on the diaphragm subsystems, as explained in Section 3.5.2.1 for Model 2, while the overall maximum displacements are further reduced due to the additional wall stiffness. Figure 3.16 includes the response histories of the average wall-line storey drift ratio ( $\Delta_w$ ) from two corner nodes in each direction and maximum storey drift ratio ( $\Delta_w + \Delta_D$ ) at the location of the MDD for floor and roof in the z direction for Models 1, 2 and 3. The MDD node location is illustrated (nodes 1 and 2) in Figure 3.4a. Although with the increase of the building's lateral stiffness there is a gradual reduction of displacements from Model 1 to Model 3, the building deflects in a more-or-less uniform pattern in the three models, with the floor and roof diaphragm exhibiting a similar response (the roof becoming much stiffer from Model 1 to Model 2). Figure

3.14 clearly shows the change of the roof diaphragm subsystem, from flexible in Model 1 to semi-rigid in Model 2 and 3.

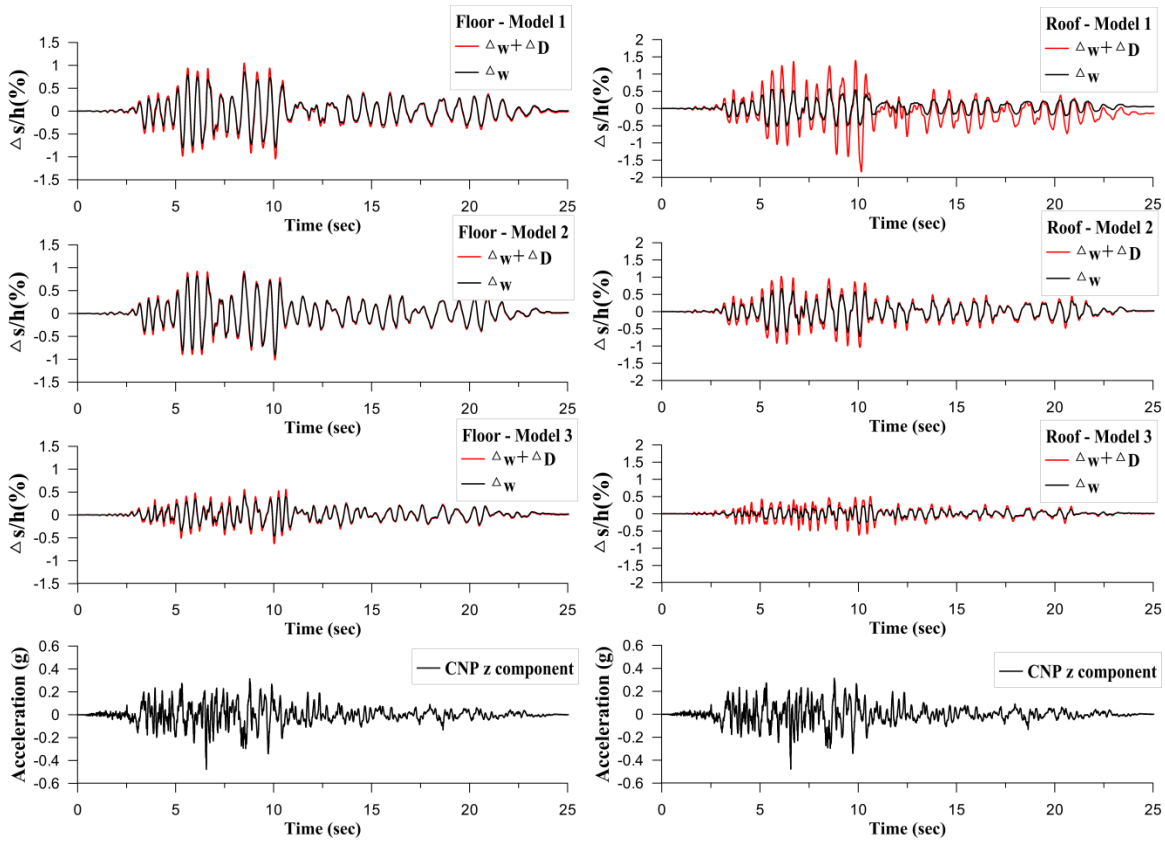


Figure 3.16: Model 1 versus Model 2 versus Model 3; first floor storey drift ratios, z direction

Moreover, it is worth noting that by increasing the wall stiffness the total base shear is amplified in both directions by an average of 1.4 (Table 3.11) compared to the shear forces transferred from the diaphragm subsystems to the walls ( $V_{dx}^{tot}$ ,  $V_{dz}^{tot}$ ). Increased wall stiffness results in higher forces being applied directly to the wall-line, considering the diaphragm stiffness compared to the lateral stiffness of each elevation. For example, the floor subsystem with gypcrete achieved a stiffness of 6.1 kN/mm while only one of the shear walls of the South elevation when sheathed with gypsum and connected to its adjacent gravity wall ( $SW_{gyp}+GW$ ) reached a lateral stiffness of 3 kN/mm, as shown in Figure 3.17. The  $SW_{gyp}+GW$  system, when

pushed to failure, exhibited a lateral stiffness almost three times higher as that of the shear wall alone (from 1.12 kN/mm to 2.97 kN/mm). This agrees with prior findings by Bian et al. (2015).

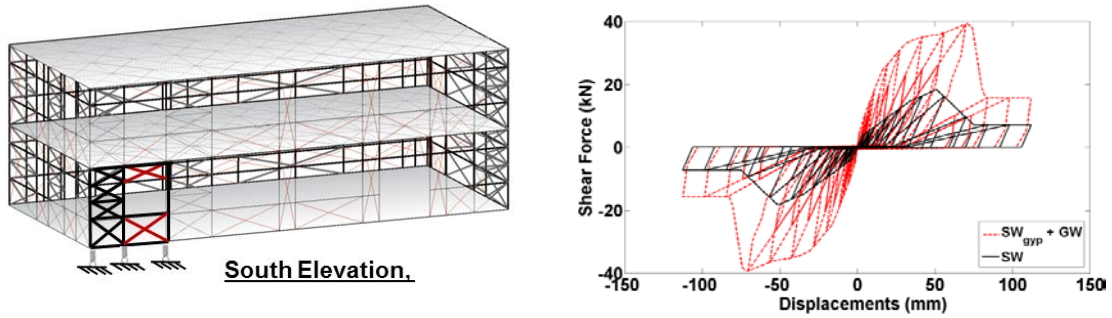


Figure 3.17: Comparison; gypsum sheathing and gravity wall effect on shear wall

Figure 3.18 includes the floor and roof diaphragm in-plane force distribution for Model 1 versus 3 in both directions. The diaphragm forces were increased, as expected for Model 3, but did not exceed the yielding point; the diaphragm did not exhibit inelastic behaviour.

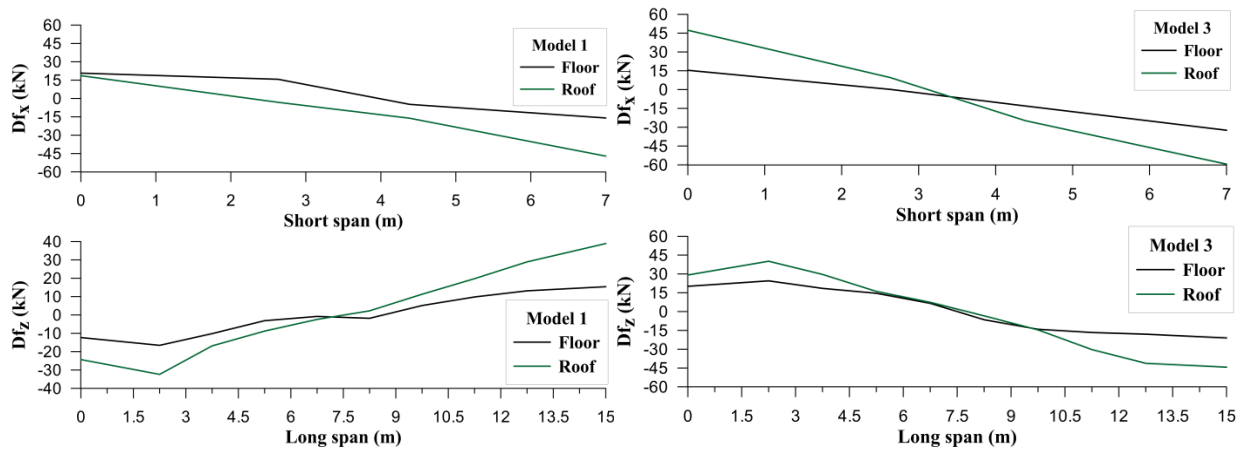


Figure 3.18: Model 1 versus 3; diaphragm shear distribution in both directions

The roof experienced higher in-plane forces than the floor, as in Model 1. For both Models, the floor and roof diaphragms exhibited an in-plane force distribution similar to that of a simply supported beam. However, close to the north wall-line at a distance  $x=2.25\text{m}$ , the shear is amplified in the  $z$  direction by an average of 1.3; indicating that following a linear distribution

assumption would not necessarily provide accurately the forces experienced by these diaphragm subsystems.

### **3.6- Conclusions**

In the work presented herein, the importance of considering the non-structural components in a numerical evaluation of a CFS framed building was examined at a system and subsystem level. The diaphragm component was tested experimentally with gypsum ceiling and gypcrete flooring non-structural details. A benchmark CFS-NEES building tested in prior work at full-scale on a shake table was modelled in an open-source frame analysis finite element program (OpenSees, Version 2.4.5) following a simplified approach and investigating three main cases; 1) only structural components, 2) non-structural components added only on the roof and floor and 3) non-structural components and gravity walls added throughout. Following are the main conclusions drawn from this work:

- ✓ The simplified modeling approach of doubling the gravity stud sections and reducing their corresponding elements in the simulation for purposes of practicality and computational efficiency proved effective in capturing the dynamic properties and peak response of the CFS building in terms of base shear forces, maximum storey displacements and wall-line storey drifts.
- ✓ Explicit modeling of the foundation and the connections between storeys is necessary for a better approximation of the holdown/chord stud response and the successful implementation of the vertical ground motion component in the analysis.
- ✓ Including the stiffening effect of the shear walls in the component modeling of the diaphragm subsystem would improve the diaphragm - shear wall interaction and the resulting peak absolute floor accelerations.

- ✓ The addition of gypsum ceiling and gypcrete flooring had a direct impact on the diaphragm subsystem's lateral response increasing the shear stiffness over 100% and the shear strength a minimum of 60%.
- ✓ The non-structural details of the diaphragm had a minimal effect on the overall seismic response of the building. The roof subsystem was primarily impacted by the added stiffness, which resulted in a reduction of the maximum relative displacements. However, base shear forces, wall-line storey drift ratios and fundamental periods were not affected.
- ✓ Adding interior gypsum and exterior OSB sheathing throughout the wall-lines of the building had the most profound effect on the building seismic response, with a reduction of the fundamental periods by an average of 35% and an increase in base shear forces by an average of 39%.
- ✓ Due to the added wall-line stiffness, higher forces are applied directly to the wall-line of the building resulting in a base shear in average 40% higher than the shear force transferred from the diaphragm to the walls in both directions. A shear wall's lateral stiffness when gypsum sheathed and connected to a gravity wall is almost three times higher than that of a shear wall with only OSB sheathing.

### **3.7- Acknowledgements**

The authors are grateful for the information and support provided by Professor Benjamin W. Schafer and Dr. Cristopher D. Moen, as well as Dr. Kara Peterman, Dr. Aritra Chatterjee, Dr. Jiazhen Leng and Dr. David A. Padilla-Liano related to the CFS-NEES building. The authors, also, appreciate greatly the Natural Sciences and Engineering Research Council of Canada (NSERC), as well as, the American Iron and Steel Institute (AISI) and the Canadian Sheet Steel Building Institute (CSSBI) for financially supporting this research project. Additionally, the

authors would like to thank Bailey Metal Products Ltd., Simpson Strong-Tie Co. Inc., Ontario Tools and Fasteners Ltd, le Groupe Beuchesne, Maxxon Corporation, Beton Autonivelant SGI, ArcelorMittal and Construction Proco Inc. for the all the materials and tools that they provided.

### 3.8- Notation

The following symbols are used in this paper:

$\text{Disp}_{\text{fmax}}$  = Maximum displacement at floor level in z direction (mm).

$\text{Disp}_{\text{rmax}}$  = Maximum relative displacement at roof level in z direction (mm).

$Df_x$  = Diaphragm shear forces in x direction (kN).

$Df_z$  = Diaphragm shear forces in z direction (kN).

$k_x$  = Shear stiffness of diaphragm in x direction (kN/mm).

$k_z$  = Shear stiffness of diaphragm in z direction (kN/mm).

$\text{MDD}_{\text{fz}}$  = Maximum diaphragm deflection at floor level in z direction (mm).

$\text{MDD}_{\text{rz}}$  = Maximum relative diaphragm deflection at roof level in z direction (mm).

$M_x$  = Moment capacity of cold-formed steel member in strong axis (kNm).

$M_y$  = Moment capacity of cold-formed steel member in weak axis (kNm).

$P_+$  = Axial strength of cold-formed steel member in tension (kN).

$P_-$  = Axial strength of cold-formed steel member in compression (kN).

$T_x$  = Fundamental period of building in x direction (sec).

$T_z$  = Fundamental period of building in z direction (sec).

$V_x^{\text{sw}}$  = Base shear based on shear wall forces in x direction (kN).

$V_z^{\text{sw}}$  = Base shear based on shear wall forces in z direction (kN).

$V_x^{\text{tot}}$  = Total base shear based on shear wall and gravity framing forces in x direction (kN).

$V_z^{\text{tot}}$  = Total base shear based on shear wall and gravity framing forces in z direction (kN).

$V_{dx}^{tot}$  = Diaphragm shear force transferred to walls in x direction (kN).

$V_{dz}^{tot}$  = Diaphragm shear force transferred to walls in z direction (kN).

$v_{x,z}$  = Shear strength of diaphragm in both directions (kN/m).

$\Delta_w + \Delta_D$  = Total storey drift ratio (wall + diaphragm) in z direction (%).

$\Delta_w$  = Average wall-line storey drift ratio (wall + diaphragm) in z direction (%).

$\Delta_{u1}/h$  = Wall-line storey drift ratio at floor level in x direction (%).

$\Delta_{u2}/h$  = Wall-line storey drift ratio at roof level in x direction (%).

$\Delta_{v1}/h$  = Wall-line storey drift ratio at floor level in z direction (%).

$\Delta_{v2}/h$  = Wall-line storey drift ratio at roof level in z direction (%).

### 3.9- References

AISI S100 (2016). "North American specification for the design of cold-formed steel structural members." *American Iron and Steel Institute*, Washington, DC.

AISI S400 (2015). "North American standard for seismic design of cold-formed steel structural systems." *American Iron and Steel Institute*, Washington DC.

AISI S907 (2013). "Test standard for cantilever test method for cold-formed steel diaphragms." *American Iron and Steel Institute*, Washington, DC.

ASCE 7 (2016). "Minimum design loads for buildings and other structures." *American Society of Civil Engineers*, Reston, VA.

ASTM D5764-97a (2013). "Standard Test Method for Evaluating Dowel-Bearing Strength of Wood and Wood-Based Products.", *American Society for Testing and Materials*, West Conshohocken, PA, USA.

Bian G., Padilla-Llano D. A., J. Leng, Buonopane S. G., Moen C. D., and Schafer B. W. (2015). "OpenSees modeling of cold formed steel framed wall system." *Proceedings of*

*8th International Conference on Behavior of Steel Structures in Seismic Areas*,  
Conference location, Shanghai, China.

Building Seismic Safety Council (2009). "NEHRP recommended seismic provisions for new buildings and other structures." *Rep. No. FEMA P750*, Building Seismic Safety Council, Washington, DC.

Buonopane S. G., Bian G., Tun T. H., and Schafer B. W. (2015). "Computationally efficient fastener-based models of cold-formed steel shear walls with wood sheathing." *Journal of Constructional Steel Research*, 110, 137-148.

Chatterjee A. (2016). "Structural system reliability with application to light steel-framed buildings." *PhD Thesis*, Virginia Polytechnic Institute and State University, Blacksburg, Virginia.

Chen Z., Nott A., Chui Y. H., Doudak G., Ni C., and Mohammad M. (2014). "Experimental study on the contribution of GWB to the lateral performance of wood shear walls." *World Conference on Timber Engineering*, Conference location, Quebec City, Canada.

Christovasilis I. P., Filiatrault A. and Wanitkorkul A. (2008). "Seismic testing of a full-scale wood structure on two shake tables." *14<sup>th</sup> World Conference on Earthquake Engineering*, Beijing, China.

CSA S136 (2016). "North American specification for the design of cold-formed steel structural members.", *Canadian Standards Association*, Rexdale, Canada.

Fiorino L. Macillo V. and Landolfo R. (2017). "Shake table tests of a full-scale two-story sheathing-braced cold-formed steel building." *Engineering Structures*, Elsevier Science. ISSN 0141-0296, 151, 633–647, doi: 10.1016/j.engstruct.2017.08.056

Florig S., Chatterjee A., O'Brien P., and Moen C. D. (2015). "Full scale tests on a cold-formed

- steel floor diaphragm with oriented strand board sheathing." *Report No. CE/VPI-ST-16/02*, American Iron and Steel Institute, Washington, DC.
- Hopkins A. K. (2013). " Large-scale tests of seismically enhanced planar walls for residential construction." *Master's thesis*, Department of Civil Engineering, California State University, Sacramento.
- Iuorio O., Fiorino L. and Landolfo R. (2014). "Testing CFS structures:The nes school BFS in Naples." *Thin - Walled Structures*, 84, 275 – 288.
- Krawinkler H., Parisi F., Ibarra L., Ayoub A., and Medina R. (2000). "Development of a testing protocol for wood frame structures." *Report W-02 covering Task 1.3.2*, CUREE/Caltech Woodframe Project. Consortium of Universities for Research in Earthquake Engineering (CUREE), Richmond, CA.
- Latreille P. (2016). "Characterization of wood sheathed cold-formed steel diaphragms under in plane loading (phase 2 of diaphragm research program)." *Master's Thesis*, McGill University, Qc, Canada.
- Leng J. (2015). "Simulation of cold-formed steel structures." *PhD Thesis*, Johns Hopkins University, Baltimore, Maryland.
- Leng J., Peterman K. D., Bian G., Buonopane S. G., Schafer B. W. (2017). "Modeling seismic response of a full-scale cold-formed steel-framed building. " *Engineering Structures*, 153, 146-165.
- Liu P., Peterman K. D., Yu C., and Schafer B. W. (2012). "Cold-formed steel shear walls in ledger-framed buildings." *Annual Stability Conference*, Conference location, Grapevine, TX.
- Lowes L. N. and Altoontash A. (2003). "Modeling reinforced-concrete beam-column joints

- subjected to cyclic loading." *Journal of Structural Engineering*, 129(12), 1686-1697.
- Lu S. (2015). "Influence of gypsum panels on the response of cold-formed steel framed shear walls." *Master's Thesis*, McGill University, Qc, Canada.
- Macillo V., Fiorino L. and Landolfo R. (2017). "Seismic response of CFS shear walls sheathed with nailed gypsum panels: Experimental tests." *Thin-Walled Structures*, Elsevier Science. ISSN 0263- 8231. 120,161 – 171 . doi: 10.1016/j.tws.2017.08.022.
- MAXXON (2016). Gyp-Crete Fire Ratings/Detail Drawings. Retrieved May 24th, 2016 from <http://www.maxxon.com/gyp-crete/drawings>.
- McKenna F. (1997). "Object-oriented finite element programming: Frameworks for analysis, algorithms, and parallel computing." *PhD Thesis*, University of California, Berkeley, California.
- Moen C. D., Tao F., and Cole R. (2016). "Monotonic and cyclic backbone response of single shear cold-formed steel screw-fastened connections." *International Colloquium on Stability and Ductility of Steel Structures*, Conference location, Timisoara, Romania.
- Padilla-Llano D. A, Moen C. D, Eatherton M. R. (2014) ."Cyclic axial response and energy dissipation of cold-formed steel framing members." *Thin-Walled Structures*, 78, 95-107.
- Padilla-Liano D. (2015). "A framework for cyclic simulation of thin-walled cold-formed steel members in structural systems. ." *PhD Thesis*, Virginia Polytechnic Institute and State University, Blacksburg, VA.
- Peterman K. D., Nakata N., and Schafer B. W. (2013). "Hysteretic Characterization of Cold-Formed Steel Stud-to-Sheathing Connections." *Journal of Constructional Steel Research*, 101, 254-264.
- Peterman K. D. (2014). "Behavior of full-scale cold-formed steel buildings under seismic

excitations." *PhD thesis*, Johns Hopkins University, Baltimore, MD.

Peterman K. D., Stehman M. J., Madsen R. L., Buonopane S. G., Nakata N., and Schafer B. W. (2016a). "Experimental seismic response of a full-scale cold-formed steel-framed building. I: System-level response." *ASCE Journal of Structural Engineering*, 142(12): 04016127.

Peterman K. D., Stehman M. J., Madsen R. L., Buonopane S. G., Nakata N., and Schafer B. W. (2016b). "Experimental seismic response of a full-scale cold-formed steel-framed building. II: Subsystem-level response." *ASCE Journal of Structural Engineering*, 142(12): 04016128

Schafer B. W. (2010). "Review: the direct strength method of cold-formed steel member design." *Journal of Constructional Steel Research*, 64(7), 766-778.

Shamim I. and Roger, C. A. (2013). "Steel sheathed / CFS framed shear walls under dynamic loading: numerical modeling and calibration," *Thin-Walled Structures*, 71, 57-71.

Shamim I. and Rogers C. A. (2015). "Numerical evaluation: AISI S400 steel-sheathed CFS framed shear wall seismic design method." *Thin-Walled Structures*, 95, 48–59.

Shrestha K.M. (2011). "Use of flexible and ductile roof diaphragms in the seismic design of single-storey steel buildings." *PhD Thesis*, McGill University, Qc, Canada.

Simpson Strong-Tie Company Inc. (2017). "Connectors for cold-formed steel construction: S/HDU Holdowns. ."Pleasanton, CA.

Swensen S., Deierlein G. G., and Miranda E. (2016). "Behavior of screw and adhesive connections to gypsum wallboard in wood and cold-formed steel-framed wallties." *Journal of Structural Engineering*, 142(4): E4015002.

Tena-Colunga A. and Abrams D.P. (1996). "Seismic behavior of structures with flexible

---

diaphragms. " *Journal of Structural Engineering*, American Society of Civil Engineers, 122, 439 – 445.

Yu C. and Li C. (2012). "Experimental investigation of cold-formed steel shear walls sheathed with steel-gypsum composite panels." *Structural Stability Research Council Annual Stability Conference*, Conference location, Structural Stability Research Council (SSRC), 298 – 309

## **Foreword to Chapter 4...**

In Chapter 3 the 3D simplified numerical modeling approach for the two-storey case study CFS building was established. Response history dynamic analyses results revealed the importance of considering non-structural components throughout the wall-line of the building in order to obtain a realistic seismic response of a CFS building. In addition, the increased flexibility of the roof compared to the floor subsystem of the CFS building was demonstrated; the stiffening effect of the non-structural components did not influence the seismic response of the building overall but had a direct effect on the maximum displacement and the wall-line storey drifts at the roof level. These initial results heightened the interest in exploring further the effect of the diaphragm's flexibility on the seismic response of a CFS building. As such, in Chapter 4 the 3D building model with non-structural components throughout the wall-line of the building is used in a parametric study where three diaphragm flexibility conditions are examined; flexible, semi-rigid and rigid. A preliminary study investigated the potential influence of the diaphragm flexibility in both the long and short side of the building. Subsequently, the 3D building model was subjected to 20 ground motion records selected and scaled for Montreal, site class C, and Vancouver, site class D, in order to clearly establish the effect of the input ground motion. Overall, the aim is to provide insight on how the dynamic properties of the building may be modified based on the change in diaphragm flexibility and to evaluate the accuracy of the two extreme, flexible and rigid, design assumptions for the diaphragm when conducting seismic analysis of a CFS building.

## CHAPTER 4: INFLUENCE OF DIAPHRAGM FLEXIBILITY ON THE SEISMIC RESPONSE OF COLD - FORMED STEEL BUILDINGS

Violetta NIKOLAIDOU<sup>1</sup>, Colin A. ROGERS<sup>2</sup>, Dimitrios G. LIGNOS<sup>3</sup>

### 4.1- Abstract

This chapter examines the influence of the in-plane diaphragm flexibility on the seismic performance of a cold-formed steel framed building. This is achieved through nonlinear response history analyses of the CFS-NEES Building including its non-structural components. Three diaphragm flexibility cases were considered; flexible, semi-rigid and rigid. The diaphragm is assumed to remain elastic. Modal analyses results showed that the dynamic properties of the building are directly influenced by the diaphragm flexibility. A preliminary study with a bidirectional design basis earthquake in the U.S. explores the potential influence of the diaphragm flexibility in both the short and long side of the building. The same building model is, subsequently, subjected to a suite of 15 ground motions only on the short, more flexible side of the building representing the design basis earthquake in Montreal, Canada. In addition, in order to include the earthquake intensity and source as parameters of the study a suite of 5 ground motions were considered for a design level earthquake in Vancouver, Canada. Clear trends were determined for the resulting forces and drifts with the increase of diaphragm flexibility. The wall-line storey drifts were reduced from the rigid to flexible system; the level of the reduction observed depended on the input ground motion. The building model comprising a rigid diaphragm system predicted the forces experienced by the shear walls in an acceptable level; however, it considerably overestimated and underestimated the wall-line and maximum storey drift ratios, respectively.

**Keywords:** cold-formed steel buildings, diaphragm flexibility, ground motions selection.

## 4.2- Introduction

Whether the diaphragm flexibility should be included in the analysis of buildings for seismic design has been the inquiry of many past studies involving timber and unreinforced masonry or concrete wall buildings with timber diaphragms (Tena-Colunga and Abrams 1996, Fleischman and Farrow 2001, Tokoro et al. 2004, Pathak and Charney 2008, Koliou et al. 2014, Nakamura et al. 2016). These structural topologies are common systems where the diaphragm is considered flexible related to the wall stiffness (RWFD: rigid wall flexible diaphragm). Some of these studies indicate that floor flexibility becomes particularly important for long narrow buildings with stiff perimeter lateral load resisting elements. Tena-Colunga and Abrams (1996) studied analytically the seismic response of two- and eight-storey buildings with unreinforced masonry or concrete shear walls with timber floor and roof diaphragms and compared it to the equivalent response if rigid diaphragms were considered; the buildings were subjected to the 1989 Loma Prieta Earthquake (Gilroy and Palo Alto). Their work showed that while the diaphragm flexibility increases higher floor accelerations can be expected in some cases, and torsional demands of the building can be considerably reduced; the rigid diaphragm assumption is not always conservative. Fleischman and Farrow (2001) explored further the differences in dynamic response of buildings with flexible diaphragms from traditional buildings, focusing on the case of long-span structures with perimeter lateral force resisting systems. Their numerical study of a three-storey long span building with perimeter shear walls subjected to the 1971 San Fernando ground motion revealed that there is a level of diaphragm flexibility above which the dynamic properties of the lateral force resisting system are modified. The isolated diaphragm mass will act independently of the perimeter mass leading to the lower modes consisting of the diaphragm

vibrations, while the higher modes are associated with the shear walls. Further, unexpected force and drift patterns leading to possible brittle diaphragm failure or structural instability due to the lateral deformation imposed on the gravity system may occur.

Tokoro et al. (2004) developed a 3D numerical model in ETABS (CSI 1999) of an instrumented three-storey building with masonry walls and wood diaphragms to highlight the possible inaccuracies of the Uniform Building Code (ICBO 1997) criteria indicating the case of flexible diaphragm in a building. The seismic response was studied under several earthquake records, and the diaphragm flexibility was evaluated based on the lateral force distribution to the vertical elements. The code displacement ratio calculation was found to be method-dependent. Pathak and Charney (2008) focused on the effect of diaphragm flexibility on light-frame wood buildings; a variety of numerical models were developed in SAP2000 (CSI 2009) subjected to the Imperial Valley and Northridge ground motions. They showed that altering the diaphragm condition from rigid to flexible had a considerable impact on the seismic response, particularly of torsionally irregular buildings. In a more recent study, Koliou et al. (2014) developed a 2D numerical model of a rigid wall-flexible diaphragm (RWFD) single-storey building able to capture the nonlinear response of such structures. The purpose was to provide engineers with a simplified yet efficient model that would allow for a large number of response history analyses of RWFD buildings incorporating the inelastic response of the roof diaphragm subsystem. Koliou suggested two updated fundamental period formulas (mechanical, semi-empirical) for these buildings and a new economical design approach allowing the diaphragm to be the main energy dissipating element. Nakamura et al. (2016) conducted a parametric study using a 3D numerical model of a single-storey unreinforced masonry walls building examining various diaphragm flexibilities under earthquake loading; their work showed that seismic demands on

shear walls can be reduced or increased based on the level of diaphragm flexibility in association with the level of strength or stiffness eccentricity present in the system.

Numerical work in cold-formed steel diaphragms involved primarily corrugated steel roof decks as part of single-storey hot rolled steel or concrete buildings (Tremblay and Rogers 2005, Shrestha 2011, Trudel-Languedoc et al. 2012 and 2014). In most of the aforementioned studies the diaphragm was simulated typically using thick shell or membrane elements; Tremblay and Rogers (2005) utilized the concept of numerically simulating the diaphragm subsystem using a deep horizontal plane truss model. In their work they studied the economic benefits of including diaphragm flexibility in the capacity design of single-storey steel buildings with bracing bents. Shrestha (2011) employed this numerical approach using the OpenSees (McKenna 1997) platform to conduct nonlinear response history analyses on single-storey steel buildings with steel corrugated roof diaphragms. He showed that for the design case of inelastic diaphragm with elastic bracing bents the wall-line displacements were reduced significantly with respect to the mid-span displacement of the diaphragm, which highlighted the role of diaphragm flexibility in the overall seismic response of the building.

Trudel-Languedoc et al. (2012) followed a simplified numerical approach using a beam to represent the diaphragm and two springs, as the beam supports, to represent the bracing bents of a single-storey steel building. Subsequently in Trudel-Languedoc et al. (2014), for a diaphragm-to-bracing deformation ratio higher than 3, the first mode of vibration no longer dominates the response; depending on the level of diaphragm flexibility it is the first mode in combination with the third mode that mobilizes 90% of the total structural mass. It was also shown that at the quarter span locations of the diaphragm for the first and third mode of vibration the interior diaphragm shear forces are higher than the end shear forces, rendering the linear shear force

distribution assumption questionable. The research work of Shrestha and Trudel-Languedoc resulted in a modified approach to determine the period of vibration, included in the NBCC (NRCC 2015), for single storey steel buildings having a flexible diaphragm (Tremblay and Rogers 2017). Recently, a new study was conducted on steel roof deck systems as part of single-storey buildings with tilt-up pre-cast concrete walls (Schafer et al. 2018). The seismic design of a RWFD building using a 3D nonlinear numerical model was undertaken. It was shown that shear demands on the roof were almost 30% of the base shear demands on the walls; this was highlighted as a unique feature of RWFD buildings and was, also, observed in the building studied in this work in the numerical results presented in Chapter 3.

For cold-formed steel (CFS) framed buildings involving wood sheathed CFS framed diaphragms, there is limited experimental and numerical work available for the individual seismic response of the diaphragm component (NAHBRC 1999, Chatterjee 2015, Florig 2015, Nikolaidou et al. 2017, Baldassino et al. 2017). To the best of the authors knowledge there is no work at present exploring the effect of the diaphragm flexibility on the seismic response of a CFS framed building. The current North American seismic design provisions of CFS framed buildings (AISI S400 & S100, CSA S136) do not include diaphragm flexibility in the seismic design; nonetheless, common practice is to consider the two extreme conditions, flexible and rigid, when calculating shear wall forces for design purposes. In the work presented herein, the influence of the diaphragm flexibility on the seismic response of a two-storey CFS framed building is explored considering three diaphragm conditions: flexible, semi-rigid and rigid based on the diaphragm flexibility definitions provided in ASCE 7 (ASCE 2016). The building's seismic response under the three diaphragm conditions is examined by conducting nonlinear response history analyses in two steps: (1) the bidirectional Canoga Park (CNP) ground motion (design

basis earthquake in the U.S.) is applied alternating the two ground motion components in the two directions; and (2) fifteen simulated records, representing Montreal Canada, site class C, and five supplemental ground motion records representing Vancouver Canada, site class D were selected, scaled and applied in the flexible side of the building (z direction). The influence of the diaphragm flexibility on resulting forces and drifts is quantified for the ground motions applied.

### 4.3- Numerical model

The 3D numerical model of the CFS-NEES Building was chosen for the purpose of conducting the diaphragm flexibility parametric study, as explained in Chapter 3. In particular, Model 3 (Chapter 3) was used, which includes non-structural components and gravity walls throughout the wall-line of the building; the diaphragm stiffness values for the floor and roof were changed to serve the parametric study. Figure 4.1 includes a brief summary of the numerical modeling approach that was followed, which is presented in detail in Chapter 3.

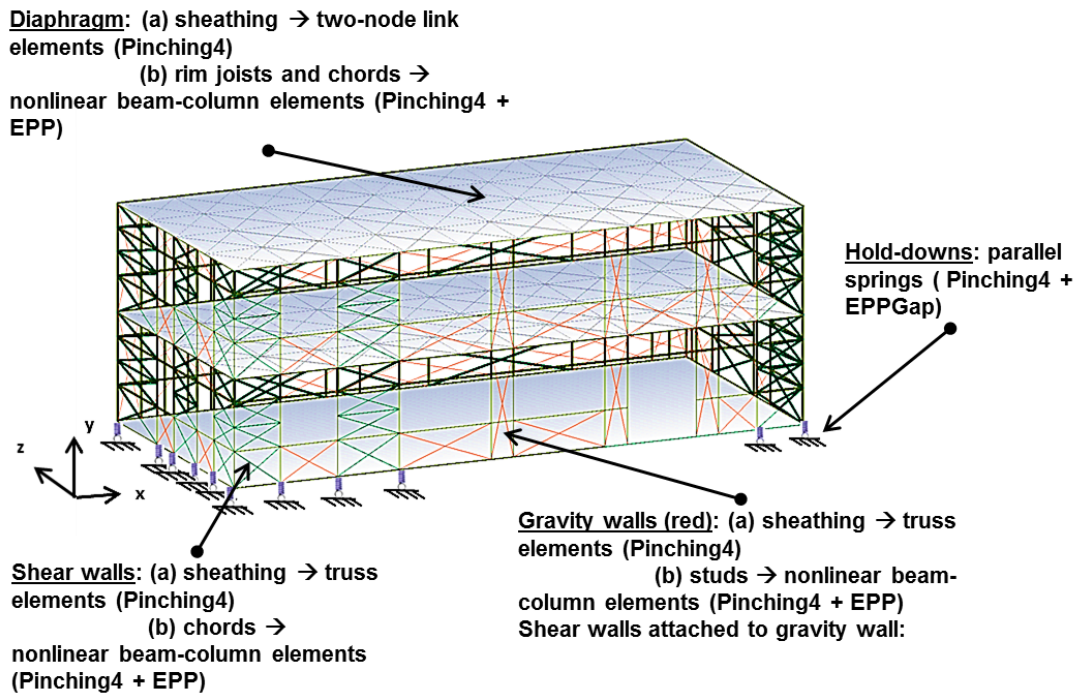


Figure 4.1: Two-storey case study building; illustration of 3D numerical model

In order to investigate the influence of diaphragm flexibility, an elastic material with shear stiffness,  $k$ , was considered for the twoNodelink elements. From the Phase 1 & 2 of the experimental program the diaphragm stiffness values for the diaphragm configurations tested ranged from 1.5 kN/mm to 6.1 kN/mm see (Chapter 2 & 3). As such, the three diaphragm conditions in the  $z$  direction (flexible side of building) were realized as follows: a) for the semi-rigid system, the diaphragm floor and roof stiffness was 3.5 kN/mm and 1.7 kN/mm, respectively, b) for a flexible floor and roof subsystem a factor of 0.1 and c) for a rigid floor and roof subsystem a factor of 100 was applied to the diaphragm stiffness. The same factor was applied to both subsystems so that the stiffness ratio between floor and roof subsystem remains the same in the analyses. The flexible condition was defined according to ASCE 7-16 (ASCE 2016), where a diaphragm is considered flexible when the maximum diaphragm displacement,  $MDD \geq 2 \times \text{Average drift of walls (2ADVE)}$ . The rigid condition was based on the  $MDD \approx 0$ .

#### **4.4- Modal analysis results: dynamic properties in $z$ direction**

Modal analyses were conducted for the three diaphragm systems to demonstrate how the diaphragm flexibility modifies the dynamic response of the building in the  $z$  direction. Table 4.1 summarizes the periods and effective mass ratios for the first four modes of vibration in the  $z$  direction. Figure 4.2 includes the corresponding mode shapes for the first four modes of the three flexibility systems offering details on how the mode shapes and their sequence changes with the changes in the diaphragm flexibility. A nomenclature was introduced for the mode shapes in order to facilitate their description; in Figure 4.2 each mode shape is named as follows: Flexibility-M-number of mode, i.e. RM1 refers to Rigid-Mode-first. OpenSees (McKenna 1997) does not allow for the direct calculation of the effective mass for each mode of vibration. Jennings and Jain (1985) proposed a method for calculating the dynamic properties of one and

two-storey buildings with flexible diaphragms; the diaphragms were considered as bending beams and the walls as shear beams. Trudel-Languedoc (2014) followed a similar concept using a lumped-mass approach in his beam model to calculate the dynamic properties of a single-storey steel building with a flexible roof subsystem. Based on these studies, the effective mass ratio herein was calculated manually using the eigenvectors, as obtained from the model, for a total of 110 nodes bearing lumped masses. The eigenvectors were scaled based on the max eigenvector values per floor.

Table 4.1: Dynamic properties of representative building; z direction

Model 3	$T_{z1}$ (sec)	$T_{z2}$ (sec)	$T_{z3}$ (sec)	$T_{z4}$ (sec)	$M_{eff 1}$ $/M_{tot}$ (%)	$M_{eff 2}$ $/M_{tot}$ (%)	$M_{eff 3}$ $/M_{tot}$ (%)	$M_{eff 4}$ $/M_{tot}$ (%)
<b>Flexible<sub>z</sub></b>	0.57	0.32	0.28	0.22	60	0.03	13.2	7.3
<b>Semi-rigid</b>	0.31	0.20	0.16	0.12	78	13	0.1	2.1
<b>Rigid</b>	0.23	0.12	0.11	0.10	94	0.1	0.5	1.7

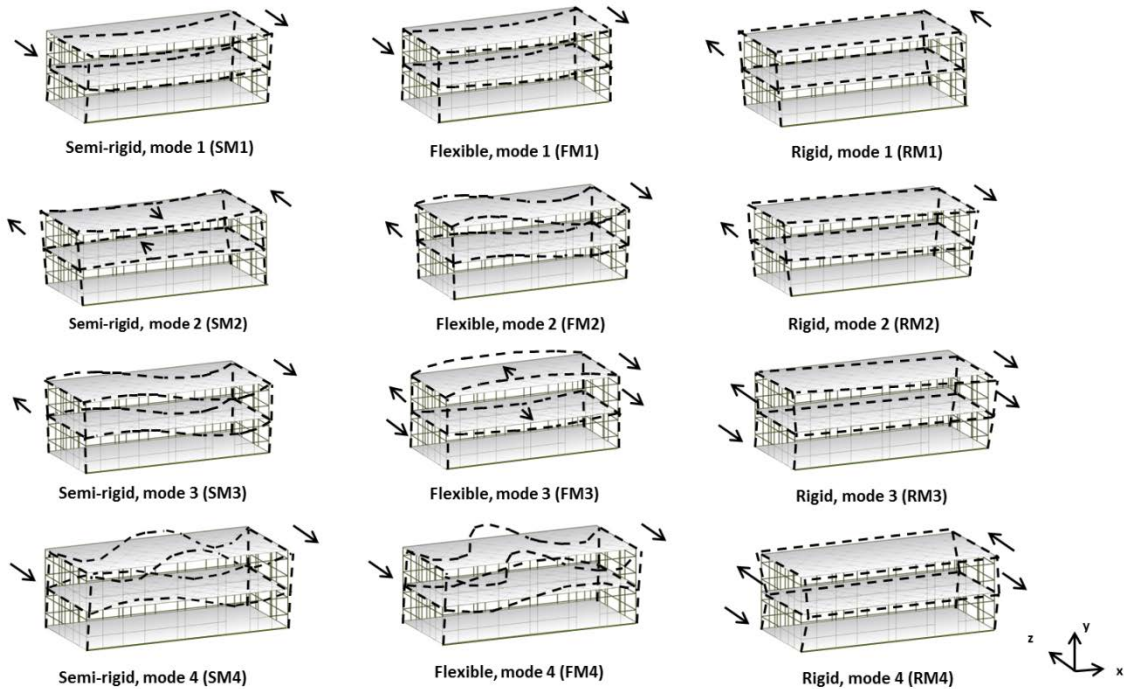


Figure 4.2: Mode shapes of the building for the three diaphragm conditions

In Table 4.1, it is shown that there is an 84% increase and 26% decrease of the fundamental

period of vibration when altering the diaphragm flexibility from a semi-rigid floor and roof system to a flexible and rigid one, respectively. Although for the rigid diaphragm system the effective mass ratio of the first mode mobilized 94% of the mass, this is not the case for the semi-rigid and flexible diaphragm systems. For the semi-rigid diaphragm system the dominant vibration mode of the building is a combination of the first and second mode ( $78\% + 13\% = 91\%$ ), while for the flexible diaphragm system it is the combination of the first, third and fourth mode that mobilizes at least 80% of the total mass ( $60\% + 13.2\% + 7.3\% = 80\%$ ).

In Figure 4.2, for the flexible diaphragm system the first three mode shapes (FM1, FM2 and FM3) include primarily the diaphragm vibrations with the wall-line perimeter eigenvectors being an order of magnitude below the inner and perimeter eigenvectors along the length of the diaphragm span. In addition, it was observed that FM2, which consists of the second diaphragm mode for the floor and roof subsystems, becomes the third mode of the semi-rigid system, SM3. This mode (FM2 & SM3) is translational for the diaphragm and torsional for the building overall, although for FM2 the wall-line eigenvectors, as explained, have a very small value compared to those of the diaphragm. The contribution of the wall's to the building's vibration increases in modes SM4 and FM4. In these modes there is comparable wall and diaphragm deformation with the roof diaphragm subsystem vibrating at each third mode while the floor vibrates at each second mode.

The rigid diaphragm system, as expected, consists of the highest wall-line eigenvector values with RM1 being translational, followed by the torsional RM2, RM3 and RM4. It is worth noting that in FM3 and RM3 there is reverse-torsion observed for the floor and roof level, which is not present in the semi-rigid diaphragm system, apart from the opposite direction translation of the roof and floor subsystems found in SM2. Therefore, for the flexible and rigid diaphragm system,

compared to the semi-rigid condition, a reduction and increase of the wall-line deformations is expected, respectively. Moreover, for the flexible diaphragm system the 84% increase of the fundamental period represents a mode shape where the diaphragm floor and roof subsystems vibrate independently of the walls. Thus, from the modal analysis it is concluded that diaphragm flexibility can change the sequence of the mode shapes (FM2 vs SM3) and the walls versus diaphragm contribution ratio in the vibration of the building.

#### **4.5- Ground motion selection and scaling**

##### **4.5.1 Montreal**

Fifteen simulated ground motion records were selected from the Earthquake Seismology Toolbox website ([www.seismotoolbox.ca](http://www.seismotoolbox.ca)) and scaled with respect to a target response spectrum. The target response spectrum was based on the modified uniform hazard design response spectrum (M\_UHDRS) included in the NBCC (NRCC 2015) for Montreal, site class C (2% in 50 years). The M\_UHDRS incorporates spectral acceleration demands for short periods ( $\leq 0.5\text{sec}$ ) and is appropriate for the short-period building discussed herein, as shown in Section 4.3. The simulated records were provided by the work of Atkinson (2009) representing moderate level earthquakes in Montreal for site class C (Eastern Canada). The selection and scaling of the ground motions was realized based on the guidelines proposed in the NBCC (2015) and described in Tremblay et al. (2015).

##### **4.5.1.1. Target period range**

A period range of interest was established as a first step based on the two limits provided in the NBCC (2015) for  $T_{min}$  and  $T_{max}$  as shown in Eq. 4.1 and 4.2 in this section. The period range was set in such a manner as to include all possible vibration modes that constitute the building's inelastic seismic response. The lower period limit,  $T_{min}$ , was taken as the period value of the highest mode required in obtaining an effective mass ratio of 90%; however, it shall not be

higher than 0.2 times the fundamental period ( $T_1$ ). The maximum period limit,  $T_{max}$ , was taken as 2 times the fundamental period; however, it shall be no less than 1.5sec.

$$T_{min} = \min[0.2T_1, T_{90\%}] \quad (4.1)$$

$$T_{max} = \max[2T_1, 1.5sec] \quad (4.2)$$

Based on Table 4.1, it is shown that for the three diaphragm conditions of the building the maximum fundamental period of vibration is 0.57sec. As such,  $T_{max}$  was chosen as 1.5sec. Given that the flexible diaphragm system up to the fourth mode (0.22sec,  $0.2 \times 0.22 = 0.044$ sec) accumulates an effective mass ratio of 80%, and that the minimum provided spectral acceleration value in the NBCC (NRCC 2015) for the modified response spectrum corresponds to a period of 0.05sec, it was decided that the lower period limit,  $T_{min}$ , will be set at 0.05sec. Therefore, the period range was  $T = [0.05 \text{ to } 1.5] \text{ sec}$ .

#### **4.5.1.2. Target response spectrum: selected ground motions for Montreal, site class C**

Based on seismic hazard deaggregation data provided by Natural Resources Canada for Montreal three scenario-specific period ranges were identified, following Method B of the NBCC (2015) guidelines. The deaggregation data were provided in terms of distance,  $R$ , and moment magnitude,  $M_w$  (Table 4.2). The two main scenarios describing seismic hazard in Montreal constitute of earthquake events with: (1) magnitude  $M_6$  at a fault distance  $R = 10$  to  $30$  km for a period range of  $0.2$  to  $1.0$ secs and (2) magnitude  $M_7$  at a distance  $R = 20$  to  $70$  km for a period range of  $0.5$  to  $2.0$  secs (Atkinson 2009).

The Engineering Seismology Toolbox provides four sets of 45 ground motion records each; two sets of  $M_6 - R [10 \text{ to } 30]$  km events and two of  $M_7 - R [15 \text{ to } 100]$  km events. Selection criteria for the ground motion records involve not only magnitude and fault distance but also the mean value and standard deviation of the target spectral acceleration over the ground motion spectral acceleration ratio ( $S_T(T)/S_g(T)$ ); the following criteria shall be met: ground motion records with

(1)  $\text{mean}(S_T(T)/S_g(T))$  between 0.5 and 2.0 and (2) the lowest  $\text{SD}(S_T(T)/S_g(T))$ . Thus, based on above criteria and Table 4.2 the following scenario-specific period ranges were identified and corresponding simulated ground motion records were selected: (1)  $T_{R1} = [0.05 \text{ to } 0.2]$  sec. with selected ground motions of magnitude M6 and distances  $R = [13 \text{ to } 21]$  km, (2)  $T_{R2} = [0.2 \text{ to } 0.5]$  secs with selected ground motions of magnitude M6 and distances  $R = [13 \text{ to } 26]$  km and (3)  $T_{R3} = [0.5 \text{ to } 1.5]$  secs with selected ground motions of magnitude M7 and distances  $R = [17 \text{ to } 50]$  km. The selection of three instead of two suites facilitated the scaling and matching process of the mean response spectrum of each suite with the modified design response spectrum (DRS) for Montreal for the three scenario-specific period ranges, as described in Section 4.5

Table 4.2: Deaggregation data, Montreal, site class C (Natural Resources Canada)

<b>Deaggregation data</b> T (sec)	<b>Mean</b>		<b>Max</b>	
	<b>M<sub>w</sub></b>	<b>R (km)</b>	<b>M<sub>w</sub></b>	<b>R (km)</b>
<b>0.05</b>	6.35	26	6.75	10
<b>0.1</b>	6.40	27	5.05	10
<b>0.2</b>	6.51	29	5.45	30
<b>0.3</b>	6.59	32	6.75	30
<b>0.5</b>	6.69	37	6.75	30
<b>1.0</b>	6.86	50	6.75	30
<b>2.0</b>	7.00	67	6.75	30
<b>5.0</b>	7.17	88	6.75	30
<b>10.0</b>	7.25	111	7.35	50

#### 4.5.1.3. Scaling of selected ground motion records; Montreal, site class C

Ground motion scaling was realized in two steps; every record was first multiplied with its corresponding mean  $(S_T(T)/S_g(T))$  value and, subsequently, a second scaling factor was applied in order for the mean response spectrum of all the records per suite to not exceed the DRS at any point in the specific period range of the suite by more than 10%. Table 4.3 includes the selected ground motions with the two scaling factors applied. Figure 4.3 includes the scaled response spectrum of each record as well as the scaled mean response spectrum of each suite compared to

the DRS. Table 4.3 includes the file that each record was selected from and the number of the record in that file; this information is provided in the column with the title “Identifier” and shown with the format “file/number of record”.

Table 4.3: Selected ground motions and scaling factors

Suites	Identifier	T (sec)	M <sub>w</sub>	R (km)	SF <sub>1</sub>	SF <sub>2</sub>
1	east6c1.acc/35	0.05 – 0.2	6	16.6	0.55	0.93
	east6c1.acc/6			12.5	0.56	
	east6c1.acc/22			14.4	0.63	
	east6c2.acc/5			21.1	1.28	
	east6c2.acc/17			21.1	1.21	
2	east6c1.acc/1	0.2 – 0.5	6	12.8	0.56	0.94
	east6c1.acc/7			12.8	0.64	
	east6c1.acc/15			10.7	0.49	
	east6c2.acc/26			24.4	1.46	
	east6c2.acc/31			25.6	1.52	
3	east7c1.acc/18	0.5 – 1.5	7	20.6	0.57	0.955
	east7c1.acc/32			25.8	0.80	
	east7c2.acc/1			41.6	1.23	
	east7c2.acc/7			45.2	1.02	
	east7c2.acc/11			50.3	1.64	

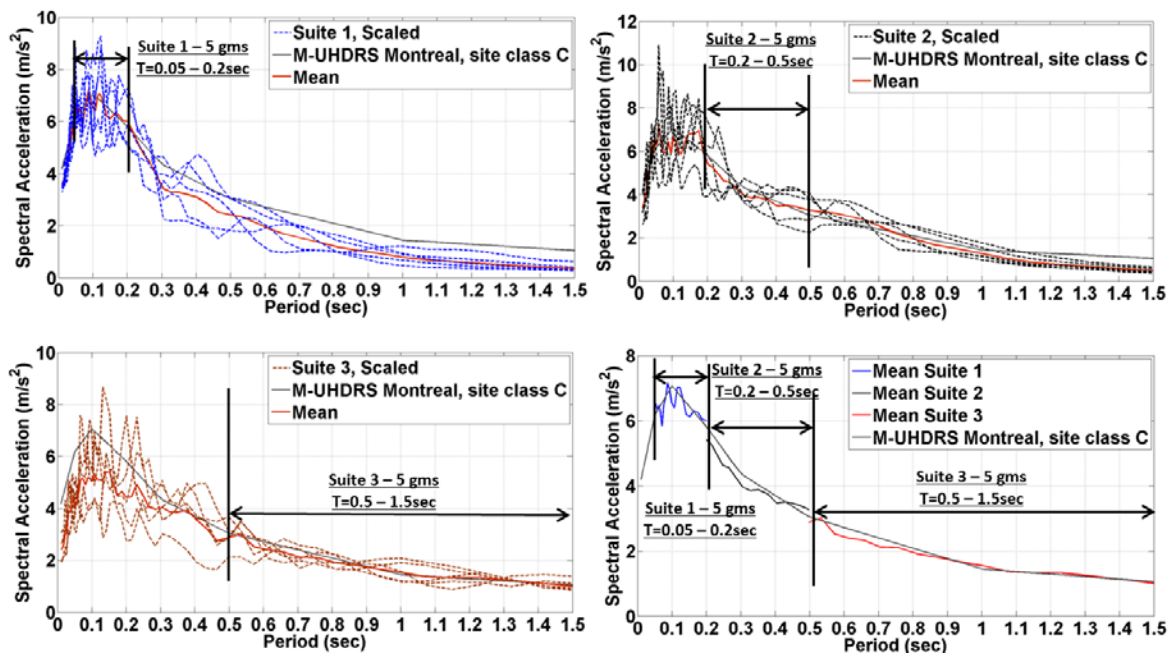


Figure 4.3: Scaled response spectra of the selected ground motion records; Montreal, site class C  
 Simulated ground motion records by Atkinson (2009) have been commonly used in research

work, given the wide selection of compatible generated ground motion records provided for the researcher. The records selected herein were chosen from the sets representing site class C no adjustment was necessary to take into account local geotechnical conditions. The chosen simulated records were generated to represent shallow crustal earthquakes, which is the dominant fault mechanism recorded from past earthquake events in Eastern Canada.

#### **4.5.2 Vancouver**

Five supplemental ground motion records were selected for Vancouver, site class D, with the purpose of exploring further the role of the diaphragm in the overall seismic response of a CFS building considering higher intensity earthquakes produced by various sources of earthquake events. Apart from crustal shallow earthquakes, in-slab earthquakes were also considered, as this type has been identified as an earthquake source that contributes to the seismic hazard of the site. Interface earthquakes were not considered as they contribute in the hazard for longer periods (1.0 to 3.0sec) than the period range of the building studied (0.05 to 1.5sec).

##### **4.5.2.1. Target response spectrum: selected ground motions for Vancouver, site class D**

A similar approach, as described in Section 4.4.1.1 for Montreal, was followed. Deaggregation data for Vancouver, site class D were based on the information provide in Tremblay et al. (2015). The selection criteria are presented in Table 4.4. Two main scenarios were identified: (1) mean moment magnitude  $M_{6.5}$  at a mean fault distance  $R = 14\text{km}$  for a period range of 0.05 to 0.8secs and (2) mean moment magnitude  $M_7$  at a mean distance  $R = 52\text{ km}$  for a period range of 0.3 to 1.5 secs. Although the selection of ground motions was based on the two scenarios described, earthquake records were selected that match the  $M_{UHDRS}$  (2% in 50 years) in the period range of interest. The PEER-NGA (Ancheta et al. 2012) and K-NET databases were relied upon to identify records for crustal shallow and in-slab earthquakes, respectively, that satisfy the criteria of Table 4.4. It should be noted that since the K-NET database does not provide

information about the shear velocity of the stations up to 30m, this information was obtained from the work of Boore et al. (2011). Moreover, the five records are based on three earthquake events; for one crustal shallow event and one in-slab event the horizontal records in the two directions were used.

Table 4.4: Selection criteria; Vancouver, site class D

$T_{\text{range}}$ (sec)	mean $M_w$	mean $R$ (km)	Earthquake source	$V_{s30}$ (m/s)
0.05 – 0.8	6.7	14	Crustal shallow	180-360
0.3 – 1.5	7	52	In-slab	

#### 4.5.2.2. Scaling of selected ground motions; Vancouver, site class D

Scaling factors for each ground motion record were selected to minimize the mean squared error (MSE) of the scaled values of each ground motion response spectrum to the  $M_{UHDRS}$  for Vancouver, site class D. Table 4.5 includes the records selected, the scale factor ( $SF_v$ ) applied and the associated MSE. Figure 4.4 illustrates the scaled response spectrum of each ground motion record with respect to the  $M_{UHDRS}$ ; each scaled response spectrum is shown also in log scale in order to illustrate how well it follows the  $M_{UHDRS}$  for the entire period range of interest, 0.05 to 1.5sec. Scaling factors were within the acceptable limits 0.2 to 5 (NBCC 2015). All scaled ground motions acceleration time-series for Montreal and Vancouver are included in Appendix E.

Table 4.5: Selected ground motion records; Vancouver, site class D

Event	No of records	Type	$M_w$	$R$ (km)	$SF_v$	MSE	$V_{s30}$ (m/s)
<b>Superstition Hills (SH)</b> <sup>1,2</sup>	2	Crustal shallow	6.5	13.03	1.85	0.0292	194
					1.41	0.0314	
<b>Northridge (CNP)</b> <sup>3</sup>	1	Crustal shallow	6.7	14.7	0.9	0.0235	267
<b>Miyagi (M)</b> <sup>4,5</sup>	2	In-slab	7	66	1.0	0.0265	246-296
					1.0	0.0244	

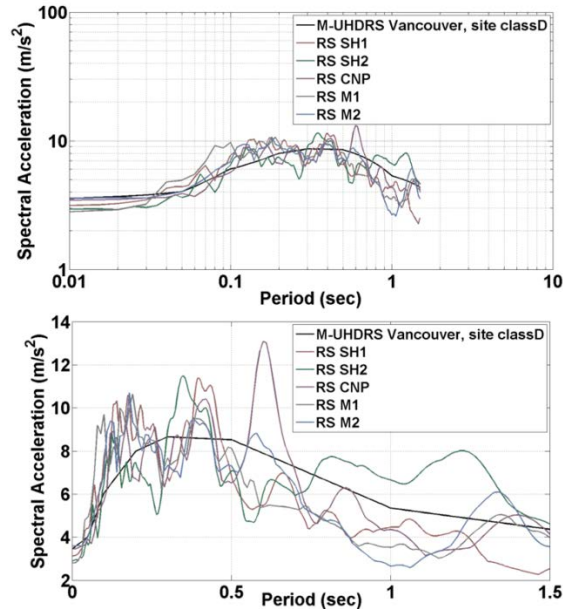


Figure 4.4: Scaled response spectra of the selected ground motion records; Vancouver, site class

D

#### 4.6- Parametric study: Step 1

In this section the results of non-linear response history analyses are presented for the building when subjected to the CNP ground motion components unscaled in the x and z direction. The analysis is repeated alternating the two components in the two directions (Part 1 & Part 2). Figure 4.3 shows the response spectra of the two ground motion components; the x and z directions indicate the directions the signals were applied initially (Part 1).

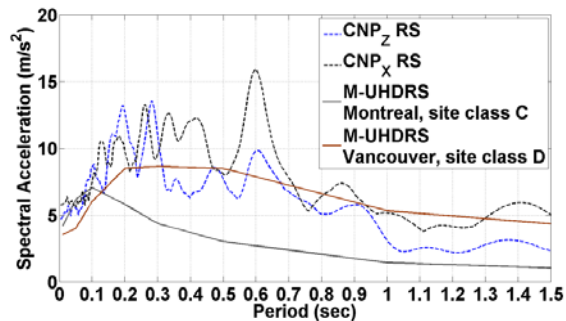


Figure 4.5: Response spectra of design level earthquake in the USA vs. the design response spectrum for Montreal, site class C and Vancouver, site class D

CNP<sub>x</sub> signal has higher amplitude than CNP<sub>z</sub>. The M\_UHDRSs for Montreal, site class C and Vancouver, site class D are included in Figure 4.5 for purposes of comparison of the CNP ground motion to the selected and scaled ground motion records applied in Step 2 of the parametric study (Section 4.6). In the studies of Humar and Popovski (2013) and Mortazavi and Humar (2016) on single-storey buildings with flexible diaphragms ground motion records were applied first in the short and then the long direction of the buildings studied for the purpose of examining the influence of the diaphragm flexibility even at the stiffer side of the building while including a wide range of relative diaphragm-to-wall-line drift ratios in their work.

#### 4.6.1. Part 1

In Tables 4.6 and 4.7, a comparison of the three diaphragm systems is demonstrated in the form of wall-line storey drift ratios, maximum diaphragm deflection values  $MDD_{f/r}$ , maximum overall floor and roof displacement values and base shear forces normalized over the seismic weight.

Table 4.6: CNP<sub>x&z</sub>, Part 1; Wall-line storey drift ratios

<b>Diaphragm System</b>	$\Delta_{u1}/h$ (%)	$\Delta_{u2}/h$ (%)	$\Delta_{v1}/h$ (%)	$\Delta_{v2}/h$ (%)
<b>Flexible</b>	0.72	0.39	0.40	0.24
<b>Semi-rigid</b>	0.69	0.35	0.41	0.26
<b>Rigid</b>	0.67	0.33	0.49	0.44

Note: Symbol definitions are provided in Section 4.10.

Table 4.7: CNP<sub>x&z</sub>, Part 1; MDD, maximum displacements and base shear forces

<b>Diaphragm System</b>	$MDD_f$ (mm)	$Disp_{fmax}$ (mm)	$MDD_r$ (mm)	$Disp_{rmax}$ (mm)	$V_x^{tot}/W$	$V_z^{tot}/W$
<b>Flexible</b>	38.7	48	83.7	90	0.78	0.43
<b>Semi-rigid</b>	8.2	19.5	14.2	20	0.82	0.40
<b>Rigid</b>	-	14.6	-	12.8	0.81	0.40

Note: Symbol definitions are provided in Section 4.10.

In Table 4.6 from the semi to rigid diaphragm system wall-line storey drift ratios (WIDRs) are decreasing in the x direction and increasing in the z with the roof showing the most considerable increase of 69%. For the flexible diaphragm system, WIDRs are decreasing for the z direction

and increasing for the x with up to 11% increase at the roof level. In Tables 4.7 the difference in base shear forces is only up to 6%; in the x direction forces are decreasing for the rigid and flexible diaphragm system while in the z direction forces are increasing. The over 100% increase in  $MDD_f$  and floor maximum displacement suggests an independent diaphragm movement from the rest of the system as explained from the modal analysis in Section 4.3.

#### 4.6.2. Part 2

Tables 4.8 and 4.9 include the results as demonstrated in Section 4.5.1 having now applied the two CNP ground motion components in the opposite directions.

Table 4.8: CNP<sub>z&x</sub>, Part 2; Wall-line storey drift ratios

<b>Diaphragm System</b>	$\Delta_{u1}/h$ (%)	$\Delta_{u2}/h$ (%)	$\Delta_{v1}/h$ (%)	$\Delta_{v2}/h$ (%)
<b>Flexible</b>	0.34	0.30	0.47	0.36
<b>Semi-rigid</b>	0.5	0.33	0.9	0.37
<b>Rigid</b>	0.48	0.25	0.995	0.65

Note: Symbol definitions are provided in Section 4.10.

Table 4.9: CNP<sub>z&x</sub>, Part 2;  $MDD_{f/r}$ , maximum displacements and base shear forces

<b>Diaphragm System</b>	$MDD_f$ (mm)	$Disp_{fmax}$ (mm)	$MDD_r$ (mm)	$Disp_{rmax}$ (mm)	$V_x^{tot}/W$	$V_z^{tot}/W$
<b>Flexible</b>	37.7	51	127.4	136.3	0.47	0.40
<b>Semi-rigid</b>	8.9	32.4	38.2	44.9	0.53	0.61
<b>Rigid</b>	-	30.7	-	17.5	0.41	0.63

Note: Symbol definitions are provided in Section 4.10.

Tables 4.8 and 4.9 demonstrate a different level of influence of the diaphragm flexibility for the building. For the base shear forces the pattern changed as in the x direction forces were decreased for both the flexible and rigid diaphragm systems with a decrease for the rigid condition up to 23%. In the z direction a decrease was observed for the flexible diaphragm system of 34.6% and a small increase of 4% for the rigid condition. For the flexible diaphragm system drift patterns changed as well since for both directions WIDRs decreased with most prominent the 48% floor WIDR reduction in the z direction. For the rigid system the WIDRs

demonstrated a similar pattern with a reduction in the x direction and an increase in the z most prominently at the roof level in the z direction (76%). It is worth noting that the WIDRs at the floor level in the flexible system and roof level in the rigid system are mostly affected in the z direction due to the fact that the floor diaphragm changed from a semi-rigid to a flexible condition while the roof diaphragm from a semi-flexible to a rigid condition, respectively.

Overall, from this preliminary response history analysis results it was observed that Part 2 loading excites the flexible side of the building, with a pronounced influence of the diaphragm flexibility on the overall seismic response of the building while in Part 1 that influence is not substantial. In Part 1 loading, which was the case during the CFS-NEES Building testing, the signal in the x direction (stiffer side of the building) dominated the response, which is demonstrated also by the normalized base shear forces in Table 4.7. The diaphragm did not influence the seismic response during the shake table testing; given, also, that the diaphragm flexibility increases with increase of the span. For the following nonlinear response history analyses ground motions are applied only in the z direction of the building in order to explore further the seismic response of a CFS building with flexible diaphragms.

#### **4.7- Parametric study: Step 2**

In this section results are presented for the case where the two-storey building in question is placed in Montreal, site class C and Vancouver, site class D. A comprehensive study was completed for Montreal exploring the effect of the fifteen ground motions (GMs) on the overall seismic response of the three flexibility systems, while the supplemental study of five GMs for Vancouver provided insight on higher intensity crustal shallow and in-slab earthquakes.

##### **4.7.1. Montreal results**

Figures 4.6 and 4.7 illustrate the flexibility of the floor and roof subsystem as a function of time for each GM of the first suite (Suite 1). The relative displacement of the diaphragm with respect

to two times the average wall-line drift is used in Figure 4.6, following the ASCE 7 (2016) definition as a reference, in order to show its dependency on the input ground motion characteristics. As an example, for the semi-rigid system overall the floor acts as a semi-rigid diaphragm; however, for GM3 and GM5 it shifts towards a semi-flexible behaviour. This is also demonstrated in Figure 4.7, where the  $MDD_f/ADVE$  ratio is close to the value of two for four peak amplitude time steps.

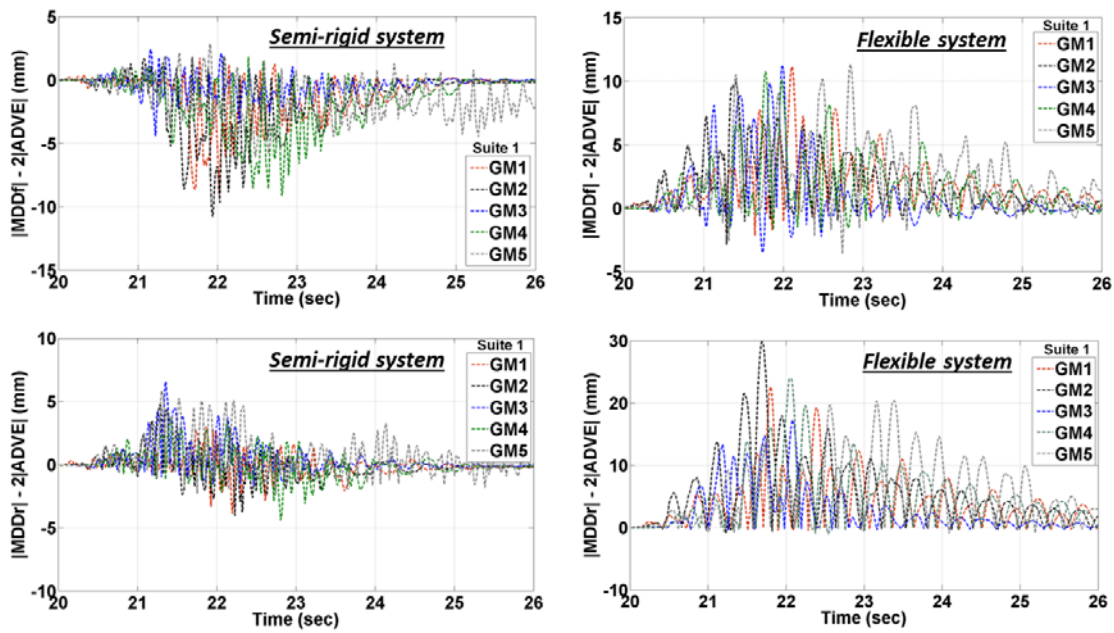


Figure 4.6: Flexibility of floor and roof subsystem for the 15GMs; Montreal

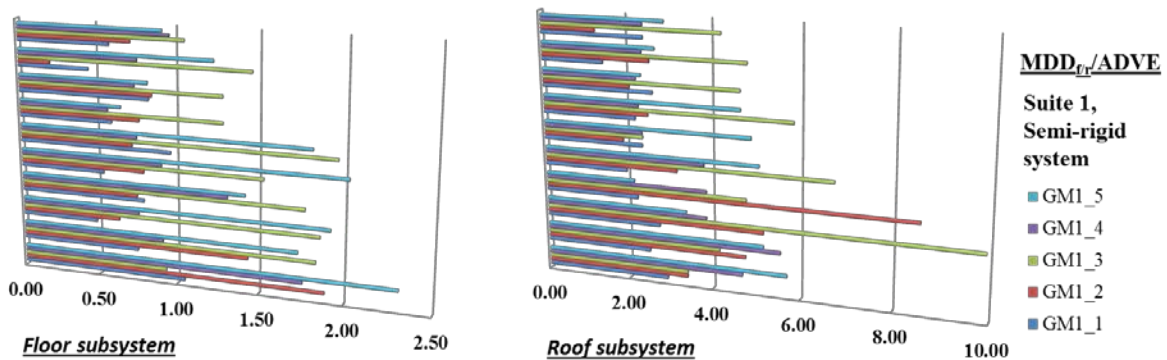


Figure 4.7:  $MDD_f/ADVE$  and  $MDD_r/ADVE$  ratios at ten peak amplitude time steps; Montreal

Figure 4.6 and 4.7 serve not only to show how the diaphragm-wall interaction changes

depending on the input lateral load, but also to illustrate the differences between the semi-rigid and flexible systems employed in the study. Figure 4.7 demonstrates the highly flexible behaviour of the roof subsystem as part of the semi-rigid system for GMs 3 and 5.

Figure 4.8 demonstrates the changes in the total base shear force for each GM with the change in diaphragm flexibility. Table 4.10 contains quantitative results (percentage difference %) while the variability of the results and a comparison of mean values are found in Table 4.14 at the end of Section 4.6.1 for the forces and drifts discussed herein. The nomenclature used for the GMs is, depending on the graph presented, as follows:  $i_j$  or  $GMi_j$  or  $GMi_j$ , where  $i$  is the suite number (i.e. 1, 2 or 3) and  $j$  is the GM number per suite (i.e. 1, 2, 3, 4 or 5).

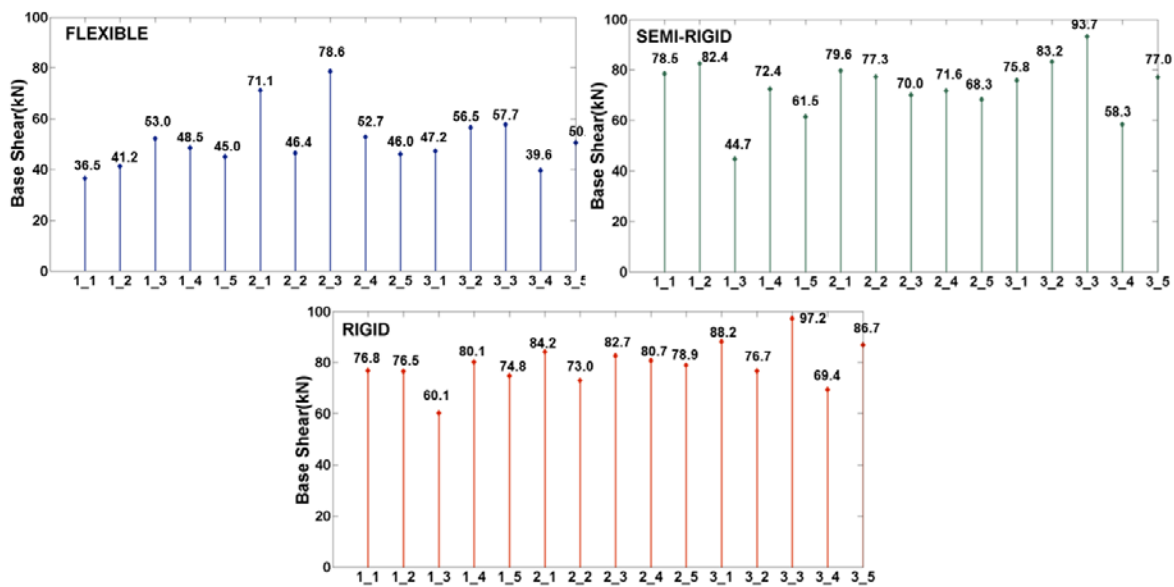


Figure 4.8: Base shear forces for the 15 GMs; Montreal

A definite increasing progression of the total base shear forces is formed as the flexibility shifts from flexible to semi-rigid to rigid (Figure 4.8). As shown in Table 4.10, for four GMs the base shear force for the rigid system is lower than for the semi-rigid; however, the reduction is less than 10%. Overall, the rigid system captures the total base shear quite accurately but only in certain GM cases, conservatively (up to 35%). Table 4.14 shows that the base shear values

obtained for the 15 GMs are close to the mean value for each flexibility system with a difference of only 8% between the semi-rigid and the rigid system. The flexible system exhibited up to 54% lower base shear forces as expected (Table 4.10) with the exception of two GMs where there was an increase of up to 20%. One of the GMs in question is GM1\_3, during which, as it was shown in Figure 4.6, the floor subsystem responds in a more flexible manner compared to the majority of the applied GMs.

Table 4.10: Comparison of base shear values for the three flexibility systems; Montreal

<b>Base Shear, <math>V_b</math></b>	<b>Semi-rigid to Flexible (%)</b>	<b>Semi-rigid to Rigid (%)</b>
<b>GM1_1</b>	53.5	2.2
<b>GM1_2</b>	50.0	7.2
<b>GM1_3</b>	-19.0	-34.5
<b>GM1_4</b>	33.0	-10.6
<b>GM1_5</b>	27.0	-21.6
<b>GM2_1</b>	11.0	-5.8
<b>GM2_2</b>	40.0	5.6
<b>GM2_3</b>	-12.0	-18.0
<b>GM2_4</b>	26.4	-12.7
<b>GM2_5</b>	32.7	-15.5
<b>GM3_1</b>	38.0	-16.4
<b>GM3_2</b>	32.0	7.8
<b>GM3_3</b>	38.0	-3.7
<b>GM3_4</b>	32.0	-19.0
<b>GM3_5</b>	35.5	-12.6

Note: Symbol definitions are provided in Section 4.10.

Table 4.11 includes the percentage difference of the shear forces for each individual shear wall (five shear walls in the z direction) at the time of the maximum wall-line storey drift ratio at floor level (maxFWIDR). A similar trend is observed for the individual shear wall forces as for the total base shear. It should be noted that the shear wall with the highest force remains the same between the three systems for each GM, which was expected since the case study building has only perimeter shear walls with equivalent rigidity levels.

Table 4.11: Comparison of shear force values for the three flexibility systems for each individual shear wall; Montreal

Shear, $V_{fw}$	Semi-rigid to Flexible (%)					Semi-rigid to Rigid (%)				
	GMs	WW1	WW2	WW3	EW4	EW5	WW1	WW2	WW3	EW4
GM1_1	53.9	59.5	58.2	56.1	57.5	-2.9	-3.1	-3.0	-0.5	-0.6
GM1_2	42.3	46.4	36.7	50.0	49.5	-1.1	-0.8	-1.3	6.5	6.6
GM1_3	0.6	0.9	-10.2	-8.8	-14.4	-29.7	-34.3	-26.4	-34.2	-32.7
GM1_4	38.5	42.4	31.9	38.4	36.4	-11.8	-13.0	-13.0	-10.3	-11.0
GM1_5	24.1	29.3	29.0	32.8	33.8	-24.9	-27.7	-28.4	-19.6	-21.3
GM2_1	20.8	24.1	27.1	14.3	17.5	-9.3	-10.5	-10.7	-8.3	-8.6
GM2_2	35.7	39.8	40.1	32.0	34.9	-3.5	-4.3	1.6	1.3	4.4
GM2_3	9.9	11.0	5.1	-0.4	-4.3	-22.8	-24.6	-24.1	-19.8	-20.3
GM2_4	24.6	29.8	31.7	24.5	28.8	-19.5	-18.5	-8.2	-18.1	-12.7
GM2_5	25.9	26.4	12.3	32.8	26.2	-22.4	-22.5	-18.0	-21.4	-18.4
GM3_1	42.2	43.4	25.5	41.9	33.6	-21.3	-21.6	-19.2	-22.7	-22.0
GM3_2	40.4	47.3	50.9	28.6	34.9	-9.2	-6.8	4.1	-2.1	6.0
GM3_3	57.4	56.1	39.0	49.5	39.5	4.3	-1.8	-18.1	3.6	-8.8
GM3_4	40.9	41.6	34.4	39.6	36.7	-34.6	-30.4	-9.3	-27.1	-17.5
GM3_5	47.9	49.2	31.8	49.3	42.1	-14.0	-14.5	-13.1	-12.0	-12.3

Note: 1. WW indicates shear wall at the west side of the building, while EW at the east side.  
 2. Symbol definitions are provided in Section 4.10.

Figure 4.9 includes a comparison of: (1) the wall-line storey drift ratios at the time of maximum wall-line storey drift ratio at floor level ( $\Delta_v/h_{\maxFWIDR}$ ); and (2) the overall storey drift ratio at the time of the maximum storey drift ratio at roof level ( $\Delta_{v2}^{\text{tot}}/h_{\maxRDR}$ ); during these times the building exhibits the highest diaphragm and base shear forces. Table 4.12 includes the quantitative results for the  $\Delta_v/h_{\maxFWIDR}$  at floor level ( $\Delta_{v1}/h_{\maxFWIDR}$ ) and the  $\Delta_{v2}^{\text{tot}}/h_{\maxRDR}$  at roof level ( $\Delta_{v2}^{\text{tot}}/h_{\maxRDR}$ ). Based on Figure 4.9, there is an evident opposite trend forming for the two storey drift ratio variables;  $\Delta_{v1}/h_{\maxFWIDR}$  is increasing from flexible to semi-rigid-to-rigid while  $\Delta_{v2}^{\text{tot}}/h_{\maxRDR}$  is decreasing. These trends were expected from the modal analysis results presented in Section 4.3 (Figure 4.2). As the diaphragm flexibility increases, the diaphragm vibrates independently of the shear walls (reduction of ADVE) while the overall storey drift ratio of the building increases (increase of  $MDD_{fT}$ ). In Table 4.14, the percentage difference of the

mean storey drift ratio variables for the flexible and the semi-rigid system show a gross underestimation or overestimation of the drifts by the flexible system.

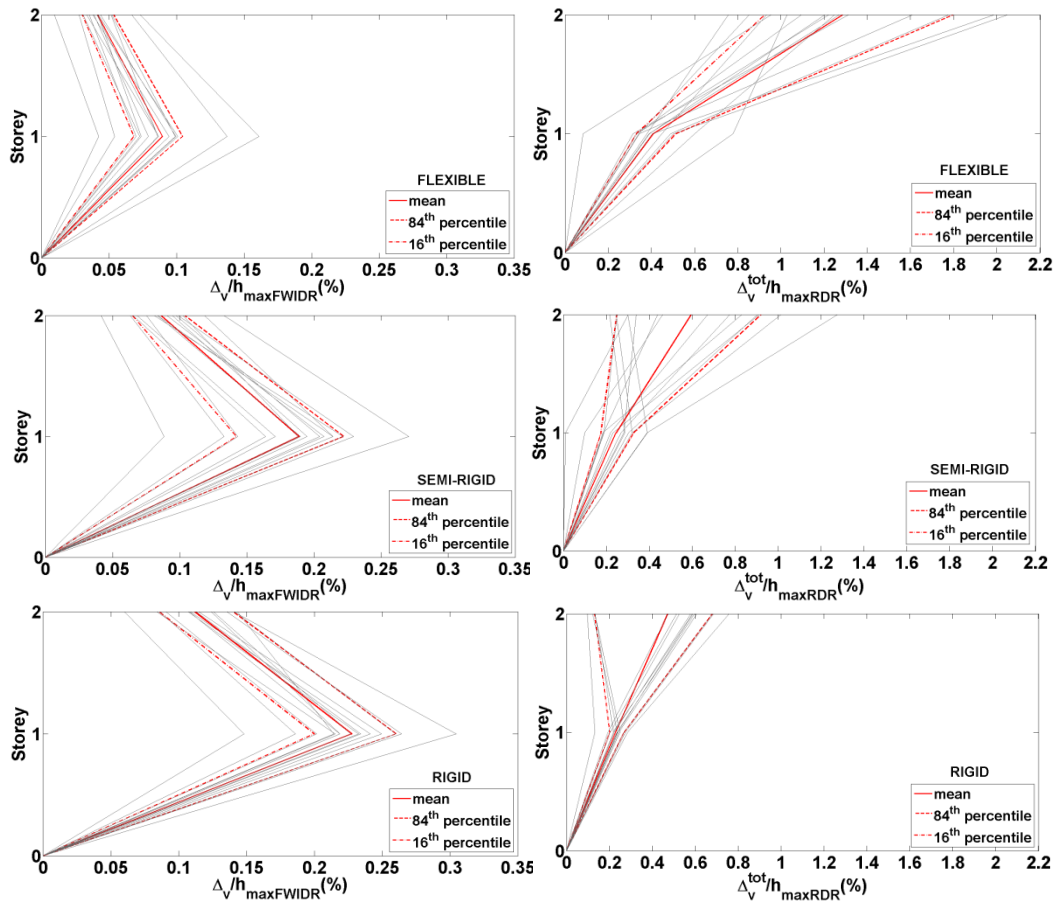


Figure 4.9: Storey drift ratios at maxFWIDR and maxRDR time; Montreal

On the other hand, focusing on the  $\Delta_{v2}^{\text{tot}}/h_{\maxRDR}$  percentage difference included in Table 4.12 for the semi-rigid and rigid system, it is observed that there is a per-case overestimation (up to 110%) or underestimation (up to 68%) of the storey drift ratios. Although the 20% percentage difference in mean storey drift ratios in Table 4.14 suggests similar results for the two systems, the equivalent 50 to 60% cov associated with the semi-rigid and rigid samples renders the mean parameter unsuitable for such a comparison as it indicates a high variability in the response of each system for each GM. Given that the relative diaphragm-to-wall-line displacement is dependent on the input GM, as illustrated in Figure 4.6, the resulting percentage difference of the

storey drift ratios between the three flexibility systems varies considerably per GM case. As such, the storey drift ratios of the building as provided by the flexible and rigid systems deviate considerably from the storey drift ratios of the semi-rigid system.

Table 4.12: Comparison of storey drift ratios for the three flexibility systems at maxFWIDR and maxRDR time; Montreal

Storey drift ratios	$\Delta_{v1}/h_{\max\text{FWIDR}}$		$\Delta_{v2}^{\text{tot}}/h_{\max\text{RDR}}$	
	Semi-rigid to Flexible (%)	Semi-rigid to Rigid (%)	Semi-rigid to Flexible (%)	Semi-rigid to Rigid (%)
<b>GM1_1</b>	79.6	-3.7	-117.6	-20.1
<b>GM1_2</b>	67.9	4.7	-307.2	55.1
<b>GM1_3</b>	-14.0	-67.1	-319.6	67.7
<b>GM1_4</b>	59.0	-20.1	-374.7	63.8
<b>GM1_5</b>	51.2	-49.3	-27.1	12.5
<b>GM2_1</b>	35.9	-16.4	-480.7	38.5
<b>GM2_2</b>	57.6	1.4	-710.9	-109.4
<b>GM2_3</b>	6.0	-40.8	-122.2	-31.3
<b>GM2_4</b>	49.9	-23.3	-95.0	35.4
<b>GM2_5</b>	39.2	-38.5	-20.6	22.8
<b>GM3_1</b>	54.7	-39.1	-21.2	24.1
<b>GM3_2</b>	60.8	1.3	-44.9	30.2
<b>GM3_3</b>	63.5	-12.5	-60.6	40.7
<b>GM3_4</b>	59.3	-39.6	-426.0	-89.9
<b>GM3_5</b>	66.1	-21.3	25.5	33.0

Note: Symbol definitions are provided in Section 4.10.

Figure 4.10 displays the shear diaphragm force distribution for the floor and roof subsystem in the two critical time steps, maxFWIDR and maxRDR, respectively, in order to illustrate how the diaphragm forces change with the increase of diaphragm flexibility.

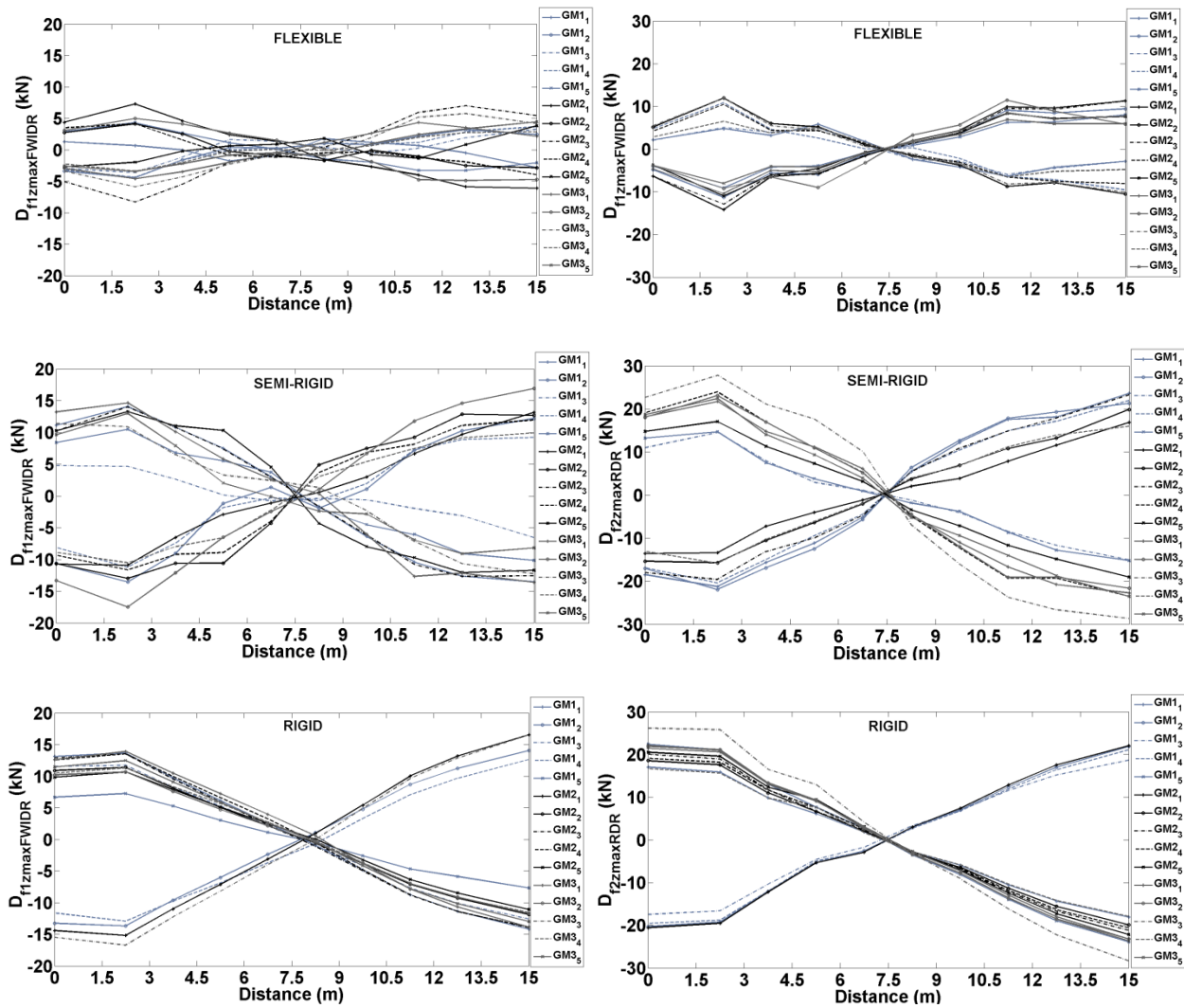


Figure 4.10: Diaphragm forces at maxFWIDR and maxRDR time; Montreal

The in-plane diaphragm forces increase with the increase in diaphragm rigidity, as expected. The semi-rigid and rigid systems exhibit the same level of forces (Table 4.13) with the exception that the rigid system exhibits a more linear force distribution while for the semi-rigid system the distribution is parabolic. For both systems the max in-plane diaphragm force is found at 1/8<sup>th</sup> locations of the diaphragm span. This phenomenon was, also, observed by Trudel-Languedoc et al. (2014), as a result of the high diaphragm modes engaging in the response of the building (Section 4.3). The cov values (defined in the Notation list in Section 4.10) presented in Table 4.14 suggest small variability in diaphragm forces for the 15GMs applied with a negligible 3%

percentage difference between the semi-rigid and the rigid system.

Table 4.13: Comparison of max diaphragm forces for the three flexibility systems at floor level at maxFWIDR and roof level at maxRDR time; Montreal

Max diaphragm forces	$D_{f1zmaxFWIDR}$		$D_{f2zmaxRDR}$	
	Semi-rigid to Flexible (%)	Semi-rigid to Rigid (%)	Semi-rigid to Flexible (%)	Semi-rigid to Rigid (%)
GM1_1	80.1	-1.0	73.1	23.5
GM1_2	67.1	-4.0	48.4	0.3
GM1_3	44.7	-91.4	60.6	-24.0
GM1_4	60.9	-15.2	50.7	4.2
GM1_5	58.6	26.6	40.2	-56.5
GM2_1	44.6	-25.9	15.6	-30.9
GM2_2	67.9	8.5	39.9	-0.4
GM2_3	40.6	0.3	44.6	9.0
GM2_4	65.3	-15.9	56.5	14.0
GM2_5	71.0	16.5	42.2	-16.4
GM3_1	68.6	4.9	54.2	-2.0
GM3_2	71.5	33.0	50.3	-0.5
GM3_3	52.0	-36.3	58.4	1.2
GM3_4	67.6	-9.4	59.0	-11.8
GM3_5	65.6	0.0	65.9	-0.3

Note: Symbol definitions are provided in Section 4.10.

Table 4.14: Variability of results between the three flexibility systems; Montreal

System Variable	Flexible (F)			Semi-rigid (S)			Rigid (R)			S-F	S-R
	$\mu$	$\sigma$	COV	$\mu$	$\sigma$	COV	$\mu$	$\sigma$	COV	$\mu$ (%)	$\mu$ (%)
$V_b/W$	0.16	0.04	0.22	0.23	0.04	0.16	0.25	0.03	0.11	30.4	-8.7
$\Delta_{v1}/h_{maxFWIDR}$	0.09	0.03	0.33	0.19	0.04	0.23	0.23	0.04	0.16	52.6	-21.1
$\Delta_{v2}^{tot}/h_{maxRDR}$	1.29	0.40	0.31	0.60	0.35	0.58	0.47	0.24	0.50	-115.0	21.7
$D_{f1zmaxFWIDR}$	4.72	1.33	0.28	12.6	2.42	0.19	13.0	2.22	0.17	62.5	-3.2
$D_{f2zmaxRDR}$	10.21	2.80	0.27	21.0	3.90	0.19	21.7	2.70	0.12	51.4	-3.3

Note: Symbol definitions are provided in Section 4.9.

#### 4.7.2. Vancouver results

Figure 4.11 presents the total base shear forces for the five representative earthquakes of the Vancouver seismic region (Section 4.4.2). As expected, there are higher force demands on the

building compared to the results of Section 4.6.1, given the higher intensity of the earthquakes applied; however, the trend of the base shear forces is similar, as for Montreal, with the forces decreasing with the increase of diaphragm flexibility.

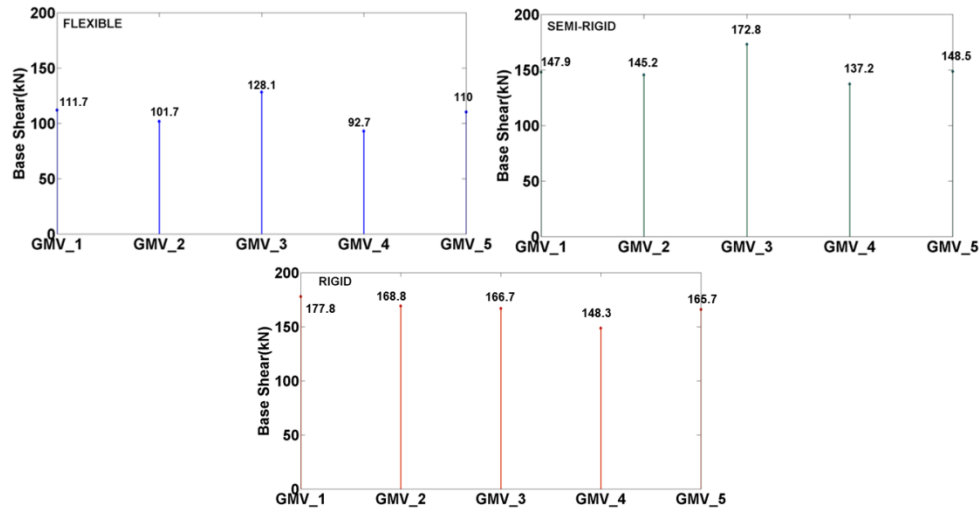


Figure 4.11: Base shear forces for the 5GMs, Vancouver, site class D

The rigid system captures the base shear forces accurately. In addition, compared to the Montreal results, there is a less pronounced reduction of base shear forces observed between the semi-rigid and flexible system (Table 4.15, around 30%). The nomenclature in the graphs is as follows: GMV<sub>i</sub>, where i is the number of the earthquake record, i.e. i=1, 2, 3, 4 or 5.

Table 4.15: Comparison of base shear values for the three flexibility systems; Vancouver

Base Shear, $V_b$	Semi-rigid to Flexible (%)	Semi-rigid to Rigid (%)
GMV_1	24.5	-20.2
GMV_2	30.0	-16.3
GMV_3	25.9	3.5
GMV_4	32.4	8.1
GMV_5	25.9	11.6

Note: Symbol definitions are provided in Section 4.10.

Figure 4.12 and Table 4.16 include the results for the storey drift ratios,  $\Delta_{v1}/h_{\max\text{FWIDR}}$  and  $\Delta^{\text{tot}}_{v2}/h_{\max\text{RDR}}$ . Similar trends are observed, as described in Section 4.6.1, encouraging further the

fact that the rigid and flexible systems do not provide accurately the response of the building. For example, there is a 60% on average underestimation of the  $\Delta_{v2}^{tot}/h_{maxRDR}$  by the rigid system.

Table 4.16: Comparison of storey drift ratios for the three flexibility systems; Vancouver

Storey drift ratios	$\Delta_{v1}/h_{maxFWIDR}$		$\Delta_{v2}^{tot}/h_{maxRDR}$	
	Semi-rigid to Flexible (%)	Semi-rigid to Rigid (%)	Semi-rigid to Flexible (%)	Semi-rigid to Rigid (%)
GMV_1	50.3	-41.8	-127.9	52.1
GMV_2	53.3	-40.8	23.3	77.8
GMV_3	36.2	0.0	-348.8	56.3
GMV_4	49.8	-15.8	-49.5	57.8
GMV_5	38.8	-28.6	-339.2	59.9

Note: Symbol definitions are provided in Section 4.10.

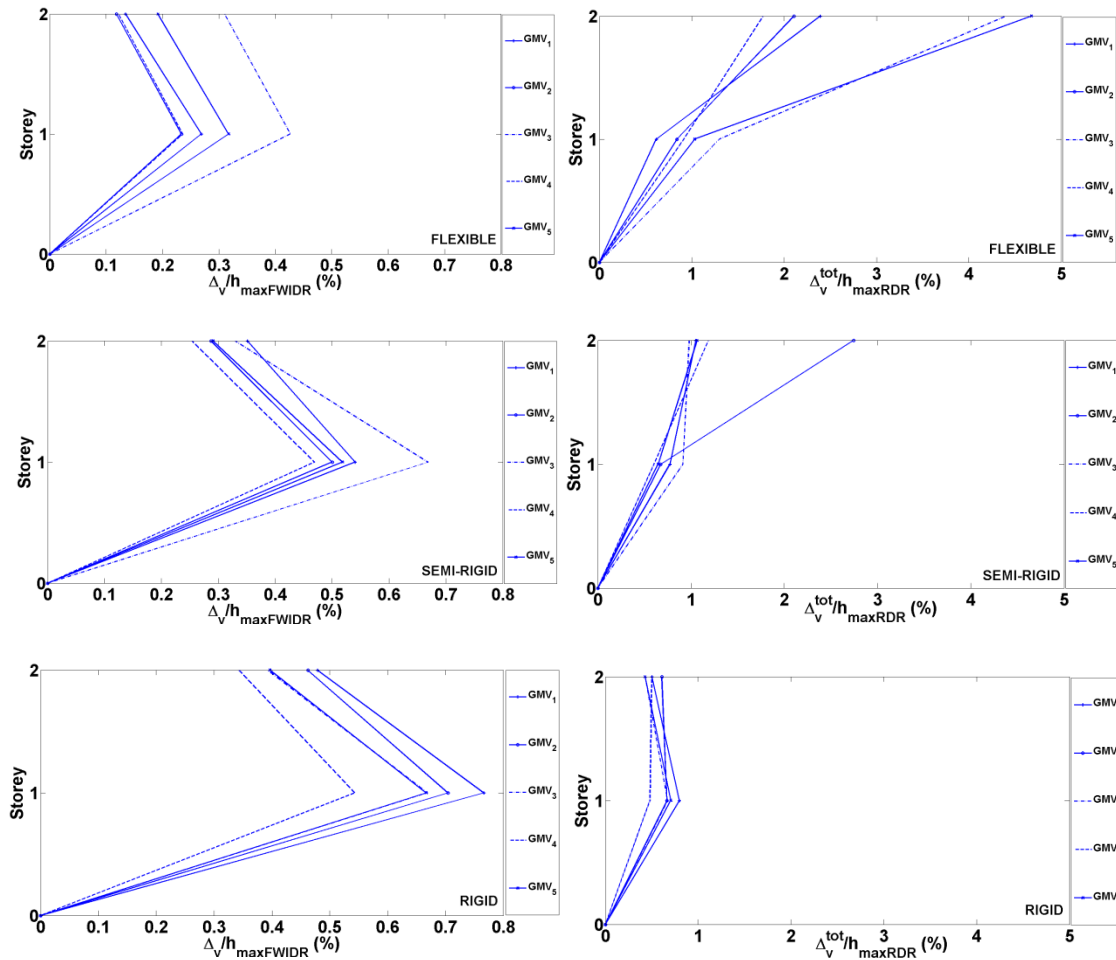


Figure 4.12: Storey drift ratios at maxFWIDR and maxRDR time; Vancouver

Figure 4.13 and Table 4.17 present the  $D_{f1zmaxFWIDR}$  and  $D_{f2zmaxRDR}$  forces distributions in order to

illustrate the change in the diaphragm forces with the increase of the diaphragm flexibility.

Table 4.17: Comparison of max diaphragm forces for the three flexibility systems; Vancouver

Max diaphragm forces	$D_{f1zmaxFWIDR}$		$D_{f2zmaxRDR}$	
	Semi-rigid to Flexible (%)	Semi-rigid to Rigid (%)	Semi-rigid to Flexible (%)	Semi-rigid to Rigid (%)
GMV_1	24.3	-31.7	49.4	-43.9
GMV_2	51.9	-107.5	46.4	-51.6
GMV_3	62.2	18.7	-5.5	-27.2
GMV_4	48.3	-46.7	51.5	-41.9
GMV_5	39.7	-48.9	37.5	-29.5

Note: Symbol definitions are provided in Section 4.10.

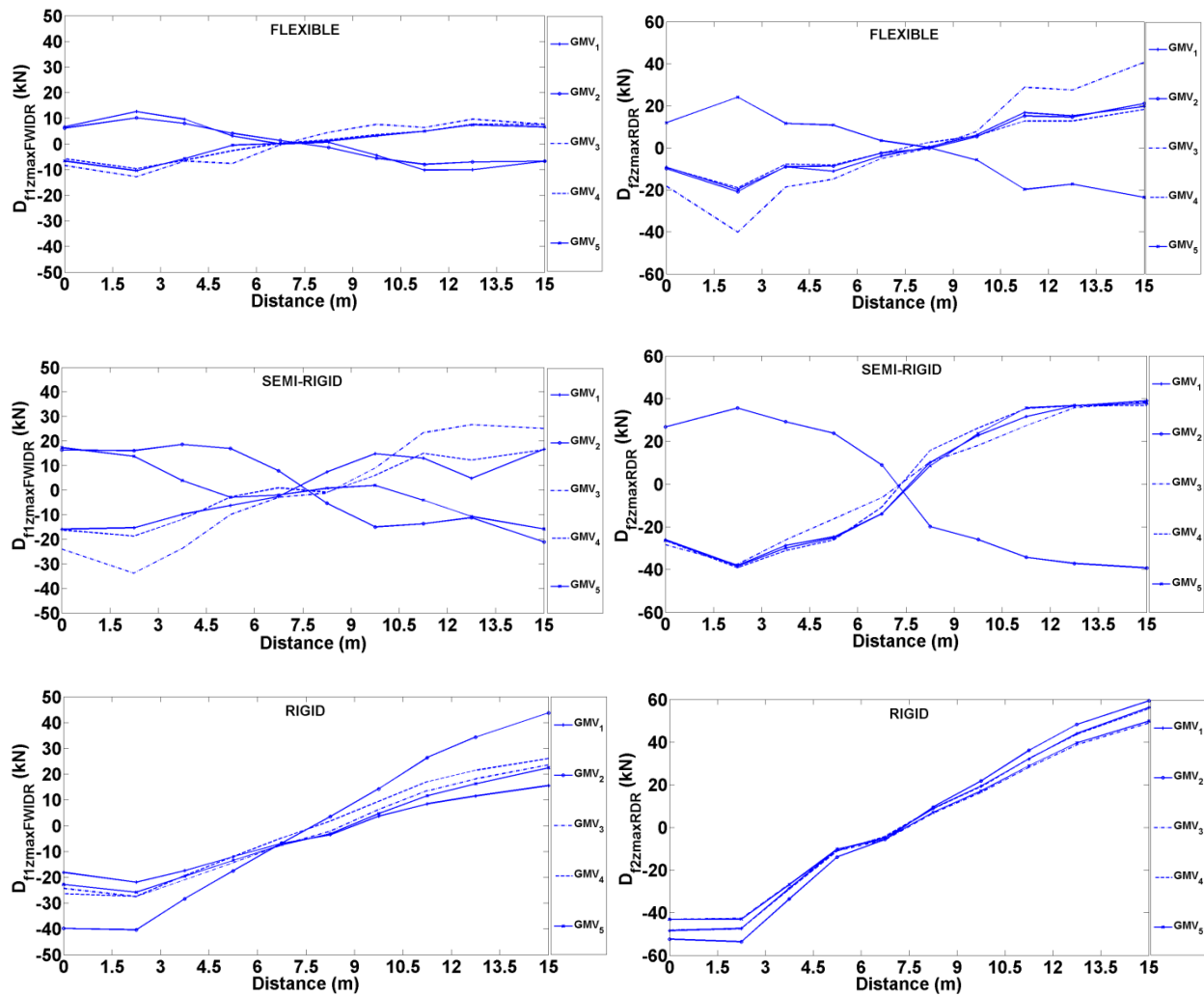


Figure 4.13: Diaphragm forces at maxFWIDR and maxRDR time; Vancouver

The diaphragm forces follow a similar pattern and distribution as described for the Montreal

earthquakes. However, for the Vancouver earthquakes, there is a more pronounced increase of the diaphragm forces of over 100% for the rigid system compared to the semi-rigid (Table 4.17).

#### **4.8- Conclusions**

In this work the effect of the diaphragm flexibility on the seismic response of a two-storey CFS building was explored by means of a parametric study incorporating three diaphragm flexibility conditions and twenty in total design level earthquakes representing seismic hazard in Montreal and Vancouver, Canada. Three flexibility systems were employed; flexible, semi-rigid and rigid.

Following are the main findings of this investigation:

- ✓ The seismic response of a low-rise, long span, narrow CFS building with perimeter wall-line non-structural components shows similarities to the seismic response observed in RWFD buildings and, thus, can be characterized as such.
- ✓ Increase in diaphragm flexibility results in fundamental period elongation and modification of the mode shape sequence and wall – to – diaphragm contribution ratio to the building oscillation.
- ✓ With the increase of diaphragm flexibility clear trends are identified for the resulting forces and drifts. The wall-line storey drifts are reduced with the increase in diaphragm flexibility, per GM cases, up to 40% and 60%; the diaphragm-wall interaction in the system is dependent on the input ground motion. The maximum storey drift is increased as expected with an underestimation from the rigid system up to 60%.
- ✓ In general, in order to obtain accurately the storey drift ratios experienced by the building, the actual diaphragm stiffness needs to be known (semi-rigid system). The resulting storey drift ratios of the flexible and rigid system showed considerable deviation from those exhibited by the semi-rigid system.

- ✓ The linear distribution assumption for the diaphragm in-plane forces is rendered questionable as a parabolic distribution is observed for the semi-rigid and flexible system.

#### 4.9- Acknowledgements

The authors greatly appreciate the papers provided by Professor Robert Tremblay for the ground motion records selection, as well as the information provided by Professor Benjamin W. Schafer and Dr. Cristopher D. Moen, Dr. Kara Peterman, Dr. Aritra Chatterjee, Dr. Jiazhen Leng and Dr. David A. Padilla-Liano related to the CFS-NEES Building. The authors are, also, grateful to the Natural Sciences and Engineering Research Council of Canada (NSERC), as well as, the American Iron and Steel Institute (AISI) and the Canadian Sheet Steel Building Institute (CSSBI) for financially supporting this research project.

#### 4.10- Notation

ADVE	= Average wall-line drift at storey level of interest (mm).
Disp <sub>fmax</sub>	= Maximum displacement at floor level in z direction (mm).
Disp <sub>rmax</sub>	= Maximum relative displacement at roof level in z direction (mm).
Df <sub>1zmaxFWIDR</sub>	= Floor diaphragm max shear forces in z direction at maxFWIDR time (kN).
Df <sub>2zmaxRDR</sub>	= Roof diaphragm shear forces in z direction at maxRDR time (kN).
Df <sub>z</sub>	= Diaphragm shear forces in z direction (kN).
MDD <sub>f</sub>	= Maximum diaphragm deflection at floor level in z direction (mm).
MDD <sub>r</sub>	= Maximum relative diaphragm deflection at roof level in z direction (mm).
M <sub>effi</sub> /M <sub>tot</sub>	= Effective mass ratio for mode i, where i=1, 2, 3, 4 (%).
M <sub>w</sub>	= Moment magnitude of ground motion record.
R	= Fault distance from station recording the ground motion (km).
SF <sub>1</sub>	= First scaling ground motions factor of linear scaling process.

$SF_2$	= Second scaling ground motions factor of linear scaling process.
$SF_V$	= Scaling factor for the Vancouver related ground motions.
$T$	= Period (sec).
$T_1$	= Fundamental period (sec).
$T_{range}$	= Period range (sec).
$T_{zi}$	= Period of building in z direction for mode I, where $i=1, 2, 3, 4$ (sec).
$V_b$	= Total base shear of building in z direction (kN).
$V_{fw}$	= Base shear of each individual shear wall in z direction (kN).
$V_x^{tot}$	= Base shear based on shear wall and gravity framing forces in x direction (kN).
$V_z^{tot}$	= Base shear based on shear wall and gravity framing forces in z direction (kN).
$meanM_w$	= Mean moment magnitude of ground motion record.
$meanR$	= Mean fault distance from station recording the ground motion (km).
$\Delta_{u1}/h$	= Wall-line storey drift ratio at floor level in x direction (%).
$\Delta_{u2}/h$	= Wall-line storey drift ratio at roof level in x direction (%).
$\Delta_{v1}/h$	= Wall-line storey drift ratio at floor level in z direction (%).
$\Delta_{v1}/h_{maxFWIDR}$	= Wall-line storey floor drift ratio in z direction at maxFWIDR time (%).
$\Delta_v/h_{maxFWIDR}$	= Wall-line storey drift ratio in z direction at maxFWIDR time (%).
$\Delta_{v2}/h$	= Wall-line storey drift ratio at roof level in z direction (%).
$\Delta_{v2}^{tot}/h_{maxRDR}$	= Max storey roof drift ratio in z direction at maxRDR time (%).
$\Delta_{v}^{tot}/h_{maxRDR}$	= Storey drift ratio in z direction at maxRDR time (%).
$\mu$	= Average of sample.
$\sigma$	= Standard deviation of sample.
$cov$	= Coefficient of variation ( $\sigma/\mu$ ).

#### 4.11- References

- AISI S100 (2016). "North American specification for the design of cold-formed steel structural members." *American Iron and Steel Institute*, Washington, DC.
- AISI S400 (2015). "North American standard for seismic design of cold-formed steel structural systems." *American Iron and Steel Institute*, Washington DC.
- Ancheta T. D., Bozorgnia Y., Chiou B., Stewart J. P., Boore D. M., Graves R., Abrahamson N. A., Campbell K. W., Idriss I. M., Youngs R. R., and Atkinson G. M. (2012). "PEER NGA-West2 Database : A Database of Ground Motions Recorded in Shallow Crustal Earthquakes in Active Tectonic." *15<sup>th</sup> World Conference on Earthquake Engineering*, Lisbon, Portugal.
- ASCE 7 (2016). "Minimum design loads for buildings and other structures." *American Society of Civil Engineers*, Reston, VA.
- Atkinson, G. M. (2009). "Earthquake time histories compatible with the 2005 National building code of Canada uniform hazard spectrum", *Canadian Journal of Civil Engineering*, 36(6), 991 – 1000.
- Baldassino N., Bernardi M., Zandonini R. and Zordan M. (2017). "Shear response of cold-formed steel floor systems." *XXVI CONGRESSO C.T.A.*, Venezia, Italy.
- Boore D. M., Thompson E. M., and Cadet H. (2011). "Regional correlations of VS30 and velocities averaged over depths less than and greater than 30 m." *Bulletin of the Seismological Society of America*, 101, 3046 – 3059, doi: 10.1785/0120110071.
- Chatterjee A. (2016). "Structural system reliability with application to light steel-framed buildings." *PhD Thesis*, Virginia Polytechnic Institute and State University, Blacksburg, Virginia.

- CSA S136 (2016). "North American specification for the design of cold-formed steel structural members.", *Canadian Standards Association*, Rexdale, Canada.
- CSI, ETABS V.7 (1999). "ETABS Users Manual, Version 7.0." *Computers and Structures, Inc.*, Berkeley, California, USA.
- CSI, SAP2000 V.14 (2009). "Linear and Non-linear Static and Dynamic Analysis and Design of Three-Dimensional Structures Basic Analysis Reference Manual". *Computers and Structures, Inc.*, Berkeley, California, USA.
- Fleischman R. B. and Farrows K. T. (2001). "Dynamic behavior of perimeter lateral-system structures with flexible diaphragms." *Earthquake Engineering and Structural Dynamics*, 30, 745 – 763.
- Florig S., Chatterjee A., O'Brien P., and Moen C. D. (2015). "Full scale tests on a cold-formed steel floor diaphragm with oriented strand board sheathing." *Report No. CE/VPI-ST-16/02*, American Iron and Steel Institute, Washington, DC.
- Humar J. and Popovski M. (2013). "Seismic response of single-storey buildings with flexible diaphragms." *Canadian Journal of Civil Engineering*, 40(9): 875-886.
- ICBO (1997). "Uniform Building Code." Whittier, CA.
- Jennings S. K. and Jain P. C. (1985). "Analytical models for low-rise buildings with flexible floor diaphragms." *Earthquake Engineering and Structural Dynamics*, 13, 225 – 241.
- Koliou M, Filiatrault A., Kelly D. J. and Lawson J. (2014). "Numerical framework for seismic collapse assessment of rigid wall-flexible diaphragm structures." *Proceedings of the 10th National Conference in Earthquake Engineering*, Earthquake Engineering Research Institute, Anchorage, AK.
- Leng J. (2015). "Simulation of cold-formed steel structures." *PhD Thesis*, Johns Hopkins

University, Baltimore, Maryland.

Liu P., Peterman K. D., Yu C., and Schafer B. W. (2012). "Cold-formed steel shear walls in ledger-framed buildings." *Annual Stability Conference*, Conference location, Grapevine, TX.

Lowes L. N. and Altoontash A. (2003). "Modeling reinforced-concrete beam-column joints subjected to cyclic loading." *Journal of Structural Engineering*, 129(12), 1686-1697.

McKenna F. (1997). "Object-oriented finite element programming: Frameworks for analysis, algorithms, and parallel computing." *PhD Thesis*, University of California, Berkeley, California.

Mortazavi P. and Humar J. (2016). "Consideration of diaphragm flexibility in the seismic design of one-storey buildings." *Engineering Structures* .127, 748 – 758.

Nakamura Y., Derakhshan H., Magenes G. and Griffith M. C. (2016). "Influence of diaphragm flexibility on seismic response of unreinforced masonry buildings. " *Journal of Earthquake Engineering*, 00, 1–26, doi: 10.1080/13632469.2016.1190799.

Nikolaidou V., Latreille P., Rogers C. A., and Lignos D. G. (2017). "Seismic performance characterization of wood-Sheathed and cold-formed steel framed floor and roof diaphragm structures." *Journal of Structural Engineering*, 144(2):04017215.

NRCC (2015). "National Building Code of Canada 2015. " *National Research Council of Canada* (NRCC), Ottawa, ON, CA.

Pathak R. and Charney F. A. (2008). "The effects of diaphragm flexibility on the seismic performance of light frame wood structures. " *The 14<sup>th</sup> World Conference on Earthquake Engineering*, Beijing, China.

Peterman K. D. (2014). "Behavior of full-scale cold-formed steel buildings under seismic

- excitations." *PhD Thesis*, Johns Hopkins University, Baltimore, MD.
- Schafer B. W., Smith B. H., Torabian S., Meimand V. and Eatherton M. R. (2018). "Modeling and performance of thin-walled steel deck in roof diaphragms under seismic demands." *8<sup>th</sup> International Conference on Thin-Walled Structures*, Lisbon, Portugal.
- Shrestha K. (2011). "Use of flexible and ductile roof diaphragms in the seismic design of single-storey steel buildings. " *PhD Thesis*, Department of Civil Engineering and Applied Mechanics, McGill University, Montréal, Canada.
- Tena-Colunga A. and Abrams D.P. (1996). "Seismic behavior of structures with flexible diaphragms. " *Journal of Structural Engineering*, American Society of Civil Engineers, 122, 439 – 445.
- Tokoro K. T., Anderson J.C. and BERTERO V. V. (2004). "Uncertainties in determining diaphragm flexibility. " *13<sup>th</sup> World Conference on Earthquake Engineering*, Vancouver, BC, paper no. 565.
- Tremblay R. and Rogers C. A. (2005). "Impact of capacity design provisions and period limits on the seismic design of low-rise steel buildings." *International Journal of Steel Structures*, 5(1), 1 – 22 .
- Tremblay R., Atkinson G. M., Bouaanani N., Daneshvar P. and Koboevic S. (2015). "Selection and scaling of ground motion time histories for seismic analysis using NBCC 2015." *11<sup>th</sup> Canadian Conference of Earthquake Engineering*, Victoria, BC, CA.
- Tremblay R. and Rogers C. A. (2017). "Canadian provisions for the seismic design of single-storey steel buildings with flexible roof diaphragms." *16<sup>th</sup> World Conference on Earthquake Engineering*, Santiago, Chile, Paper No. 2537.
- Trudel-Languedoc S., Tremblay R., Shrestha K., Rogers C. A. (2012). "Seismic force and

ductility demand on the braced bents of single-storey buildings with flexible roof diaphragms." *15<sup>th</sup> World Conference on Earthquake Engineering*, Lisbon, Portugal. Paper No. 5294.

Trudel-Languedoc S., Tremblay R., Rogers C. A. (2014). "Dynamic seismic response and design of single-storey structures with flexible steel roof deck diaphragms." *10<sup>th</sup> U.S. National Conference on Earthquake Engineering*, Earthquake Engineering Research Institute, Anchorage, U.S.A., Paper No. 387.

## **CHAPTER 5: SUMMARY AND CONCLUSIONS**

### **5.1- Overview**

The general objective of this research was to provide insight on the lateral response to seismic loading of wood sheathed / cold-formed steel (CFS) framed diaphragms to offer guidance on their design and structural detailing. Further, the intent was to improve the state of knowledge as to the influence of diaphragm flexibility on the seismic response of CFS framed buildings, comprised of structural and non-structural components. The research approach of this dissertation included both experimental and numerical work. Diaphragm configurations with various structural and non-structural components were tested under monotonic and reversed cyclic loading and, subsequently, numerically modeled in the OpenSees platform (Mckenna 1997). The diaphragm model was incorporated in a 3D numerical model of a two-storey case study CFS building following a phenomenological modeling approach. The effect of non-structural components and of diaphragm flexibility was investigated on the overall seismic response of the building by means of response history nonlinear dynamic analyses.

### **5.2- Summary and conclusions**

#### **5.2.1 Diaphragm experimental program**

An experimental program comprising nine diaphragm configurations (a total of sixteen tests) subjected to monotonic and quasi-static reversed cyclic loading was realized in the Jamieson Structures Laboratory at McGill University. The cantilever test approach was followed to characterize their general behaviour and their in-plane shear strength and stiffness. All diaphragm specimens had a 1.7:1 length-to-width aspect ratio. The structural detailing of a typical roof (lighter) and floor (heavier) CFS diaphragm was followed as the basis for the diaphragm configurations. The program was completed in two phases; Phase 1 included only structural elements, and highlighted the contribution of screw size and full-height blocking to the

diaphragm's lateral response, while Phase 2 included other types of structural details, as well as non-structural gypsum sheathing and gypcrete topping. In this dissertation, Phase 1 of the experimental program with the corresponding shear strength and stiffness values is presented in detail (four diaphragm configurations, ten tests) including the design of the test setup required to accommodate the tests (Appendix C). From Phase 2, only the results of the two diaphragm configurations with non-structural components are described; the detailed information for Phase 2 can be found in Latreille (2016).

#### **5.2.1.1 Roof configuration**

The bare steel framing of the unblocked roof configuration did not contribute to the shear resistance of the diaphragm. It was necessary for the framing to be attached to OSB sheathing panels for a shear resistance to be developed. For the OSB sheathed / CFS framed unblocked roof configuration, the main sheathing-to-framing failure modes included the desirable tilting of the screws (ductile mode) followed by the screws tearing out of or pulling through the wood. Due to the lack of blocking underneath, lift-off of the OSB panels was observed in the post-peak response of the roof specimen in the intermediate panel locations.

The addition of blocking for the OSB sheathed / CFS framed blocked roof configuration prevented the lift-off of the OSB panels and led to a secondary lateral resistance mechanism being activated in the post-peak response, where the load was resisted by the underlying steel framing by means of bending action. The resulting shear stiffness was increased by 70% accompanied by an over 100% increase in shear strength. The beneficial contribution of blocking to the lateral resistance of the diaphragm component was demonstrated.

The addition of a non-structural gypsum ceiling at the underside of the OSB sheathed/CFS framed unblocked roof configuration led to a further 60% increase of shear strength and an over 100% increase of shear stiffness. Similar failure modes for the sheathing-to-framing connections

were observed in the intermediate panel locations as observed for the reference unblocked roof configuration. Half of the gypsum panels were disconnected from the CFS framing by the end of the test due to failure of the drywall gypsum-to-framing connections. The sizable contribution of the non-structural gypsum ceiling to the diaphragm's lateral resistance was highlighted.

#### **5.2.1.2 Floor configuration**

The bare steel framing of the unblocked floor configuration exhibited negligible shear stiffness and strength. It was necessary to install the OSB sheathing panels for the diaphragm to take on in-plane load. For the tongue and groove (T&G) OSB sheathed / CFS framed floor configuration with #10 sheathing-to-framing screws, the main failure mode was shear fracture of the screws; this screw size proved to be inappropriate for the thickness of the connected steel and wood components if a ductile connection response were sought. The T&G characteristic facilitated the construction process and prevented lift-off of the OSB panels. It also allowed for a secondary resistance mechanism to be activated, which involved the contact/bearing action along the edges of the intermediate panels, once all the sheathing-to-framing screws had failed. As such, it is recommended that T&G OSB panels should be used for the roof configuration as well.

The larger #12 screw size led to a somewhat more ductile sheathing-to-framing screw connection behaviour, as shear fracture of the screws was avoided. Due to the high uplift forces in the interface between the CFS framing and the OSB sheathing, distortion of the joist flanges in sporadic locations was observed after testing. Despite the 50% increase in the diaphragm shear strength, there was no discernable effect on the shape of the overall diaphragm in-plane force versus deformation response. Given the improved sheathing-to-framing connection performance and the overall increase in shear strength of the diaphragm, #12 screws are recommended to be used for the floor configuration.

The addition of non-structural gypcrete topping increased the shear strength and stiffness by over

100%. It led to the creation of a high strength composite sheathing material (gypcrete + OSB) that increased substantially the sheathing-to-framing connection resistance; tilting of the screws was prohibited by the strong composite panel material. The in-plane tension field forces present due to the applied loading led to cracking of the gypcrete in the intermediate panel locations, where the gypcrete was acting alone (gap between panels). The considerable contribution of the non-structural gypcrete topping to the diaphragm's lateral stiffness and strength was demonstrated.

### **5.2.1.3 Design predictions**

In an effort to obtain design deflection values the shear wall and diaphragm deflection equations from the AISI S400 Standard (2015) (Eq. 2.1 and 2.2 in this thesis) were employed by adopting appropriate assumptions for their use. For the design level shear strength of the specimens, the design deflection values calculated using Eq. 2.1 and 2.2 were in agreement with the experimental values; however, these equations were not able to capture accurately the deflection at the ultimate shear strength level of the diaphragm specimens. Furthermore, relevant design shear strength values to the experimental ones could not be obtained, given that, at present, the corresponding Table F2.4-1 (Table 1.1 in this thesis) available in the AISI S400 Standard (2015) does not include design shear strength values for the case of OSB panels, and does not take into account the size of the screws as an influential parameter in the design shear strength calculations.

## **5.2.2 Numerical modeling**

### **5.2.2.1 Diaphragm subsystem**

A 2D numerical model of the diaphragm configurations tested for the experimental program was created in the OpenSees platform (McKenna 1997). It simulated the conditions of the cantilever testing approach and comprised a pair of twoNodelink elements representing the sheathing

connected to the joist framing. The hysteretic force versus deformation pinching behaviour exhibited by the diaphragm specimens, with the associated stiffness and strength degradation, was adequately captured by the Pinching4 component model (Lowe and Altoontash 2003), implemented in the twoNodelink elements and calibrated using the experimental data. Subsequently, for the purpose of incorporating semi-rigid diaphragms in 3D nonlinear numerical models of CFS buildings, a mesh element was identified from the initial 2D diaphragm model to construct the full size floor and roof assemblies of a CFS building.

#### **5.2.2.2 CFS building model**

The case study building incorporated into this research project was the CFS-NEES Building (Peterman 2014). It was the first full-scale two-storey CFS framed building tested experimentally under dynamic loading. Various construction phases were evaluated during the laboratory test program, where non-structural components were added in sequential fashion. The building featured shear walls, diaphragms and gravity walls. A simplified phenomenological numerical modeling approach was employed to simulate the building's response to seismic loading, where section properties were doubled for the gravity studs allowing the gravity stud elements to be reduced by half in the analysis.

For the diaphragm simulation, half of the floor and roof of the CFS-NEES Building were modeled in the OpenSees platform using the mesh element approach. Information provided in subsequent numerical and experimental work from Chatterjee (2016) and Florig et al. (2015) was utilized in the decision to apply a confinement factor of 1.5 to the shear stiffness of the floor and roof subsystems. This was done to represent the stiffening effect of the shear walls “confining” the movement of the diaphragm in a real CFS framed building.

The shear walls were modeled using a pair of truss elements, incorporating the Pinching4 component model, to represent the sheathing connected to the stud framing, and zerolength

spring elements to simulate the holdown/chord stud nonlinear load versus deformation response. A subpanel approach was followed, as presented by Leng (2015), that allowed for a better interaction of the shear walls with the gravity framing, and facilitated the subsequent insertion of the non-structural elements. Interior gypsum sheathing was added to the shear walls by updating the Pinching4 parameters based on the experimental work of Liu et al. (2012).

The gravity walls in the 3D model, which comprised exterior OSB and interior gypsum, were simulated using a pair of truss elements as for the shear walls and employing the subpanel approach for walls with different height-to-width ratios. The steel connections of the gravity studs to the bottom track were represented by zerolength spring elements.

The work of Padilla-Liano (2015) was relied upon for the simulation of the nonlinear force versus deformation response of diaphragm and shear wall chords, rim joists, gravity studs and horizontal members throughout the structure as nonlinear beam-column elements.

### **5.2.2.3 CFS building model verification**

The simplified modeling approach followed for the CFS-NEES Building was verified using the experimental data available from Phase 1/2a of the experimental program (Peterman 2014), where the structure comprised only structural elements. Nonlinear response history analysis was conducted subjecting the 3D building model to the Canoga Park (CNP) ground motion record of the Northridge 1994 earthquake. This was considered as a design basis earthquake (DBE, 10% probability of exceedance in 50 years) in urban Southern California in the three directions; the results obtained from the model were compared with the measured experimental data from Peterman. It was demonstrated that the 3D model, although more flexible, adequately captured the peak response of the building in terms of wall-line storey drift ratios, maximum overall displacements and total base shear forces, as well as the fundamental periods of vibration and mode shapes recorded in both directions. The increased flexibility of the building model could be

attributed to the isolated component experimental testing relied upon to implement the components' force-deformation response in the building model; during the shake table testing the CFS buildings responded as a unit receiving the loading. Further, the uniform mass distribution made for the analysis, which did not match the CFS-NEES Building in particular, but were chosen as a general assumption for the modeling of CFS buildings could have led to a more flexible response. The assumed continuous connections between the floor levels and the foundation led to an unrealistic response of the holdown when the vertical component of the CNP record was applied; further work focusing on modelling explicitly the foundation and the connection between storey levels is necessary. Nonetheless, the resulting forces and drifts obtained by subjecting the 3D building model to the x and z CNP component were in close proximity to the initial results obtained when all three components of the CNP record were considered. As such, it was decided that for the scope of this research work, only the two principal horizontal directions would be considered for the subsequent nonlinear response history dynamic analyses. After verifying the accuracy of the model, relative deformation of the floor and roof subsystem compared to the wall-line drifts in the z direction (more flexible side of building) revealed that the roof subsystem was considerably more flexible than the floor subsystem; the roof subsystem was not adequately instrumented during the CFS-NEES Building testing but, high accelerations observed on the roof mid-span offered an indication of the roof diaphragm's flexibility.

### **5.2.3 Effect of non-structural components on the seismic response of a CFS building**

The 3D building model was subjected to the CNP ground motion in the two horizontal directions by means of nonlinear response history analysis with non-structural elements being added gradually to the diaphragms and the wall-line perimeter throughout. The addition of non-structural components on the floor and roof (gycrete topping and gypsum ceiling, respectively)

did not have a substantial effect on the dynamic properties, the overall base shear forces and the maximum displacements and wall-line storey drifts of the building in the two directions. Only the roof subsystem was primarily impacted by the addition of the non-structural gypsum ceiling in the z direction, given the higher prior flexibility of the unblocked OSB sheathed roof subsystem. The added stiffness on the roof subsystem resulted in a reduction of the maximum relative displacement and a corresponding modest increase of the wall-line storey drift in the roof level in the z direction.

The most profound increase of the building's lateral stiffness occurred with the addition of interior gypsum and exterior OSB sheathing throughout the wall-lines of the building, which led to a reduction of the fundamental periods of vibration by an average of 35% and an increase in base shear forces by an average of 39%. The gravity walls and framing attained a dominant lateral load resisting role, given the vast area of gravity walls sheathing that was added compared to the equivalent shear walls sheathing area (almost twice in the South and North elevations in the x direction). Furthermore, focusing on an individual shear wall, the addition of interior gypsum sheathing in combination with the connection of a shear wall to an adjacent gravity wall resulted in an increase of the shear wall's lateral stiffness by three times the equivalent one of a shear wall with only OSB sheathing. Due to the added wall stiffness higher forces were directly applied to the wall-line of the building; as such, the shear forces transferred from the diaphragm to the walls in both directions were 40% lower than the total base shear experienced by the shear walls; this phenomenon has been highlighted as a unique feature of a particular category of buildings known as rigid wall flexible diaphragm (RWFD) buildings (Schafer et al. 2018).

#### **5.2.4 Effect of diaphragm flexibility on the seismic response of a CFS building**

Three diaphragm flexibility conditions were considered for the 3D building model, flexible, semi-rigid and rigid, in the context of a parametric study aiming to investigate the influence of

the diaphragm flexibility on the dynamic properties and seismic response of a CFS building including non-structural components throughout the wall-line perimeter. Modal analysis revealed that diaphragm flexibility modifies the fundamental period, the mode shape sequence and wall-to-diaphragm contribution ratio to the oscillation of the building. In a preliminary study, the 3D building model was subjected to the bidirectional CNP ground motion by alternating the two horizontal components of ground motion in the two directions. The preliminary response history analysis results indicated that when the building is subjected to a bidirectional ground motion the diaphragm might not be excited during the analyses due to the motion of the stiffer side of the building dominating the response. As such, twenty ground motion records were applied only in the more flexible, z direction of the CFS building representing seismic hazard in Montreal, site class C and Vancouver, site class D, in accordance with the guidelines included in the NBCC (NRCC 2015). From the results of this parametric study, clear trends for the forces and drifts were identified for the majority of the ground motions applied as the flexibility of the diaphragm increases; reduction of the base shear forces, decrease of the wall-line storey drift ratios and increase of the maximum storey drift ratio. Per ground motion case, the influence of diaphragm flexibility on the resulting force and drifts would be less or more pronounced depending on the input ground motion. Also, the linear force distribution assumed for the diaphragm subsystem was rendered questionable, given that a pronounced parabolic in-plane diaphragm force distribution was observed in the semi-rigid system with the maximum in-plane diaphragm force found at  $1/8^{\text{th}}$  locations of the diaphragm span. Overall, from the results provided by the rigid system, it is concluded that the rigid diaphragm assumption can be used to accurately and (per ground motion case) conservatively capture the base shear forces experienced by the shear walls. However, in order for accurate storey drift ratios to be obtained as experienced by the building,

the actual diaphragm flexibility needs to be known (semi-rigid system). The resulting storey drift ratios of the flexible and rigid system showed considerable deviation from those exhibited by the semi-rigid system.

### **5.3- Original contributions**

The original contributions of this dissertation are the following:

- Development of a database of shear strength and stiffness values for OSB sheathed / CFS framed floor and roof diaphragm configurations with various structural characteristics.
- Evaluation of the design guidelines for diaphragms currently available in the AISI S400 Standard (2015).
- Recommendation of a simplified phenomenological modeling approach of a 3D building model able to predict the peak seismic response of a two-storey CFS building.
- Identification of the wall-line non-structural components as substantial contributors to the lateral resistance of a two-storey CFS building compared to the diaphragm non-structural components.
- Quantification of the influence of diaphragm flexibility on the dynamic properties and seismic response of a two-storey CFS building.
- Evaluation of the rigid diaphragm condition as a valid design assumption for accurate prediction of base shear forces and storey-drifts of a two-storey CFS building.

### **5.4- Recommendations for future work**

In this dissertation the diaphragm's lateral response and its contribution to the seismic response of CFS buildings has been investigated in detail. However, there remains the need for additional research studies to develop further our knowledge of the subject, as described below:

- ✓ Diaphragm component: Further experimental and numerical work on CFS framed diaphragm subsystems is necessary for a complete shear strength and stiffness database to

become available to professional engineers. Diaphragm configurations with various span lengths and non-structural elements should be considered, as well as various boundary conditions through the use of an updated testing setup able to include the stiffening effect of the walls to the diaphragm. In addition, dynamic testing of diaphragm configurations would provide insight on their isolated period of vibration and damping ratio, enabling the development of a design procedure to be included in the AISI S400 Standard for diaphragm design in Canada, and for the further investigation of the diaphragm's response as part of a CFS building. Experimental data could be used for the diaphragm deflection equation available at present in the AISI S400 Standard (Eq. C-F2.4.3-1) to be updated, so as to accurately capture the deflection at the ultimate shear strength of the diaphragm component. Acknowledging the practical difficulties related to full-scale diaphragm experimental testing, future studies could rely, alternatively, on fastener-based numerical models to capture the nonlinear force versus deformation hysteretic response of the diaphragm component. The basis of the numerical modeling approach lies on the availability of the nonlinear force versus deformation response of the sheathing-to-framing connections, which is acquired via physical testing.

✓ CFS building model: With respect to implementing the diaphragm component in 3D nonlinear CFS building models, the explicit simulation of the diaphragm-to-shear wall connection as well as the possible coupling effect provided by interior walls and their connection to the diaphragms between storeys should be considered for future work. Experimental work is necessary for the inclusion of these elements, which could potentially add to the overall lateral stiffness of the building and of the diaphragm component itself, while improving the force transfer between shear walls and diaphragms, as the shear forces transferred would be limited by the capacity of these connections. Further, CFS beam-column members have proven to exhibit a

rather complicated nonlinear force-deformation/moment-rotation response, given that buckling modes govern their axial and flexural resistance. Padilla-Liano's work (2015) offered considerable insight as to how the response of CFS beam-column members can be simulated; however, additional laboratory testing is necessary to better simulate the nonlinear behaviour of these members including the interaction of all three buckling modes. Other numerical simulation advancements involve the explicit modeling of the connections between floors and of the foundation flexibility. With these improvements, the vertical ground motion component and the vertical load path in the building could be implemented in the response history dynamic analyses. Another parameter that needs to be explored further is the damping ratio considered for the dynamic analysis. Experimental work of the CFS-NEES Building revealed damping ratios up to 10%, which calls for further investigation of the damping ratio effect on CFS buildings. Structural assessment of various CFS archetype buildings following the FEMA P-695 method (FEMA 2009), accounting for the flexibility of the shear walls and diaphragms is required to make recommendations on seismic design parameters, such as  $R_d$ ,  $R_o$  and the building height limit while considering uncertainties and sources of variability in the seismic performance. Overall, although an effort was made to simplify the CFS building model, further simplification is necessary for the model to be, ultimately, effectively used by professional engineers. The modeling techniques presented can be used for the construction of CFS buildings with various storey heights and plan views taking into account the limitations of these structures with respect to allowable span (limitations in CFS stud spacing) and height. Finally, it is important to note that the dynamic response of CFS buildings depends on the combined action of its components, namely diaphragms, shear walls, gravity walls and non-structural finishing and their in-between connections; this should be taken into account in their design.

## LIST OF REFERENCES

- Adams J. and Halchuk S. (2003). "Fourth generation seismic hazard maps of Canada: values for over 650 Canadian localities intended for the 2005 National Building Code of Canada." Open File 4459, *Geological Survey of Canada*, Ottawa, CA.
- AISI S100 (2016). "North American specification for the design of cold-formed steel structural members." *American Iron and Steel Institute*, Washington, DC.
- AISI S400 (2015). "North American standard for seismic design of cold-formed steel structural systems." *American Iron and Steel Institute*, Washington DC.
- AISI S907 (2013). "Test standard for cantilever test method for cold-formed steel diaphragms." American Iron and Steel Institute, Washington, DC.
- Ancheta T. D., Bozorgnia Y., Chiou B., Stewart J. P., Boore D. M., Graves R., Abrahamson N. A., Campbell K. W., Idriss I. M., Youngs R. R., and Atkinson G. M. (2012). "PEER NGA-West2 Database : A Database of Ground Motions Recorded in Shallow Crustal Earthquakes in Active Tectonic." *15<sup>th</sup> World Conference on Earthquake Engineering*, Lisbon, Portugal.
- APA (2007). "Diaphragms and shear walls." *Design/Construction Guide Form No. L350A*, The Engineered Wood Association.
- ASTM A653 (2015a). "Standard specification for steel sheet, zinc-coated (galvanized) or zinc-iron alloy-coated (galvannealed) by the hot-dip process.", *American Society for Testing and Materials*, West Conshohocken, PA.
- ASTM D4442 (2015). "Standard test methods for direct moisture content measurement of wood and wood base materials.", *American Society for Testing and Materials*, West Conshohocken, PA.

- ASTM A370 (2016). "Standard test methods and definitions for mechanical testing of steel products.", *American Society for Testing and Materials*, West Conshohocken, PA.
- ASCE 7 (2016). "Minimum design loads for buildings and other structures." *American Society of Civil Engineers*, Reston, VA.
- ASTM D5764-97a (2013). "Standard Test Method for Evaluating Dowel-Bearing Strength of Wood and Wood-Based Products.", *American Society for Testing and Materials*, West Conshohocken, PA, USA.
- Atkinson, G. M. (2009). "Earthquake time histories compatible with the 2005 National building code of Canada uniform hazard spectrum", *Canadian Journal of Civil Engineering*, 36(6), 991 – 1000.
- Baldassino N., Bernardi M., Zandonini R. and Zordan M. (2017). "Shear response of cold-formed steel floor systems." *XXVI CONGRESSO C.T.A.*, Venezia, Italy.
- Bian G., Padilla-Llano D. A., J. Leng, Buonopane S. G., Moen C. D., and Schafer B. W. (2015). "OpenSees modeling of cold formed steel framed wall system." *Proceedings of 8th International Conference on Behavior of Steel Structures in Seismic Areas*, Conference location, Shanghai, China
- Boore D. M., Thompson E. M., and Cadet H. (2011). "Regional correlations of VS30 and velocities averaged over depths less than and greater than 30 m." *Bulletin of the Seismological Society of America*, 101, 3046 – 3059, doi: 10.1785/0120110071.
- Boudreault F. A., Blais C., Rogers C. A. (2007). "Seismic Force Modification Factors for Light-Gauge Steel-Frame – Wood Structural Panel Shear Walls." *Canadian Journal of Civil Engineering*, 34(1), 55 – 65.
- Bott, W. J. (2005) ".Horizontal stiffness of wood diaphragms. " *Master's thesis*, Virginia

Polytechnic Institute, Blacksburg, VA.

- Branston A. E., Boudreault F. A., Chen C. Y., and Rogers C. A. (2006). "Light-gauge steel-frame wood structural panel shear wall design method." *Canadian Journal of Civil Engineering*; (33(7)), 872-889.
- Brignola A., Pampanin S. and Podestà S. (2012). "Experimental Evaluation of the In-Plane Stiffness of Timber Diaphragms." *Earthquake Spectra* 28(4): 1687-1709.
- Building Seismic Safety Council (2009). "NEHRP recommended seismic provisions for new buildings and other structures." *Rep. No. FEMA P750*, Building Seismic Safety Council, Washington, DC.
- Buonopane S. G., Bian G., Tun T. H., and Schafer B. W. (2015). "Computationally efficient fastener-based models of cold-formed steel shear walls with wood sheathing." *Journal of Constructional Steel Research*, 110, 137-148.
- Carr A. J. (2004). "Ruaumoko - Dynamic Analysis of 2-Dimensional Inelastic Structures." Christchurch, New Zealand: University of Canterbury.
- Carr A. J. (2007). "Ruaumoko - Dynamic Analysis of 2-Dimensional Inelastic Structures." Christchurch, New Zealand: University of Canterbury.
- Carr A. J. (2008). "Ruaumoko User Manual." Christchurch, New Zealand: University of Canterbury.
- Chatterjee A. (2016). "Structural system reliability with application to light steel-framed buildings." *Ph.D. thesis*, Virginia Polytechnic Institute and State University, Blacksburg, Virginia.
- Chen C. Y. (2004). "Testing and Performance of Steel Frame / Wood Panel Shear Walls." *Master's Thesis*, Department of Civil Engineering and Applied Mechanics, McGill

University, Montreal, CA.

Chen Z., Nott A., Chui Y. H., Doudak G., Ni C., and Mohammad M. (2014). "Experimental study on the contribution of GWB to the lateral performance of wood shear walls." *World Conference on Timber Engineering*, Conference location, Quebec City, Canada.

Christovasilis I. P., Filiatrault A. and Wanitkorkul A. (2008). "Seismic testing of a full-scale wood structure on two shake tables." *14<sup>th</sup> World Conference on Earthquake Engineering*, Beijing, China.

CSA S136 (2016). "North American specification for the design of cold-formed steel structural members.", *Canadian Standards Association*, Rexdale, Canada.

CSI, ETABS V.7 (1999). "ETABS Users Manual, Version 7.0." *Computers and Structures, Inc.*, Berkeley, California, USA.

CSI, SAP2000 V.14 (2009). "Linear and Non-linear Static and Dynamic Analysis and Design of Three-Dimensional Structures Basic Analysis Reference Manual". *Computers and Structures, Inc.*, Berkeley, California, USA.

Dassault-Systems (2016). "Abaqus 2016 Online Documentation", <http://50.16.225.63/v2016/>

Dassault-Systems (2013). "ABAQUS 6.13 documentation."

Dassault-Systems (2014). "ABAQUS/Standard User's Manual, Version 6.14. " Providence, RI: Simulia.

Della Corte G., Fiorino L., and Landolfo R. (2005). "Seismic behaviour of sheathed cold-formed structures: numerical study." *Journal of Structural Engineering*, 132 (4), 558 – 569.

Dolan J. D. and Madsen B. (1992). "Monotonic and Cyclic Tests of Timber Shear Walls." *Canadian Journal of Civil Engineering*, 19(3), 415 – 422.

Dolan J. D. and Easterling W. S. (2000). "Monotonic and cyclic tests of light-frame shear walls

- with various aspect ratios and tie-down restraints." *Report No. TE-2000-001*, Virginia Polytechnic Institute and State University, Blacksburg, VA.
- FEMA (1998). "Handbook for the Seismic Evaluation of Buildings: A Prestandard FEMA-310." *Federal Emergency Management Agency*, prepared for FEMA by the American Society for Civil Engineers for FEMA, California.
- FEMA 461 (2007). "Interim protocols for determining seismic performance characteristics of structural and nonstructural components through laboratory testing." *Federal Emergency Management Agency*, Document No. FEMA 461. 2007.
- FEMA P695 (2009). "Quantification of Building Seismic Performance Factors." *Federal Emergency Management Agency*, Redwood City, CA, USA.
- Fiorino L. , Iuorio O. , Macillo V., and Landolfo R. (2012). "Performance-based design of sheathed CFS buildings in seismic area." *Thin - Walled Structures*, 61, 248–257.
- Fiorino L. Macillo V. and Landolfo R. (2017). "Shake table tests of a full-scale two-story sheathing-braced cold-formed steel building." *Engineering Structures*, Elsevier Science. ISSN 0141-0296, 151, 633–647, doi: 10.1016/j.engstruct.2017.08.056.
- Fiorino L., Shakeel S., Macillo V. and Landolfo R. (2018). "Seismic response of CFS shear walls sheathed with nailed gypsum panels: Numerical modelling." *Thin-Walled Structures*, Elsevier Science. ISSN 0263-8231, 122, 359-370, doi: 10.1016/j.tws.2017.10.028.
- Filiatrault A. and Sullivan T. (2014). "Performance-based seismic design of nonstructural building." *Earthquake Engineering and Engineering Vibration*, 13, 17 – 46.
- Fleischman R. B. and Farrows K. T. (2001). "Dynamic behavior of perimeter lateral-system structures with flexible diaphragms." *Earthquake Engineering and Structural Dynamics*, 30, 745 – 763.

- Florig S., Chatterjee A., O'Brien P., and Moen C. D. (2015). "Full scale tests on a cold-formed steel floor diaphragm with oriented strand board sheathing." *Report No. CE/VPI-ST-16/02*, American Iron and Steel Institute, Washington, DC.
- Fuentes S., Fournely E. and Bouchaïr A. (2014). "Experimental study of the in-plan stiffness of timber floor diaphragms." *European Journal of Environmental and Civil Engineering*, 18(10), 1106 – 1117, doi: 10.1080/19648189.2014.881760.
- Giancoli, D. (2009). "Physics for Scientists and Engineers with Modern Physics," Pearson Education, Inc, 4th Edition.
- Goda K., and Atkinson G. M. (2011). "Seismic performance of wood-frame house in southwestern British Columbia." *Earthquake Engineering and Structural Dynamics*, 40(8), 903 – 924.
- Halchuk S., Allen T., Adams J., and Rogers G. (2014). "Fifth generation seismic hazard model input files as proposed to produce values for the 2015 National Building Code of Canada." *Geological Survey of Canada, Open File 7576*, Ottawa, CA.
- Hopkins A. K. (2013). "Large-scale tests of seismically enhanced planar walls for residential construction." *Master's thesis*, Department of Civil Engineering, California State University, Sacramento.
- Humar J. and Popovski M. (2012). "Seismic response of single-storey buildings with flexible diaphragms." *3<sup>rd</sup> International Structural Specialty Conference*, Paper STR 1014, Edmonton, Alberta.
- Humar J. and Popovski M. (2013). "Seismic response of single-storey buildings with flexible diaphragms." *Canadian Journal of Civil Engineering*, 40(9): 875-886.
- IBC, ICC (2015). "International building code." *International Code Council, Inc.*, Washington,

- DC, 2015.
- ICBO (1997). "Uniform Building Code." Whittier, CA.
- Iuorio O., Fiorino L. and Landolfo R. (2014). "Testing CFS structures: The new school BFS in Naples." *Thin - Walled Structures*, 84, 275 – 288.
- Itani, R. Y., Polensek A. and Cheung C. K. (1988). "Characteristics of wood diaphragms: experimental and parametric studies." *Wood and Fiber Science*, 20(4), 438 – 456.
- Jennings S. K. and Jain P. C. (1985). "Analytical models for low-rise buildings with flexible floor diaphragms." *Earthquake Engineering and Structural Dynamics*, 13, 225 – 241.
- Koliou M. (2014). "Seismic analysis and design of rigid wall-flexible roof diaphragm structures." *Ph.D. thesis*, University at Buffalo, State University of New York, Buffalo, NY.
- Krawinkler H., Parisi F., Ibarra L., Ayoub A., and Medina R. (2000). "Development of a testing protocol for wood frame structures." *Report W-02 covering Task 1.3.2*, CUREE/Caltech Woodframe Project. Consortium of Universities for Research in Earthquake Engineering (CUREE), Richmond, CA.
- Lafontaine A., Chen Z., Doudak G. (M.ASCE), and Chui Y. H. (2017). "Lateral Behavior of Light Wood-Frame Shear Walls with Gypsum Wall Board." *Journal of Structural Engineering*, 143(8).
- Landolfo R., Fiorino L., Della Corte G. (2006). "Seismic behaviour of sheathed cold-formed structures: physical tests." *Journal of Structural Engineering*, 132, 570 – 81.
- Latreille P. (2016). "Characterization of wood sheathed cold-formed steel diaphragms under in plane loading (phase 2 of diaphragm research program)." *Master's thesis*, McGill University, QC, CA.
- Leng J. (2015). "Simulation of cold-formed steel structures." *Ph.D. Thesis*, Johns Hopkins

University, Baltimore, Maryland.

- Leng J., Peterman K. D., Bian G., Buonopane S. G., Schafer B. W. (2017). "Modeling seismic response of a full-scale cold-formed steel-framed building." *Engineering Structures*, 153, 146-165.
- LGSEA (1998). "Lateral Load Resisting Elements: Diaphragm Design Values." *Tech Note 558b-1*, Light Gauge Steel Engineers Association, Washington, DC, 1998.
- Liu P., Peterman K. D., Yu C., and Schafer B. W. (2012). "Cold-formed steel shear walls in ledger-framed buildings." *Annual Stability Conference*, Conference location, Grapevine, TX.
- Lowes L. N. and Altoontash A. (2003). "Modeling reinforced-concrete beam-column joints subjected to cyclic loading." *Journal of Structural Engineering*, 129(12), 1686-1697.
- Lu S. (2015). "The Influence of Gypsum Sheathing on the Lateral Resistance of Cold-formed Steel Shear Walls." *Master's thesis*, Department of Civil Engineering and Applied Mechanics, McGill University, Montreal, Qc, Canada.
- Macillo V., Fiorino L. and Landolfo R. (2017). "Seismic response of CFS shear walls sheathed with nailed gypsum panels: Experimental tests." *Thin-Walled Structures*, Elsevier Science. ISSN 0263- 8231. 120,161 – 171 . doi: 10.1016/j.tws.2017.08.022.
- Madsen R. L., Nakata N., Schafer B. W. (2011). "CFS-NEES Building Structural Design Narrative." *Research Report RR01*, access at [www.ce.jhu.edu/cfsness](http://www.ce.jhu.edu/cfsness).
- MAXXON (2016). Gyp-Crete Fire Ratings/Detail Drawings. Retrieved May 24th, 2016 from <http://www.maxxon.com/gyp-crete/drawings>.
- McKenna F. (1997). "Object-oriented finite element programming: Frameworks for analysis, algorithms, and parallel computing." *Ph.D. thesis*, University of California, Berkeley,

California.

- Moen C. D., Tao F., and Cole R. (2016). "Monotonic and cyclic backbone response of single shear cold-formed steel screw-fastened connections." *International Colloquium on Stability and Ductility of Steel Structures*, Conference location, Timisoara, Romania.
- Mortazavi P. and Humar J. (2016). "Consideration of diaphragm flexibility in the seismic design of one-storey buildings." *Engineering Structures* .127, 748 – 758.
- Nakamura Y., Derakhshan H., Magenes G. and Griffith M. C. (2016). "Influence of diaphragm flexibility on seismic response of unreinforced masonry buildings." *Journal of Earthquake Engineering*, 00, 1–26, doi: 10.1080/13632469.2016.1190799.
- NDS (1991). "National Design Specification for Wood Construction." ANSI/NFoPA, *American Forest & Paper Association*, 1991.
- NAHB Research center (1999). "Innovative residential floor construction: Horizontal diaphragm values for cold-formed steel framing." *U.S. Department of Housing and Urban Development*, Upper Marlboro, MD.
- Nikolaidou V., Latreille P., Rogers C. A., and Lignos D. G. (2015). "Characterization of CFS framed diaphragm behavior." *Report CM – 432*, American Iron and Steel Institute, Washington, DC.
- Nikolaidou V., Latreille P., Rogers C. A., and Lignos D. G. (2017). "Characterization of cold-formed steel framed/wood-sheathed floor and roof diaphragm structures." *16<sup>th</sup> World Conference on Earthquake Engineering*, Conference location, 452.
- NIST, Madsen R. L., Castle T. A., and Schafer B. W. (2016). "Seismic design of cold-formed steel lateral load resisting systems: A guide for practicing engineers." *GCR 16-917-38*, Applied Technology Council and the Consortium of Universities for Research in

- Earthquake Engineering for the National Institute of Standards and Technology, NEHRP Seismic Design Technical Brief No. 12, Gaithersburg, MD.
- NRCC (2015). "National Building Code of Canada 2015." *National Research Council of Canada*, Ottawa, ON, Canada.
- Padilla-Llano D. A, Moen C. D, Eatherton M. R. (2014) ."Cyclic axial response and energy dissipation of cold-formed steel framing members." *Thin-Walled Structures*, 78, 95-107.
- Padilla-Liano D. (2015). "A framework for cyclic simulation of thin-walled cold-formed steel members in structural systems." *Ph.D. thesis*, Virginia Polytechnic Institute and State University, Blacksburg, VA.
- Pathak R. and Charney F. A. (2008). "The effects of diaphragm flexibility on the seismic performance of light frame wood structures." *The 14<sup>th</sup> World Conference on Earthquake Engineering*, Beijing, China.
- Pan C. L. and Shan M. Y. (2011). "Monotonic shear tests of cold-formed steel wall frames with sheathing." *Thin-Walled Structures*, 49(2), 363-370.
- Piazza M., Baldessari C. and Tomasi, R. (2008). "The role of in-plane floor stiffness in the seismic behaviour of traditional buildings." *14<sup>th</sup> World Conference on Earthquake Engineering*, Beijing, China.
- Peterman K. D., Nakata N., and Schafer B. W. (2013). "Hysteretic Characterization of Cold-Formed Steel Stud-to-Sheathing Connections." *Journal of Constructional Steel Research*, 101, 254-264.
- Peterman K. D. (2014). "Behavior of full-scale cold-formed steel buildings under seismic excitations." *Ph.D. thesis*, Johns Hopkins University, Baltimore, MD.

- Peterman K. D., Stehman M. J., Madsen R. L., Buonopane S. G., Nakata N., and Schafer B. W. (2016a). "Experimental seismic response of a full-scale cold-formed steel-framed building. I: System-level response." *ASCE Journal of Structural Engineering*, 142(12): 04016127.
- Peterman K. D., Stehman M. J., Madsen R. L., Buonopane S. G., Nakata N., and Schafer B. W. (2016b). "Experimental seismic response of a full-scale cold-formed steel-framed building. II: Subsystem-level response." *ASCE Journal of Structural Engineering*, 142(12): 04016128.
- Richard N., Daudeville L., Prion H., and Lam F. (2002). "Timber shear walls with large openings: experimental and numerical prediction of the structural behaviour." *Canadian Journal of Civil Engineering*, 29, 713 – 724.
- Schafer B. W. (2010). "Review: the direct strength method of cold-formed steel member design." *Journal of Constructional Steel Research*, 64(7), 766-778.
- Schafer B.W. , Ayhan D. , Leng J., Liu P. , Padilla-Llano D. , Peterman K. D., Stehman M., Buonopane S. G. , Eatherton M., Madsen R., Manley B. , Moen C. D. , Nakata N., Rogers C. A., Yu C. (2016). "Seismic response and engineering of cold-formed steel framed buildings." *Structures*, 8, 197-212.
- Schafer B. W., Smith B. H., Torabian S., Meimand V. and Eatherton M. R. (2018). "Modeling and performance of thin-walled steel deck in roof diaphragms under seismic demands." *8<sup>th</sup> International Conference on Thin-Walled Structures*, Lisbon, Portugal.
- Serrette R. L., Nguyen H. and Hall G. (1996). "Shear wall values for light weight steel framing." *Report No. LGSRG-3-96*, Santa Clara University, Department of Civil Engineering, Santa Clara, CA, USA.

- Serrette R. L., Hall G., Matchen B., Nguyen, H. and Williams A. (1997). "Additional shear wall values for light weight steel framing." *Report No. LGSRG- 1-97*, Santa Clara University, Department of Civil Engineering, Santa Clara, CA, USA.
- Serrette R. L. and Chau K. (2003). "Estimating the response of cold-formed steel-frame shear walls." Santa Clara University, Department of Civil Engineering. Santa Clara. CA.
- Serrette R. L., Morgan K. A., and Sorhouet M. A. (2002). "Performance of cold-formed steel-framed shear walls: Alternative configurations." *Report No. LGSRG-06-02*, Santa Clara University, Department of Civil Engineering, Santa Clara, CA.
- SFA (2013). "A guide to fire and acoustic data for cold-formed steel floor, wall & roof assemblies." *Steel Framing Alliance*, Washington, DC.
- Shamim I. and Roger, C. A. (2013). "Steel sheathed / CFS framed shear walls under dynamic loading: numerical modelling and calibration," *Thin-Walled Structures*, 71, 57-71.
- Shamim I., DaBreo J., and Rogers C. A. (2013). "Dynamic testing of single-and double-story steel-sheathed cold-formed steel-framed shear walls." *Journal of Structural Engineering*, 139(5), 807-817.
- Shamim I. and Rogers C. A. (2015). "Numerical evaluation: AISI S400 steel-sheathed CFS framed shear wall seismic design method." *Thin-Walled Structures*, 95, 48–59.
- Shrestha K. (2011). "Use of flexible and ductile roof diaphragms in the seismic design of single-storey steel buildings." *Ph.D. thesis*, Department of Civil Engineering and Applied Mechanics, McGill University, Montréal, Canada.
- Simpson Strong-Tie Company Inc. (2017). "Connectors for cold-formed steel construction: S/HDU Hold-downs. ."Pleasanton, CA.
- Stewart W.G. (1987). "The seismic design of plywood sheathed shear walls." *Ph.D. thesis*,

Department of Civil Engineering, Christchurch, New Zealand.

- Swensen S., Deierlein G. G., and Miranda E. (2016). "Behavior of screw and adhesive connections to gypsum wallboard in wood and cold-formed steel-framed wallties." *Journal of Structural Engineering*, 142(4): E4015002.
- TECO (2008). "TECHTIP. Design capacities for oriented strand board."  [<www.pfsteco.com/techtips/pdf/tt\\_osbdesigncapacities>](http://www.pfsteco.com/techtips/pdf/tt_osbdesigncapacities).
- Tena-Colunga A. and Abrams D. P. (1996). "Seismic behavior of structures with flexible diaphragms." *Journal of Structural Engineering*, American Society of Civil Engineers, 122, 439 – 445.
- Tissell J. R. (1993). "Wood structural panel shear walls". *Report No. 154*, The Engineered Wood Association, American Plywood Association (APA), Tacoma, WA, USA.
- Tissell J. R. and Elliot J. R. (2004). "Plywood diaphragms." *Research Report 138*, American Plywood Association (APA), Tacoma, WA.
- Tokoro K. T., Anderson J.C. and BERTERO V. V. (2004). "Uncertainties in determining diaphragm flexibility." *13<sup>th</sup> World Conference on Earthquake Engineering*, Vancouver, BC, paper no. 565.
- Tremblay R. and Stierner S. F. (1996). "Seismic behaviour of single-storey steel structures with a flexible roof diaphragm." *Canadian Journal of Civil Engineering*, 23(1), 49 – 62.
- Tremblay R. and Rogers C. A. (2005). "Impact of capacity design provisions and period limits on the seismic design of low-rise steel buildings." *International Journal of Steel Structures*, 5(1), 1 – 22.
- Tremblay R., Atkinson G. M., Bouaanani N., Daneshvar P. and Koboevic S. (2015). "Selection and scaling of ground motion time histories for seismic analysis using NBCC 2015." *11<sup>th</sup>*

*Canadian Conference of Earthquake Engineering, Victoria, BC, CA.*

- Tremblay R. and Rogers C. A. (2017). "Canadian provisions for the seismic design of single-storey steel buildings with flexible roof diaphragms." *16<sup>th</sup> World Conference on Earthquake Engineering*, Santiago, Chile, Paper No. 2537.
- Trudel-Languedoc S., Tremblay R., Shrestha K., Rogers C. A. (2012). "Seismic force and ductility demand on the braced bents of single-storey buildings with flexible roof diaphragms." *15<sup>th</sup> World Conference on Earthquake Engineering*, Lisbon, Portugal. Paper No. 5294.
- Trudel-Languedoc S., Tremblay R., Rogers C. A. (2014). "Dynamic seismic response and design of single-storey structures with flexible steel roof deck diaphragms." *10<sup>th</sup> U.S. National Conference on Earthquake Engineering*, Earthquake Engineering Research Institute, Anchorage, U.S.A., Paper No. 387.
- Vamvatsikos D. and Cornell C. A. (2002). "Incremental Dynamic Analysis." *Earthquake Engineering and Structural Dynamics*, 31(4), 491 – 514.
- Yu C. and Li C. (2012). "Experimental investigation of cold-formed steel shear walls sheathed with steel-gypsum composite panels." *Structural Stability Research Council Annual Stability Conference*, Structural Stability Research Council (SSRC), 298 – 309.
- Zhao Y. (2002). "Cyclic performance of cold-formed steel stud shear walls." *Master's thesis*, Department of Civil Engineering and Applied Mechanics, McGill University, Montreal, CA.

## APPENDIX A: PINCHING4 PARAMETERS

### A.1- Diaphragm Specimens

Pinching4 parameters for the specimens subjected to reverse cyclic loading are presented in Table A.1 from a calibrated OpenSees 2D model of 3.51x6.1m based on the diaphragm specimen dimensions (Chapter 2).

Table A.1: Pinching4 parameters; diaphragm specimens

Specimen	P (N)	$\delta$ (m)	rDisp	rForce	uForce	gk	gd	gf	ge
<b>4-RU-C</b>			0.85	0.40	-0.20	0.90	0.01	0.20	4.6
	18163.4	0.0140				0.90	0.05	0.20	
	19941.9	0.0351				1.20	0.10	2.00	
	11836.8	0.0659				1.20	0.10	2.00	
	6596.0	0.1744				0.85	0.90	0.03	
<b>6-F#10-C</b>			0.85	0.40	-0.20	0.90	0.01	0.20	4.6
	25423.0	0.0108				0.90	0.05	0.20	
	26881.0	0.0250				1.20	0.10	2.00	
	19359.0	0.0410				1.20	0.10	2.00	
	10146.0	0.1300				0.85	0.90	0.03	
<b>8-RB-C</b>			0.70	0.60	-0.45	0.90	0.01	0.20	4.6
	36152.0	0.0180				0.90	0.05	0.20	
	47347.0	0.0570				1.20	0.10	2.00	
	19621.0	0.0610				1.20	0.10	2.00	
	14577.0	0.1570				0.50	0.50	0.04	
<b>10-F#12-C</b>			0.65	0.40	-0.30	0.90	0.01	0.20	4.6
	37318.1	0.0171				0.90	0.05	0.20	
	41808.0	0.0480				1.20	0.10	2.00	
	32245.0	0.0560				1.20	0.10	2.00	
	16327.0	0.1770				0.55	0.80	0.04	
<b>15-RGYP-C</b>			0.60	0.35	-0.25	0.90	0.01	0.20	4.6
	29271.00	0.0160				0.90	0.03	0.20	
	29738.00	0.0330				1.20	0.10	2.00	
	12886.00	0.0800				1.20	0.10	2.00	
	10029.00	0.1170				0.65	0.80	0.02	
<b>16-FCRETE-M</b>			0.65	0.40	-0.30	0.90	0.01	0.20	4.6
	71137.6	0.0189				0.90	0.05	0.20	
	86414.7	0.0489				1.20	0.10	2.00	
	55394.0	0.0611				1.20	0.10	2.00	
	32653.3	0.1629				0.55	0.80	0.04	

Similar parameters can be considered for the case of monotonic loading up to the peak point. The calibration was based on matching the total energy and the per cycle energy dissipated by the 2D model compared to the specimen during testing. A symmetrical material is assumed. For the 16-FCRETE-M specimen only the elastic stiffness was used in the model. The backbone points are presented here; similar pinching parameters could be assumed for this specimen as for the 10-F#12-C specimen.

Table A.2 contains the equivalent spring mechanics formulas for springs in parallel and in series used in order to generate Pinching4 parameters for a smaller product mesh elements, having the 3.51mx6.1m 2D diaphragm model as the reference element.

Table A.2: Formulas for Pinching4 parameters generation for a mesh element

<b>Axial stiffness, strength and deformation of the link element in the product mesh element based on the initial reference 2D diaphragm model</b>		
<p>Diaphragm Specimen 2D Model Cantilever Test Approach</p>	<p>Mesh element <math>\theta_2 &gt; \theta_1</math></p>	<p>Mesh element <math>\theta_2 &lt; \theta_1</math></p>
$\text{for } \theta_2 < \theta_1 \rightarrow K_{b2} = iK_{b1} \frac{\cos\theta_1^2}{\cos\theta_2^2}, V_{b2} = jV_{b1} \frac{\cos\theta_1}{\cos\theta_2}, \delta_{b2} = \frac{1}{i} \delta_{b1} \frac{\cos\theta_2}{\cos\theta_1}$ $\text{for } \theta_2 > \theta_1 \rightarrow K_{b2} = \frac{i}{j} K_{b1} \frac{\cos\theta_1^2}{\cos\theta_2^2}, V_{b2} = \frac{1}{j} V_{b1} \frac{\cos\theta_1}{\cos\theta_2}, \delta_{b2} = \frac{1}{i} \delta_{b1} \frac{\cos\theta_2}{\cos\theta_1}$		

**Notes:**  $\theta_1$  = initial angle of reference element (3.51x6.1m)

$\theta_2$  = angle of product mesh element

$K_{b1}$  = brace/link axial stiffness of reference element

$K_{b2}$  = brace/link axial stiffness of product mesh element

$V_{b1}$  = brace/link shear strength of reference element

$V_{b2}$  = brace/link shear strength of product mesh element

$\delta_{b1}$  = brace/link axial deformation of reference element

$\delta_{b2}$  = brace/link axial deformation of product mesh element

$i$  = number of rows

$j$  = number of pairs of braces/links per row.

## A.2- CFS-NEES Building: material properties

### A.2.1. Floor & Roof

In Table A.3 Pinching4 parameters of the 1.53x1.75m mesh element are presented, as they were inserted in the 3D OpenSees model of the CFS-NEES Building (Chapter 3) following the formulas of Table A.2.

Table A.3: Pinching4 parameters; floor & roof subsystems (No CF)

<b>Specimen</b>	<b>P (N)</b>	<b><math>\delta</math> (m)</b>	<b>rDisp</b>	<b>rForce</b>	<b>uForce</b>	<b>gk</b>	<b>gd</b>	<b>gf</b>	<b>ge</b>
<b>Floor</b>			0.85	0.40	-0.20	0.90	0.01	0.20	4.6
<b>(6-F#10-C)</b>	8389.59	0.0041				0.90	0.05	0.20	
	8870.73	0.0095				1.20	0.10	2.00	
	6388.47	0.0156				1.20	0.10	2.00	
	3348.18	0.0494				0.85	0.90	0.03	
<b>Roof</b>			0.85	0.40	-0.20	0.90	0.01	0.20	4.6
<b>(4-RU-C)</b>	5993.9	0.0053				0.90	0.05	0.20	
	6580.8	0.0133				1.20	0.10	2.00	
	3906.2	0.0250				1.20	0.10	2.00	
	2176.7	0.0663				0.85	0.90	0.03	

### A.2.2. Shear walls and gravity walls

For the shear walls and gravity walls the parameters for the Pinching4 material and the subpanel approach can be found in Leng (2015).

### A.2.3. Gravity elements (Studs, Chords, Rim joists, walls)

In Table A.4 the Pinching4 parameters used for the gravity elements are presented based on the work of Padilla-Liano (Padilla-Liano 2015). Tables 7.3, 7.7, 7.8 and 7.9 of Padilla-Liano's thesis contain the formulas used in order to derive the parameters for the chord studs of the shear walls, the chords and rim joists of the diaphragms as well as the double gravity studs and single horizontal framing members used to construct the model.

Table A.4: Pinching4 parameters; gravity elements (+/-)

Specimen	P (N)	$\epsilon$ (mm/mm)	rDisp	rForce	uForce	gk	gd	gf	ge
<b>Double 600s162-54</b>	261490/-115870	0.00177/-0.00092				0.0	0.0	0.0	1.7
	284030/-133340	0.00238/-0.00130	0.381/ 0.419	0.892/ 0.457	0.210 /-0.022	0.51	0.0	0.43	
	293550/-74650	0.01357/-0.00250				0.0	0.0	0.0	
	218410/-39840	0.01696/-0.00861				0.13	0.0	0.57	
<b>Double 600s162-33</b>	100960/-36530	0.00117/-0.00055				1.0	1.0	1.0	
	109660/-42100	0.00157/-0.00083	0.381/ 0.419	0.892/ 0.457	0.210 /-0.022	0.0	0.0	0.0	1.7
	113330/-22410	0.00895/-0.00160				0.51	0.0	0.43	
	84320/-11310	0.01119/-0.00566				0.0	0.0	0.0	
<b>1200t200- 97</b>	324120/-117280	0.00177/-0.00083				0.13	0.0	0.57	
	352060/-135150	0.00238/-0.00125	0.381/ 0.419	0.892/ 0.457	0.210 /-0.022	0.45	0.0	0.43	
	363860/-71950	0.01357/-0.00243				0.0	0.0	0.0	
	27072/-36300	0.01696/-0.00858				0.08	0.0	0.57	
<b>1200s250- 97</b>	411330/-165470	0.00177/-0.00088				1.0	1.0	1.0	
	446780/-190660	0.00238/-0.00127	0.381/ 0.419	0.892/ 0.457	0.210 /-0.022	0.0	0.0	0.0	2.1
	461760/-104150	0.01357/-0.00247				0.48	0.0	0.43	
	343560/-54120	0.01696/-0.00859				0.1	0.0	0.57	
<b>1200t200- 68</b>	262320/-71670	0.00177/-0.00072				1.0	1.0	1.0	
	284930/-82240	0.00238/-0.00120	0.381/ 0.419	0.892/ 0.457	0.210 /-0.022	0.0	0.0	0.0	1.0
	294480/-41090	0.01357/-0.00237				0.39	0.0	0.43	
	219100/-19180	0.01696/-0.00857				0.0	0.0	0.0	
<b>1200s200- 54</b>	221350/-57140	0.00177/-0.00069				0.0	0.0	0.0	0.9
	240430/-65460	0.00238/-0.00120	0.381/ 0.419	0.892/ 0.457	0.210 /-0.022	0.38	0.0	0.43	
	248480/-32310	0.01357/-0.00236				0.0	0.0	0.0	
	184880/-14850	0.01696/-0.00856				0.03	0.0	0.57	
<b>600t150-54</b>	118440/-44880	0.00177/-0.00085				1.0	1.0	1.0	
	128650/-51720	0.00238/-0.00126	0.381/ 0.419	0.892/ 0.457	0.210 /-0.022	0.46	0.0	0.43	
	132960/-27840	0.01357/-0.00244				0.0	0.0	0.0	
	98930/-14230	0.01696/-0.00858				0.09	0.0	0.57	
					1.0	1.0	1.0	1.8	

## APPENDIX B: FASTENER FAILURE MODES (EXPERIMENTAL PROGRAM)

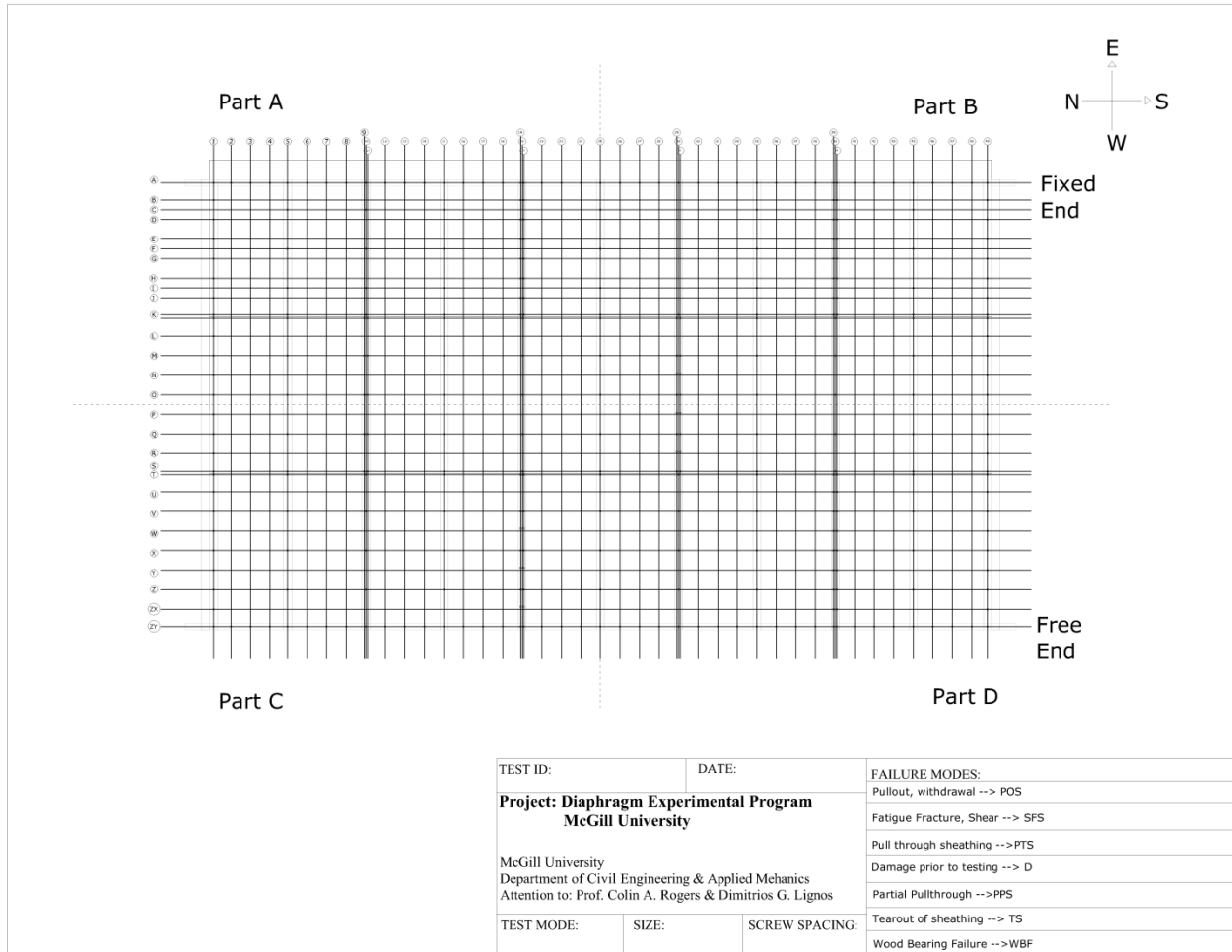
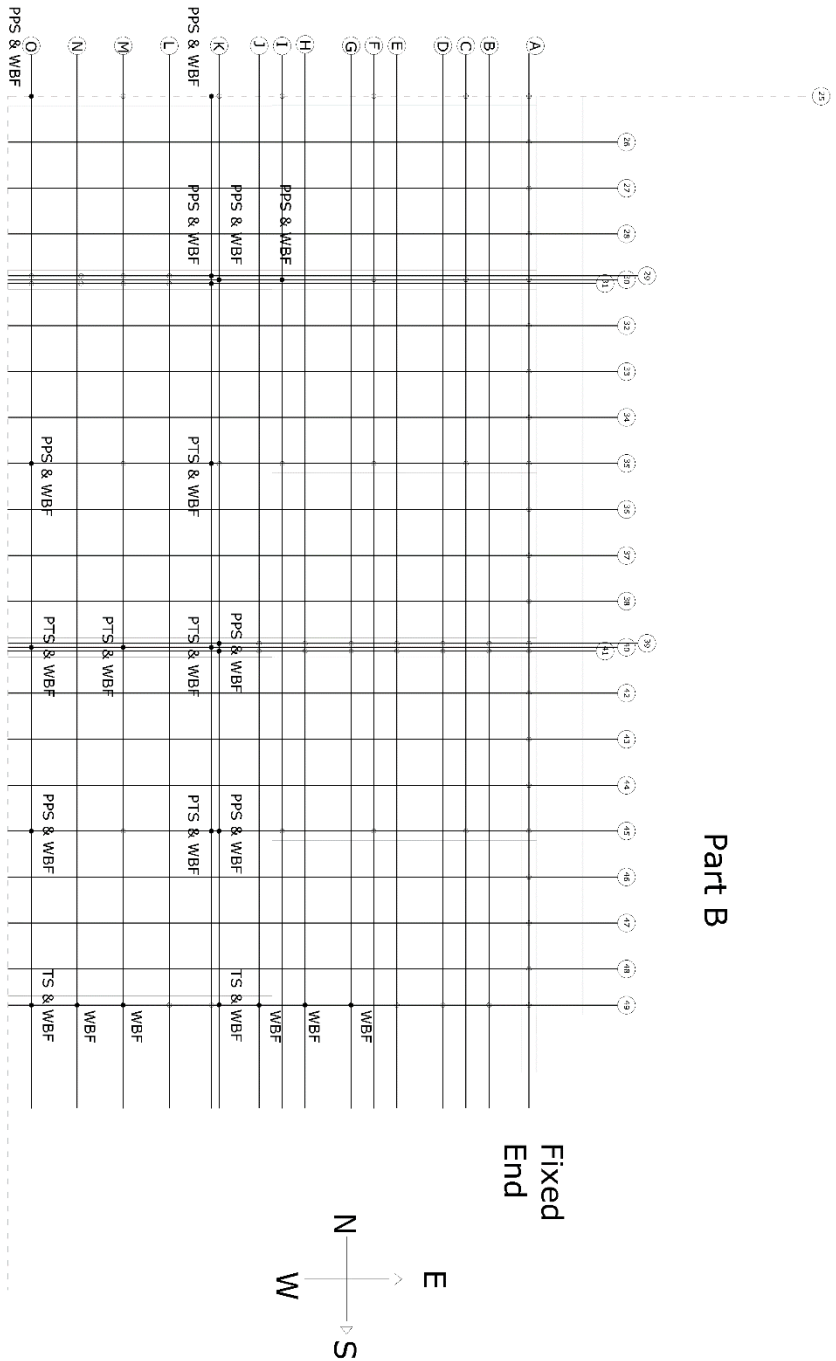


Figure B.1: General template; sheathing-to-framing screw location

Following are the failure modes of the sheathing-to-framing screws, as recorded during testing of the diaphragm specimens. For each diaphragm specimen failure modes are presented separately in four one-quarter parts of the specimen (Part A, B, C and D, Figure A.1) for purposes of clarity.



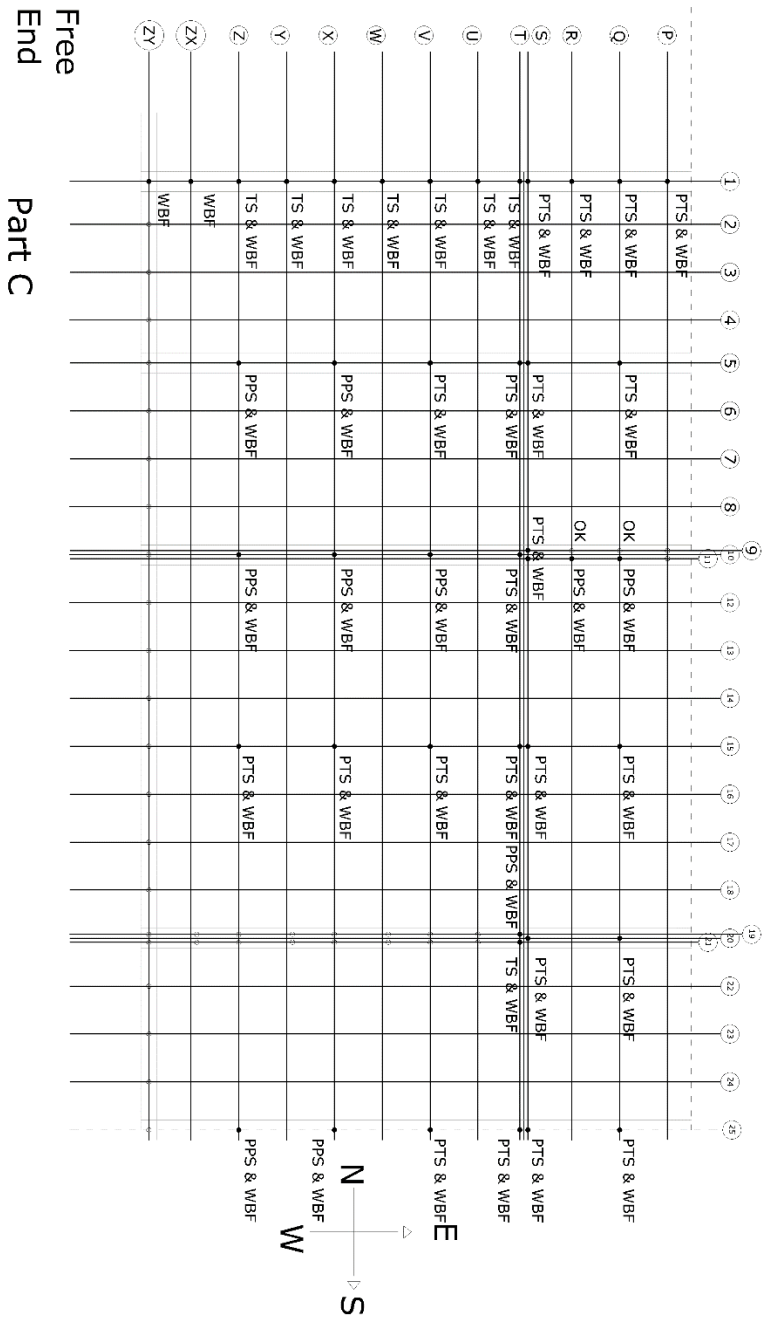
## Part B



Note: If failure mode not indicated then the connection at that location has not failed

TEST ID: 3-RU-M	DATE: 04 June 2015	FAILURE MODES:
<b>Project: Diaphragm Experimental Program</b>		Pullout, withdrawal --> POS
<b>McGill University</b>		Fatigue Fracture, Shear --> SFS
McGill University Department of Civil Engineering & Applied Mechanics Attention to: Prof. Colin A. Rogers & Dimitrios G. Lignos		Pull through sheathing --> PTS
Damage prior to testing --> D		Partial Pullthrough --> PPS
TEST MODE: Monotonic	SIZE: 3.66x6.1m	Tearout of sheathing --> TS
	SCREW SPACING: 150/300mm	Wood Bearing Failure --> WBF

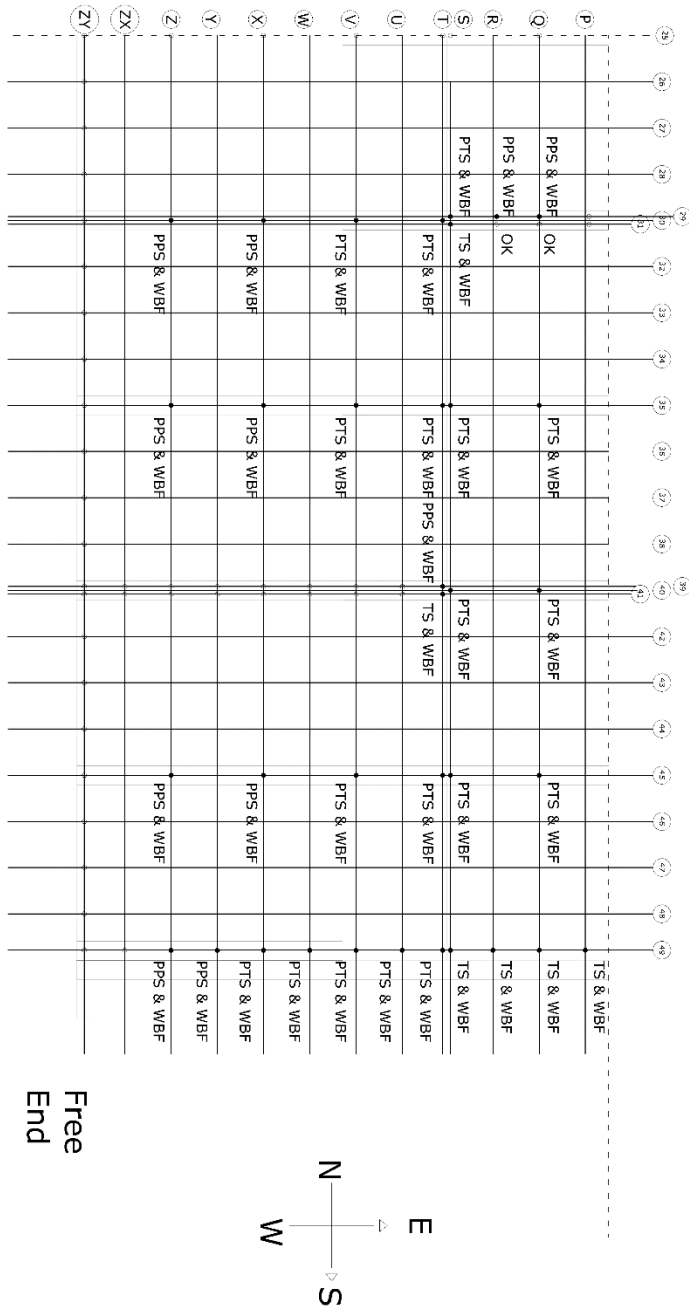
Figure B.3: 3-RU-M-B, Screw failure modes



Note: If failure mode not indicated then the connection at that location has not failed

TEST ID: 3-RU-M	DATE: 04 June 2015	FAILURE MODES:
<b>Project: Diaphragm Experimental Program</b> <b>McGill University</b>		Pullout, withdrawal --> POS
McGill University Department of Civil Engineering & Applied Mechanics Attention to: Prof. Colin A. Rogers & Dimitrios G. Lignos		Fatigue Fracture, Shear --> SFS
TEST MODE: Monotonic	SIZE: 3.6x6.1m	Pull through sheathing --> PTS
	SCREW SPACING: 150/300mm	Damage prior to testing --> D
		Partial Pullthrough --> PPS
		Tearout of sheathing --> TS
		Wood Bearing Failure --> WBF

Figure B.4: 3-RU-M-C, Screw failure modes



Note: If failure mode not indicated then the connection at that location has not failed

TEST ID: 3-RU-M

DATE: 04 June 2015

FAILURE MODES:

Project: Diaphragm Experimental Program

McGill University

- Pullout, withdrawal --> POS
- Fatigue Fracture, Shear --> SFS
- Pull through sheathing --> PTS
- Damage prior to testing --> D
- Partial Pullthrough --> PPS
- Tearout of sheathing --> TS
- Wood Bearing Failure --> WBF

McGill University  
 Department of Civil Engineering & Applied Mechanics  
 Attention to: Prof. Colin A. Rogers & Dimitrios G. Liganos

TEST MODE: Monotonic

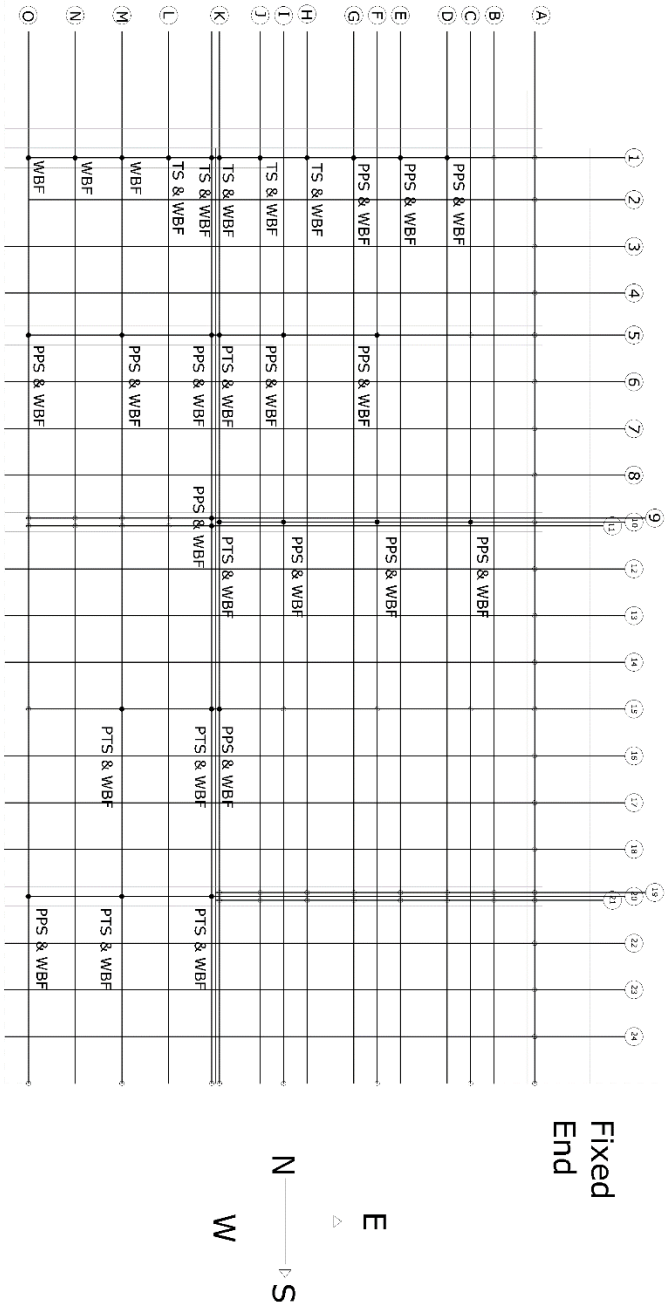
SIZE: 3.66x6.1m

SCREW SPACING: 150/300mm

Failure modes: Pullout, withdrawal --> POS; Fatigue Fracture, Shear --> SFS; Pull through sheathing --> PTS; Damage prior to testing --> D; Partial Pullthrough --> PPS; Tearout of sheathing --> TS; Wood Bearing Failure --> WBF

Figure B.5: 3-RU-M-D, Screw failure modes

# Part A

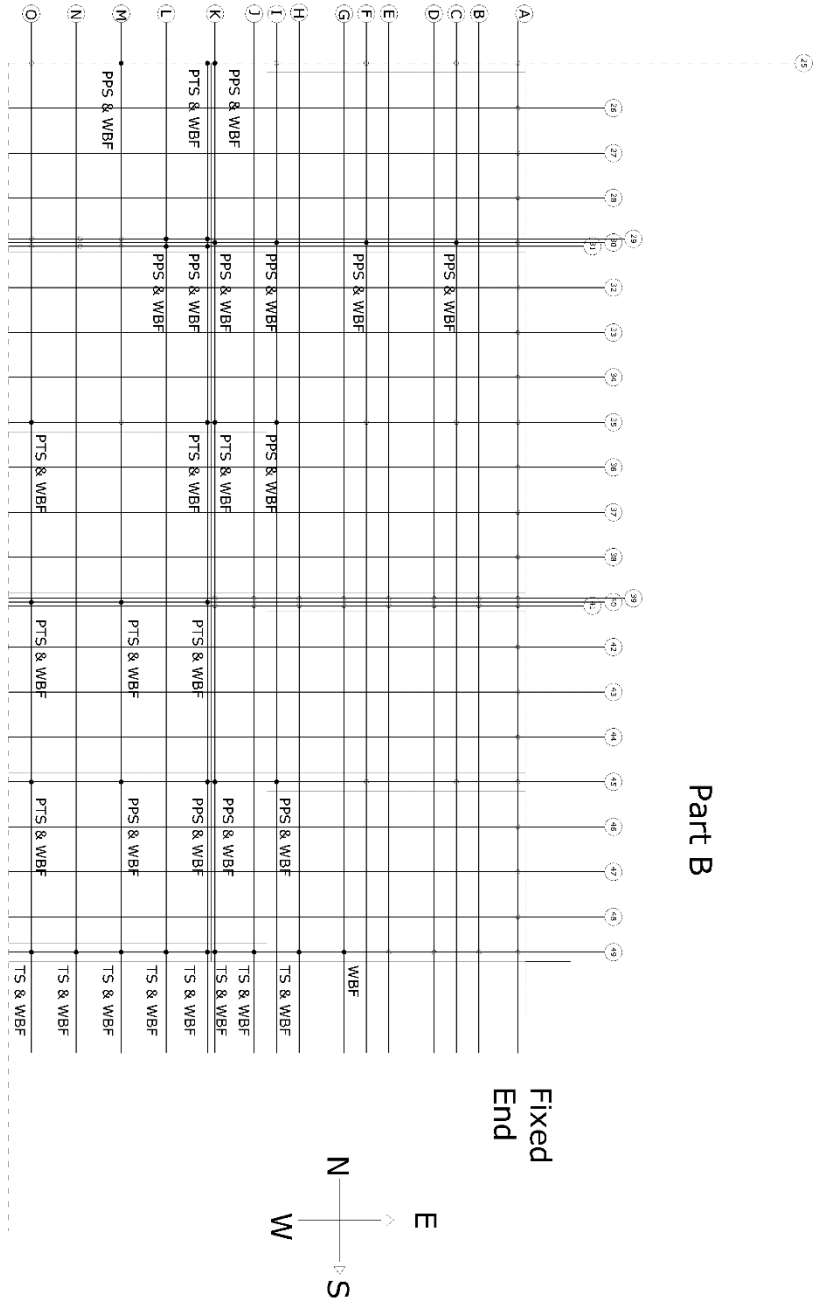


Note: If failure mode not indicated then the connection at that location has not failed

TEST ID: 4-RU-C	DATE: 09 June 2015	FAILURE MODES: Pullout, withdrawal --> POS
<b>Project: Diaphragm Experimental Program</b> <b>McGill University</b>		
McGill University Department of Civil Engineering & Applied Mechanics Attention to: Prof. Colin A. Rogers & Dimitrios G. Lignos		
TEST MODE: Cyclic	SIZE: 3.66x6.1m	SCREW SPACING: 150/300mm
		Tearout of sheathing --> TS
		Wood Bearing Failure --> WBF
		Fatigue Fracture, Shear --> SFS
		Pull through sheathing --> PTS
		Damage prior to testing --> D
		Partial Pullthrough --> PPS

Figure B.6: 4-RU-C-A, Screw failure modes

Part B



Note: If failure mode not indicated then the connection at that location has not failed

TEST ID: 4-RU-C      DATE: 09 June 2015

FAILURE MODES:  
Pullout, withdrawal --> POS

**Project: Diaphragm Experimental Program**  
**McGill University**

McGill University  
Department of Civil Engineering & Applied Mechanics  
Attention to: Prof. Colin A. Rogers & Dimitrios G. Lignos

Fatigue Fracture --> SFS  
Pull through sheathing --> PTS  
Damage prior to testing --> D

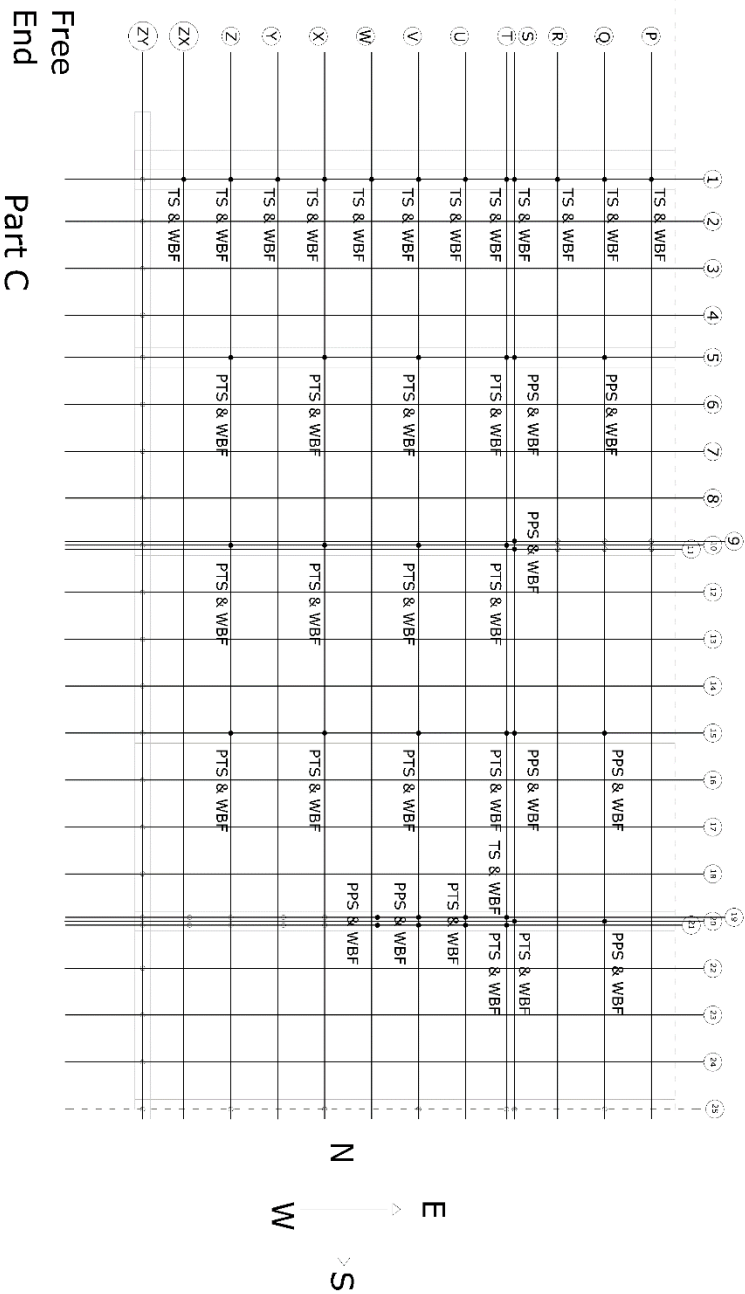
TEST MODE:  
Cyclic

SIZE:  
3.66x6.1m

SCREW SPACING:  
150/300mm

Tearout of sheathing --> TS  
Wood Bearing Failure --> WBF

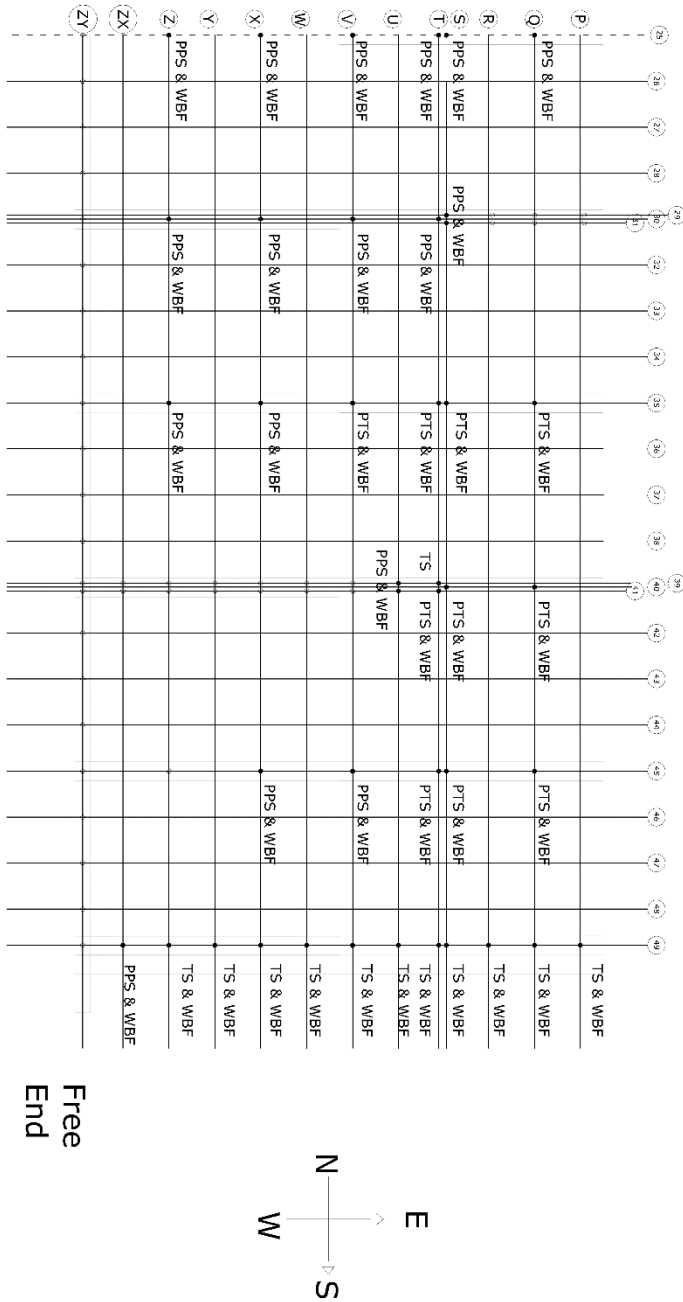
Figure B.7: 4-RU-C-B, Screw failure modes



Note: If failure mode not indicated then the connection at that location has not failed

TEST ID: 4-RU-C	DATE: 09 June 2015	FAILURE MODES:
Project: Diaphragm Experimental Program McGill University		Pullout, withdrawal --> POS
McGill University Department of Civil Engineering & Applied Mechanics Attention to: Prof. Colin A. Rogers & Dimitrios G. Lignos		Fatigue Fracture, Shear --> SFS
		Pull through sheathing --> PTS
		Damage prior to testing --> D
		Partial Pullthrough --> PPS
		Tearout of sheathing --> TS
TEST MODE: Cyclic	SIZE: 3.66x6.1m	SCREW SPACING: 150/300mm
		Wood Bearing Failure --> WBF

Figure B.8: 4-RU-C-C, Screw failure modes



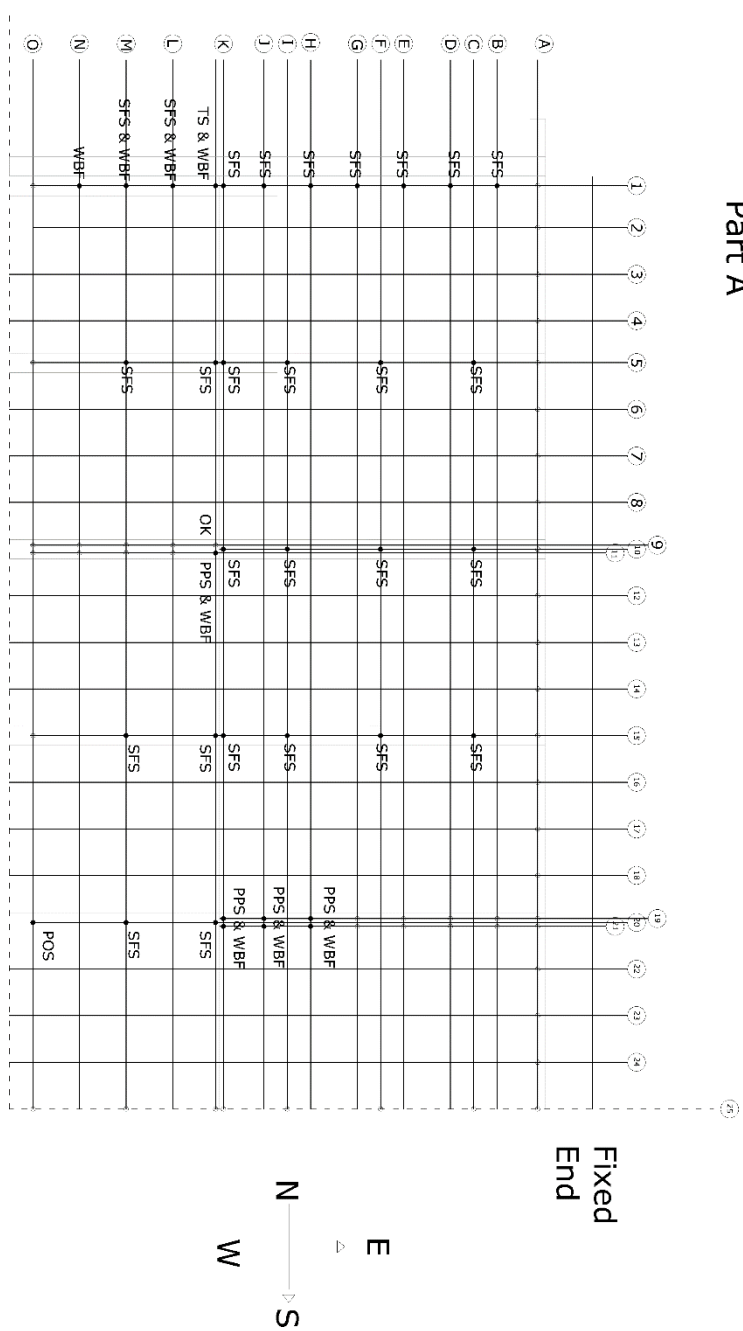
Note: If failure mode not indicated then the connection at that location has not failed

**Part D**

TEST ID: 4-RU-C	DATE: 09 June 2015	FAILURE MODES:
Project: Diaphragm Experimental Program		Pullout, withdrawal --> POS
McGill University		Fatigue Fracture, Shear --> SFS
McGill University		Pull through sheathing --> PTS
Department of Civil Engineering & Applied Mechanics		Damage prior to testing --> D
Attention to: Prof. Colin A. Rogers & Dimitrios G. Lignos		Partial Pullthrough --> PPS
TEST MODE: Cyclic	SIZE: 3,66x6,1m	Tearout of sheathing --> TS
	SCREW SPACING: 150/300mm	Wood Bearing Failure --> WBF

Figure B.9: 4-RU-C-D, Screw failure modes

# Part A

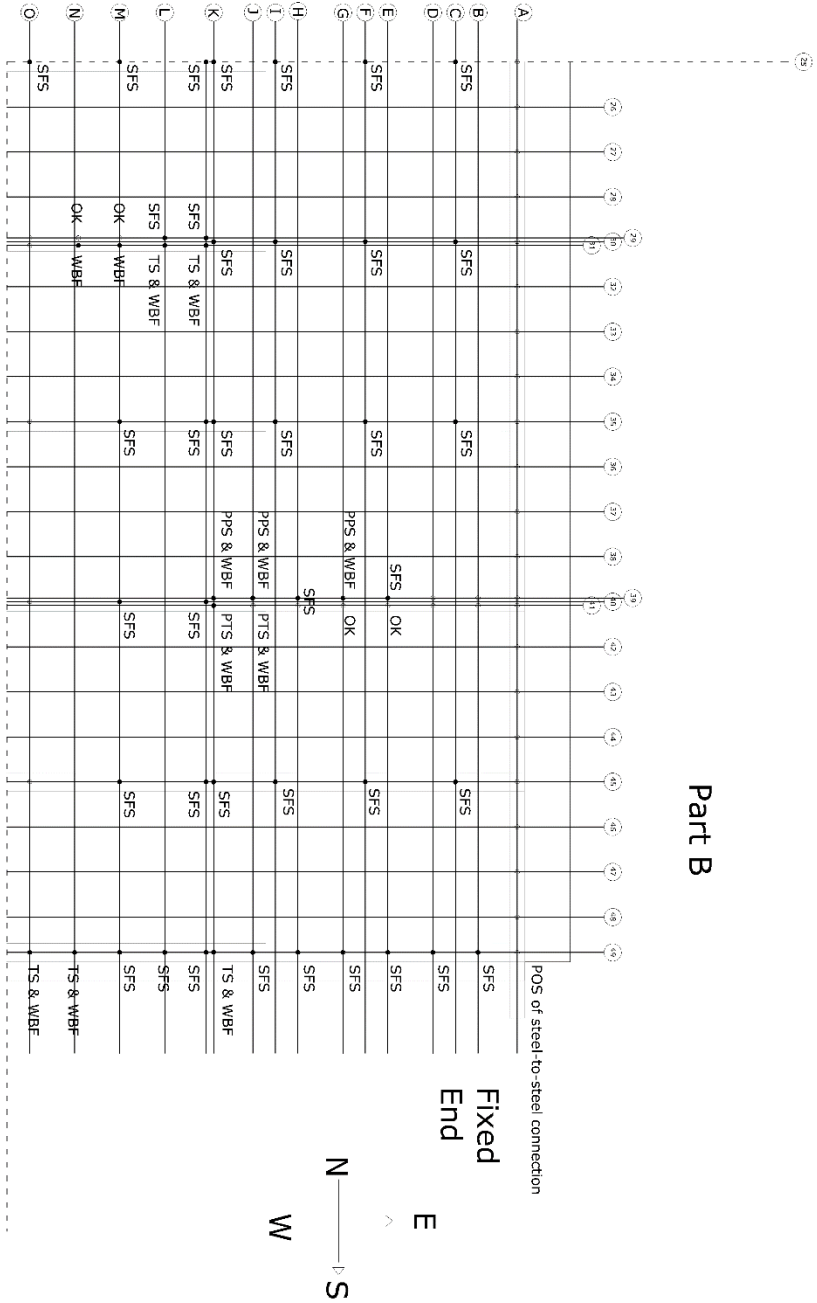


Note: If failure mode not indicated then the connection at that location has not failed

TEST ID: 5-F#10-M	DATE: 12 June 2015	FAILURE MODES:
<b>Project: Diaphragm Experimental Program</b>		Pullout, withdrawal --> POS
<b>McGill University</b>		Fatigue Fracture, Shear --> SFS
McGill University Department of Civil Engineering & Applied Mechanics Attention to: Prof. Colin A. Rogers & Dimitrios G. Lignos		Pull through sheathing --> PTS Damage prior to testing --> D
TEST MODE: Monotonic	SIZE: 3.66x6.1m	Partial Pullthrough --> PPS
	SCREW SPACING: 150/300mm	Tearout of sheathing --> TS
		Wood Bearing Failure --> WBF

Figure B.10: 5-F#10-M-A, Screw failure modes

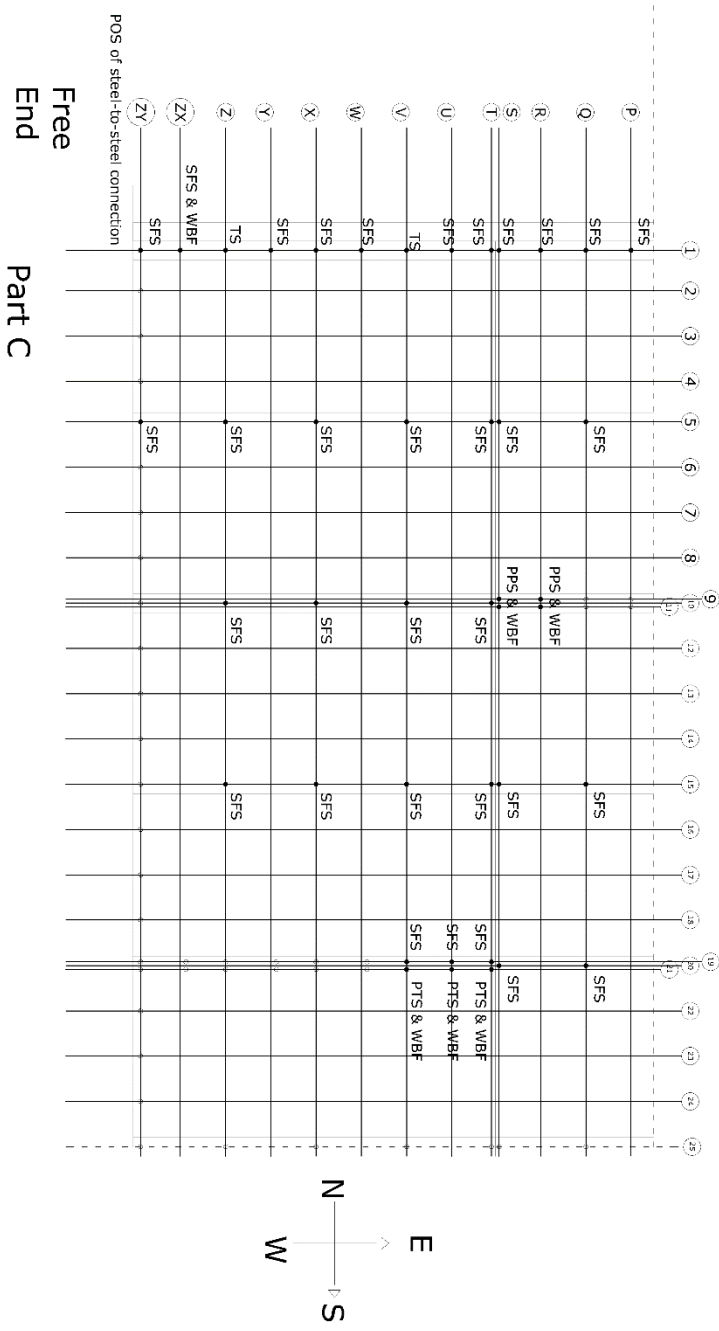
## Part B



Note: If failure mode not indicated then the connection at that location has not failed

TEST ID: 5-F#10-M	DATE: 12 June 2015	FAILURE MODES:
<b>Project: Diaphragm Experimental Program</b> McGill University		Pullout, withdrawal --> POS
McGill University Department of Civil Engineering & Applied Mechanics Attention to: Prof. Colin A. Rogers & Dimitrios G. Lignos		Fatigue Fracture, Shear --> SFS
		Pull through sheathing --> PTS
		Damage prior to testing --> D
		Partial Pullthrough --> PPS
		Tearout of sheathing --> TS
TEST MODE: Monotonic	SIZE: 3,66x6,1m	Wood Bearing Failure --> WBF
	SCREW SPACING: 150/300mm	

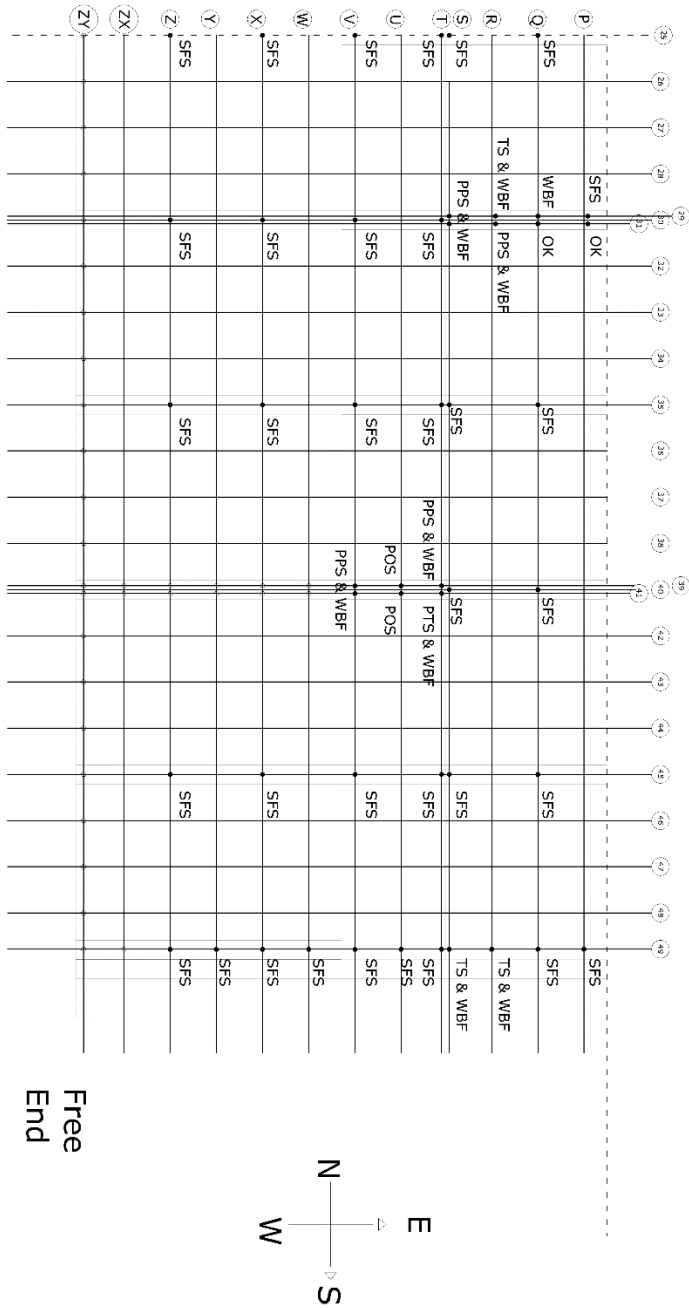
Figure B.11: 5-F#10-M-B, Screw failure modes



Note: If failure mode not indicated then the connection at that location has not failed

TEST ID: 5-F#10-M	DATE: 12 June 2015	FAILURE MODES:
<b>Project: Diaphragm Experimental Program</b>		Pullout, withdrawal --> POS
<b>McGill University</b>		Fatigue Fracture, Shear --> SFS
McGill University Department of Civil Engineering & Applied Mechanics Attention to: Prof. Colin A. Rogers & Dimitrios G. Lignos		Pull through sheathing --> PTS
TEST MODE: Monotonic	SIZE: 3.66x6.1m	Damage prior to testing --> D
	SCREW SPACING: 150/300mm	Partial Pullthrough --> PPS
		Tearout of sheathing --> TS
		Wood Bearing Failure --> WBF

Figure B.12: 5-F#10-M-C, Screw failure modes



Note: If failure mode not indicated then the connection at that location has not failed

TEST ID: 5-F#10-M      DATE: 12 June 2015      FAILURE MODES:

Project: Diaphragm Experimental Program  
 McGill University

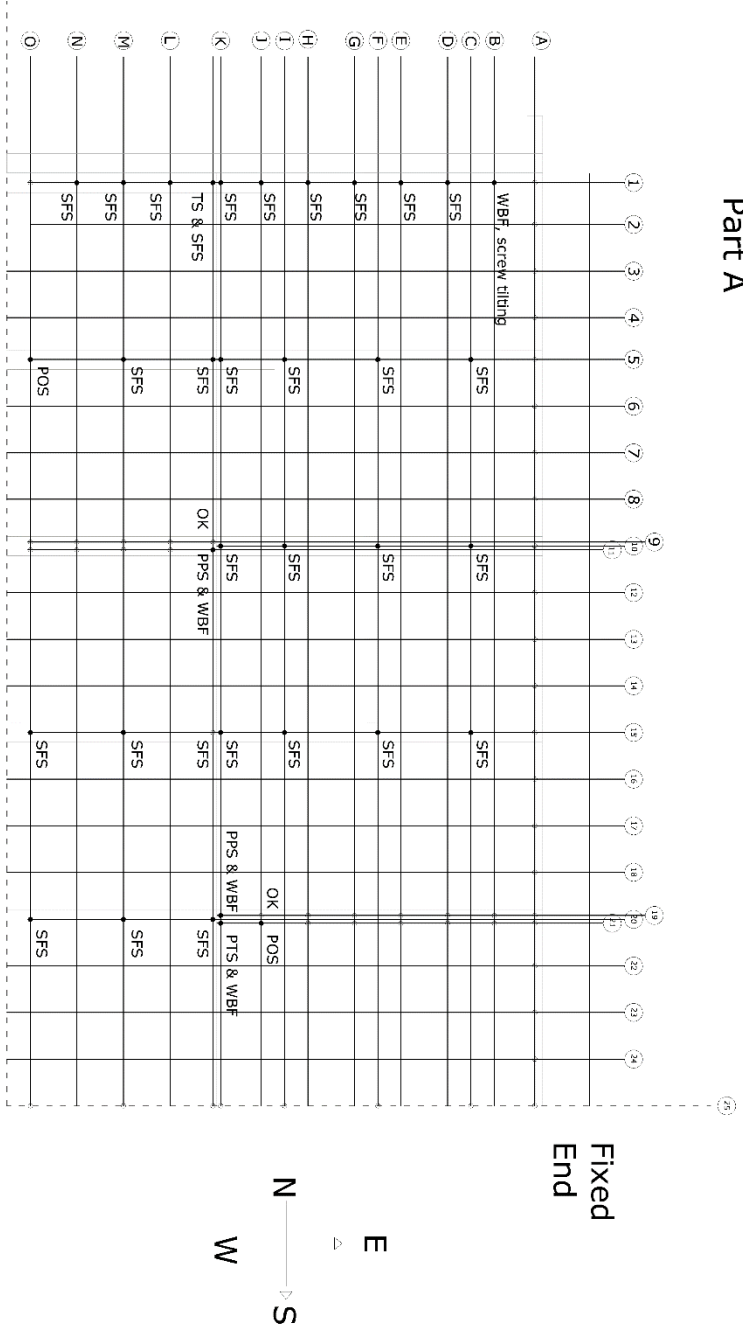
McGill University  
 Department of Civil Engineering & Applied Mechanics  
 Attention to: Prof. Colin A. Rogers & Dimitrios G. Lignos

TEST MODE: Monotonic      SIZE: 3.66x6.1m      SCREW SPACING: 150/300mm

FAILURE MODES:  
 Pullout, withdrawal --> POS  
 Fatigue Fracture, Shear --> SFS  
 Pull through sheathing --> PTS  
 Damage prior to testing --> D  
 Partial Pullthrough --> PPS  
 Tearout of sheathing --> TS  
 Wood Bearing Failure --> WBF

Figure B.13: 5-F#10-M-D, Screw failure modes

Part A

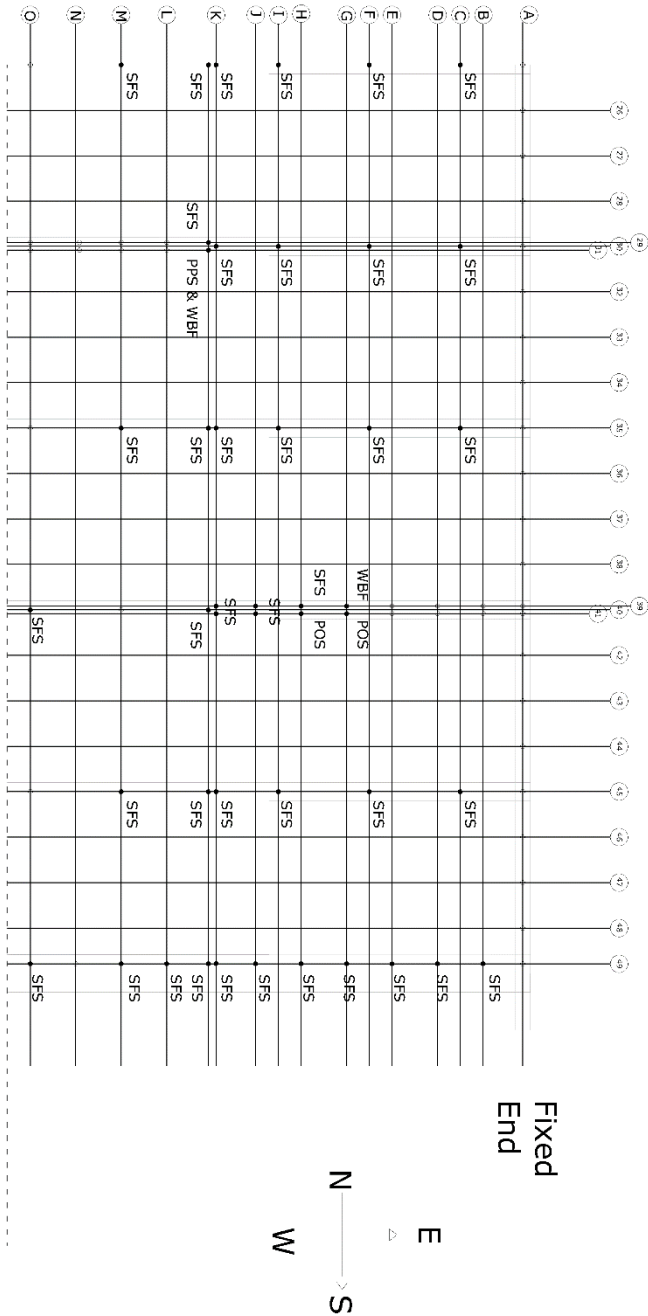


Note: If failure mode not indicated then the connection at that location has not failed

TEST ID: 6-F#10-C	DATE: 17 June 2015	FAILURE MODES:
<b>Project: Diaphragm Experimental Program</b>		Pullout, withdrawal --> POS
<b>McGill University</b>		Fatigue Fracture, Shear --> SFS
McGill University Department of Civil Engineering & Applied Mechanics Attention to: Prof. Colin A. Rogers & Dimitrios G. Lignos		Pull through sheathing --> PTS
		Damage prior to testing --> D
		Partial Pullthrough --> PPS
TEST MODE: Cyclic	SIZE: 3.66x6.1m	Tearout of sheathing --> TS
	SCREW SPACING: 150/300mm	Wood Bearing Failure --> WBF

Figure B.14: 6-F#10-C-A, Screw failure modes

Part B



Note: If failure mode not indicated then the connection at that location has not failed

TEST ID: 6-F#10-C

DATE: 17 June 2015

FAILURE MODES:

Project: Diaphragm Experimental Program

McGill University

McGill University

McGill University  
Department of Civil Engineering & Applied Mechanics  
Attention to: Prof. Colin A. Rogers & Dimitrios G. Lignos

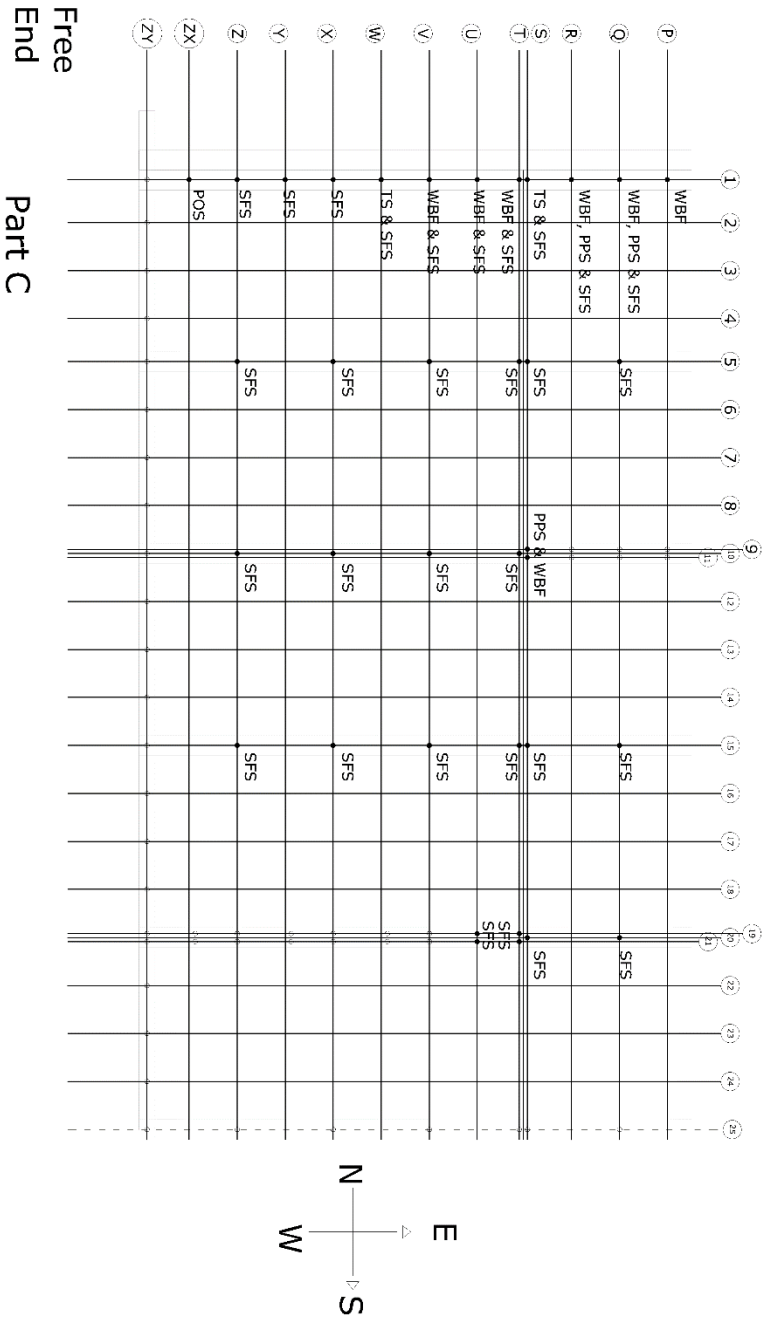
TEST MODE:  
Cyclic

SIZE:  
3.6x6.1m

SCREW SPACING:  
150/300mm

FAILURE MODES:  
Pullout, withdrawal --> POS  
Fatigue Fracture, Shear --> SFS  
Pull through sheathing --> PTS  
Damage prior to testing --> D  
Partial Pullthrough --> PPS  
Tearout of sheathing --> TS  
Wood Bearing Failure --> WBF

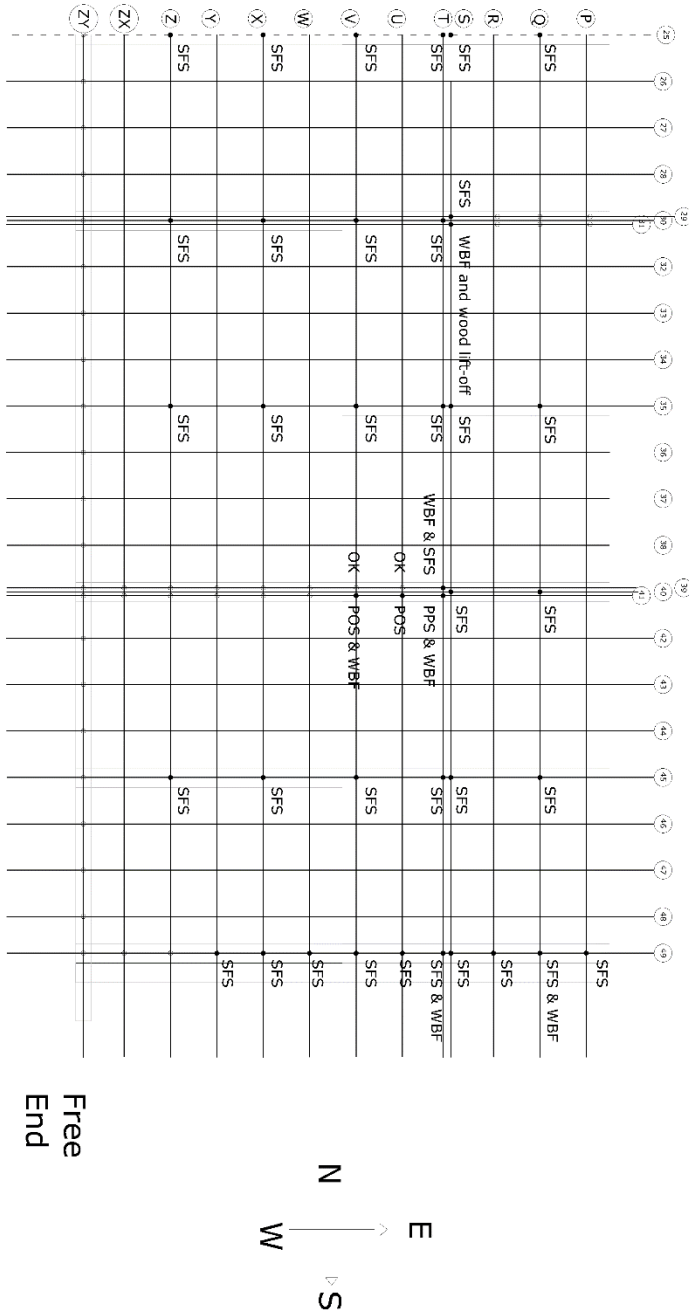
Figure B.15: 6-F#10-C-B, Screw failure modes



Note: If failure mode not indicated then the connection at that location has not failed

TEST ID: 6-F#10-C	DATE: 17 June 2015	FAILURE MODES:
<b>Project: Diaphragm Experimental Program</b> <b>McGill University</b>		Pullout, withdrawal --> POS Fatigue Fracture, Shear --> SFS
McGill University Department of Civil Engineering & Applied Mechanics Attention to: Prof. Colin A. Rogers & Dimitrios G. Lignos		
TEST MODE:	SIZE:	SCREW SPACING:
Cyclic	3.66x6.1m	150/300mm
		Tearout of sheathing --> TS Wood Bearing Failure --> WBF

Figure B.16: 6-F#10-C-C, Screw failure modes



Note: If failure mode not indicated then the connection at that location has not failed

TEST ID: 6-F#10-C DATE: 17 June 2015

FAILURE MODES:  
Pullout, withdrawal --> POS

Project: Diaphragm Experimental Program  
McGill University

Fatigue Fracture, Shear --> SFS  
Pull through sheathing --> PTS

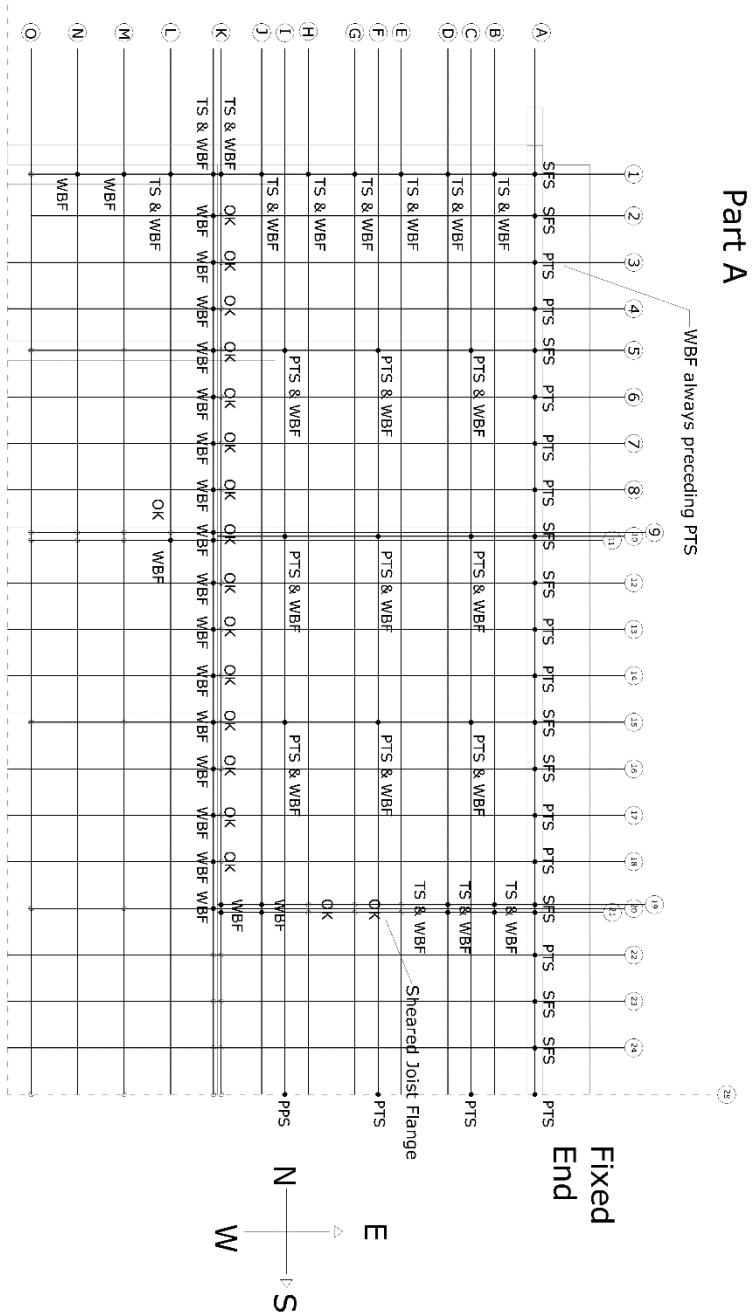
McGill University  
Department of Civil Engineering & Applied Mechanics  
Attention to: Prof. Colin A. Rogers & Dimitrios G. Lignos

Damage prior to testing --> D  
Partial Pullthrough --> PPS

TEST MODE: Cyclic SIZE: 3.66x6.1m SCREW SPACING: 150/300mm

Tearout of sheathing --> TS  
Wood Bearing Failure --> WBF

Figure B.17: 6-F#10-C-D, Screw failure modes

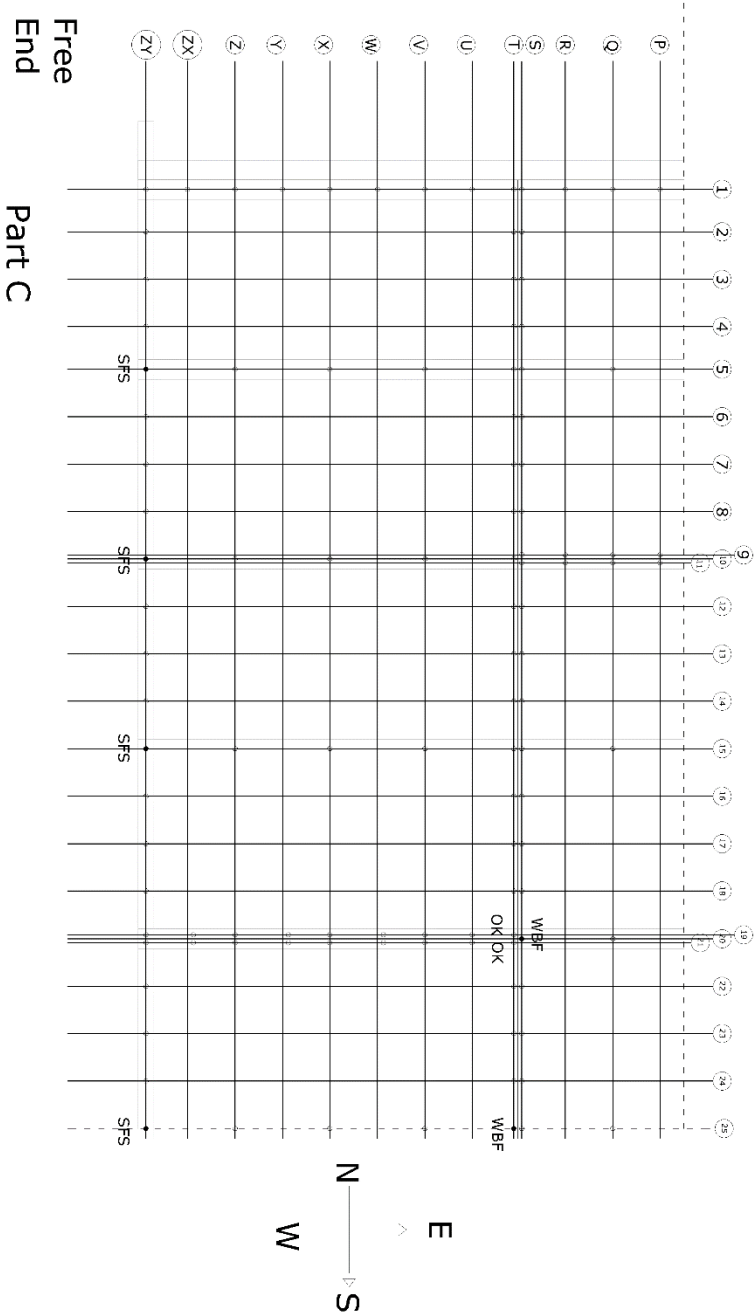


Note: If failure mode not indicated then the connection at that location has not failed

TEST ID: 7-RB-M	DATE: 26 June 2015	FAILURE MODES:
Project: Diaphragm Experimental Program McGill University		
McGill University Department of Civil Engineering & Applied Mechanics Attention to: Prof. Colin A. Rogers & Dimitrios G. Lignos		
TEST MODE: Monotonic	SIZE: 3.66x6.1m	SCREW SPACING: 150/300mm
		Pullout, withdrawal --> POS
		Fatigue Fracture, Shear --> SFS
		Pull through sheathing --> PTS
		Damage prior to testing --> D
		Partial Pullthrough --> PPS
		Tearout of sheathing --> TS
		Wood Bearing Failure --> WBF

Figure B.18: 7-RB-M-A, Screw failure modes

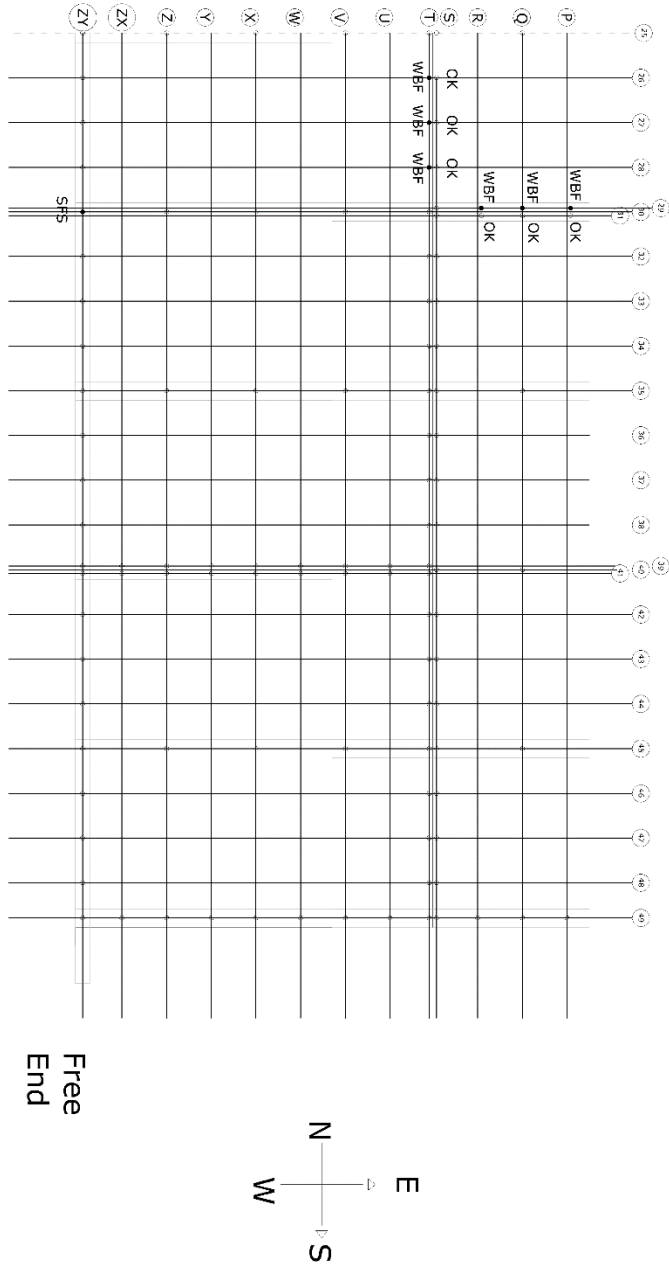




Note: If failure mode not indicated then the connection at that location has not failed

TEST ID: 7-RB-M	DATE: 26 June 2015	FAILURE MODES:
<b>Project: Diaphragm Experimental Program</b> <b>McGill University</b>		Pullout, withdrawal --> POS
McGill University Department of Civil Engineering & Applied Mechanics Attention to: Prof. Colin A. Rogers & Dimitrios G. Lignos		Fatigue Fracture, Shear --> SFS
TEST MODE: Monotonic	SIZE: 3.66x6.1m	Pull through sheathing --> PTS
	SCREW SPACING: 150/300mm	Damage prior to testing --> D
		Partial Pullthrough --> PPS
		Tearout of sheathing --> TS
		Wood Bearing Failure --> WBF

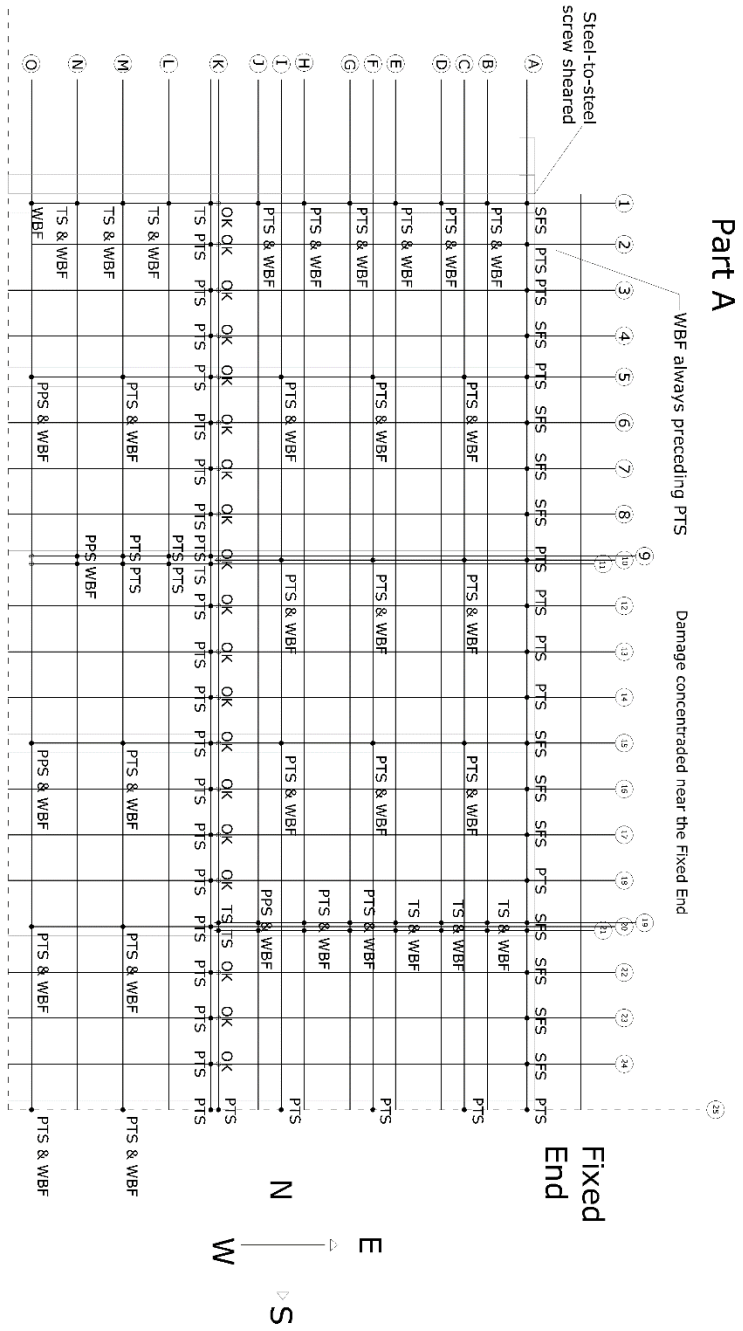
Figure B.20: 7-RB-M-C, Screw failure modes



Note: If failure mode not indicated then the connection at that location has not failed

TEST ID: 7-RB-M	DATE: 26 June 2015	FAILURE MODES: Pullout, withdrawal --> POS
<b>Project: Diaphragm Experimental Program</b>		
<b>McGill University</b>		
McGill University Department of Civil Engineering & Applied Mechanics Attention to: Prof. Colin A. Rogers & Dimitrios G. Lignos		
TEST MODE: Monotonic	SIZE: 3.66x6.1m	SCREW SPACING: 150/300mm
		Tearout of sheathing --> TS
		Wood Bearing Failure --> WBF
		Partial Pullthrough --> PPS
		Damage prior to testing --> D
		Pull through sheathing --> PTS
		Fatigue Fracture, Shear --> SFS

Figure B.21: 7-RB-M-D, Screw failure modes



Note: If failure mode not indicated then the connection at that location has not failed

TEST ID: 8-RB-C	DATE: 30 June 2015	FAILURE MODES:
<b>Project: Diaphragm Experimental Program</b> McGill University		Pullout, withdrawal --> POS
McGill University Department of Civil Engineering & Applied Mechanics Attention to: Prof. Colin A. Rogers & Dimitrios G. Lignos		Fatigue Fracture, Shear --> SFS
TEST MODE: Cyclic		Pull through sheathing --> PTS
SIZE: 3.66x6.1m	SCREW SPACING: 150/300mm	Damage prior to testing --> D
		Partial Pullthrough --> PPS
		Tearout of sheathing --> TS
		Wood Bearing Failure --> WBF

Figure B.22: 8-RB-C-A, Screw failure modes

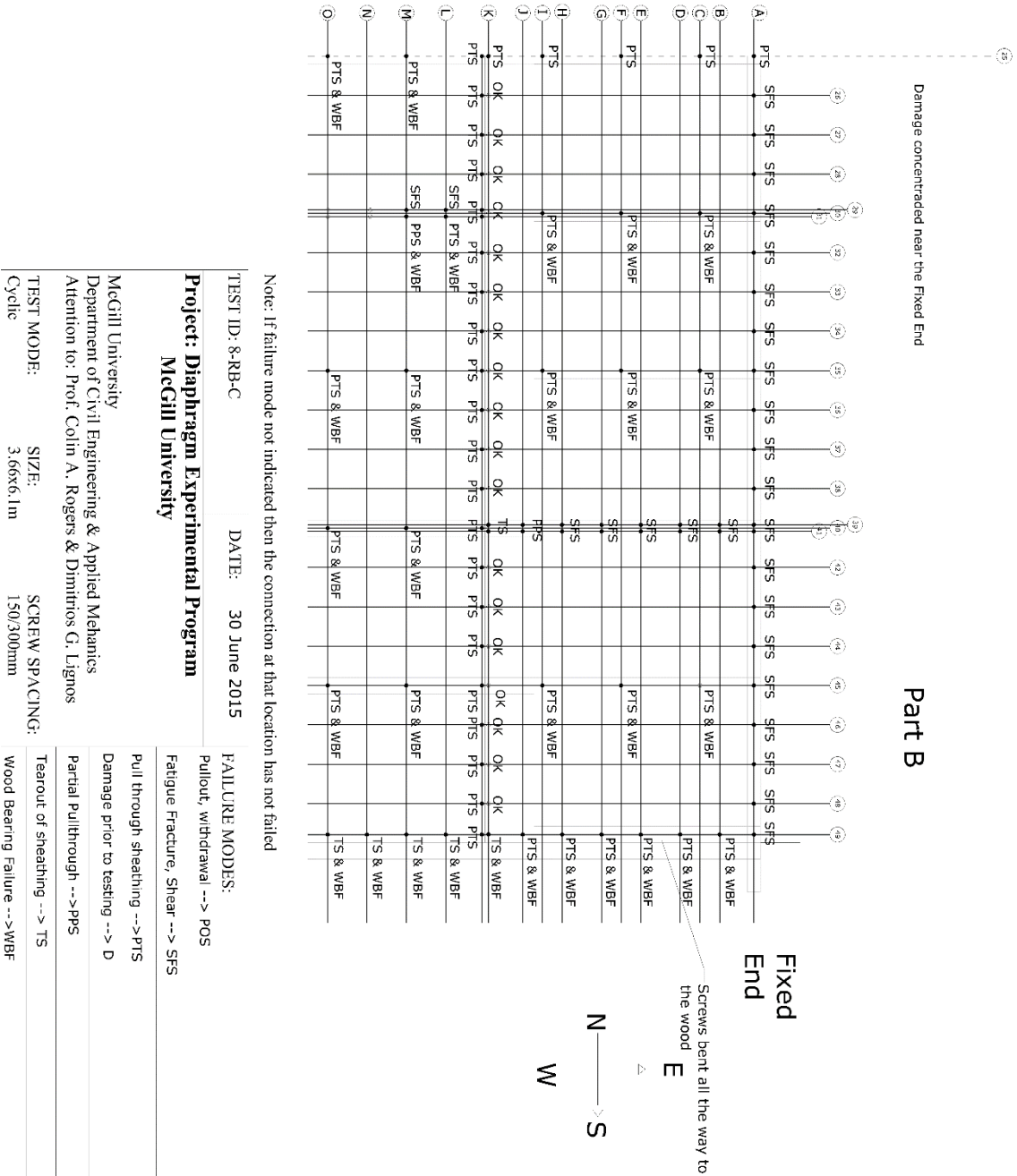
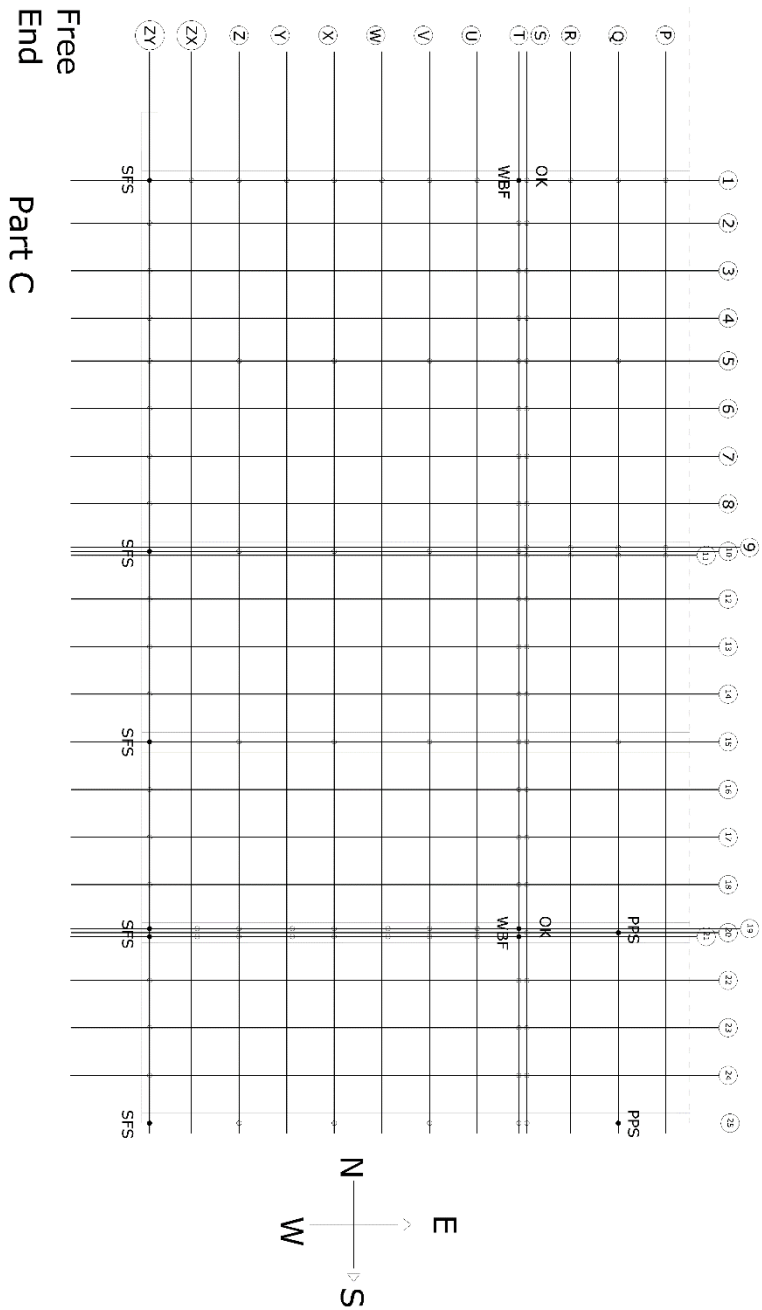


Figure B.23: 8-RB-C-B, Screw failure modes

Screws tilted but ok

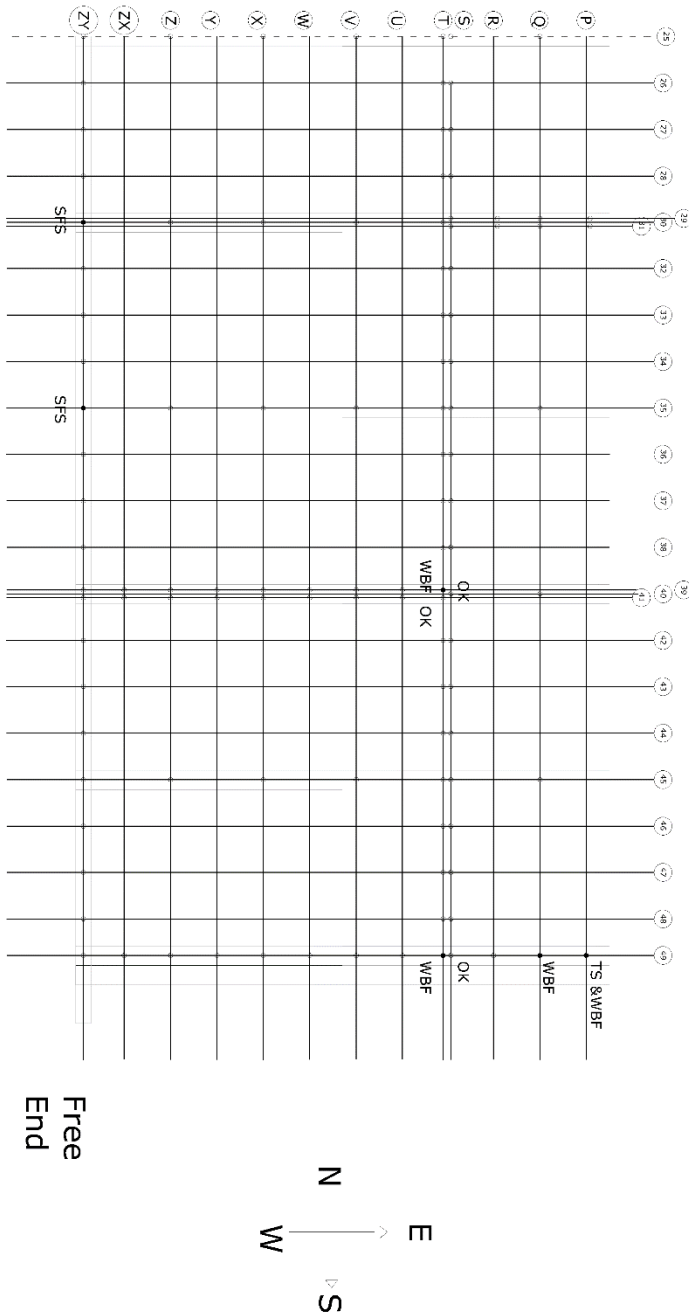


Note: If failure mode not indicated then the connection at that location has not failed

TEST ID: 8-RB-C	DATE: 30 June 2015	FAILURE MODES:
<b>Project: Diaphragm Experimental Program</b> <b>McGill University</b>		Pullout, withdrawal --> POS
McGill University Department of Civil Engineering & Applied Mechanics Attention to: Prof. Colin A. Rogers & Dimitrios G. Lignos		Fatigue Fracture, Shear --> SFS
		Pull through sheathing --> PTS
		Damage prior to testing --> D
		Partial Pullthrough --> PPS
		Tearout of sheathing --> TS
TEST MODE: Cyclic	SIZE: 3.66x6.1m	SCREW SPACING: 150/300mm
		Wood Bearing Failure --> WBFB

Figure B.24: 8-RB-C-C, Screw failure modes

Screws tilted but ok



Note: If failure mode not indicated then the connection at that location has not failed

**Part D**

TEST ID: 8-RB-C      DATE: 30 June 2015

FAILURE MODES:

**Project: Diaphragm Experimental Program**  
**McGill University**

Pullout, withdrawal --> POS

Fatigue Fracture, Shear --> SFS

Pull through sheathing --> PTS

Damage prior to testing --> D

Partial Pullthrough --> PPS

Tearout of sheathing --> TS

McGill University  
 Department of Civil Engineering & Applied Mechanics  
 Attention to: Prof. Colin A. Rogers & Dimitrios G. Lignos

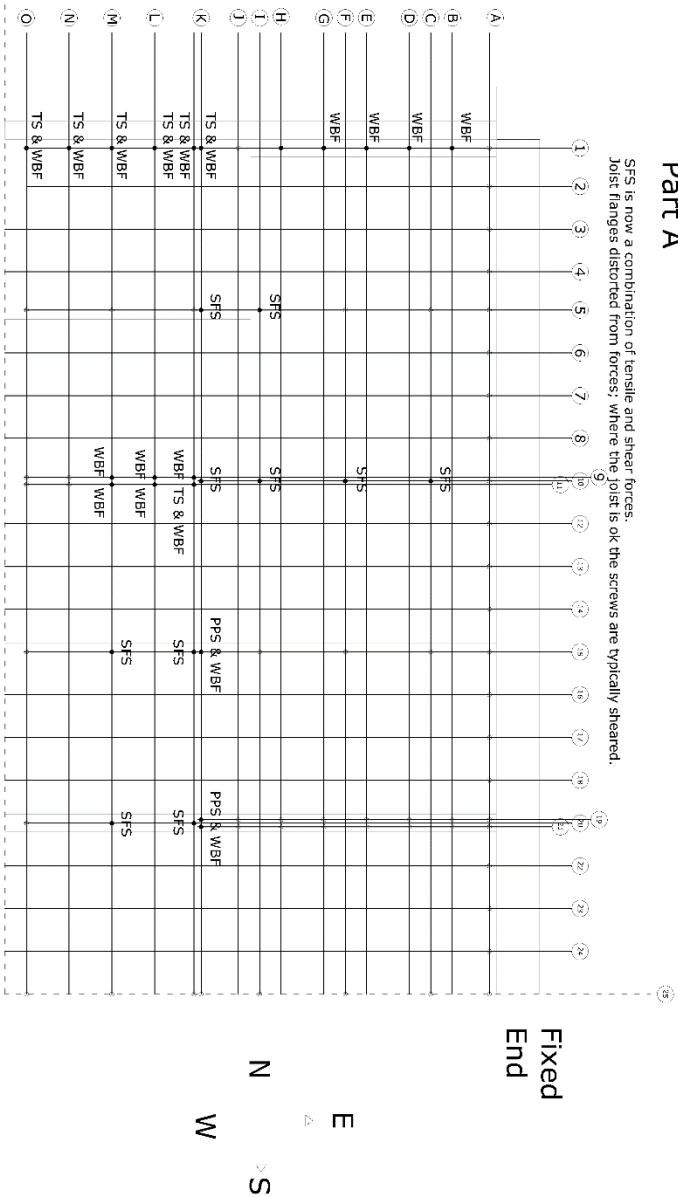
Wood Bearing Failure --> WBF

TEST MODE: Cyclic      SIZE: 3.66x6.1m      SCREW SPACING: 150/300mm

Figure B.25: 8-RB-C-D, Screw failure modes

# Part A

SFS is now a combination of tensile and shear forces. Joist flanges distorted from forces, where the joist is ok the screws are typically sheared.



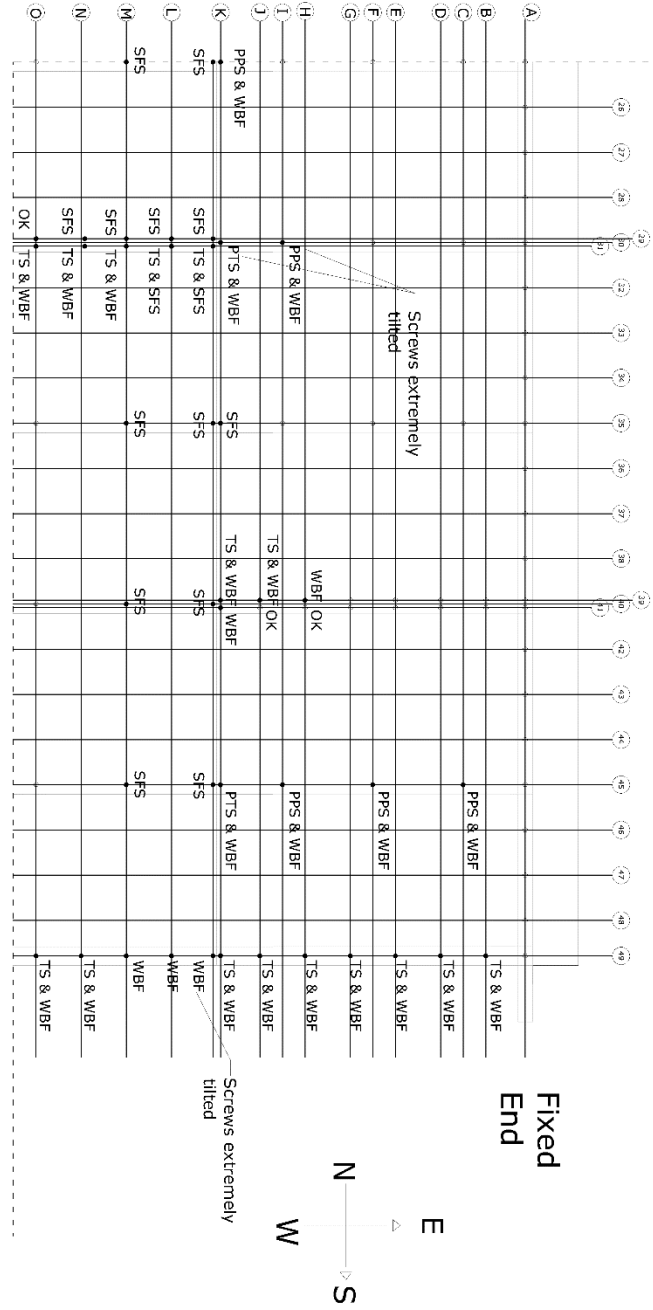
Note: If failure mode not indicated then the connection at that location has not failed

TEST ID: 9-F#12-M	DATE: 03 July 2015	FAILURE MODES:
<b>Project: Diaphragm Experimental Program</b>		Pullout, withdrawal --> POS
<b>McGill University</b>		Fatigue Fracture, Shear --> SFS
McGill University Department of Civil Engineering & Applied Mechanics Attention to: Prof. Colin A. Rogers & Dimitros G. Lignos		Pull through sheathing --> PTS
TEST MODE: Monotonic		Damage prior to testing --> D
SIZE: 3.66x6.1m	SCREW SPACING: 150/300mm	Partial Pullthrough --> PPS
Tearout of sheathing --> TS		Wood Bearing Failure --> WBF

Figure B.28: 9-F#12-M-A, Screw failure modes

Steel-to-steel block connection sheared, observed in this section

## Part B



Note: If failure mode not indicated then the connection at that location has not failed

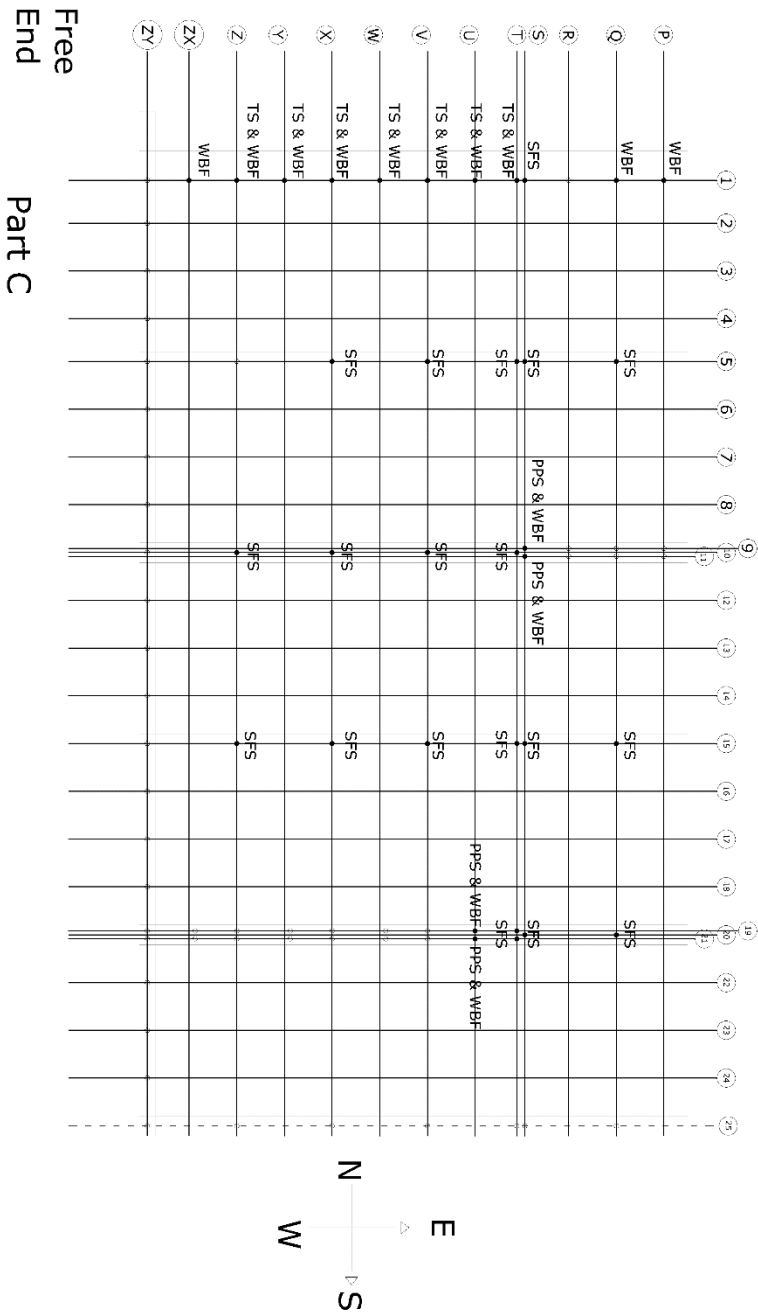
TEST ID: 9-F#12-M DATE: 03 July 2015 FAILURE MODES: Pullout, withdrawal --> POS

**Project: Diaphragm Experimental Program**  
 McGill University Fatigue Fracture, Shear --> SFS

McGill University  
 Department of Civil Engineering & Applied Mechanics  
 Attention to: Prof. Colin A. Rogers & Dimitrios G. Lignos  
 Pull through sheathing --> PTS  
 Damage prior to testing --> D  
 Partial Pullthrough --> PPS  
 Tearout of sheathing --> TS  
 Wood Bearing Failure --> WBF

TEST MODE: Monotonic SIZE: 3.66x6.1m SCREW SPACING: 150/300mm

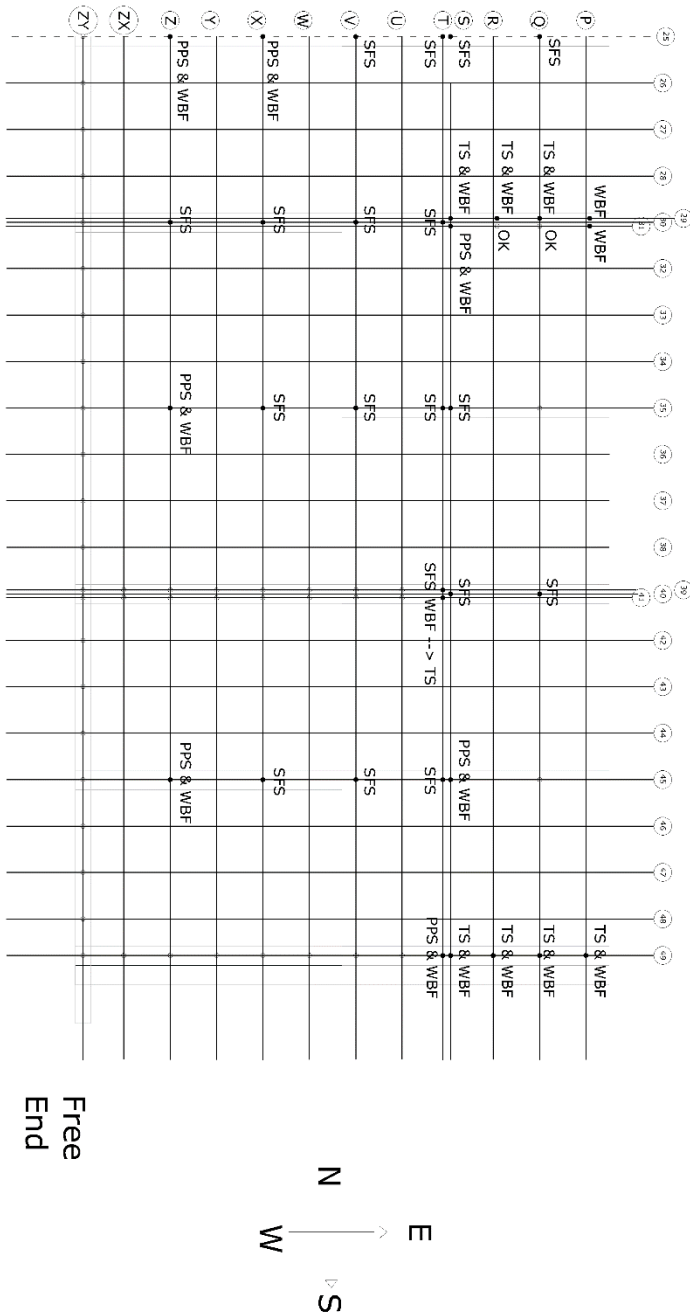
Figure B.29: 9-F#12-M-B, Screw failure modes



Note: If failure mode not indicated then the connection at that location has not failed

TEST ID: 9-F#12-M	DATE: 03 July 2015
<b>Project: Diaphragm Experimental Program</b> <b>McGill University</b>	
McGill University Department of Civil Engineering & Applied Mechanics Attention to: Prof. Colin A. Rogers & Dimitrios G. Lignos	
TEST MODE: Monotonic	SIZE: 3.66x6.1m
SCREW SPACING: 150/300mm	
<b>FAIL MODES:</b> Pullout, withdrawal --> POS Fatigue Fracture, Shear --> SFS Pull through sheathing --> PTS Damage prior to testing --> D Partial Pullthrough --> PPS Tearout of sheathing --> TS Wood Bearing Failure --> WBF	

Figure B.30: 9-F#12-M-C, Screw failure modes



Note: If failure mode not indicated then the connection at that location has not failed

TEST ID: 9-F#12-M

DATE: 03 July 2015

FAILURE MODES:

Pullout, withdrawal --> POS

**Project: Diaphragm Experimental Program**  
**McGill University**

Fatigue Fracture, Shear --> SFS

Pull through sheathing --> PTS

Damage prior to testing --> D

McGill University  
 Department of Civil Engineering & Applied Mechanics  
 Attention to: Prof. Colin A. Rogers & Dimitrios G. Lignos

Partial Pullthrough --> PPS

TEST MODE:

Monotonic

SIZE:

3,66x6,1m

SCREW SPACING:

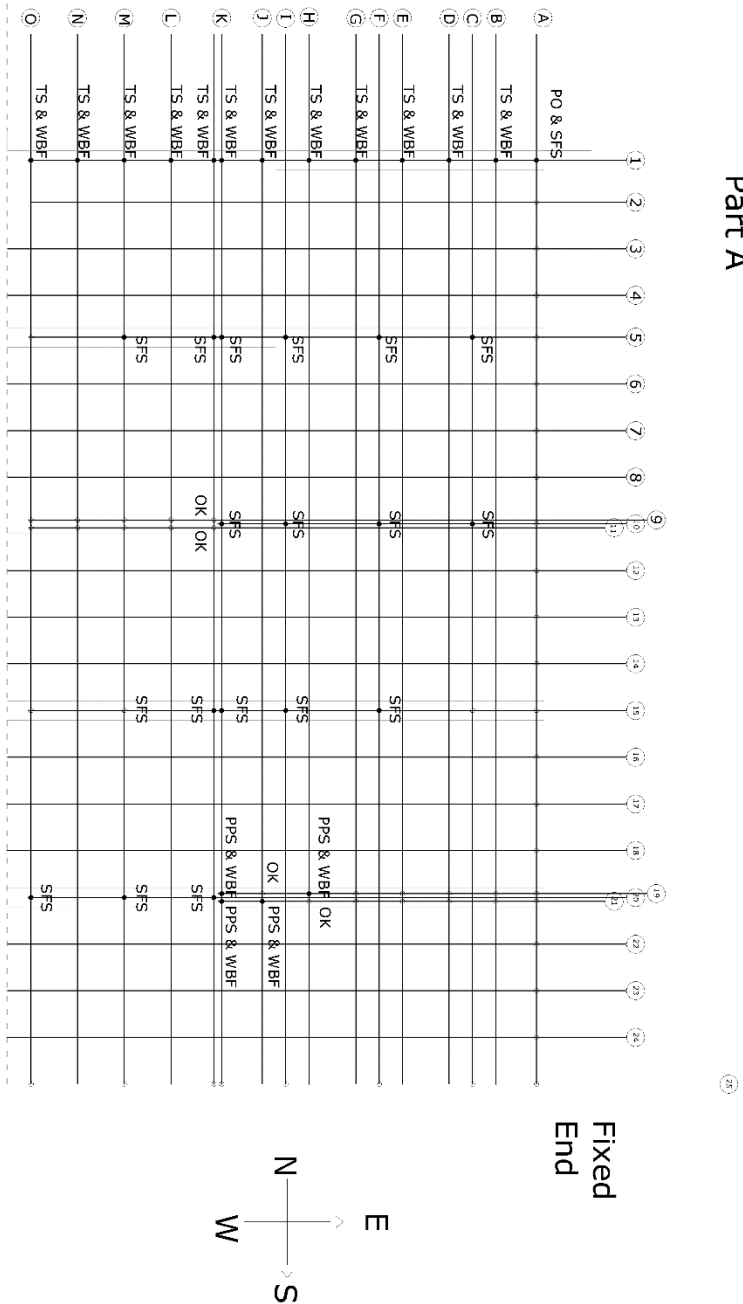
150/300mm

Tearout of sheathing --> TS

Wood Bearing Failure --> WBFB

Figure B.31: 9-F#12-M-D, Screw failure modes

Part A

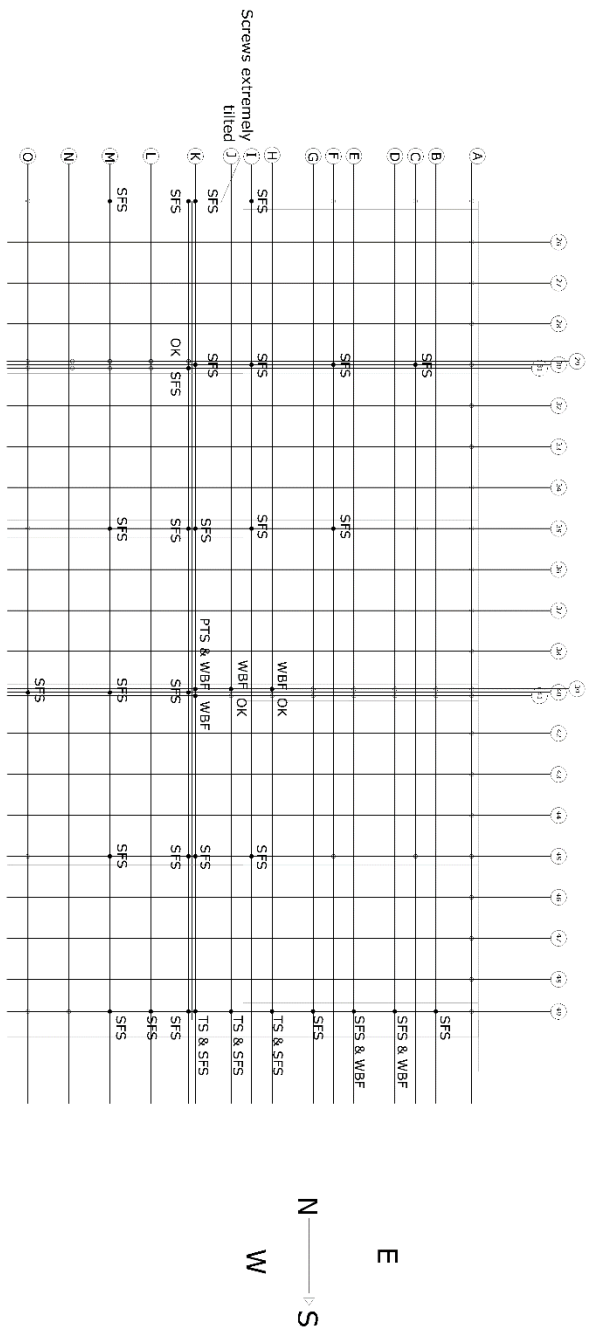


Note: If failure mode not indicated then the connection at that location has not failed

TEST ID: 10-F#12-C	DATE: 08 July 2015	FAILURE MODES:
<b>Project: Diaphragm Experimental Program</b>		Pullout, withdrawal --> POS
<b>McGill University</b>		Fatigue Fracture, Shear --> SFS
McGill University Department of Civil Engineering & Applied Mechanics Attention to: Prof. Colin A. Rogers & Dimitrios G. Lignos		Pull through sheathing --> PTS
		Damage prior to testing --> D
		Partial Pullthrough --> PPS
TEST MODE: Cycle	SIZE: 3.66x6.1m	Tearout of sheathing --> TS
	SCREW SPACING: 150/300mm	Wood Bearing Failure --> WBF

Figure B.32: 10-F#12-C-A, Screw failure modes

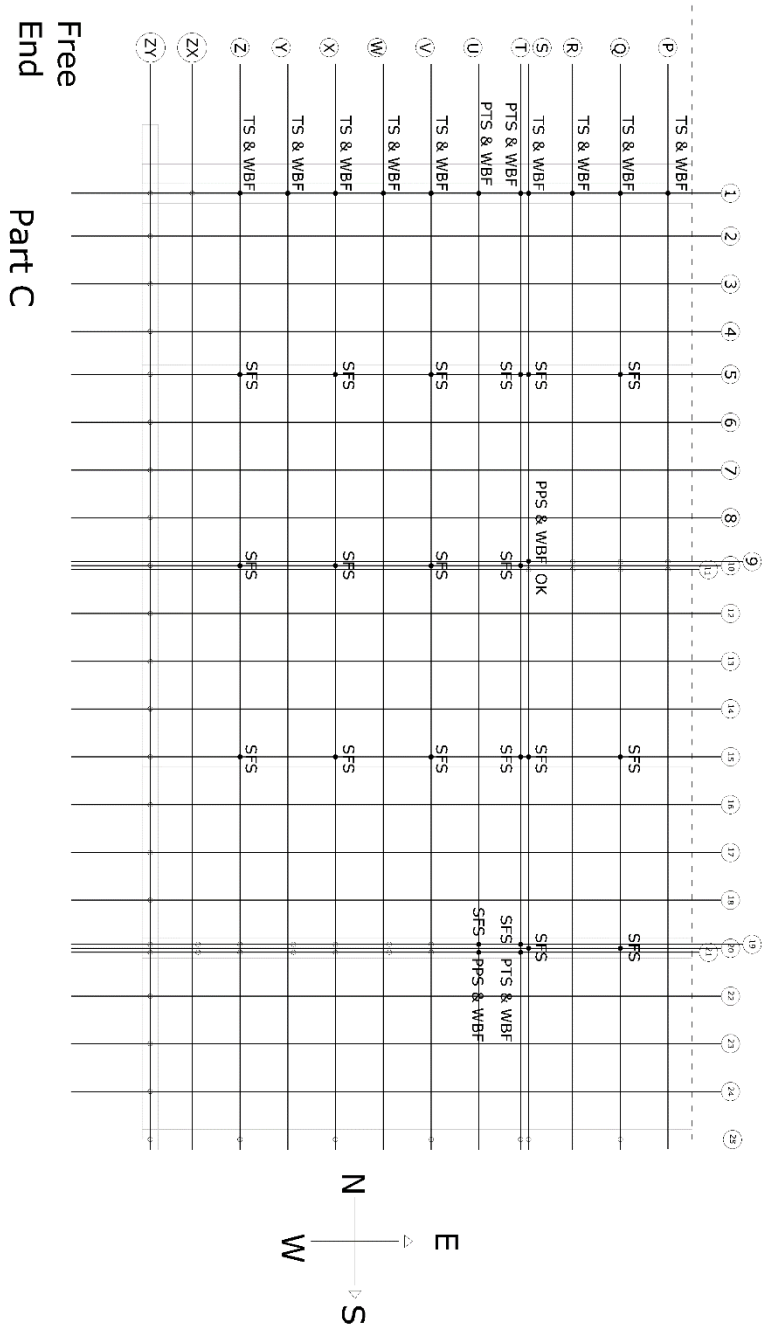
Part B



Note: If failure mode not indicated then the connection at that location has not failed

TEST ID: 10-F#12-C	DATE: 08 July 2015	FAILURE MODES:
<b>Project: Diaphragm Experimental Program</b>		Pullout, withdrawal --> POS
<b>McGill University</b>		Fatigue Fracture, Shear --> SFS
McGill University Department of Civil Engineering & Applied Mechanics Attention to: Prof. Colin A. Rogers & Dimitrios G. Lignos		Pull through sheathing --> PTS
TEST MODE: Cycle		Damage prior to testing --> D
SIZE: 3.66x6.1m	SCREW SPACING: 150/300mm	Partial Pullthrough --> PPS
		Tearout of sheathing --> TS
		Wood Bearing Failure --> WBF

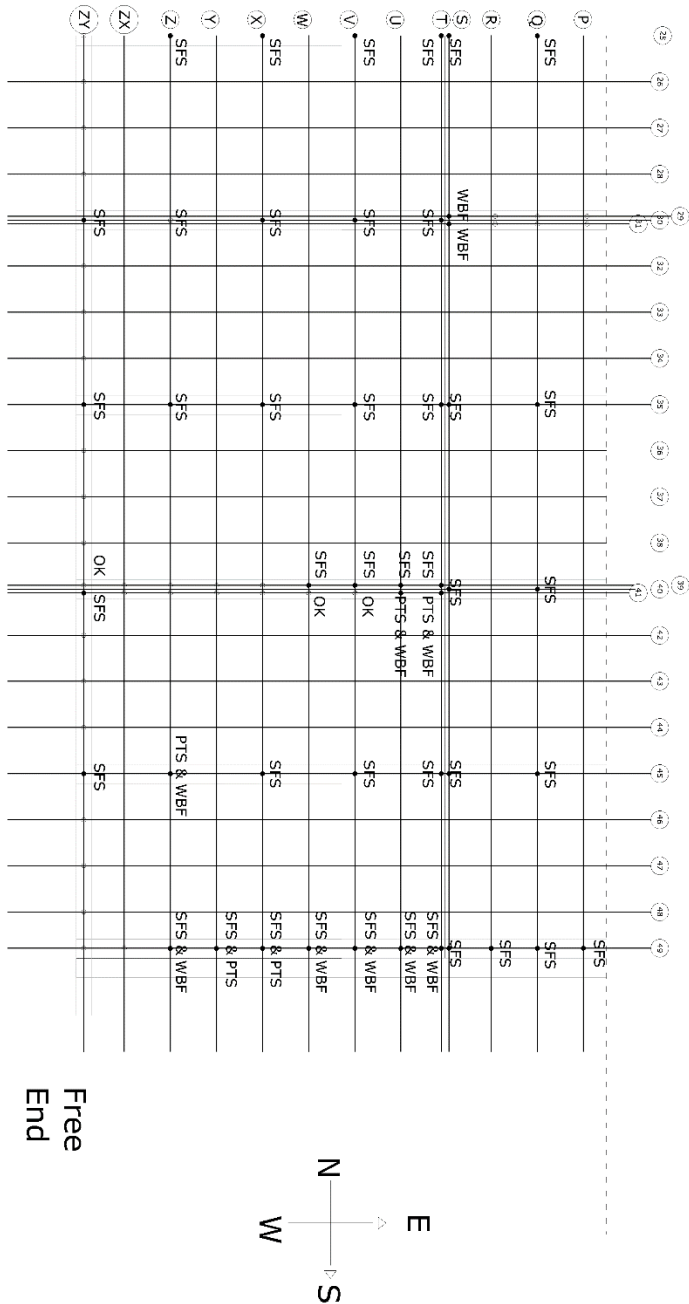
Figure B.33: 10-F#12-C-B, Screw failure modes



Note: If failure mode not indicated then the connection at that location has not failed

TEST ID: 10-F#12-C	DATE: 08 July 2015	FAILURE MODES:
<b>Project: Diaphragm Experimental Program</b>		Pullout, withdrawal --> POS
<b>McGill University</b>		Fatigue Fracture, Shear --> SFS
McGill University		Pull through sheathing --> PTS
Department of Civil Engineering & Applied Mechanics		Damage prior to testing --> D
Attention to: Prof. Colin A. Rogers & Dimitrios G. Lignos		Partial Pullthrough --> PPS
TEST MODE:	SIZE:	Tearout of sheathing --> TS
Cyclic	3.66x6.1m	Wood Bearing Failure --> WBF
	SCREW SPACING:	
	150/300mm	

Figure B.34: 10-F#12-C-C, Screw failure modes



Note: If failure mode not indicated then the connection at that location has not failed

Part D

Free End

TEST ID: 10-F#12-C	DATE: 08 July 2015	FAILURE MODES:
<b>Project: Diaphragm Experimental Program</b>		Pullout, withdrawal --> POS
<b>McGill University</b>		Fatigue Fracture, Shear --> SFS
McGill University Department of Civil Engineering & Applied Mechanics Attention to: Prof. Colin A. Rogers & Dimitrios G. Lignos		
TEST MODE:	SIZE:	SCREW SPACING:
Cyclic	3,66x6,1m	150/300mm
Pull through sheathing --> PTS Damage prior to testing --> D Partial Pullthrough --> PPS Tearout of sheathing --> TS Wood Bearing Failure --> WBF		

Figure B.35: 10-F#12-C-D, Screw failure modes

## APPENDIX C: TEST SETUP DESIGN

### C.1. General overview

A brief summary of the test-setup design of the diaphragm experimental program is presented.

Figure A.1 demonstrates the self-reacting test setup assembly, as presented in Chapter 2.

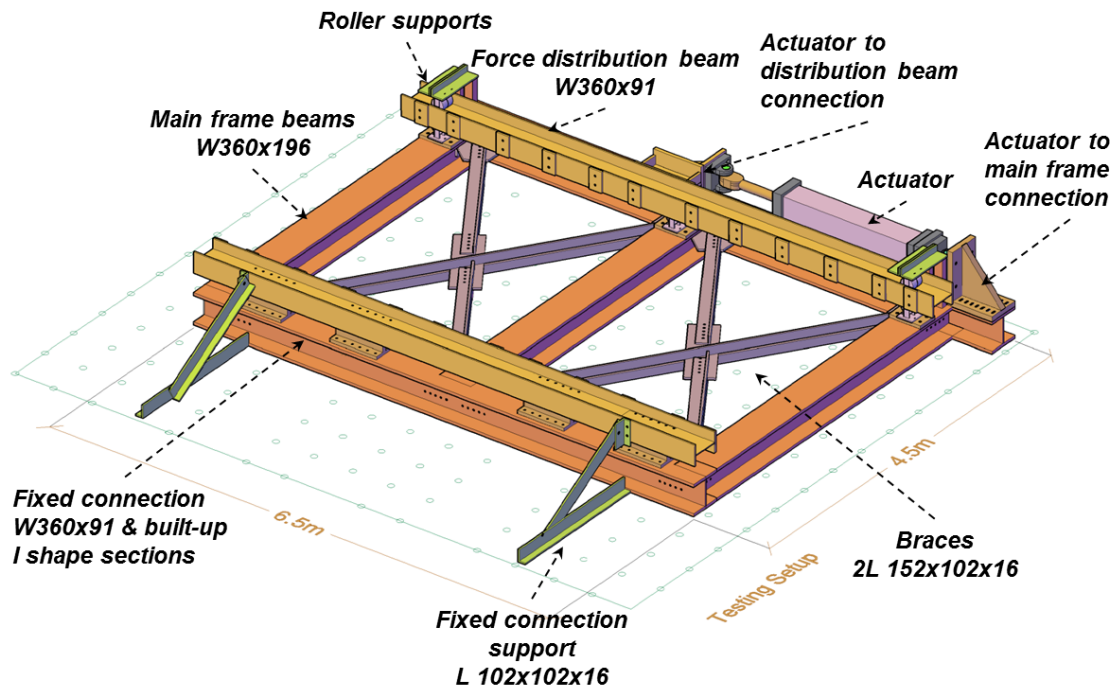


Figure C.1: Test setup of the diaphragm experimental program (Chapter 2)

SAP2000 commercial software (CSI 2009) was relied upon in order to design the test frame. A braced frame configuration was chosen comprised of 3 pin connected short beams, 2 long continuous beams and 4 pin connected braces (Figure C.2). Based on the capacities exhibited from CFS and wood shear walls and diaphragms of past experimental programs included in the aforementioned literature review as well as on the maximum capacities observed on sheathed CFS framed shear wall testing performed at McGill University (Lu 2015) the maximum capacity of the specimens was found not greater than 200KN.

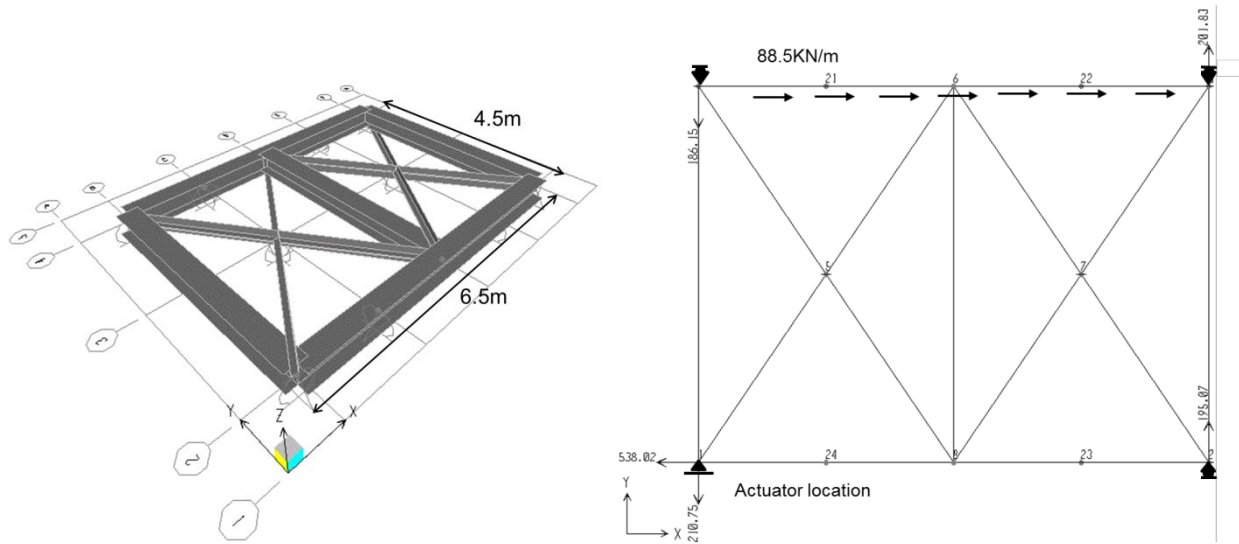


Figure C.2: Test frame configuration

However, a conservative approach was followed for the design load considered. The actuator chosen for this application had a tensile capacity of 450kN and compressive capacity of 650kN. It was decided that the test frame will be designed based on the actuator's tensile capacity. A safety factor of 1.2 was implemented leading to a maximum load of 540kN considered for design, which is almost 3 times higher than the maximum diaphragm capacity observed in literature. The diaphragm specimens' plan dimensions are 3.66x6.1m in order to satisfy the aspect ratio limits of AISI S907 Standard (2013) and due to space limitations in the lab. To this end, the overall out-to-out frame dimensions are 4.5x6.5m (Figure C.2). A uniform load of  $540/6.1=88.5\text{kN/m}$  was applied in the SAP2000 model on the side where the diaphragm will be bolted. A maximum shear capacity of 50kN was assumed for the anchor rods to be used. The anchor rods were expected to take mainly the uplift forces resulting from the self-weight of the members and small eccentricities of the applied lateral load. Most of the in-plane forces would be taken by the frame and not the strong floor; thus, 4 roller supports were implemented in the SAP2000 model restricting the y direction while allowing the free movement of the frame in the x direction as would be expected based on the loading applied. The x direction degree of

freedom was only restrained in the actuator location (left down corner, simplification for where the actuator connects to the main beams of the braced frame). This support simulated the reaction force applied on the frame from the actuator. The frame sections were chosen so that the frame remains elastic throughout the testing process and has adequate stiffness to exhibit the minimum possible deformation. It was expected that the design was mainly based on maximum deformations allowed and not on member capacities; thus a limit of  $L/1125$  (4mm) was used, where  $L=4.5\text{m}$ . The final frame sections chosen were: W360x196 sections for the perimeter beams, W360x262 for the centre beam and 2L 152x102x16 angle sections with 25.4mm spacing for the braces. Based on these sections additional calculations were carried out for the gusset plate dimensions and connection configurations between the beams and the braces. An ABAQUS (Dassault-Systems 2013) model of the built-up I-shapes of the fixed connection configuration was also created in order to predict the stresses developed.

### **C.2. Angles connected through centre gusset plate**

Summary: Initially a 2L 152x102x19 angle sections was chosen connected with 5 A325, 25.4mm diameter bolts through a 1074x340x25.4mm gusset plate. After the calculations were finalized a reduction of thickness was deemed acceptable. Thus, 2L 152x102x16 angles were used in the end, given that the final force level was at 300kN instead of 600kN.

#### **Angle Properties**

p.7-77HB

<b><u>Single</u></b>			<b><u>Double</u></b>	
t=	19.1	mm		
b=	102	mm		
d=	152	mm		
c=	132.9	mm		
A=	4490	mm <sup>2</sup>	8970	mm <sup>2</sup>
a=	82.9	mm		
y=	52.5	mm	52.5	mm
I <sub>x</sub> =	10200000	mm <sup>4</sup>	20300000	mm <sup>4</sup>

**Angle Properties (Continued)**

<u>Single</u>			<u>Double</u>		
$I_y=$	3660000	mm <sup>4</sup>	21856223.9		mm <sup>4</sup>
$r_x=$	47.6	mm	47.6		mm
$S_x=$	102000	mm <sup>3</sup>	206000		mm <sup>3</sup>
$S_y=$	49200000	mm <sup>3</sup>			
$r_y=$	28.6	mm	49.4		mm
$r_y$ or $r_z=$	21.9	mm	80.9		mm
$x=$	27.5	mm			
$J$	546000	mm <sup>4</sup>	1092000		
$C_w=$	712000000	mm <sup>6</sup>	1424000000		
$r_x=$	51	mm			
$y_o=$	32.3	mm	43.00		mm
$x_o=$	33.6	mm			
$\Omega=$	0.586		0.718		

**Max Force 600KN (Compression-Tension, initial assumption)**

$t=$	19.1	mm	$d=$	152	mm	
$F_y=$	300	Mpa	$A_g=$	8970	mm <sup>2</sup>	for 2 angles
$F_u=$	450	Mpa				

**Check single angle and the member resistance**

$F_y$  for angles 300MPa

**Slenderness**

For the rest 345 Mpa

Assume short beams 4.5m so unbraced length  
 $L_x=2.72m$

$r_y=$	21.9	mm	$L_{un}=$	2718	mm	$r_y=$	43.3
			$r_x=$	47.6	for 2L		for 10mm
			$r_y=$	49.4	for 25.4mm spacing		
So $L_y/r_y=$		124.1					<200 & 300 tension & compression

**Class of section**

$170/(F_y^{(1/2)})=$	9.8	ok		
$145/(F_y^{(1/2)})=$	8.4	ok		
$d/t=$	8.0	$< 200/((345)^{(1/2)})=$	11.6	Class 3 for a not continuously connected angle
p. 2-24 HB			ok	
$T_r = \phi F_y A_g=$			2421.9	kN

**Compression**

<b>X-axis</b>	$L_x=2718\text{mm}$				
P.4-144 HB	Cr for double angle				
$KL/r_x=$	57.1	$KL/r_y=$	55.1	$C_w=$	1424000000 for 2 angles
$\lambda=$	0.70	$KL/r_y'=$	41.4	$G=$	77000 its 2*value
$C_r=$	1893.9	kN	$L_e=$	2982.2	$J=$ 1092000

<b>Y-axis</b>	$L_y=2718\text{mm}$				
$x_o=$	0	$y=$	52.5	mm	
$r_o=$	80.9	$y_o=$	43.00	mm	
$\Omega=$	0.718				
$\rho_o=$	60.4				
$\rho_i=$	41.4				
$\rho_e=$	73.2				
$F_{ey}=$	368.2				
$F_{ez}=$	1437.2				
$F_{eyz}=$	338.7				
$\lambda=$	0.94				
$C_{ry}=$	1530.4	kN	ok		

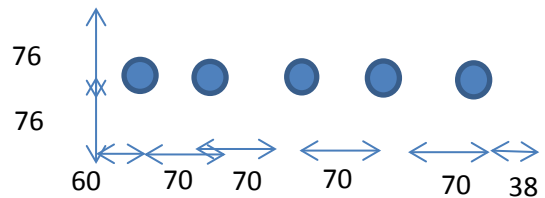
1" ASTM 325 Bolts  $d_b= 25.4 \text{ mm}$   
 $A_g \text{ single} = 4490 \text{ mm}^2$

**Net section fracture**

$A_n=2(A_g-(d_b+4)*19.1)= 7856.9 \text{ mm}^2$   
 $A_{ne}=0.8*A_n= 6285.5 \text{ mm}^2$  for shear lag  
 $T_r=0.75*A_{ne}*450= 2121.4 \text{ kN}$

**Block Shear**

$p= 70 \text{ mm}$   
 end dist= $38 \text{ mm}$   
 end dist= $60 \text{ mm}$   
 edge dist.= $76 \text{ mm}$   
 $76 \text{ mm}$



Threads in shear plane

$A_n= 1170.8 \text{ mm}^2$   
 $A_{gv}=(2p+edge)*19.1= 6073.8 \text{ mm}^2$   
 $T_r= 2(0.75(0.6*A_n*F_u+0.6*A_{gv}*(F_y+F_u)*0.5))= 2524.1 \text{ kN}$

**Bolt Spacing**

Min pitch=  $2.7(d_b)=$  69 mm  
 Max edge= 150mm or  $12(25.4)=$  305 mm  
 Min edge= 32mm or 44mm  
 Min end=  $1.5d_b=$  38  
 $s \geq 2.666*d_b \rightarrow 50.8\text{mm}$  so 62mm ok

$t_p=$  25.4 mm or 1in  
 $F_{up}=$  450 MPa  
 $F_{ub}=$  825 MPa  
 $A_b=$  507  $\text{mm}^2$   
 $n_b=$  5  
 $n_{\text{bearing}}=$  4  
 bolts for bearing

### Bolts

For bolts assume worst case thread in plane  
 Two shear planes

$V_r=0.7*0.6*0.8*n_b*2*A_b*F_u=$  1405.4 kN

$B_r=3*0.8*n_b*t_p*d_b*F_{up}=$  2095.8 kN

$t_{\text{angle}}=19.1\text{mm}$  as it is the smaller one between angle and gusset plate!

Also  $L_{\text{connection}}=$  280  $< 15d_b=$  381 mm  
 so no further reduction for  $V_r$

### Slip critical check $\longrightarrow$

### Controls

Take worst case factors

$k_s=$  0.33  $m=$  2

$c_1=$  0.82 for A325 bolts

$V_s=0.53*c_1*k_s*m*n*A_b*F_u=$  599.9 kN ok

$L$  from end gusset to end angle= 251.8 mm

Seismic detailing 2006

$w_{nt}=$  277.32 mm

$A_n=(w_{nt}-2(d_b+4))*20=$  5550.3

$A_{ne}=0.6*A_n=$  3330.2

$T_r=0.75*A_{ne}*450=$  1123.9 kN **ok**

Based on the values seen before in strength the gusset plate will meet all the requirements.

$T_r=0.9*A_{gpp}*F_y=$  1377.7 kN yielding of gusset plate

Gusset plate web crippling and buckling check for the case of 600kN compressive force

### Gusset Stability (AISC)

t=	25.4	mm
L=	251.8	mm
$r=t/(12^{1/2})=$	7.33	mm
K=	1.2	
KL/r=	41.2	<200 ok
A=	7043.8	mm <sup>2</sup>
$F_e=\pi^2E/(KL/r)^2=$	1162.4	Mpa
$\phi R_n=0.9(0.658^{F_y/F_e})F_yA=$	1931.6	kN

and Whitmore section buckling strength:

$$\phi R_{wb}=0.75F_e w_{nt} t = 6140.6 \text{ kN}$$

### Slenderness limit!

$$3/4(E/F_y)^{1/2} = 18.1 \quad \text{so max free edge dimension --> } 458.7 \text{ mm}$$

### Center Connection

Same configuration can be used since maximum load considered in braces is 600kN.

As explained in the Summary of the section, the final choice was a double 152x102x16mm angle section for the braces given that from analysis the load would be closer to 300kN. As such, below are the calculations for the slenderness limits after the thickness reduction.

### Angle Properties

p.7-77HB

	<u>Single</u>		<u>Double</u>	
t=	16	mm		
b=	102	mm		
d=	152	mm		
c=	136	mm		
A=	3790	mm <sup>2</sup>	7570	mm <sup>2</sup>
a=	86	mm		
y=	51.40	mm	51.40	mm
I <sub>x</sub> =	8730000	mm <sup>4</sup>	17500000	mm <sup>4</sup>
I <sub>y</sub> =	3170000	mm <sup>4</sup>	18031819.3	mm <sup>4</sup>
r <sub>x</sub> =	48	mm	48	mm
S <sub>x</sub> =	86800	mm <sup>3</sup>	174000	mm <sup>3</sup>
S <sub>y</sub> =	41900000	mm <sup>3</sup>		
r <sub>y</sub> =	28.6	mm	48.81	mm
r <sub>y</sub> or r <sub>z</sub> =	22	mm	81.05	mm
x=	26.4	mm		
J	319000	mm <sup>4</sup>	638000	
C <sub>w</sub> =	427000000	mm <sup>6</sup>		
r <sub>x</sub> =	51.6	mm		
y <sub>o</sub> =	32.3	mm	43.4	mm

$x_o = 34.4$  mm  
 $\Omega = 0.585$  0.713

**Max Force 300 kN**

$t = 16$  mm       $d = 152$  mm  
 $F_y = 300$  Mpa       $A_g = 7570$  mm<sup>2</sup> for 2 angles  
 $F_u = 450$  Mpa

**Check single angle and the member resistance**

$F_y$  for angles 300MPa  
 For the rest 345 Mpa

**Slenderness**

Assume short beams 4.5m so unbraced length  $L_x = 2.72$ m

$r_y = 22$  mm       $L_{un} = 2718$  mm       $r_y = 42.7$   
 $r_x = 48$  for 2L      for 10mm  
 $r_y = 48.81$  for 25.4mm spacing  
 So  $L_y/r_y = 123.55$  < 200 & 300 tension & compression  
 and for capacity design -->  $170/(F_y^{(1/2)}) = 9.81$  ok       $\longrightarrow$  8.92  
 $145/(F_y^{(1/2)}) = 8.37$

**Class of section**

$d/t = 9.50$  <  $200/((345)^{(1/2)}) = 11.55$  Class 3 for a not  
 p. 2-24 HB ok continuously connected  
 angle  
 $T_r = \phi F_y A_g = 2043.9$  kN

**Compression**

**X-axis,  $L_x = 2718$ mm**

P.4-144 HB, Cr for double angle

$KL/r_x = 56.63$        $KL/r_y = 55.69$        $C_w = 854000000$  for 2 angles  
 $\lambda = 0.70$        $KL/r_y = 61.77$        $G = 77000$  its 2\*value  
 $C_r = 1605.78$  kN       $L_e = 3551.36$        $J = 638000$

**Y-axis,  $L_y = 2718$ mm**

$x_o = 0$        $y = 51.40$   
 $r_o = 81.05$        $y_o = 43.4$   
 $\Omega = 0.713$   
 $\rho_o = 72.77$   
 $\rho_i = 61.77$   
 $\rho_e = 95.45$   
 $F_{ey} = 216.66$   
 $F_{ez} = 990.51$   
 $F_{eyz} = 201.85$   
 $\lambda = 1.22$   
 $C_{ry} = 973.81$  kN

### C.3. Angles to main beams connection through gusset plates

Summary: Double 152x102x16 angles connected to 267x260x416 gusset plates of 25.4mm thickness (see fabrication drawings at the end of the Appendix). The same 5-bolt connection configuration was used, as presented in Section C.1.

### C.4. Main beams connection through gusset plates

Summary: A W360X262 section was initially chosen for the main beams of the braced framed. Based on the results W360x196 sections were selected instead for all beams except the centre beam, which remained W360x262. (See fabrication drawings at the end of the Appendix). All connections between the main beams comprised of A325 1in bolts n=10 bolted connected in the web of W360x262/196 beams with 368x214x25.4 plates (420x218x25.4 based on available plate sizes). Gusset plates were welded directly on the plates. Calculations are shown indicatively for one of the connections.

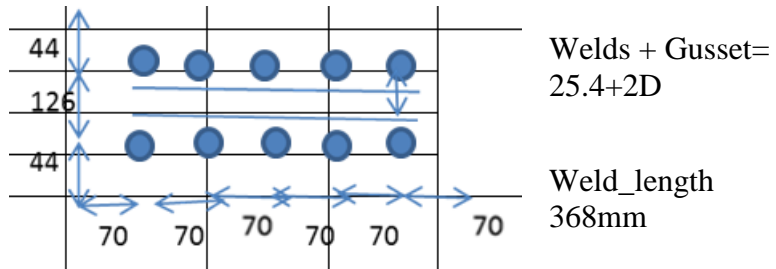
<b>Center Connection</b>	<i>I</i>				
Use same bolts as before		1" A325	$T_o =$	227	kN min pretension
$t_p =$	25.4	mm	$F_u =$	450	MPa
$t_w =$	21.1	mm	$F_y =$	345	MPa
$A_b =$	507	mm <sup>2</sup>	<b>Tension=</b>	340	kN
$A_g =$	5435.6	mm <sup>2</sup>	<b>Shear=</b>	500	kN
$d_b =$	25.4	mm	<b>Moment</b>	71.4	kN m --> Mz
Comment:			=		
Calculate bolts based on tension and shear and after for moment			$e =$	210	mm
<b>Check plate</b>					<u>Plate:</u> mm
					$t =$ 25.4
					$b =$ 214
					$d =$ 420
<b>Net section fracture</b>					
$A_n = (A_g - 2(d_b + 4)t) =$	3942.1	mm <sup>2</sup>			Gusset side welded at this plate
No shear lag for the plate connected to the web					same size as d of this plate! (initial

assumption)

$$T_r = 0.75 * A_{ne} * 450 = 1330.1 \text{ kN}$$

### Block Shear

$s = 126 \text{ mm}$   
 $p = 70 \text{ mm}$   
 $\text{end dist} = 70 \text{ mm}$   
 $\text{edge dist.} = 44 \text{ mm}$   
 $44 \text{ mm}$



$$A_n = (s - (db + 4))t = 2453.6 \text{ mm}^2$$

$$A_{gv} = (7p + \text{edge})t = 8090.0 \text{ mm}^2$$

$$T_r = 2(0.75(0.6 * A_n * F_u + 0.6 * A_{gv} * (F_y + F_u) * 0.5)) = 4174.1 \text{ kN}$$

### Bolt Spacing

$\text{Min } o/c = 2.7(db) = 69 \text{ mm} \text{ ok}$   
 $\text{Max edge} = 150 \text{ mm or } 12(20) = 305 \text{ mm} \text{ ok}$   
 $\text{Min edge} = 32 \text{ mm or } 44 \text{ mm} \text{ ok}$   
 $\text{Min end} = 1.5db = 38 \text{ mm} \text{ ok}$

### Plug Shear

$$A_{gv} = 4 * (7p + \text{edge}) * t = 35560.0 \text{ mm}^2$$

$$T_r = 0.75 * (0.6 A_{gv} (F_y + F_u) 0.5) = 6360.8 \text{ KN}$$

Strength of plate in tension ok!

$t_p = 25.4 \text{ mm} \text{ or } 1 \text{ in}$   
 $F_{up} = 450 \text{ MPa}$   
 $F_{ub} = 825 \text{ MPa}$   
 $A_b = 507 \text{ mm}^2$   
 $n_b = 10$   
 $n_{bearing} = 8$

bolts for bearing

### Bolts

For bolts assume worst case thread in plane

$$T_r = 0.75 * 0.8 * A_b * F_u * n_b = 2509.6 \text{ KN}$$

$$V_r = 0.7 * 0.6 * 0.8 * n_b * 1 * A_b * F_u = 2810.8 \text{ KN}$$

$$B_r = 3 * 0.8 * n_b * t_p * d_b * F_{up} = 4630.5 \text{ KN}$$

$t = 21.1 \text{ mm}$

Also  $L_{connection} = 280 \text{ mm} < 15d_b = 381 \text{ mm}$   
 No further reduction to  $V_r$ .

**Slip critical check**  $\longrightarrow$  **this controls!**

Take worst case factors

$k_s = 0.33$   $m = 1$

$c_1 = 0.82$  for A325 bolts

$V_s = 0.53 * c_1 * k_s * m * n * A_b * F_u = 599.9 \text{ kN}$  ok

**Service limit for fatigue**  $\rightarrow$  stress/bolt =  $67.1 \text{ MPa} < 214 \text{ MPa}$

**Also**

$T_o = 227 \text{ kN}$

$n = 5$

$A_p = 11962.3 \text{ mm}^2$

$T_{sep} = 236.6 \text{ kN} > 34 \text{ kN per bolt}$  ok

Additional tensile force in bolt due to  $M_z$  moment:

Assume an increase of 80% due to prying forces!

Max force at the furthest left up and bottom bolt adding to the existing tension force!

Moment arm =  $153.52 \text{ mm}$

Force/per 2 edge bolts =  $340.0 \text{ KN}$

So Force/bolt =  $170.0 \text{ kN}$

Total force =  $233.24 \text{ kN} < T_r = 251.0 \text{ KN}$  ok

If no prying forces =  $204.0$  its ok

**Fillet Welds**  
 Electrode E49XX for A572 Gr.50 or 350W  
 base metal

Choose for 500KN shear only!

$X_u = 490 \text{ MPa}$

$V_r = 0.67 * 0.67 * A_m * F_u = 250 \text{ kN} \rightarrow A_m = 1614 \text{ mm}^2$  controls!

or

$V_r = 0.67 * 0.67 * 0.707 * A_m * X_u * 1 = 250 \text{ kN} \rightarrow A_m = 1608 \text{ mm}^2$

For  $\theta = 0$  and one orientation fillet welds

**Size limitations**

Max D

For  $t_1 = 25.4 > 6 \rightarrow D < 23.4 \text{ mm}$

Min D

For  $20 \text{ mm} < t_2 \rightarrow D > 8 \text{ mm}$

L> 40 mm So D= 8 mm  
 or L<sub>req</sub>= 202 mm  
 L> 32 mm (weld length will be revised. Use full plate length for now)

**SHEAR-TENSION INTERACTION BOLTS**

$V/V_s + 1.9T/(nA_bF_u) < 1 \rightarrow$  0.83 <1 ok  
 $(V_f/V_r)^2 + (T_f/T_r)^2 < 1 \rightarrow$  0.05 <1 ok

**WEB CHECKS** for W360x196 Extra slenderness and connection checks for the main beams

h/w 19.5  
 $621(k_v/f_y)^{1/2}$  77.3  
 $502(k_v/f_y)^{1/2}$  54.6  
 $h/w \leq 439(k_v/f_y)^{1/2}$

**STOCKY WEB**

$F_s = 0.66F_y$   
 $F_s$  227.7 Mpa  
 $\Phi$  0.9  
 $A_w$  5241.44 mm<sup>2</sup>  
 $V_r$  1074.1 kN Full section

diameter of bolt holes 29.4 mm<sup>2</sup>  
 area lost from holes 964.3 mm<sup>2</sup>  
 $V_r(\text{reduced})$  876.5 kN Reduced section

$V_r > V_f$  OK

**Yielding / fracture**

$T_f$  500 kN  
 $\Phi$  0.9  
 $A_g$  3837.6 mm<sup>2</sup>  
 $F_y$  345 Mpa

$T_r$  1191.6 kN

$T_r > T_f$  OK

$\Phi_u$  0.75  
 $A_n$  1582.6 mm<sup>2</sup>  
 $A_{ne}$  1582.6 mm<sup>2</sup> 12.3.3.1  $A_{ne} = A_n$   
 $F_u$  450 Mpa

$T_r$  534.1 kN

$T_r > T_f$  OK

### Block Shear

$\Phi_u$  0.75  
 $U_t$  0.6 Web-Connect  
 $A_n$  1582.6 mm<sup>2</sup>  
 $F_u$  450 Mpa

$A_{gv}$  11480 mm  
 $F_y$  345 Mpa

$T_r$  2374 kN

$T_r > T_f$  OK

### Plug Shear

$\Phi_u$  0.75  
 $A_{gv}$  22960

$T_r$  4107 kN

$T_r > T_f$  OK

### Coped Beams

p.9-9 AISC

$d$ = 372 mm  $\longleftrightarrow$  14.65 in  
 $d_c$ = 74.4 mm  $\leq 0.2d$  2.93 in  
 $c$ = 178.8 mm  $> 0.2d$  7.04 in  
 $f_d$ = 2  
 $h_o$ = 297.6 mm 11.72 in  
 $t_w$ = 0.65 in  
 $F_{cr}=F_yQ$   
 $F_y$ = 50 ksi  
 $\lambda$ = 0.363  $< 0.7$   
 $Q$ = 1  
so  $F_{cr}=F_y$  ok

### C.5. Actuator-to-distribution beam connection

Summary: The bolted connection of the W360x91 distribution beam to the 426x254x20/15mm plate is described below. A total of 12 bolts 1" A325 are used. Four holes were subsequently added to the plate to facilitate the placement of the actuator; as such, in the end the plate was 782x254x40 mm.

Use same bolts as before	1" A325	To=	227	kN min pretension
$t_p=$	20 mm	Fu=	450	MPa
$t_f=$	16.8 mm	Fy=	345	MPa
$A_b=$	507 mm <sup>2</sup>	<b>Tension=</b>	154.3	kN per bolt( $M_z$ )
$A_g=$	5080 mm <sup>2</sup>	<b>Shear=</b>	540	kN
$d_b=$	25.4 mm	<b>Moment=</b>	75.6	kNm
		<b>eccentricity=</b>	140	mm
		<u>Plate:</u>		mm
		t=	20	
		b=	254	
		d=	426	

#### Check plate

#### Net section fracture

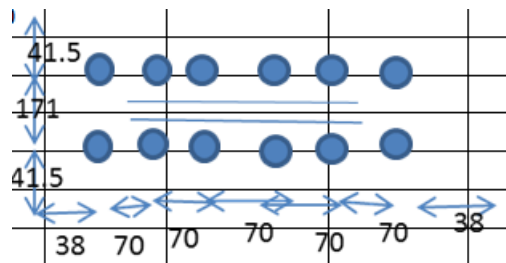
$$A_n=(A_g-2(d_b+4)*t)= 3904 \text{ mm}^2$$

No shear lag for the plate connected to the flange

$$T_r=0.75*A_{ne}*450= 1317.6 \text{ kN} >540\text{KN}$$

#### Block Shear

s=	171 mm
p=	70 mm
end dist=	38 mm
edge dist.=	41.5 mm
	41.5 mm



$$A_n=(s-(d_b+4))t= 2832.00 \text{ mm}^2$$

$$A_{gv}=(2p+edge)t= 7760 \text{ mm}^2$$

$$T_r= 2(0.75(0.6*A_n*F_u+0.6*A_{gv}*(F_y+F_u)*0.5))= 3923.1 \text{ kN}$$

#### Bolt Spacing

Min o/c=	2.7( $d_b$ )= 69	mm	mm	ok
Max edge=	150mm or 12(25.4)= 304.8	mm	mm	ok

Min edge=	32mm or 44mm		mm	ok
Min end=	1.5d <sub>b</sub> = 38	mm	mm	ok

### Plug Shear

$A_{gv}=4*(2p+edge)*t=$	31040	mm <sup>2</sup>		
$T_r=0.75*(0.6A_{gv}(F_y+F_u)0.5)=$		5552.3	KN	

Strength of plate in tension ok!

t <sub>p</sub> =	15	mm	or 1in
F <sub>up</sub> =	450	MPa	
F <sub>ub</sub> =	825	MPa	
A <sub>b</sub> =	507	mm <sup>2</sup>	
n <sub>b</sub> =	12		
n <sub>bearing</sub> =	10		

bolts for bearing

### Bolts

For bolts assume worst case thread in plane

$T_r=0.75*0.8*A_b*F_u*n_b=$	3011.6	KN
-----------------------------	--------	----

$V_r=0.7*0.6*0.8*n_b*1*A_b*F_u=$	1686.5	KN
----------------------------------	--------	----

$B_r=3*0.8*n_b*t_p*d_b*F_{up}=$	4114.8	KN
---------------------------------	--------	----

t=15mm thinner plate

### Slip critical check → controls!

Take worst case factors

k <sub>s</sub> =	0.33		m=	1
c <sub>1</sub> =	0.82	for A325 bolts		
$V_s=0.53*c_1*k_s*m*n*A_b*F_u=$		719.9	KN	>540KN OK

**Service limit for fatigue** --> stress/bolt= 24.7 MPa < 214MPa

### Also

T <sub>o</sub> =	227	KN		
n=	7			
A <sub>p</sub> =	22459.1	mm <sup>2</sup>		
T <sub>sep</sub> =	232.1	KN	>	12.5 kN per bolt ok

Welds must resist the following force:

Force:	540	kN
Eccentricity:	0.07	m
Moment:	37.8	kNm
Force couple:	270	kN
Total force:	810	kN
For each side:	405	kN for each side of 254mm plate
For each weld:	202.5	kN since two welds per side!

### Fillet Welds

Electrode E49XX for A572 Gr.50 or 350W base metal

$X_u =$	490	MPa
$V_r = 0.67 * 0.67 * A_m * F_u =$	202.5	kN --> $A_m = 1308 \text{ mm}^2$
or		
$V_r = 0.67 * 0.67 * 0.707 * A_m * X_u * 1 =$	202.5	kN --> $A_m = 1302 \text{ mm}^2$
For $\theta = 0$ and one orientation fillet welds		

### Size limitations for welds

Max D

For $t_1 = 20 > 6 \rightarrow D <$	42	mm
------------------------------------	----	----

Min D

For $20 \text{mm} < t_2 \rightarrow D >$	8	mm
--	---	----

$t_2 = 75 \text{mm}$  adapter plate

$L >$	40	mm	So	$D =$	8	mm
-------	----	----	----	-------	---	----

or

$L_{req} =$	163	mm
-------------	-----	----

$L >$	32	mm
-------	----	----

$D =$	8	mm
-------	---	----

$L_{req} =$	163	mm
-------------	-----	----

### Plate Stability (AISC)

$t =$	15	mm	
$L =$	140	mm	
$r = t / (12^{1/2}) =$	4.33	mm	
$K =$	1.2		
$KL/r =$	38.8	<200 ok	
$A =$	2100	$\text{mm}^2$	
$F_e = \pi^2 E / (KL/r)^2 =$	1311.3	Mpa	
$\phi R_n = 0.9 (0.658^{(F_y/F_e)}) * F_y * A =$	584.1	kN ok	<540kN ok

and Whitmore section buckling strength:

$\phi R_{wb} = 0.75 F_e * W_{nt} * t =$	2065.4	kN
---	--------	----

Some other checks to be sure...

And basically  $A_p F_p > F_{total}$  force

So  $A = 2100$  so  $A * f = 724.5$  ok  
 $F_p = 345$

$b_e / t < 200 / (F_y^{1/2}) = 10.8$  at least class 3

### C.6. Actuator to main beam connection

Summary: A325 1" bolts  $n=10$  bolted at flange of W360x262 (W360x196 in the end) with 398x356x50 plate (575x374x60 final size). Actuator connected on a 609x398x65mm plate (595x374x60 final size). The two plates are connected using a diagonal section welded at both of them of 705x609x356x65 (787x553x515x60). Extra slotted holes were added to facilitate the placement of the actuator (14 in total); this explains the final sizes of the plates in the fabrication drawings as well as the thicknesses available in practice.

Use same bolts as before	1" A325	$T_o = 227$	kN min pretension
$t_p = 50$	mm	$F_u = 450$	MPa
$t_f = 33.3$	mm	$F_y = 345$	MPa
$A_b = 507$	mm <sup>2</sup>		
$A_g = 19900$	mm <sup>2</sup>	<b>Shear = 540</b>	kN Uplift
$d_b = 25.4$	mm	<b>Moment = 164.7</b>	kNm --> Mz
Comment:		$e = 305$	mm
			<u>Plate:</u> mm

#### Check plate

Choose 10 bolts with same distances as before!

$t = 50$   
 $b = 398$   
 $d = 356$

#### Net section fracture

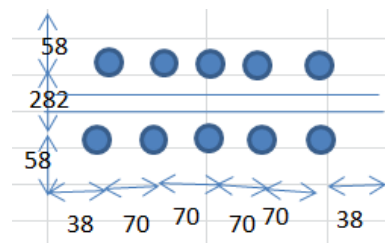
$A_n = (A_g - 2(d_b + 4) * t) = 16960$  mm<sup>2</sup>

No shear lag for the plate connected to the flange

$T_r = 0.75 * A_{ne} * 450 = 5724.00$  kN

#### Block Shear

$s = 232$  mm  
 $p = 70$  mm  
 end dist = 38 mm  
 edge dist. = 83 mm  
 83 mm



Bolt details:	p.6-158HB				
F=	1.24	in -->	31.5	mm	421mm
H <sub>b</sub> =	0.50	in	11.9	mm	
Thread_length=	1.4	in	34.9	mm	
Bolt_length=	3.5	in	88.9	mm	
W=	1.25	in	31.8	mm	
Hnut=	0.73437	in	18.7	mm	
Area=	0.334	in <sup>2</sup>	A <sub>b</sub> =	507	mm <sup>2</sup>

Threads in shear plane!

$$A_n = (s - (d_b + 4))t = 10130.0 \text{ mm}^2$$

$$A_{gv} = (2p + \text{edge})t = 15900 \text{ mm}^2$$

$$T_r = 2(0.75(0.6A_n F_u + 0.6A_{gv}(F_y + F_u)0.5)) = 9790.9 \text{ kN}$$

### Bolt Spacing

Min o/c=	2.7(d <sub>b</sub> )=	69	mm	mm	ok
Max edge=	150mm or 12(25.4)=	304.8	mm	mm	ok
Min edge=	32mm or 44mm			mm	ok
Min end=	1.5d <sub>b</sub> =	38	mm	mm	ok

### Plug Shear

$$A_{gv} = 4(2p + \text{edge})t = \frac{6360}{0} \text{ mm}^2$$

$$T_r = 0.75(0.6A_{gv}(F_y + F_u)0.5) = 11376.5 \text{ kN}$$

Strength of plate in tension ok!

t <sub>p</sub> =	50	mm	or 1in
F <sub>up</sub> =	450	MPa	
F <sub>ub</sub> =	825	MPa	
A <sub>b</sub> =	507	mm <sup>2</sup>	
n <sub>b</sub> =	10		
n <sub>bearing</sub> =	8		

bolts for bearing

### Bolts

For bolts assume worst case thread in plane

$$T_r = 0.75 * 0.8 * A_b * F_u * n_b = 2509.7 \text{ kN}$$

$$V_r = 0.7 * 0.6 * 0.8 * n_b * 1 * A_b * F_u = 1405.4 \text{ kN}$$

$$B_r = 3 * 0.8 * n_b * t_p * d_b * F_{up} = 10972.8 \text{ kN}$$

**Slip critical check**

→ **controls!**

$$k_s = 0.33 \quad m = 1$$

$$c_1 = 0.82 \quad \text{for A325 bolts}$$

$$V_s = 0.53 * c_1 * k_s * m * n * A_b * F_u = 599.9 \text{ kN} > 540 \text{ kN} \quad \text{ok}$$

**Service limit for fatigue** --> stress/bolt = 33.3 MPa < 214 MPa

**Also**

$$T_o = 227 \text{ KN}$$

$$n = 9$$

$$A_p = 41766.6 \text{ mm}^2$$

$$T_{sep} = 229.8 \text{ KN} > 16.9 \text{ kN per bolt} \quad \text{so ok}$$

**Prying forces**

Assume 1.2 increase so for 10 bolts:

Now for the moment:

Based on triangular force distribution of the bolts with respect to the point of the intersection of the vertical and horizontal plate max force for the two edge bolts is = 337.5  
 So total for each bolt: 168.8  
 Tr per bolt: 251 kN ok

**Fillet Welds**

Electrode E49XX for A572 Gr.50 or 350W base metal

1. 398x356x50 to 705x609x356x65 (two fillet welds, one at each side)

$$X_u = 490 \text{ MPa}$$

$$V_r = 0.67 * 0.67 * A_m * F_u = 270 \text{ kN} \rightarrow A_m = 1743 \text{ mm}^2 \quad \text{controls}$$

or

$$V_r = 0.67 * 0.67 * 0.707 * A_m * X_u * 1 = 270 \text{ kN} \rightarrow A_m = 1736 \text{ mm}^2$$

For  $\theta=0$  and one orientation fillet welds

**Size limitations**

Max D

$$\text{For } t_1 = 50 > 6 \rightarrow D < 48 \text{ mm}$$

Min D

$$\text{For } 20 \text{ mm} < t_2 \rightarrow D > 8 \text{ mm}$$

$t_2 = 65$

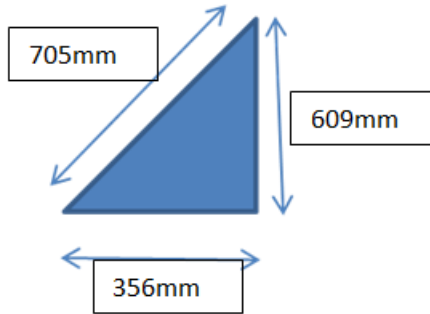
$$L > 40 \text{ mm} \quad \text{So } D = 8 \text{ mm}$$

$$\text{or } L_{req} = 218 \text{ mm}$$

$$L > 32 \text{ mm}$$

**Slenderness limit!**

$$3/4(E/F_y)^{(1/2)} = 18.06 > L_e/t = 705.4/65 = 10.9$$



stress applied  $(540)/\text{area} = 13.64 \text{ MPa} < F_y$  so ok  
 Welds must resist the 540kN forces  
 Also compressive or tensile force of 272.5kN for the plate

**Fillet Welds**

Electrode E49XX for A572 Gr.50 or 350W base metal

609x398x65 to 705x609x356x65 (two fillet welds, one at each side)

$$X_u = 490 \text{ MPa}$$

$$V_r = 0.67 * 0.67 * A_m * F_u = 270.0 \text{ kN} \rightarrow A_m = 1743 \text{ mm}^2$$

or

$$V_r = 0.67 * 0.67 * 0.707 * A_m * X_u * 1 = 270.0 \text{ kN} \rightarrow A_m = 1736 \text{ mm}^2$$

For  $\theta=0$  and one orientation fillet welds

**Size limitations for welds**

Max D

$$\text{For } t_1 = 65 > 6 \rightarrow D < 62 \text{ mm}$$

Min D

$$\text{For } 20\text{mm} < t_2 \rightarrow D > 8 \text{ mm}$$

$t_2 = 65\text{mm}$

$$L > 40 \text{ mm} \text{ So } D = 8 \text{ mm}$$

$$\text{or } L_{req} = 218 \text{ mm}$$

$$L > 32 \text{ mm}$$

$$D = 8 \text{ mm}$$

$$\text{length} = \text{length of plate sizes} \quad L_{req} = 218 \text{ mm}$$

**Plate Stability (AISC)**

for 705x609x356x65 plate

$$t = 65 \text{ mm}$$

$$L = 335 \text{ mm} \text{ assuming half of the diagonal length}$$

$$r = t / (12^{1/2}) = 18.8 \text{ mm}$$

$K=$  1.2  
 $KL/r=$  21.42 <200 ok  
 $A=$  21775 mm<sup>2</sup>  
 $F_e=\pi^2E/(KL/r)^2=$  4300.54 Mpa  
 $\phi R_n=0.9(0.658^{(F_y/F_e)}) * F_y * A=$  6537.9 KN ok  
 And  $A_p F_p > F_{total}$  force  
 So  $A=$  21775 so  $A * f=$  7512.4 ok  
 $F_p=$  345  
 $bel/t < 200 / (F_y^{1/2})=$  10.8 at least class 3  
 $670/65=$  10.3

### C.7. Fixed built-up connection; I-Shapes

The shapes are made of two plates for the flanges of 600x260x40 and 600x280x40, respectively, welded on a 600x272x60 plate for the web. Initially the thickness of the web was considered 70mm and a simple ABAQUS (Dassault-Systems 2013) model of the I-Shape was built applying primarily concentrated load on the location of the bolts at the top and bottom plates. Given the conservative loads assumed in the calculations in the end a 60mm plate was decided for the web.

Figure C.3 illustrates the model.

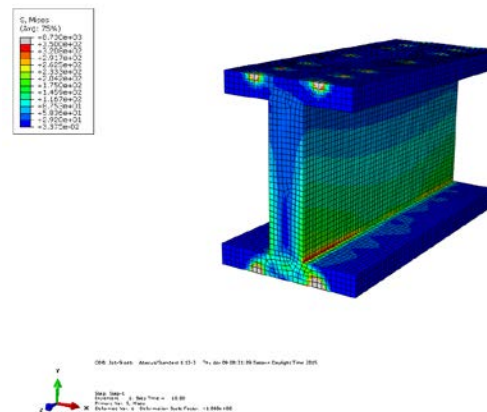


Figure C.3: Built-up I-shapes of fixed connection

### C.8. Roller support system of distribution beam

Summary: 4 rollers (Figure C.4) used (details shown in the figure below) for uplift restraint and support. An HSS 102x76x10 is welded at the top on 2L 152x89x16 angles and bolted with ½” bolts to the rollers. The bottom rollers are bolted directly to the main beam.

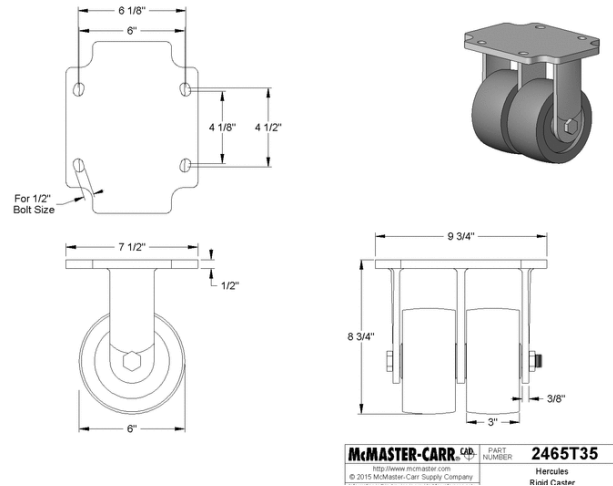


Figure C.4: Rollers for the support of the distribution beam

### C.9. Fabrication drawings

Figures C.5 to C.20 include the fabrication drawings of the test setup.

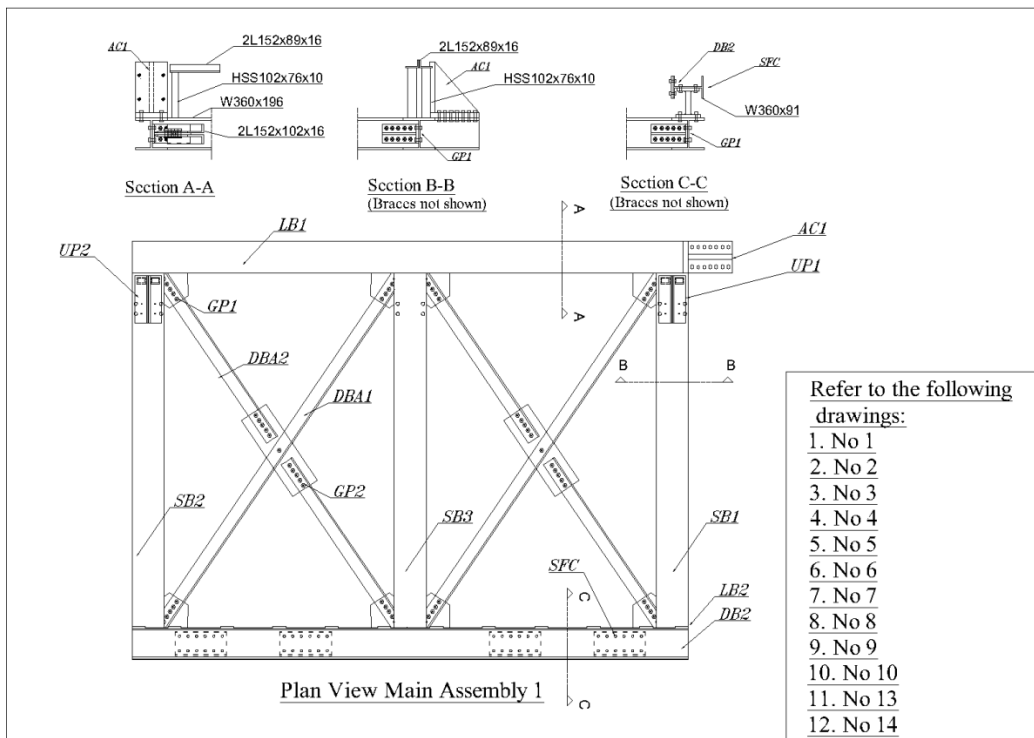


Figure C.5: Test set-up plan view and reference to the related fabrication drawings

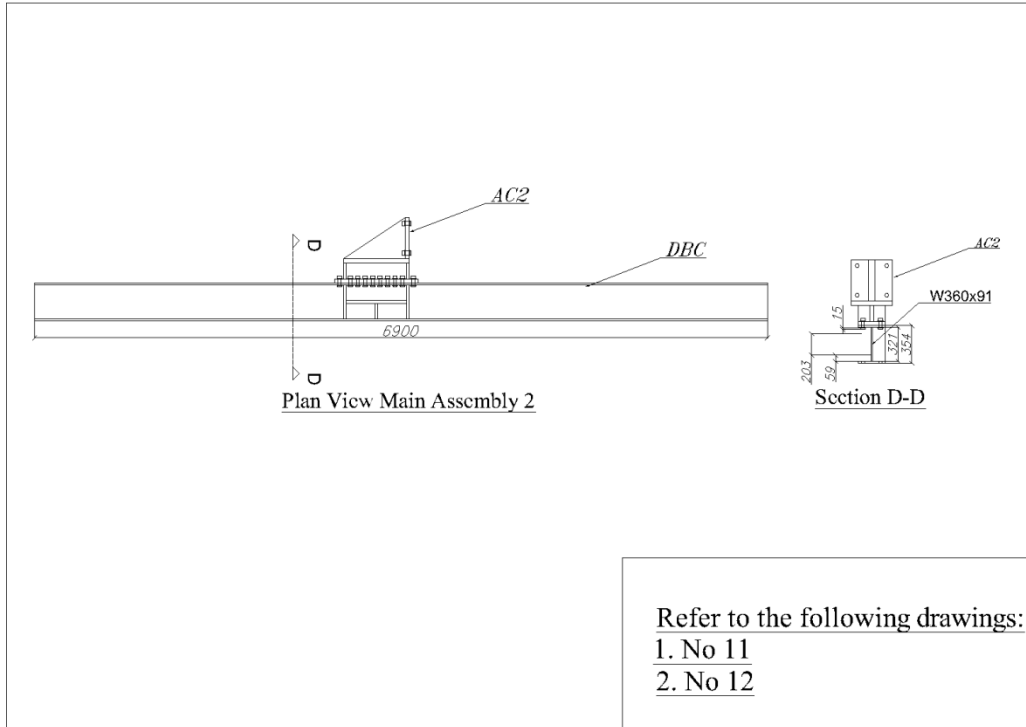


Figure C.6: Distribution beam plan view and reference to the related fabrication drawings

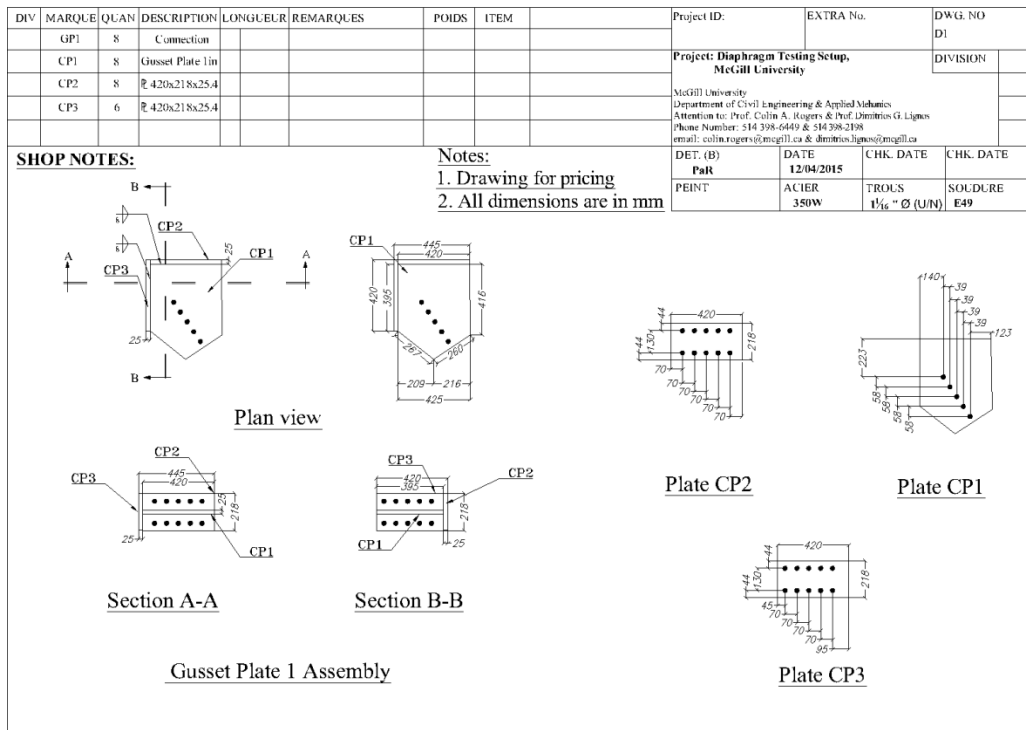


Figure C.7: Main beam-to-beam connections

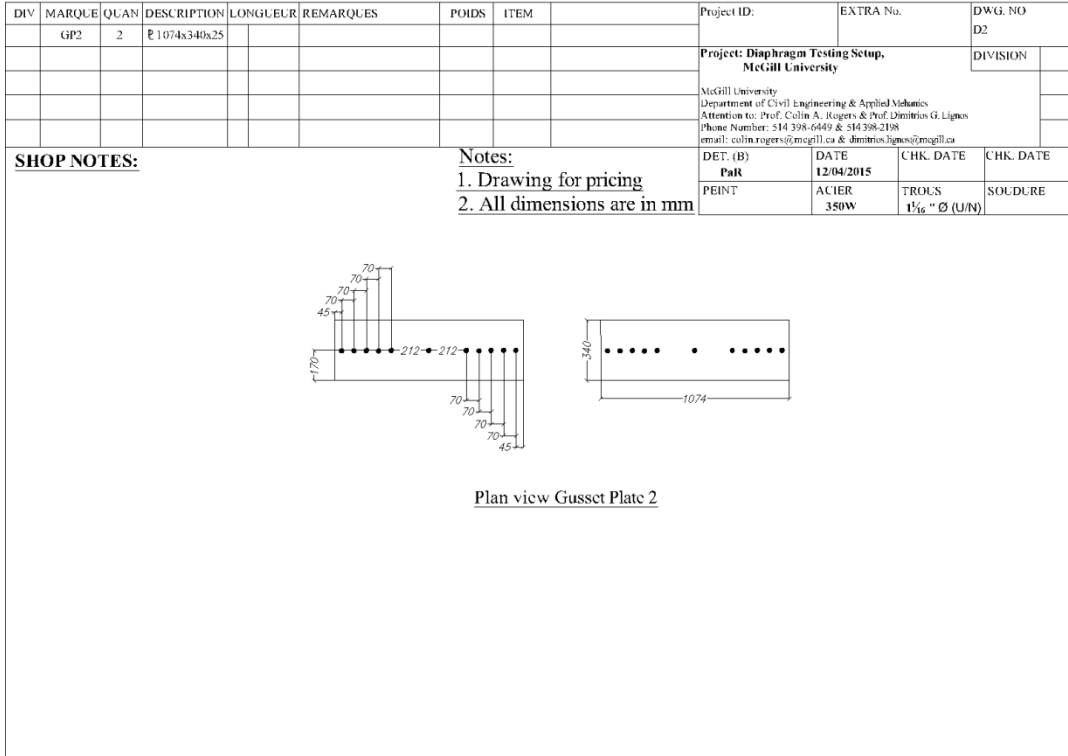


Figure C.8: Double angle-to-angle connection plate (braces)

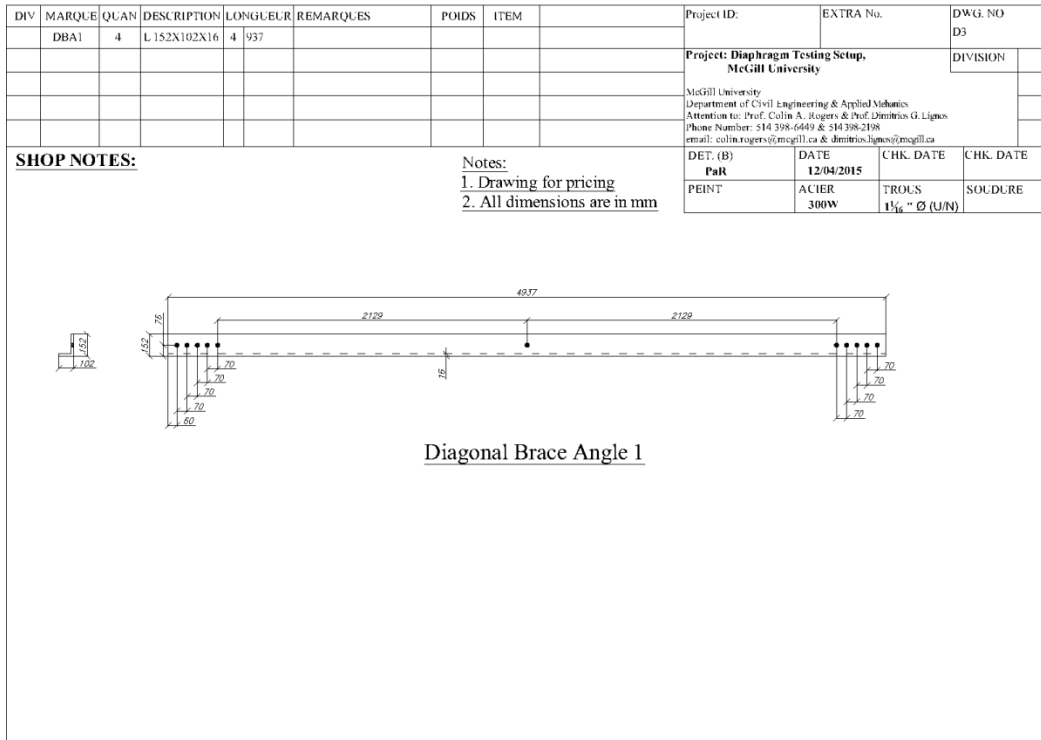


Figure C.9: Diagonal brace angle 1

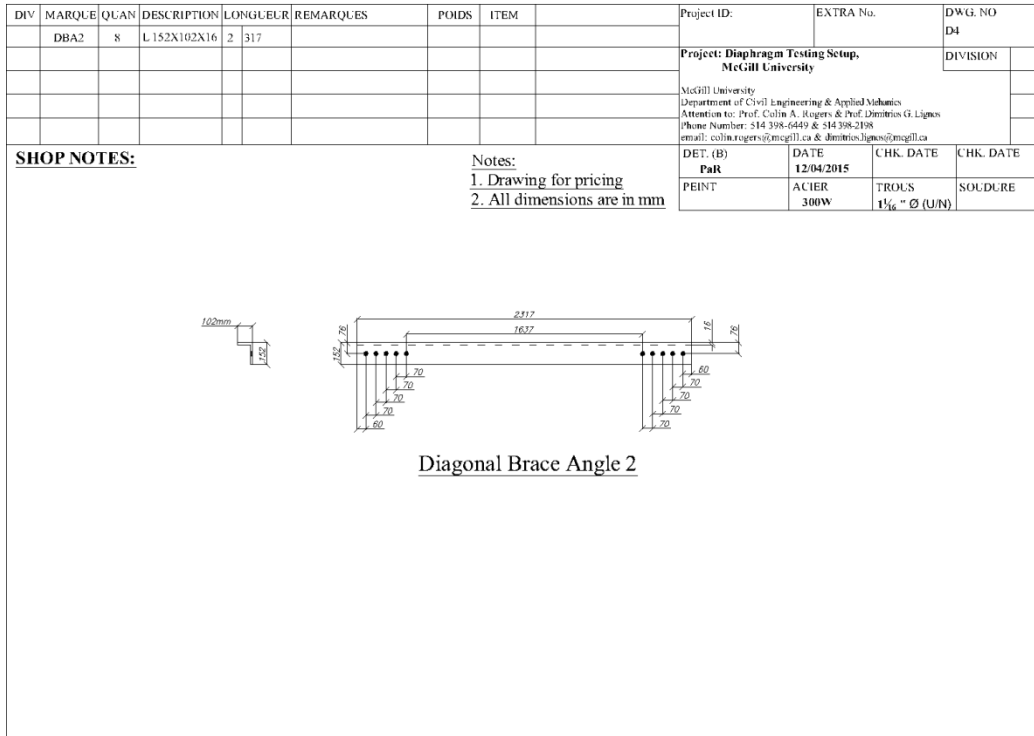


Figure C.10: Diagonal brace angle 2

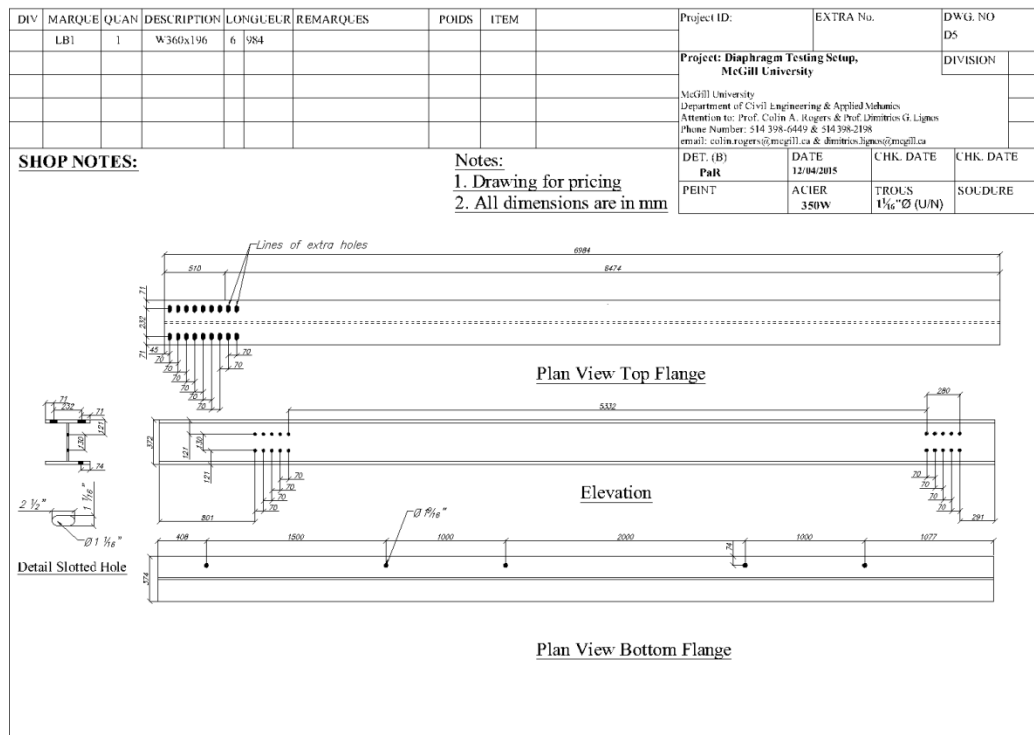


Figure C.11: Main beam connected to actuator

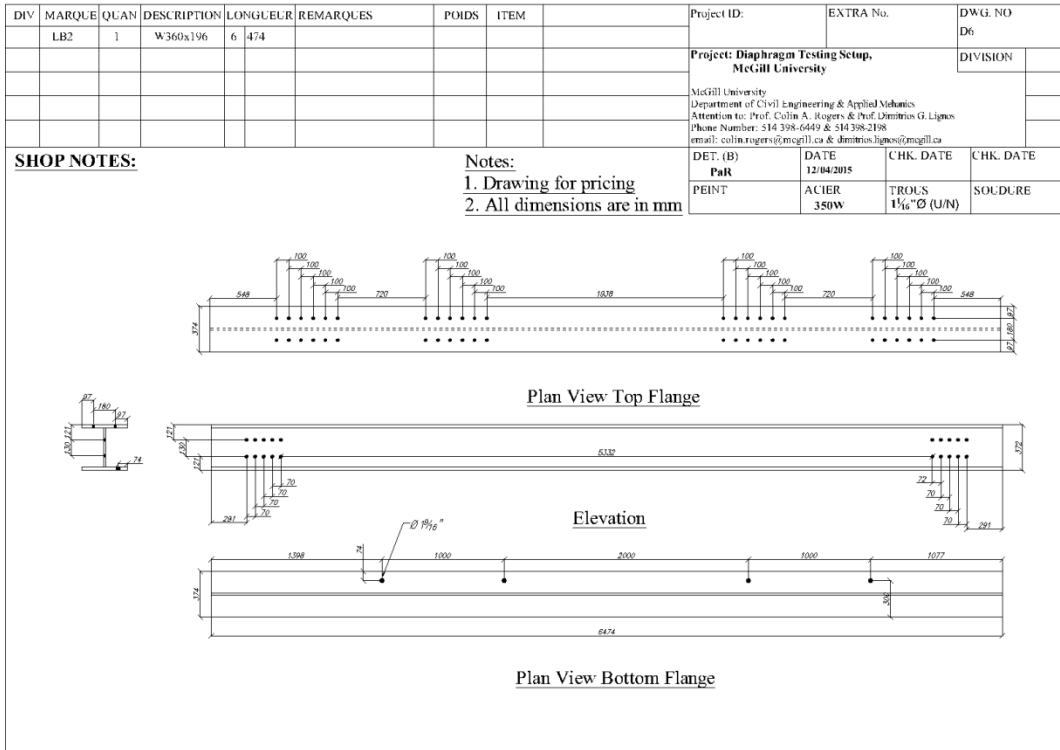


Figure C.12: Main beam connected to built-up I-shapes in fixed connection location

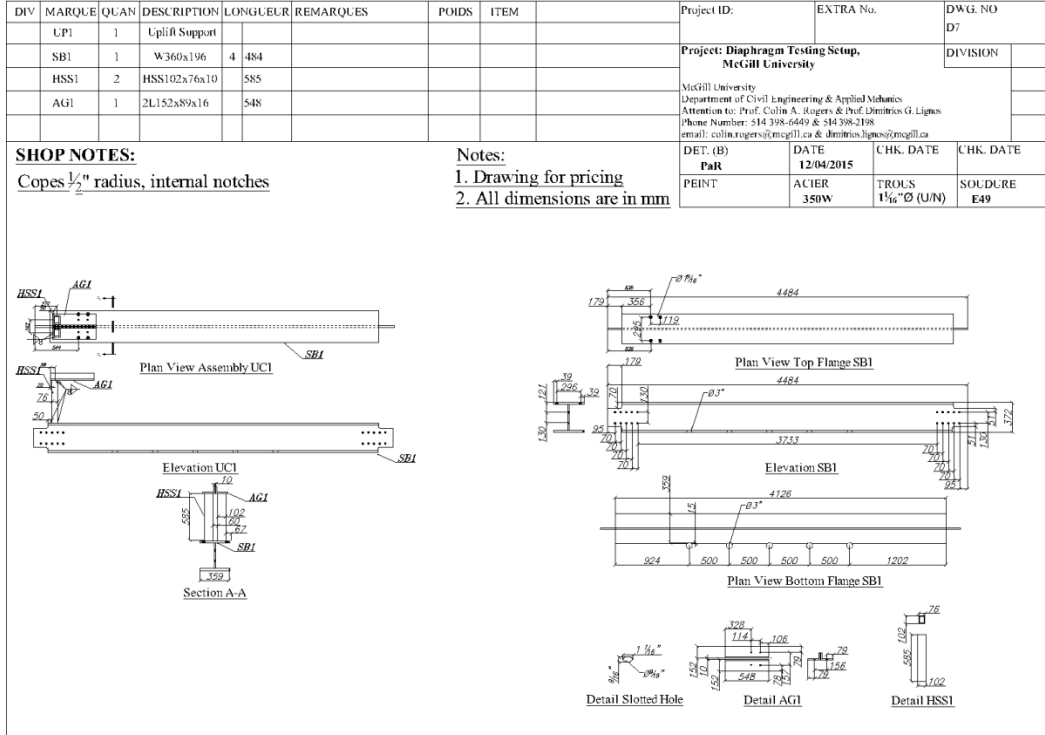


Figure C.13: Main beam 1 connected to the uplift support for the distribution beam

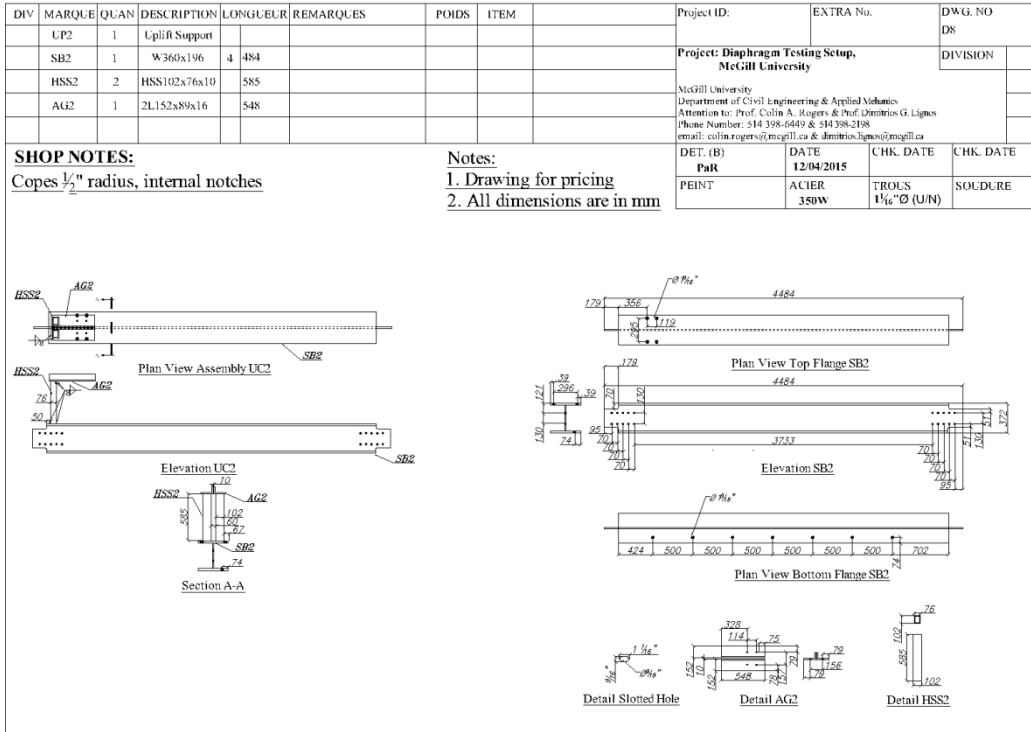


Figure C.14: Main beam 2 connected to the uplift support for the distribution beam

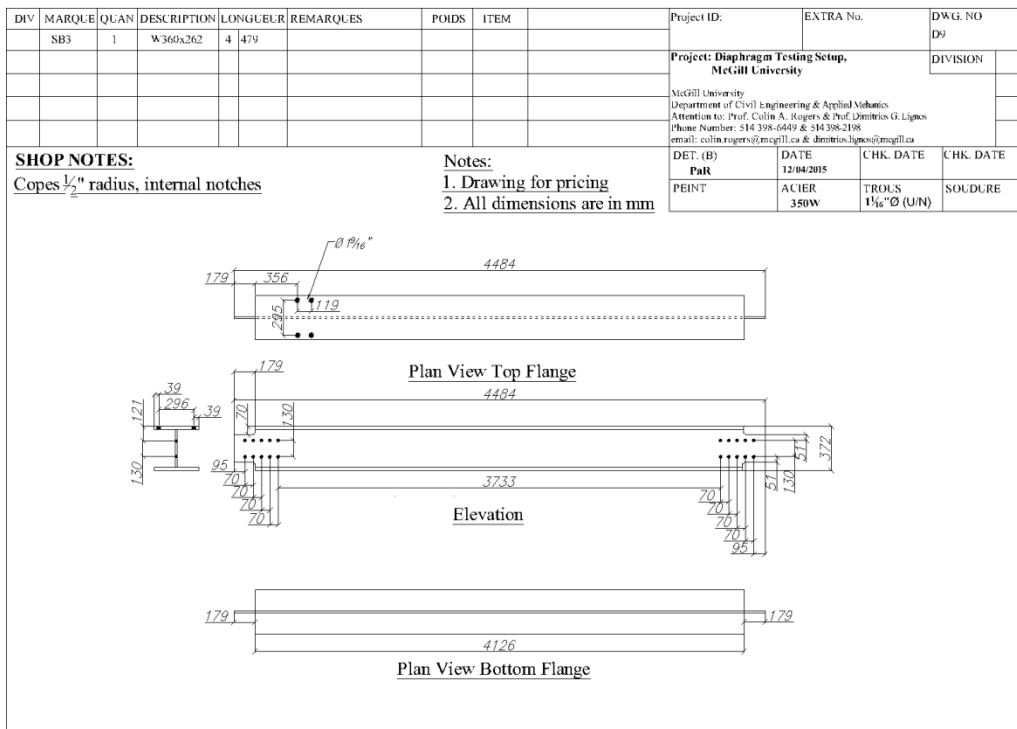


Figure C.15: Centre main beam connected to middle roller support for the distribution beam

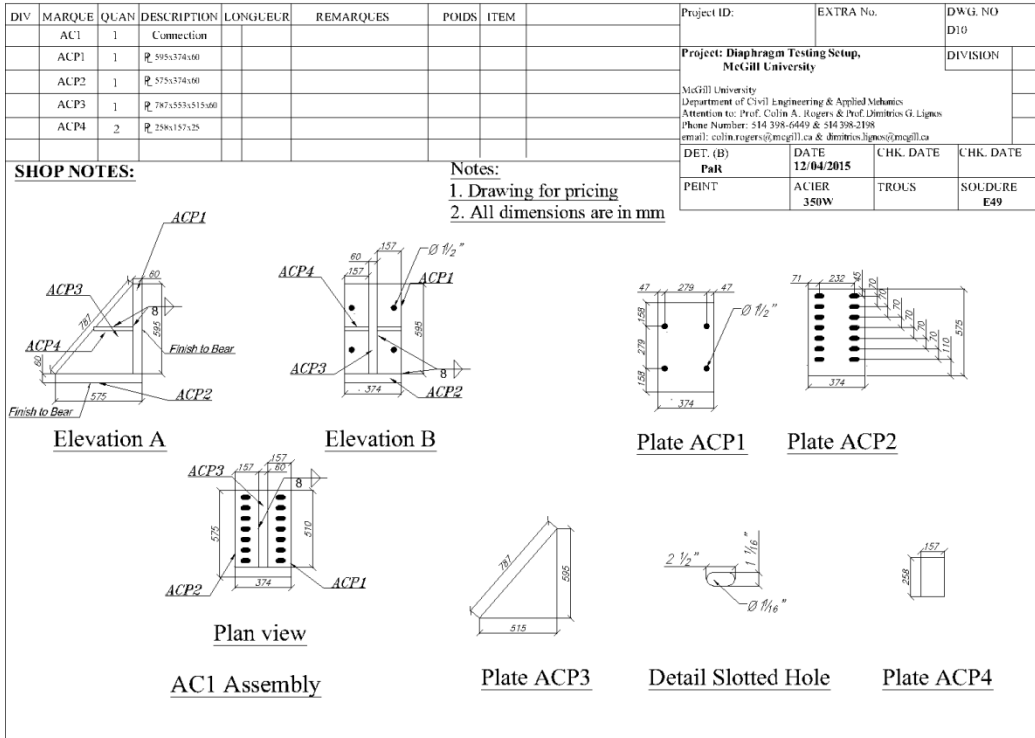


Figure C.16: Actuator-to-main beam connection

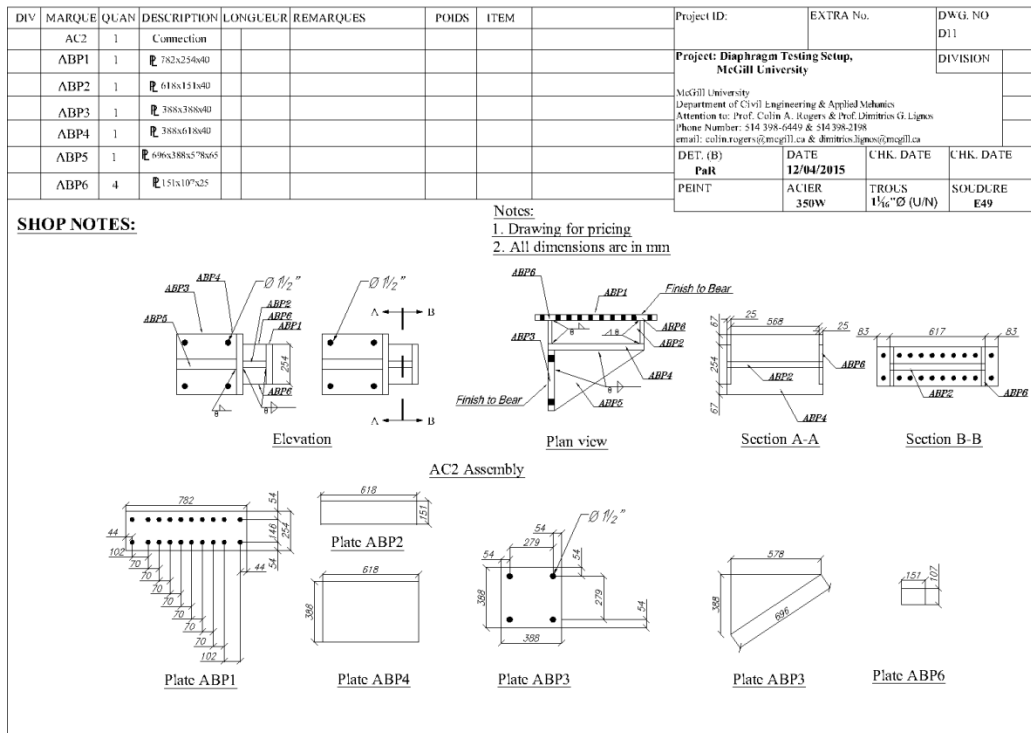


Figure C.17: Actuator-to-distribution beam connection

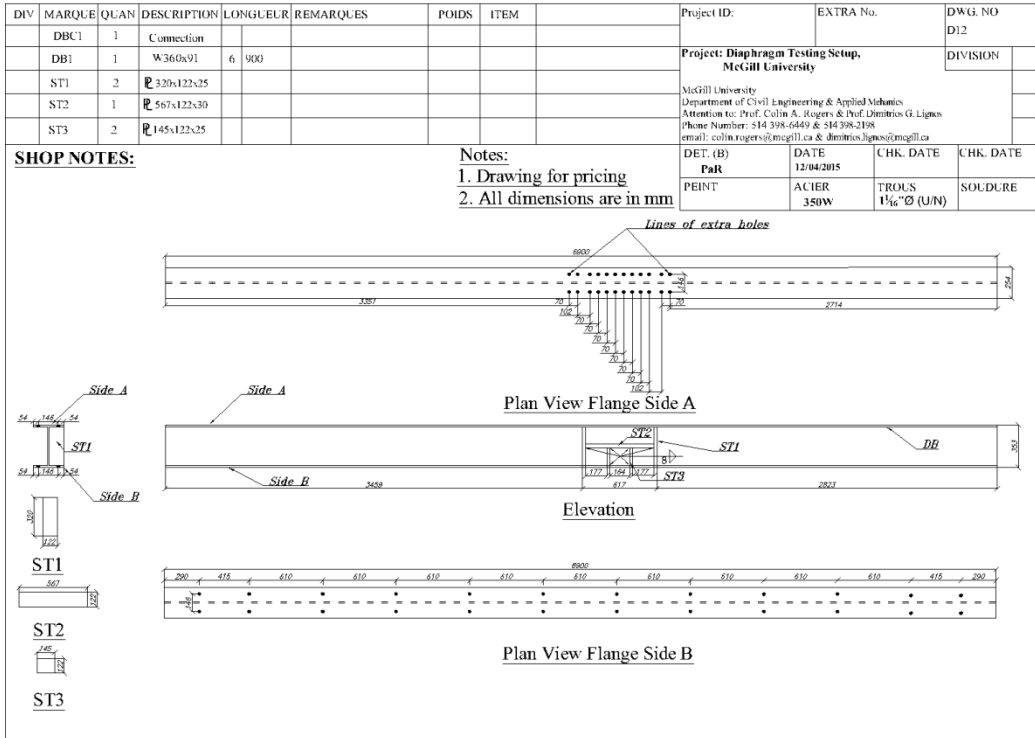


Figure C.18: Distribution beam

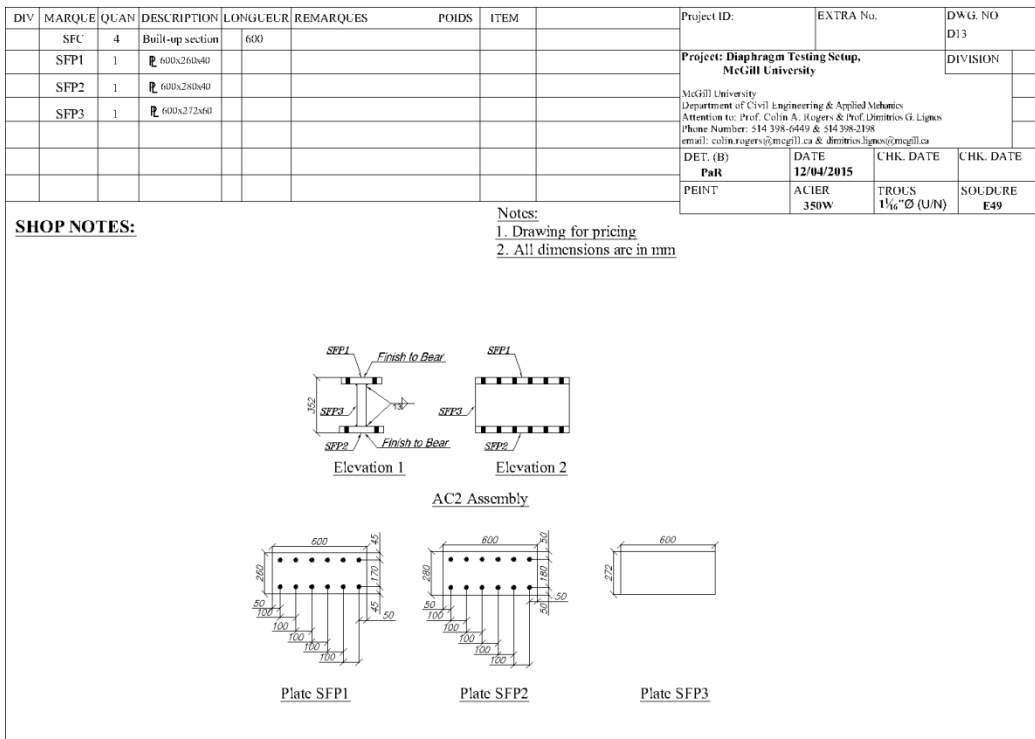


Figure C.19: Built-up I-shapes; fixed connection



## APPENDIX D: SUPPLEMENTAL MATERIAL TEST RESULTS

### D.1- Tensile coupon tests

Table 2.3 in Chapter 2 includes the average tensile properties of steel as obtained from the tensile coupon testing of the rim joists and joists for the floor and roof specimens of the diaphragm experimental program phase 1. Following are the corresponding stress-strain curves and young's modulus obtained for each coupon tested following the nomenclature explained in Table 2.3.

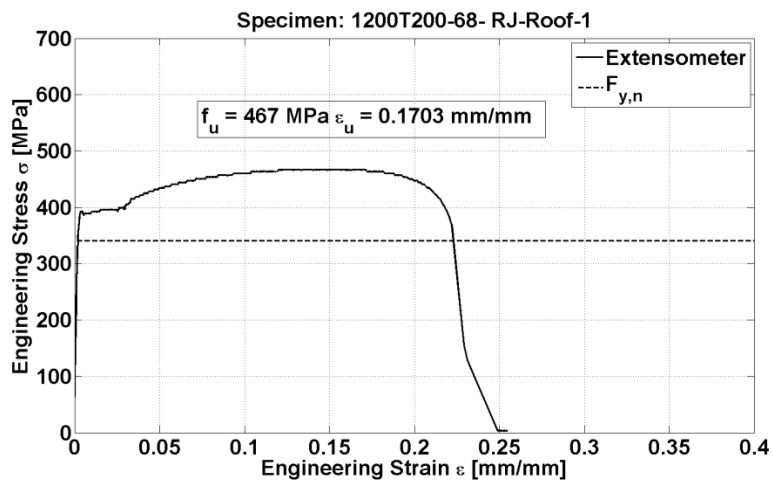


Figure D.1: Stress-strain curve of specimen RJ - Roof - 1

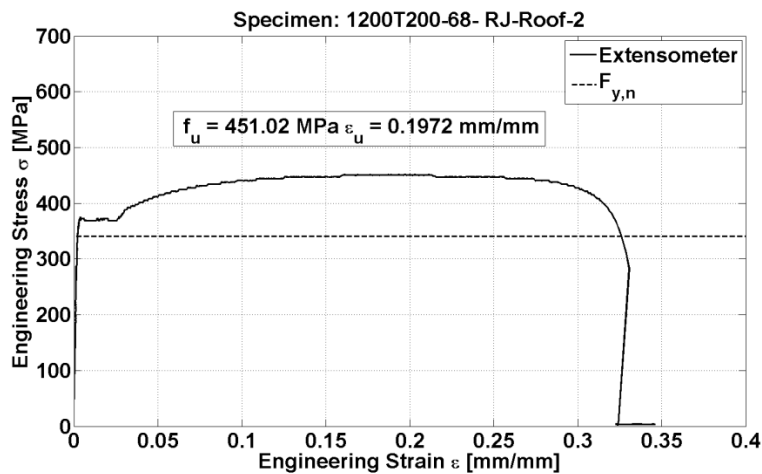


Figure D.2: Stress-strain curve of specimen RJ - Roof - 2

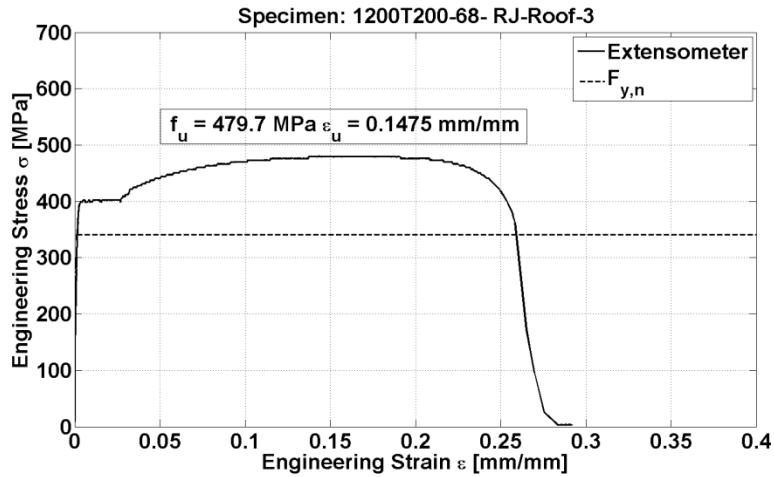


Figure D.3: Stress-strain curve of specimen RJ - Roof - 3

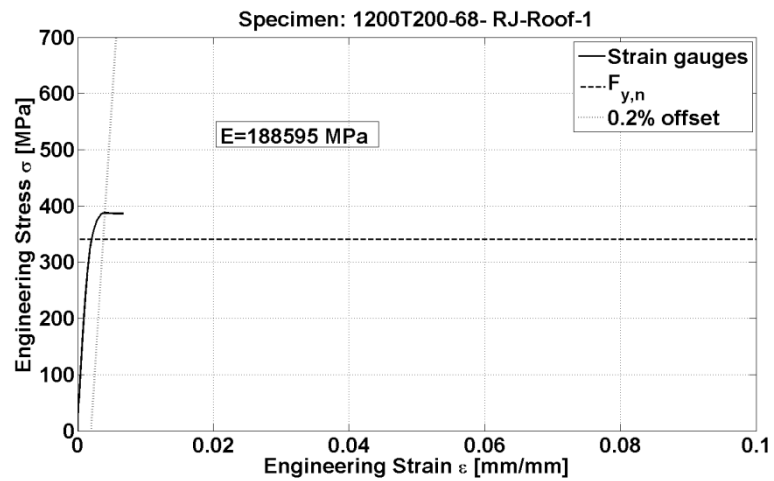


Figure D.4: Young's modulus based on specimen RJ - Roof - 1

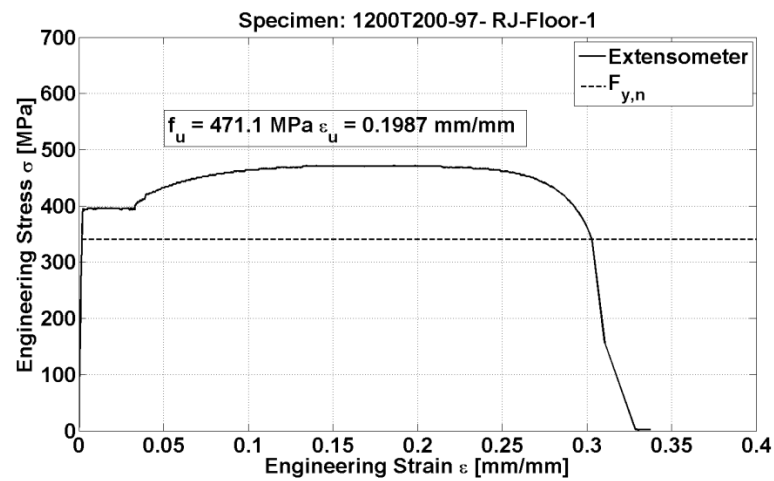


Figure D.5: Stress-strain curve of specimen RJ - Floor - 1

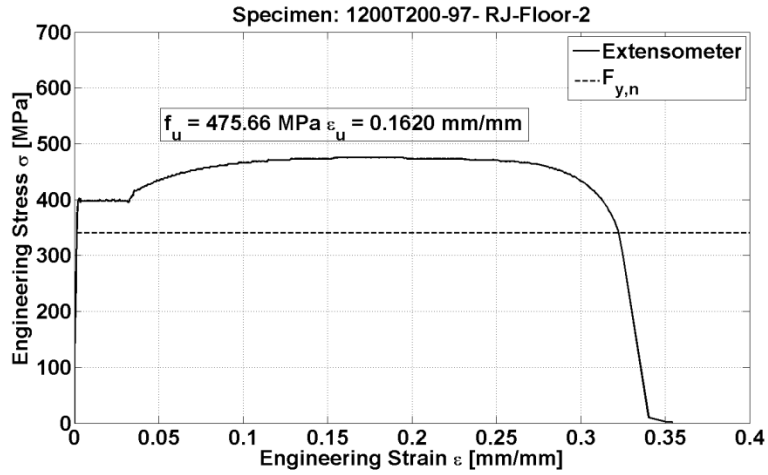


Figure D.6: Stress-strain curve of specimen RJ - Floor - 2

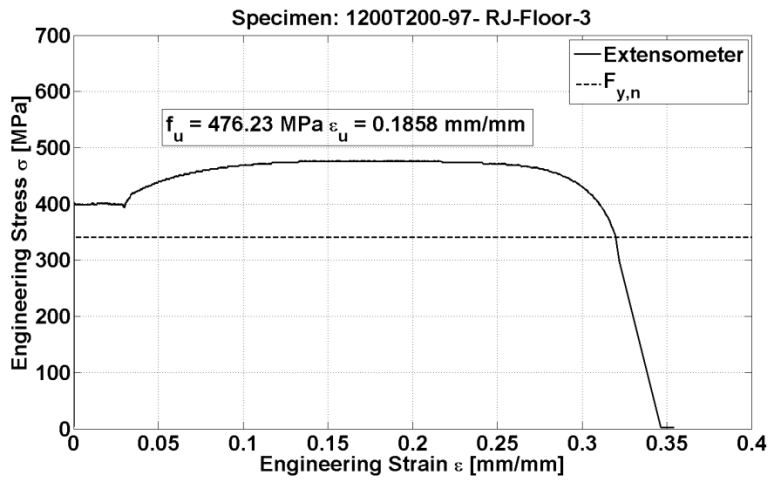


Figure D.7: Stress-strain curve of specimen RJ - Floor - 3

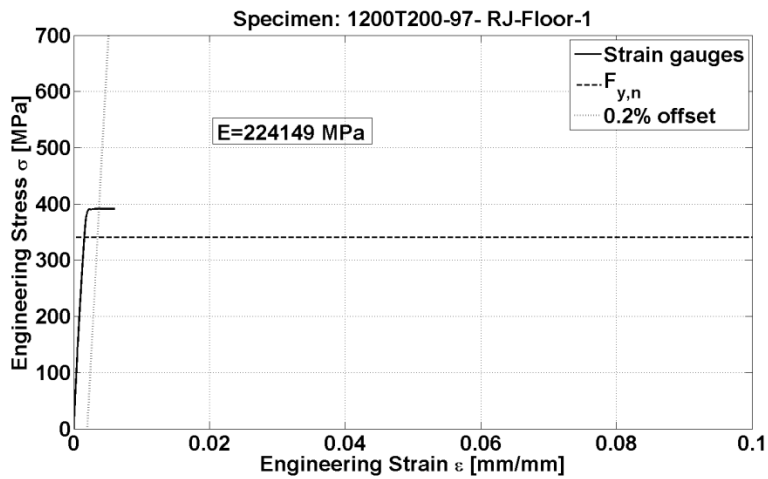


Figure D.8: Young's modulus based on specimen RJ - Floor - 1

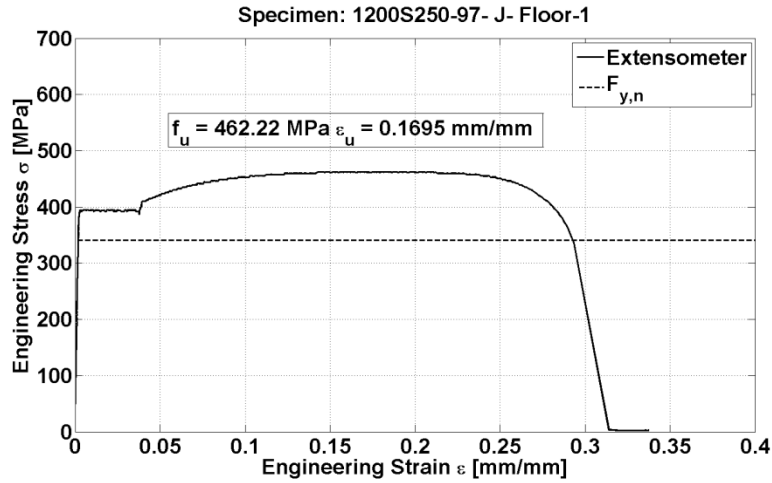


Figure D.9: Stress-strain curve of specimen J - Floor - 1

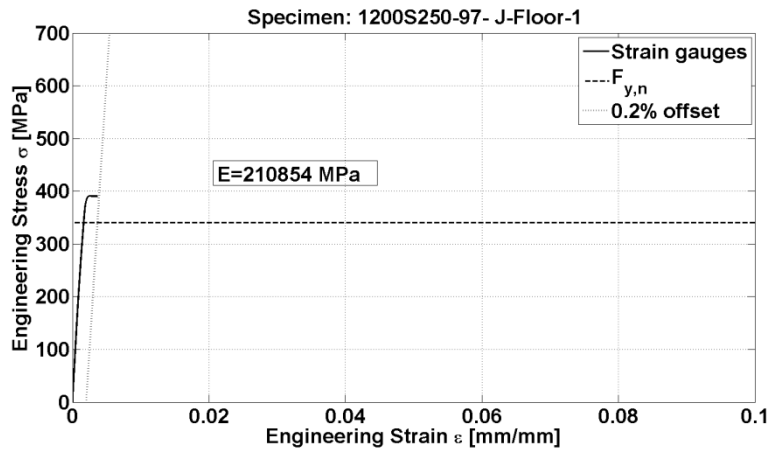


Figure D.10: Young's modulus based on specimen J - Floor - 1

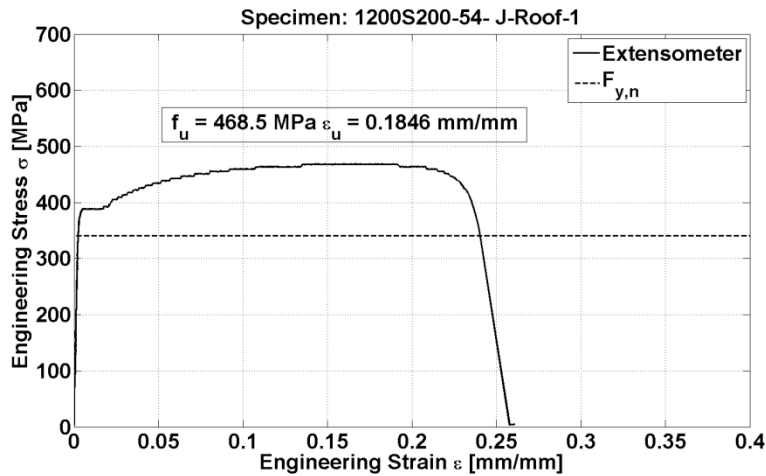


Figure D.11: Stress-strain curve of specimen J - Roof - 1

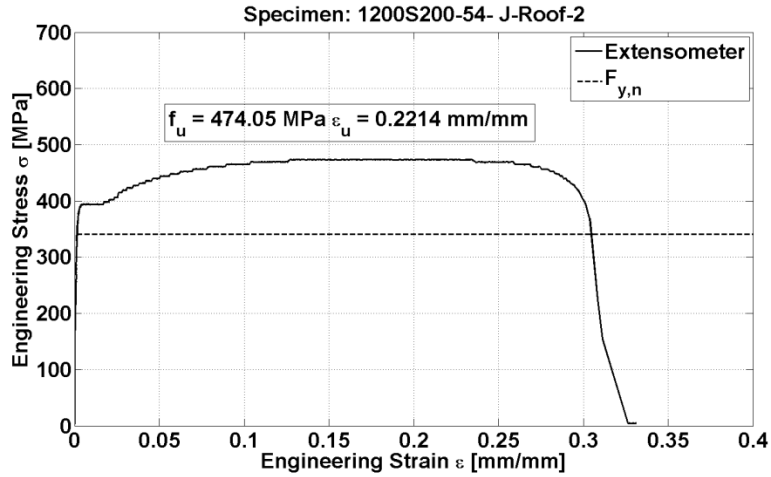


Figure D.12: Stress-strain curve of specimen J - Roof - 2

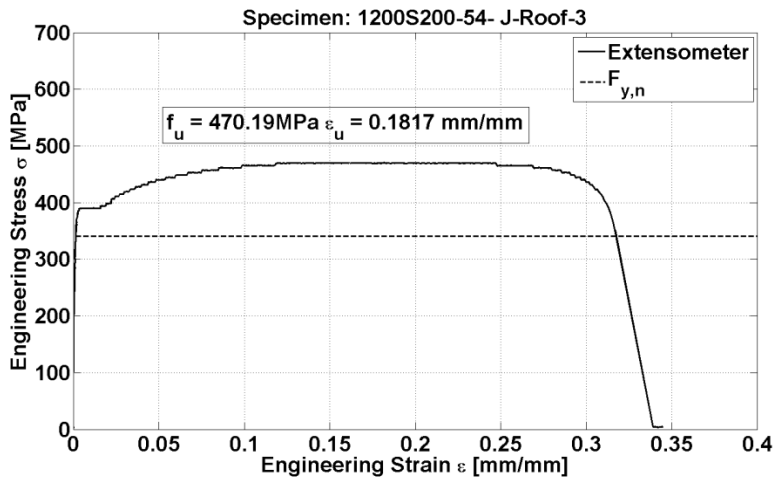


Figure D.13: Stress-strain curve of specimen J - Roof - 3

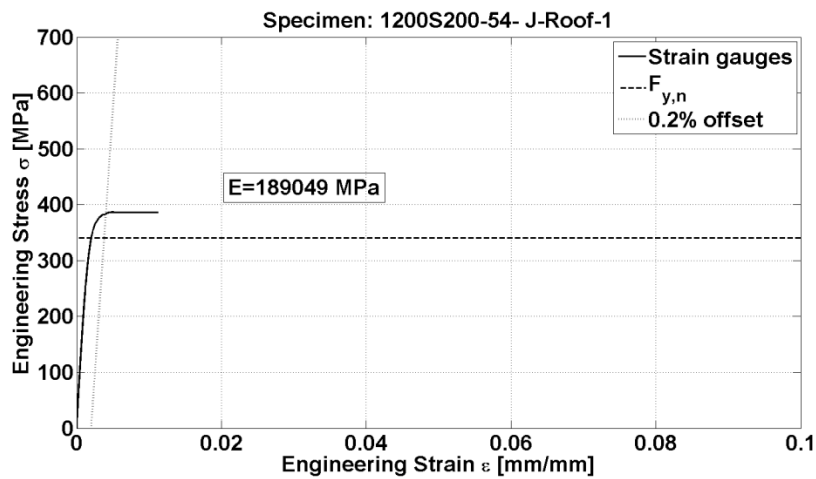


Figure D.14: Young's modulus based on specimen J - Roof - 1

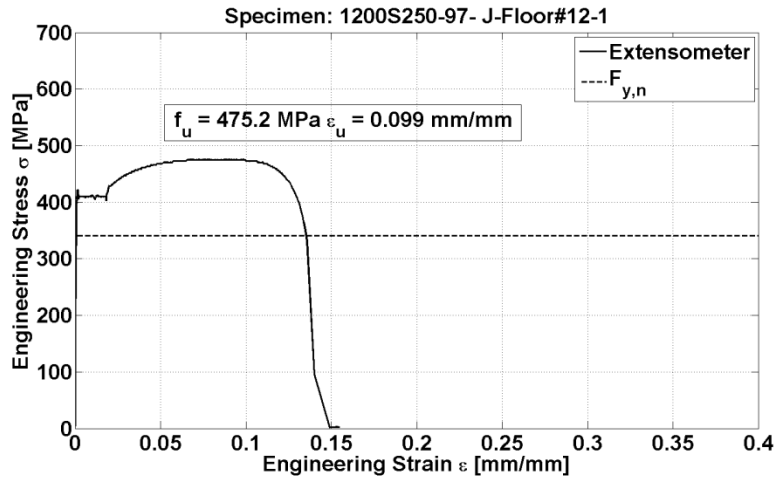


Figure D.15: Stress-strain curve of specimen J - Floor#12 - 1

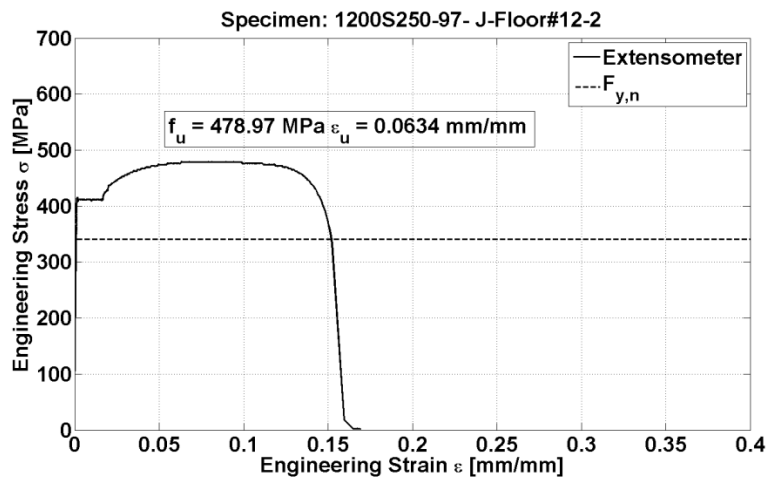


Figure D.16: Stress-strain curve of specimen J - Floor#12 - 2

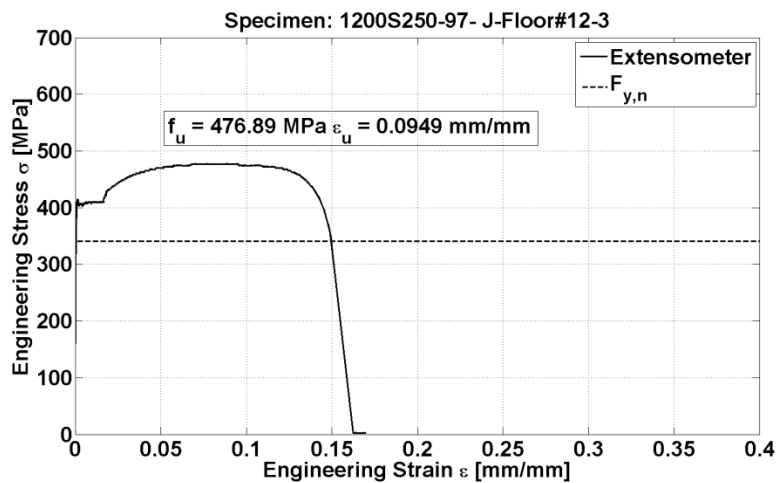


Figure D.17: Stress-strain curve of specimen J - Floor#12 - 3

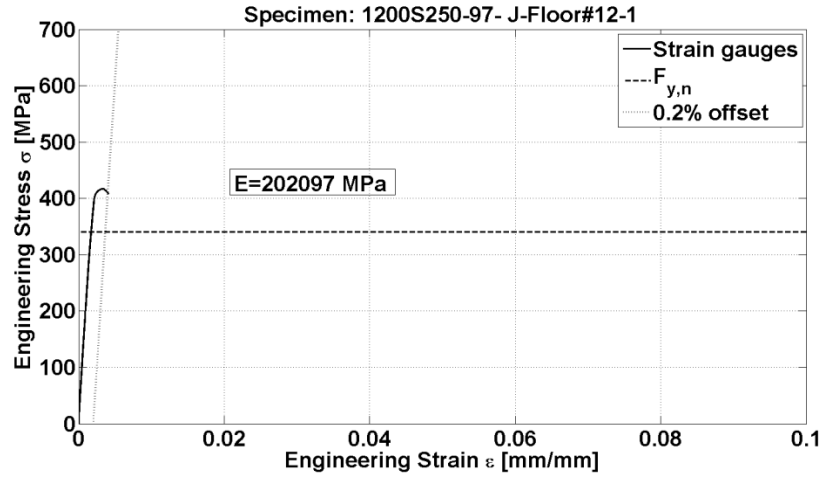


Figure D.18: Young's modulus based on specimen J - Floor#12 - 1

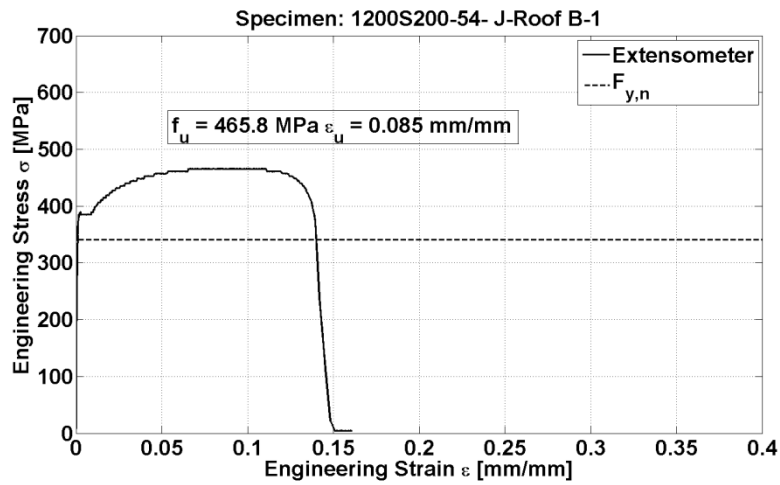


Figure D.19: Stress-strain curve of specimen J - Roof B - 1

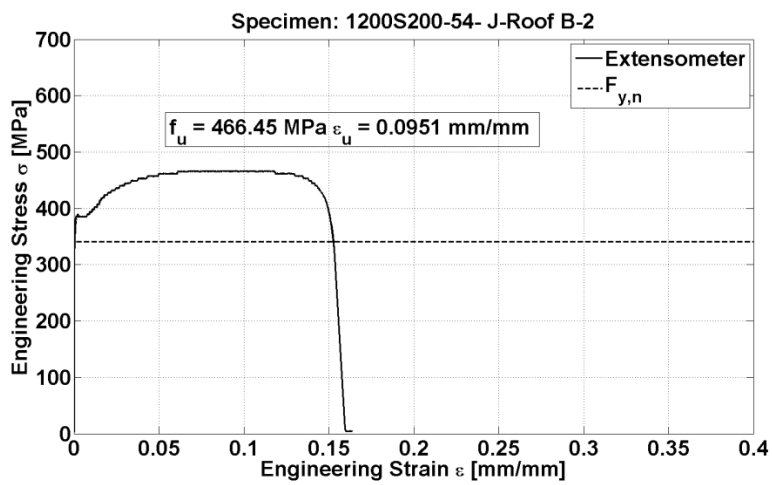


Figure D.20: Stress-strain curve of specimen J - Roof B - 2

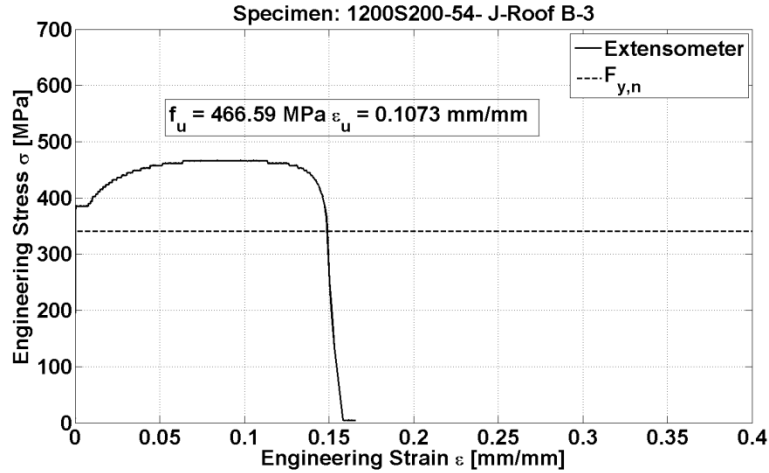


Figure D.21: Stress-strain curve of specimen J - Roof B - 3

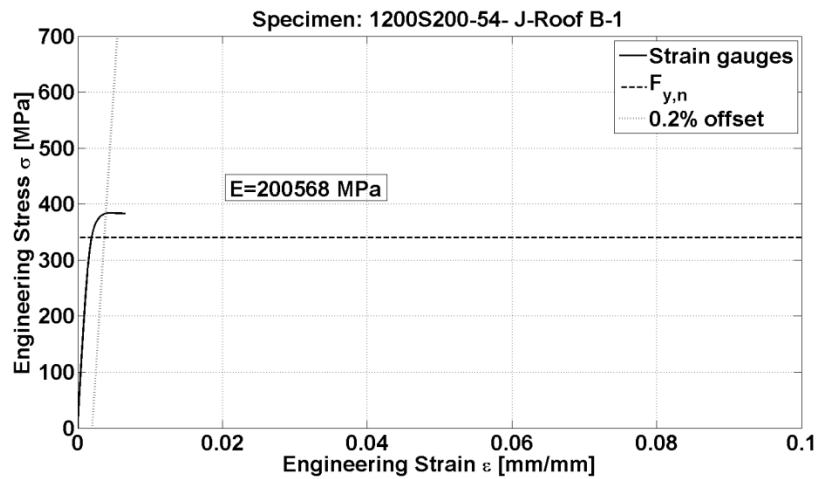


Figure D.22: Young's modulus based on specimen J - Roof B - 1

## D.2- Moisture content measurement

Table D.1 includes the moisture content measurements, as described in Chapter 2, Section 2.4 and the corresponding nomenclature found in the Notes of the Table D.1. It should be noted that the moisture content was measured following Equ. D.1:

$$MC = \frac{\text{Initial weight} - \text{Oven-dry weight}}{\text{Oven-dry weight}} \times 100\% \quad (\text{D.1})$$

Table D.1: Moisture content measurement

Wood Blocks		Green mass (g)	Oven dry Mass (g)	MC (%)	Average MC (%)
CR	1	59.22	57.25	3.4	3.6
	2	43.47	41.79	4.0	
	3	56.78	55.00	3.2	
CF	1	75.54	71.85	5.1	5.3
	2	79.50	75.54	5.2	
	3	78.19	74.13	5.5	
BMR	1	56.70	54.34	4.3	4.1
	2	47.32	45.4	4.2	
	3	47.33	45.61	3.8	
BCR	1	56.65	54.49	4.0	3.9
	2	55.8	53.73	3.9	
	3	51.6	49.68	3.9	
#12FM	1	85.32	82.29	3.7	3.5
	2	66.57	64.22	3.7	
	3	72.89	70.71	3.1	
#12FC	1	80.22	76.22	5.2	5.1
	2	79.58	75.49	5.4	
	3	75.24	71.93	4.6	

**Notes:**

CR: Roof specimen, cyclic loading

CF: Floor specimen, cyclic loading

BMR: Roof specimen blocked, monotonic loading

BCR: Roof specimen blocked, cyclic loading

#12FM: Floor specimen with #12 screws, monotonic loading

#12FC: Floor specimen with #12 screws, cyclic loading

**D.3- Dowel bearing strength test**

Initially, the moisture content of the wood panels used to extract the wood specimens had to be measured (Table D.2, an average of 6%).

Table D.2: Moisture content measurement; extra samples

Specimen	Diameter (mm)	Thickness (mm)	Initial Weight (g)	Oven-Dry weight (g)	Moisture Content (%)
R1	79.38	11	33.33	31.35	6.3
R2	77.79	12	34.21	32.19	6.3
R3	79.38	12	33.1	31.15	6.3
F1	80.96	20	55.57	52.71	5.4
F2	79.38	20	55.36	52.32	5.8
F3	77.79	19	55.92	53.14	5.2

Three extra specimens from one roof (11mm) and one floor(18mm) wood panel were oven-dried based on the ASTM D4442 (2015), Method B, as described in Chapter 2, Section 2.4 and their moisture content is shown in Table D.2. Following the method in ASTM D5764-97a (2013), Table D.3 includes the results from the dowel bearing strength tests followed by the corresponding graphs.

Table D.3: Dowel bearing strength test results

<b>Sample</b>	<b>Axis</b>	<b>Length (mm)</b>	<b>Width (mm)</b>	<b>Thickness (mm)</b>	<b>Max Load (kN)</b>	<b>Bearing Strength (MPa)</b>
<b>R1//</b>	weak	77.51	51.53	10.87	2.60	35.70
<b>R2//</b>	weak	77.16	51.16	10.88	5.00	68.59
<b>R3//</b>	weak	77.37	51.00	10.92	2.00	27.34
<b>R4//</b>	weak	76.98	51.05	10.84	4.00	55.08
<b>R5//</b>	weak	77.20	51.29	10.98	4.80	65.25
<b>R6//</b>	weak	77.10	51.43	11.04	3.00	40.56
<b>R7//</b>	weak	77.28	50.48	11.14	2.30	30.82
<b>R8//</b>	weak	77.08	51.42	11.01	2.30	31.18
<b>R9//</b>	weak	77.35	51.28	11.32	3.40	44.83
<b>R10//</b>	weak	77.61	51.37	11.34	3.10	40.80
<b>R1L</b>	strong	76.71	50.66	11.41	3.00	39.24
<b>R2L</b>	strong	76.88	50.76	11.13	2.20	29.50
<b>R3L</b>	strong	76.79	50.73	11.28	2.80	37.05
<b>R4L</b>	strong	76.92	50.68	11.30	3.40	44.91
<b>R5L</b>	strong	77.14	50.75	11.13	2.50	33.53
<b>R6L</b>	strong	76.73	50.76	11.25	2.97	39.40
<b>R7L</b>	strong	76.74	50.73	11.31	2.82	37.21
<b>F1//</b>	weak	79.73	51.64	18.35	5.60	45.55
<b>F2//</b>	weak	79.13	51.19	18.32	3.90	31.77
<b>F3//</b>	weak	79.63	51.59	18.27	3.00	24.51
<b>F4//</b>	weak	79.33	51.02	18.46	5.00	40.43
<b>F5//</b>	weak	79.09	51.73	18.43	5.80	46.97
<b>F6//</b>	weak	79.71	51.65	18.39	4.40	35.71
<b>F7//</b>	weak	79.47	51.40	18.44	4.30	34.80
<b>F1L</b>	strong	79.80	51.55	18.40	4.15	33.66
<b>F2L</b>	strong	80.03	51.45	18.20	4.05	33.21
<b>F3L</b>	strong	79.93	51.57	18.12	5.90	48.60
<b>F4L</b>	strong	79.53	51.52	18.35	4.60	37.42
<b>F5L</b>	strong	79.29	51.39	18.25	3.85	31.49
<b>F6L</b>	strong	80.46	51.47	18.14	3.60	29.62
<b>F7L</b>	strong	80.59	51.93	18.45	4.40	35.59

In Table D.3 specimens were tested for both wood orientations, along the strong axis (L) and along the weak axis (//). Seven specimens for each orientation and each case, floor or roof, were tested with the exception of roof // specimens were 10 were tested leading to a total of 31 wood samples tested. For the FL specimens the mean was 35.66 and coefficient of variation 0.18 comparable to Florig et al. (2015), as explained in Section 3.4.2 of Chapter 3.

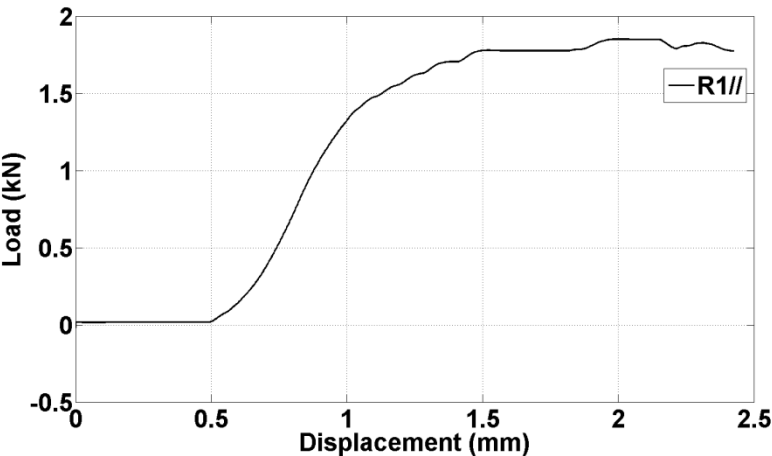


Figure D.23: Load - displacement curve of specimen R1//

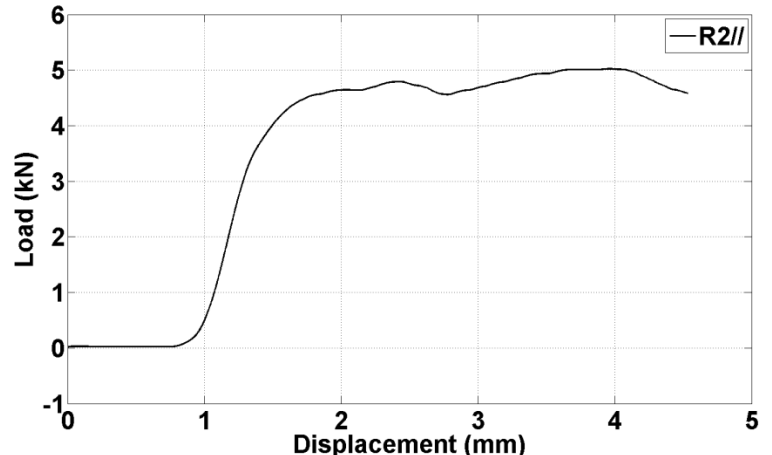


Figure D.24: Load - displacement curve of specimen R2//

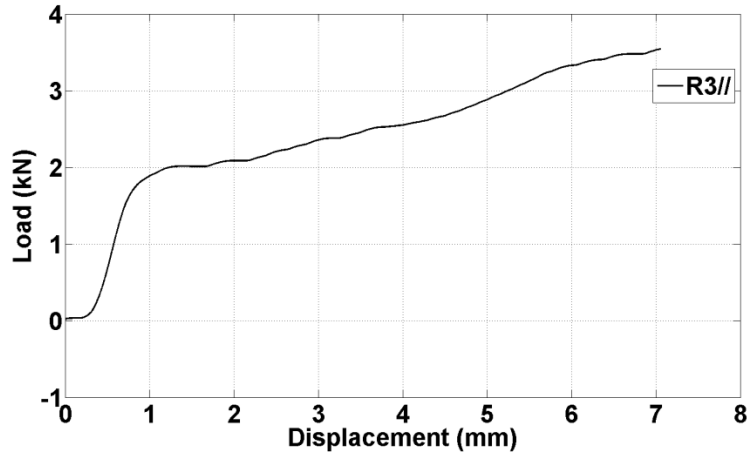


Figure D.25: Load - displacement curve of specimen R3//

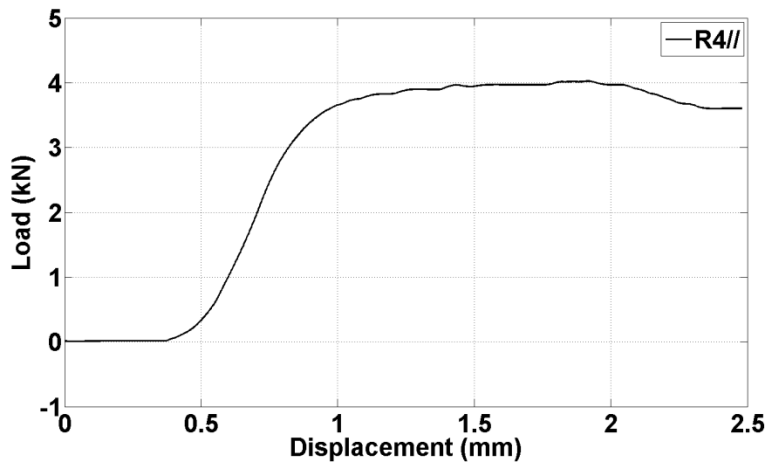


Figure D.26: Load - displacement curve of specimen R4//

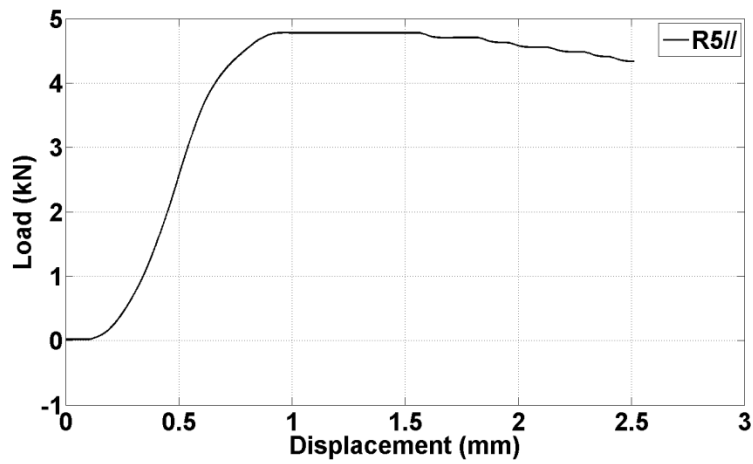


Figure D.27: Load - displacement curve of specimen R5//

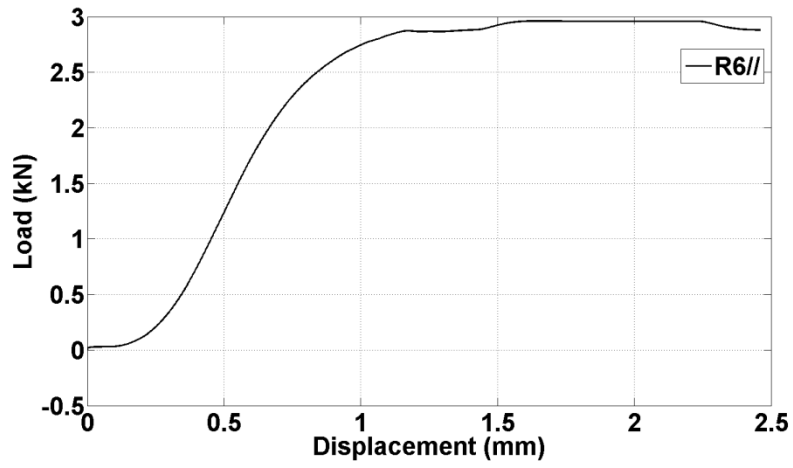


Figure D.28: Load - displacement curve of specimen R6//

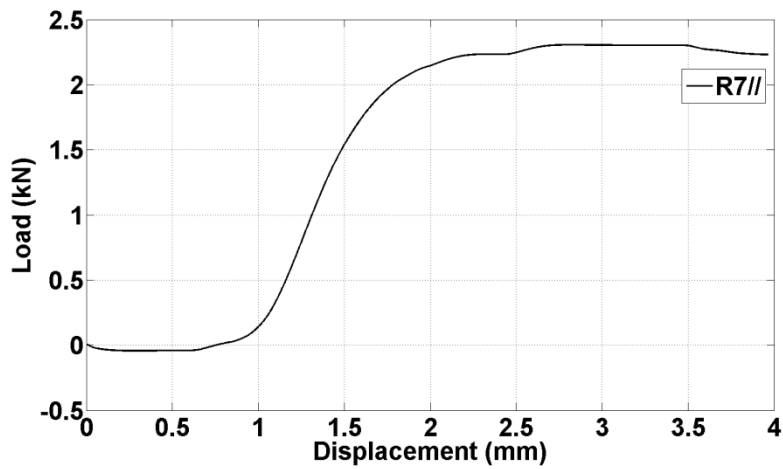


Figure D.29: Load - displacement curve of specimen R7//

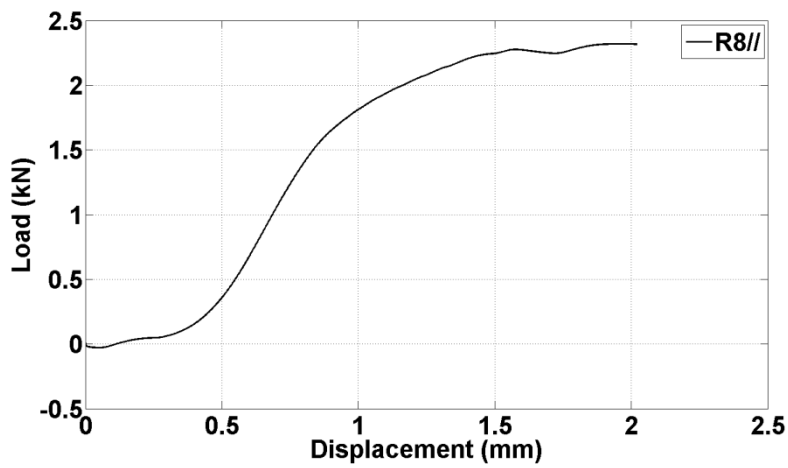


Figure D.30: Load - displacement curve of specimen R8//

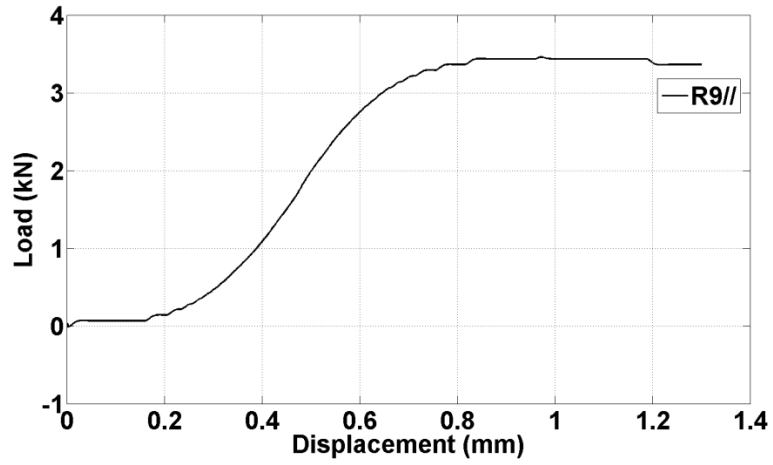


Figure D.31: Load - displacement curve of specimen R9//

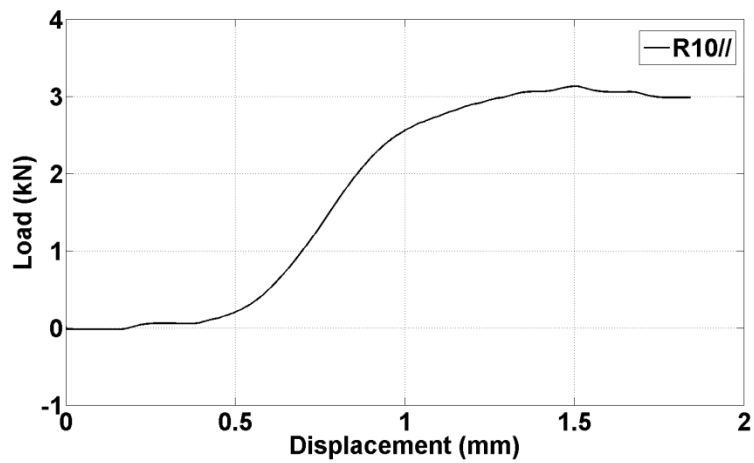


Figure D.32: Load - displacement curve of specimen R10//

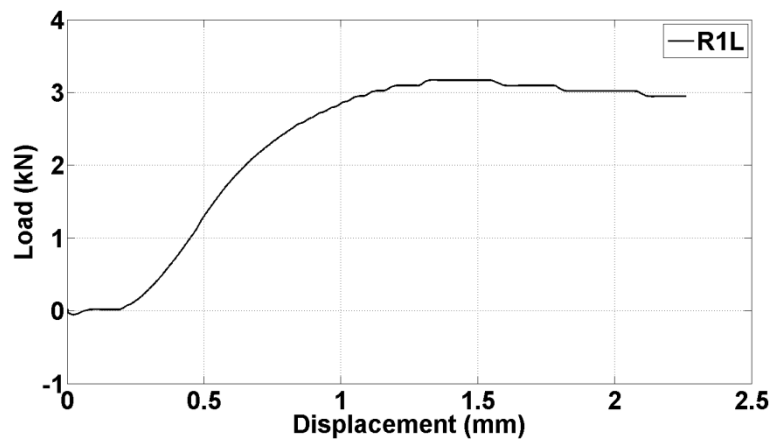


Figure D.33: Load - displacement curve of specimen R1L

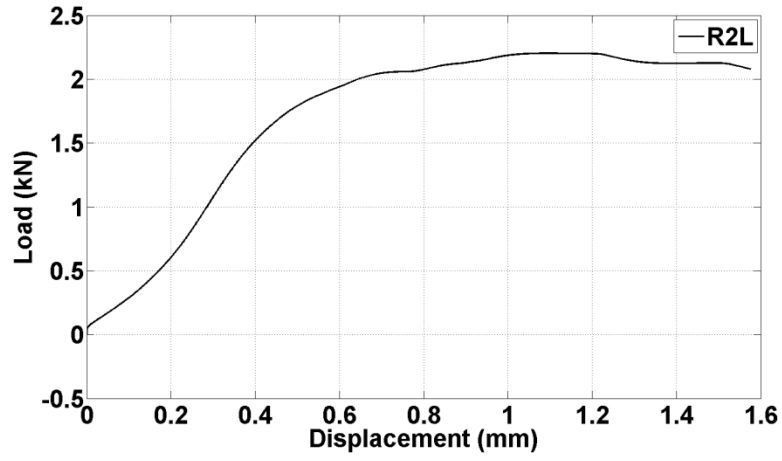


Figure D.34: Load - displacement curve of specimen R2L

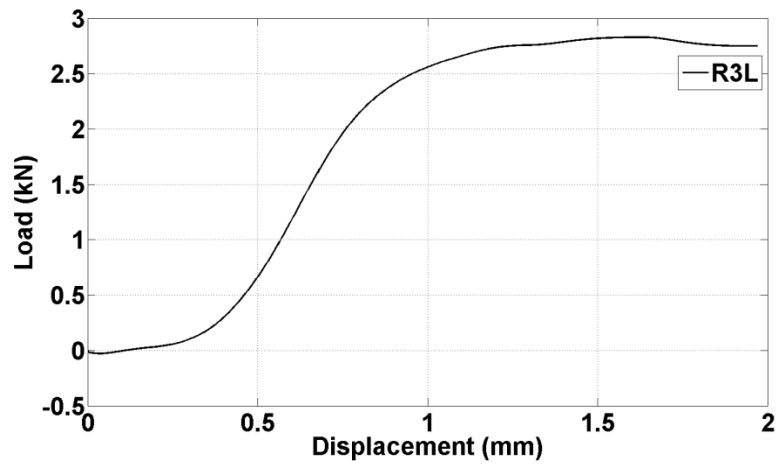


Figure D.35: Load - displacement curve of specimen R3L

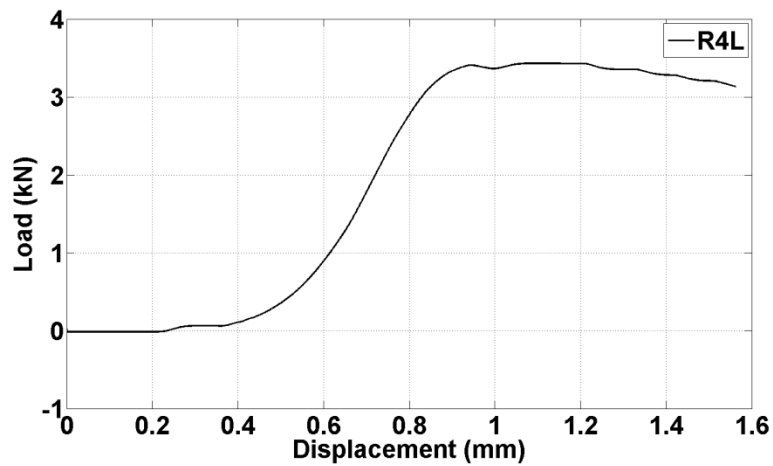


Figure D.36: Load - displacement curve of specimen R4L

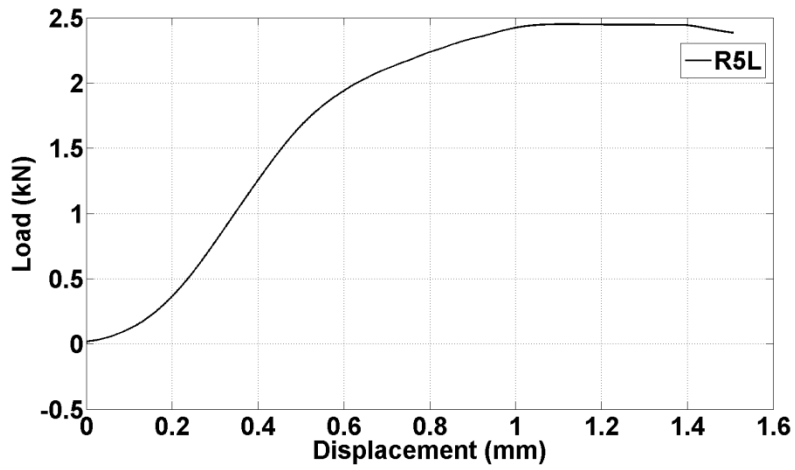


Figure D.37: Load - displacement curve of specimen R5L

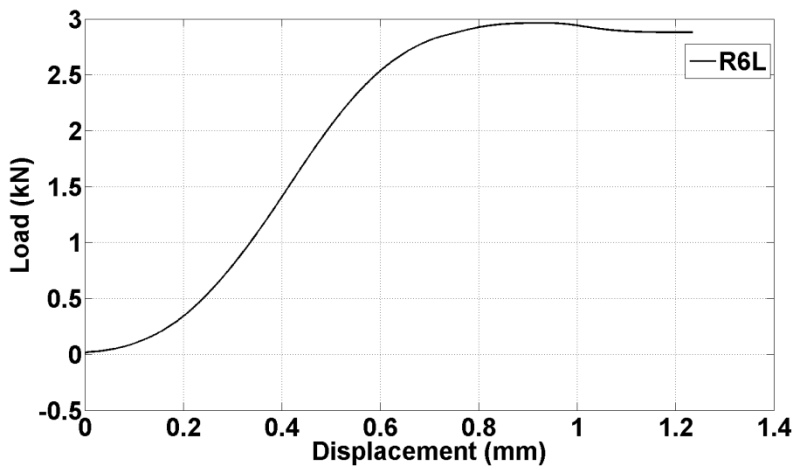


Figure D.38: Load - displacement curve of specimen R6L

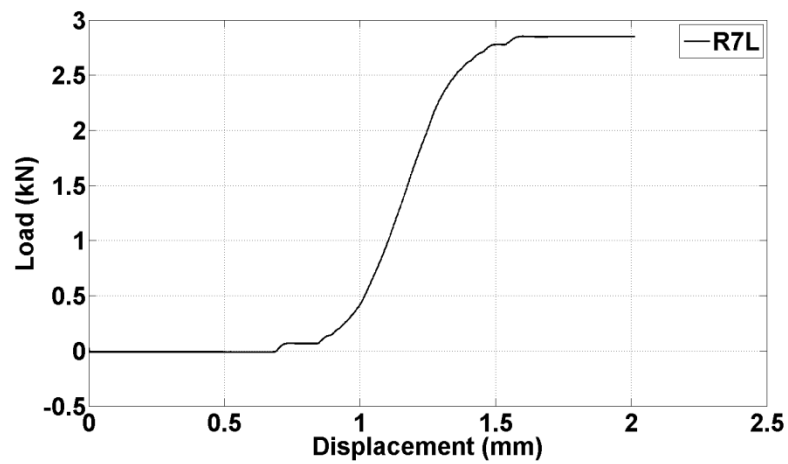


Figure D.39: Load - displacement curve of specimen R7L

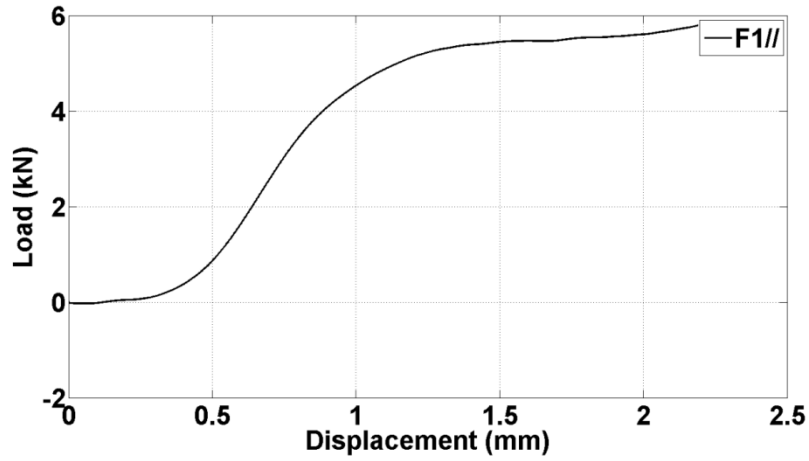


Figure D.40: Load - displacement curve of specimen F1//

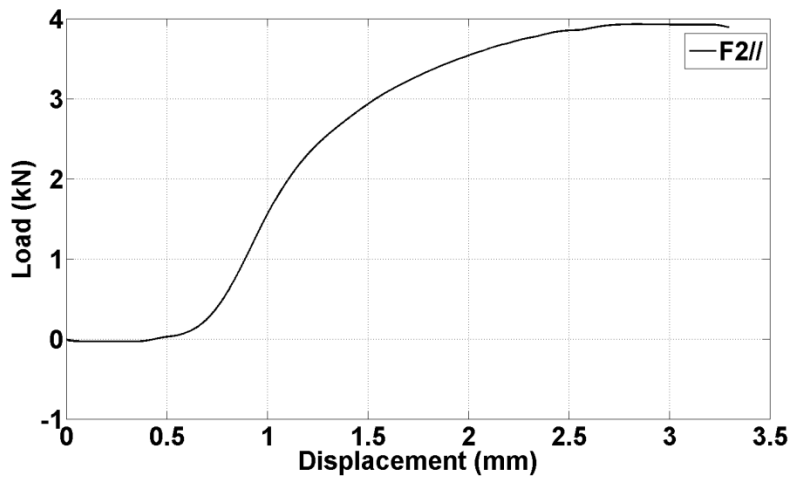


Figure D.41: Load - displacement curve of specimen F2//

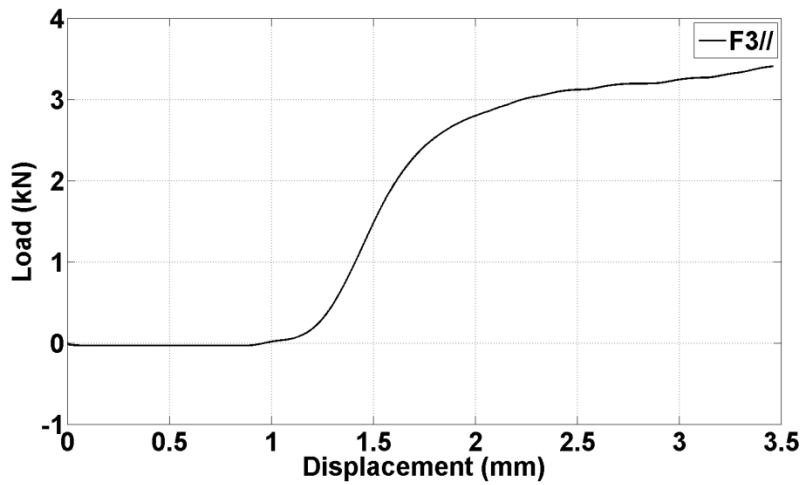


Figure D.42: Load - displacement curve of specimen F3//

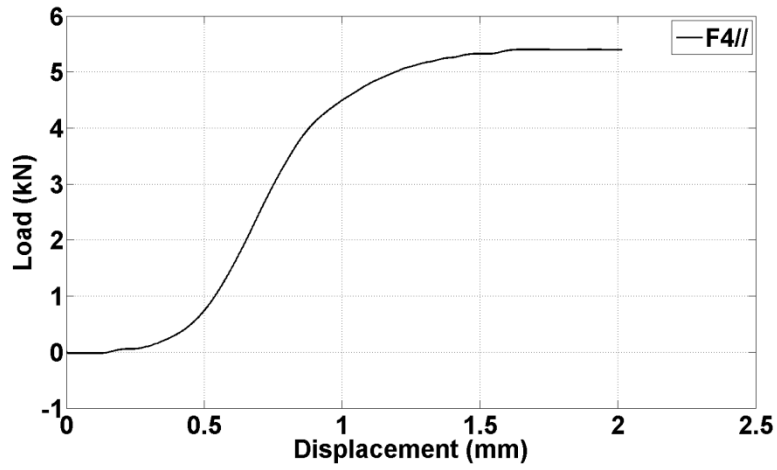


Figure D.43: Load - displacement curve of specimen F4//

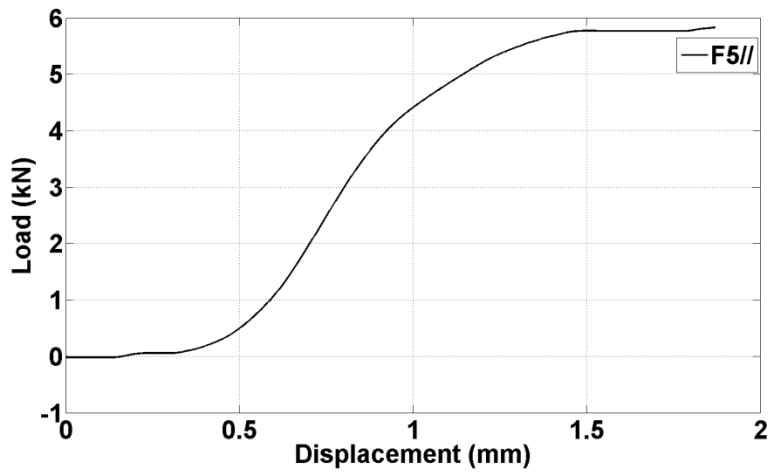


Figure D.44: Load - displacement curve of specimen F5//

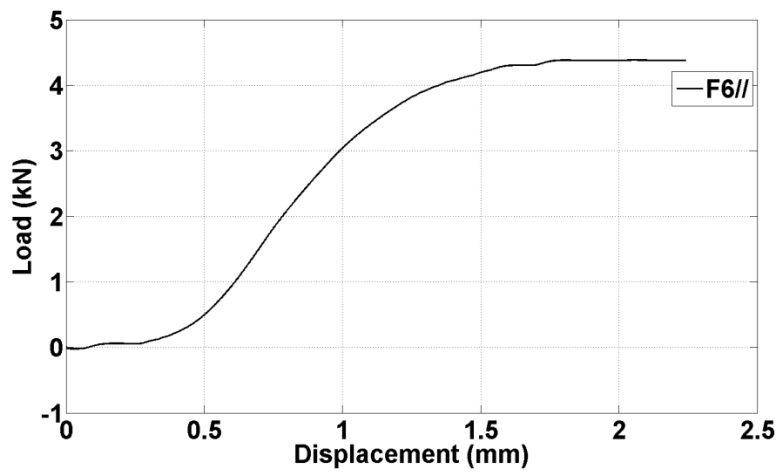


Figure D.45: Load - displacement curve of specimen F6//

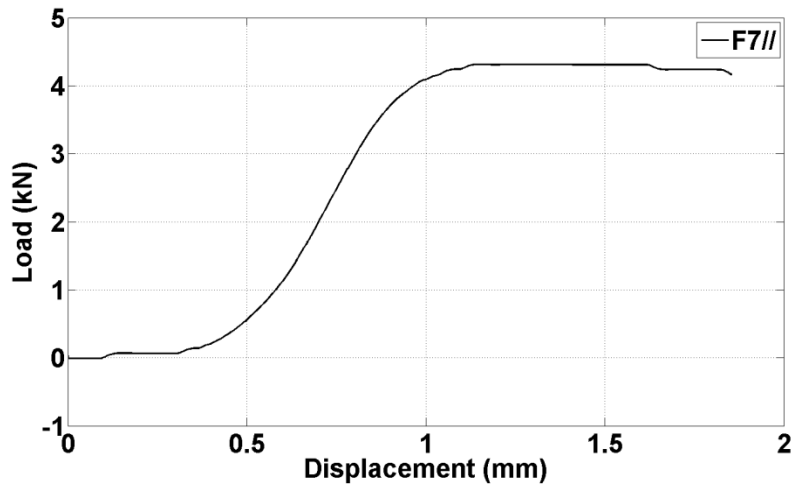


Figure D.46: Load - displacement curve of specimen F7//

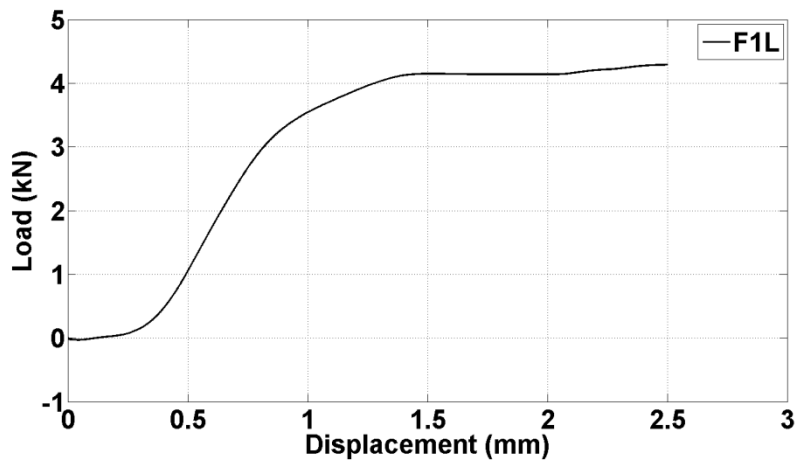


Figure D.47: Load - displacement curve of specimen F1L

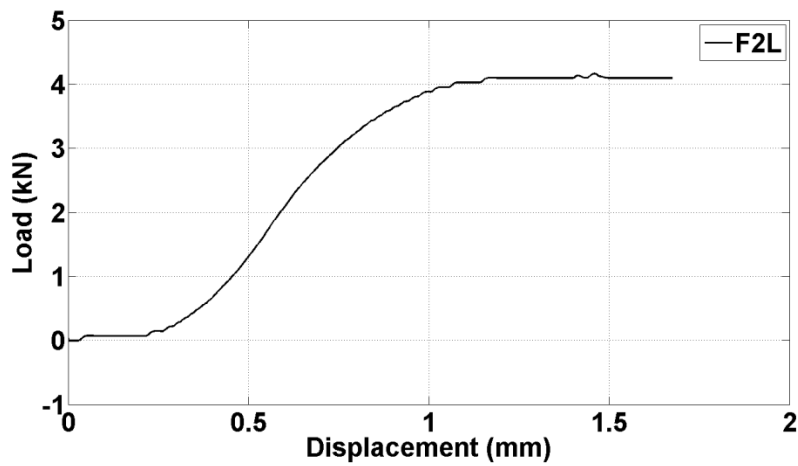


Figure D.48: Load - displacement curve of specimen F2L

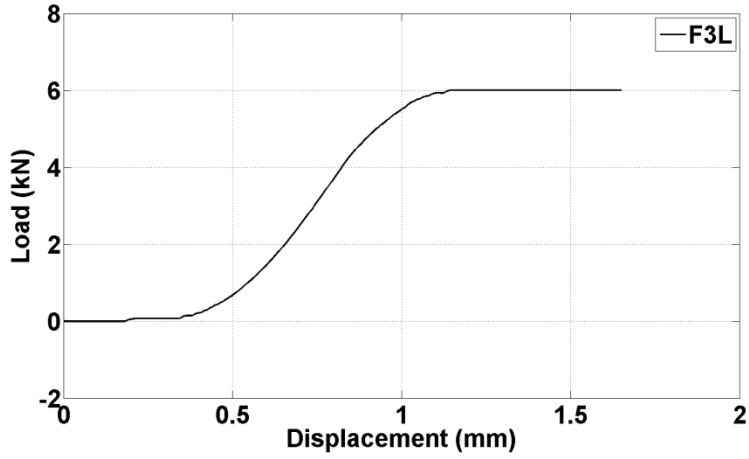


Figure D.49: Load - displacement curve of specimen F3L

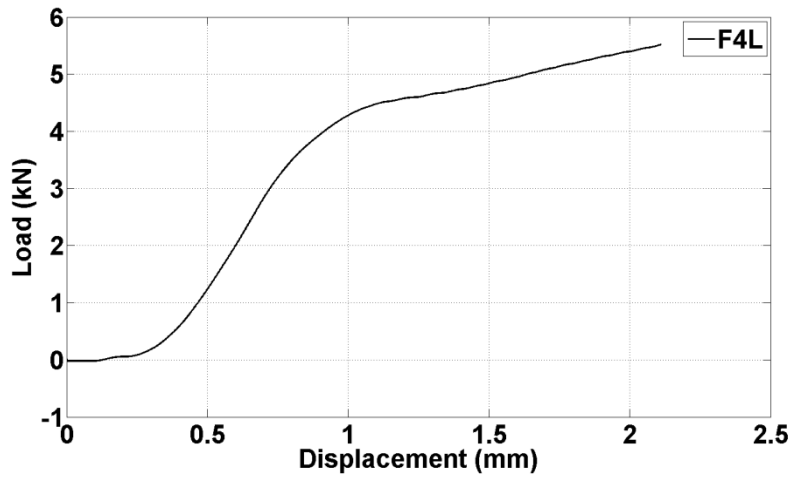


Figure D.50: Load - displacement curve of specimen F4L

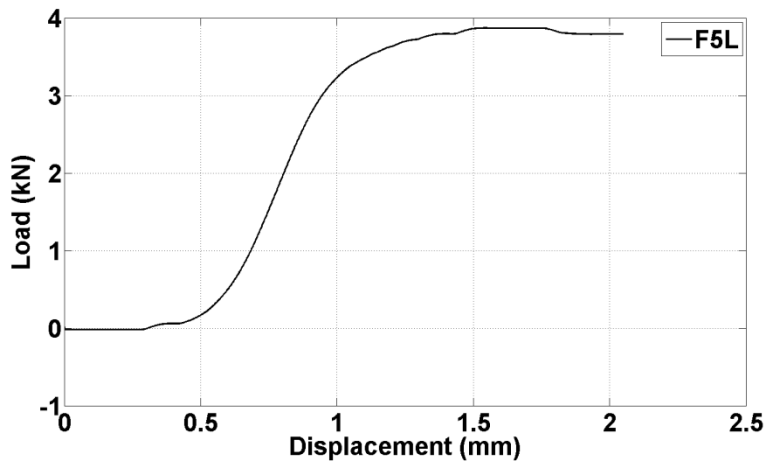


Figure D.51: Load - displacement curve of specimen F5L

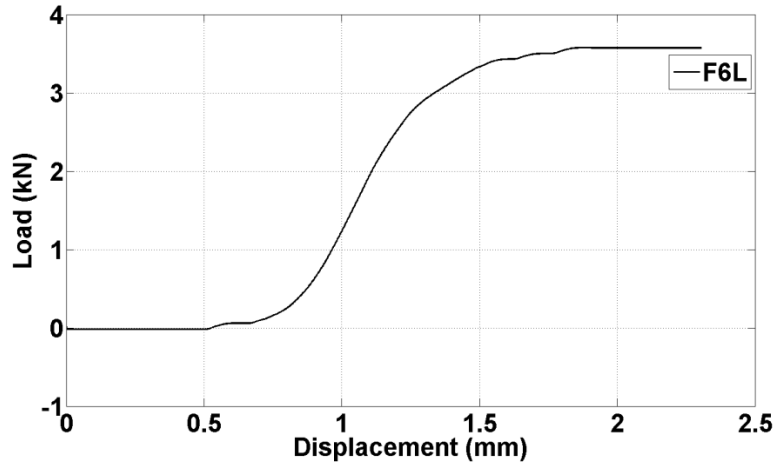


Figure D.52: Load - displacement curve of specimen F6L

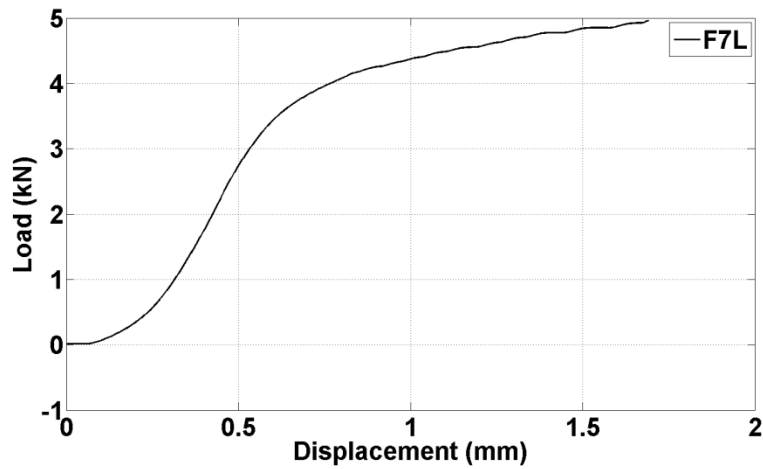


Figure D.53: Load - displacement curve of specimen F7L

#### D.4- Related figures to auxiliary tests described

Figure D.54, D.55 and D.56 demonstrate a tensile coupon test, the oven-dry method for the moisture content tests and a dowel bearing test, respectively



Figure D.54: Tensile coupon tests



Figure D.55: Oven-dry method for moisture content measurements

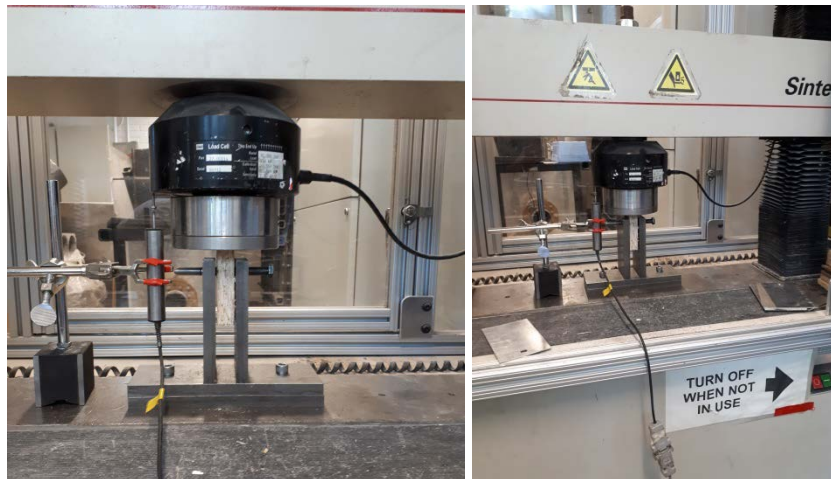


Figure D.56: Dowel bearing strength test

# APPENDIX E: SUPPLEMENTAL RESPONSE HISTORY ANALYSES

## DATA

This Appendix includes supplemental graphs and results that refer to Chapter 3 and Chapter 4.

1. Figures E.1, 2, 3 and 4 include comparisons of the experimental and numerical values of the absolute acceleration response histories in the four corners of the two-storey CFS building studied at the floor and roof level in the x and z direction. The results refer to Model 1 subjected to the CNP earthquake in the three directions, as presented in Section 3.5.1 of Chapter 3.

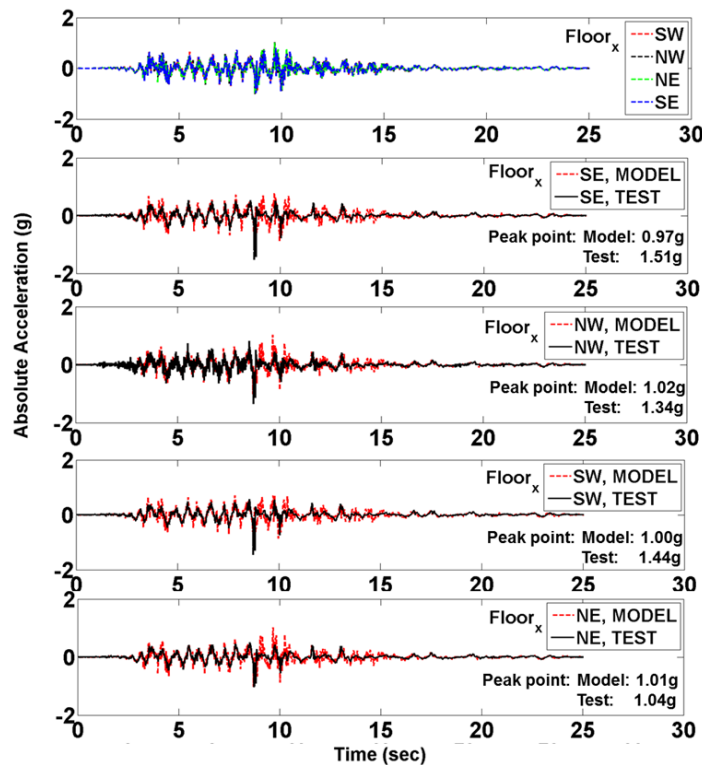


Figure E.1: Absolute acceleration response histories at floor level in the x direction

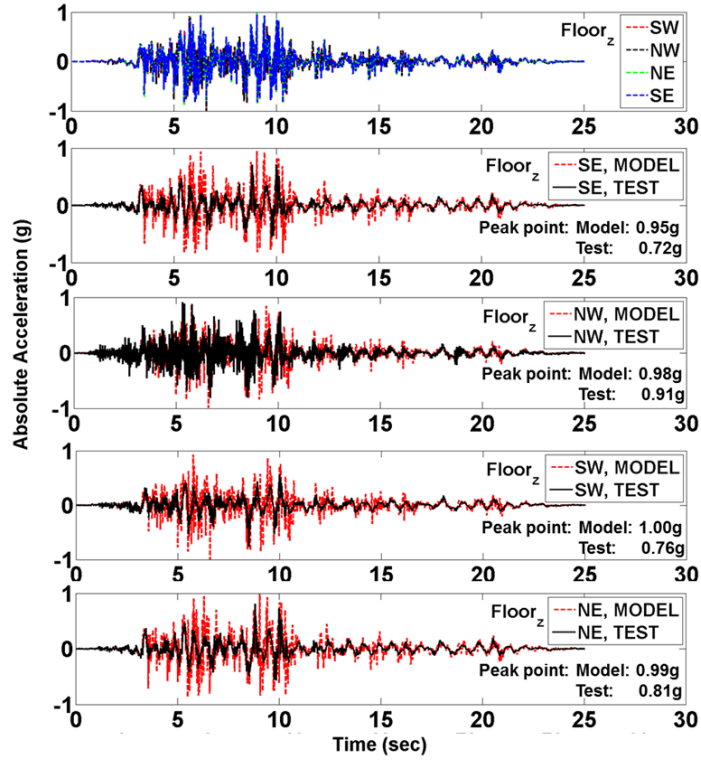


Figure E.2: Absolute acceleration response histories at floor level in the z direction

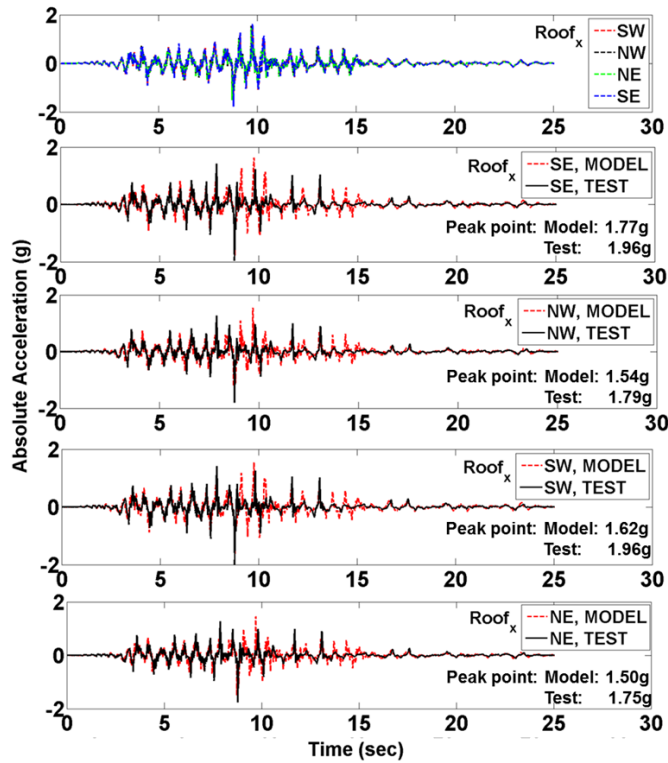


Figure E.3: Absolute acceleration response histories at roof level in the x direction

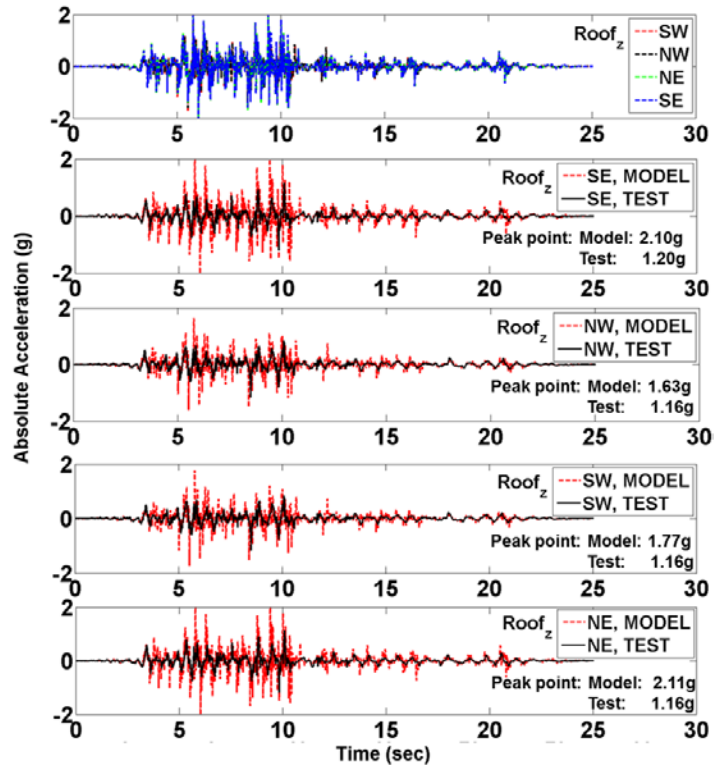


Figure E.4: Absolute acceleration response histories at roof level in the z direction

2. Figure E.5 includes the 15 ground motion acceleration graphs for the ground motion records selected to represent design level seismic hazard of Montreal for site class C (Chapter 4). Figure E.6 includes the 5 ground motion acceleration graphs that were selected for Vancouver, site class D.

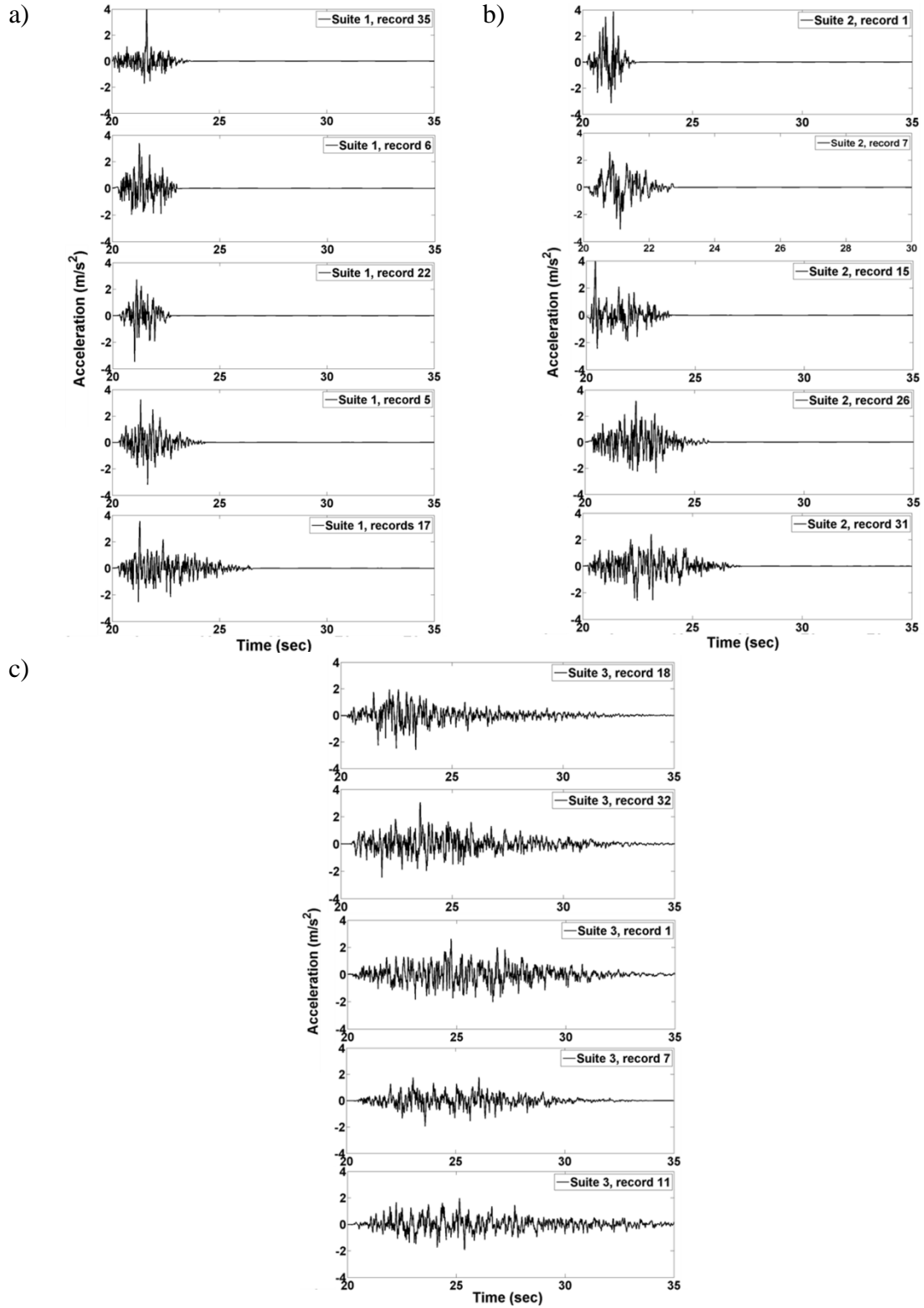


Figure E.5: Scaled ground motions for Montreal, site class C: a) suite 1,  $T=0.05$  to  $0.2$  sec, b) suite 2,  $T=0.2$  to  $0.5$  sec and c) suite 3,  $T=0.5$  to  $1.5$  sec

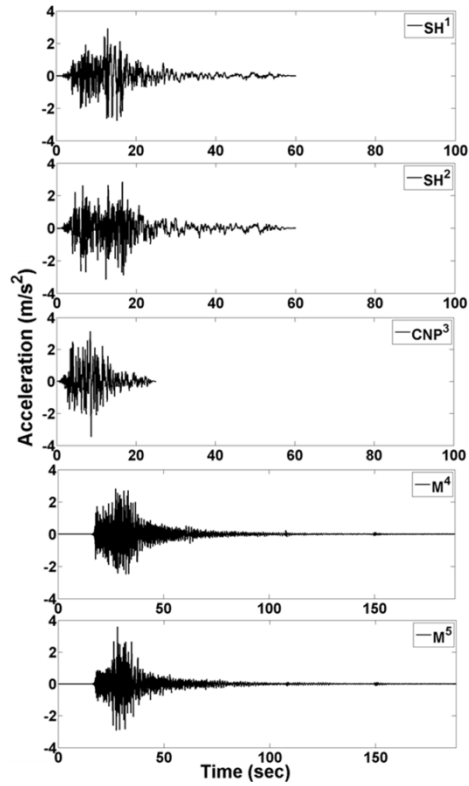


Figure E.6: Scaled ground motions for Vancouver, site class D

3. Figures E.7 & E.8 include the story drift ratios at maxRWIDR (maximum wall-line roof drift ratio) and maxFDR (maximum floor drift ratio) times as obtained from the response history analyses for Montreal, site class C and Vancouver, site class D for the three flexibility systems (Chapter 4).

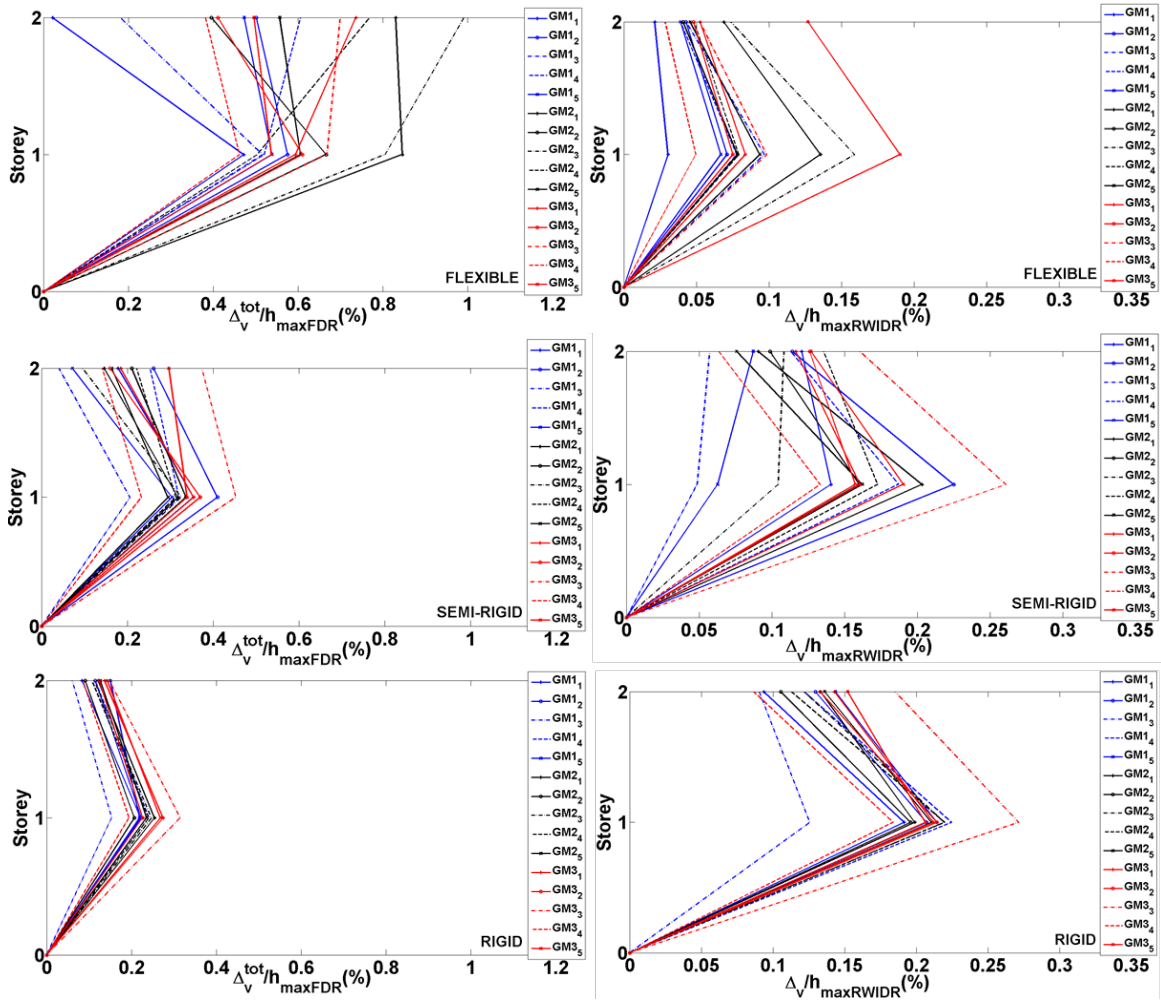


Figure E.7: Storey drift ratios at maxRWIDR and maxFDR time; Montreal, site class C

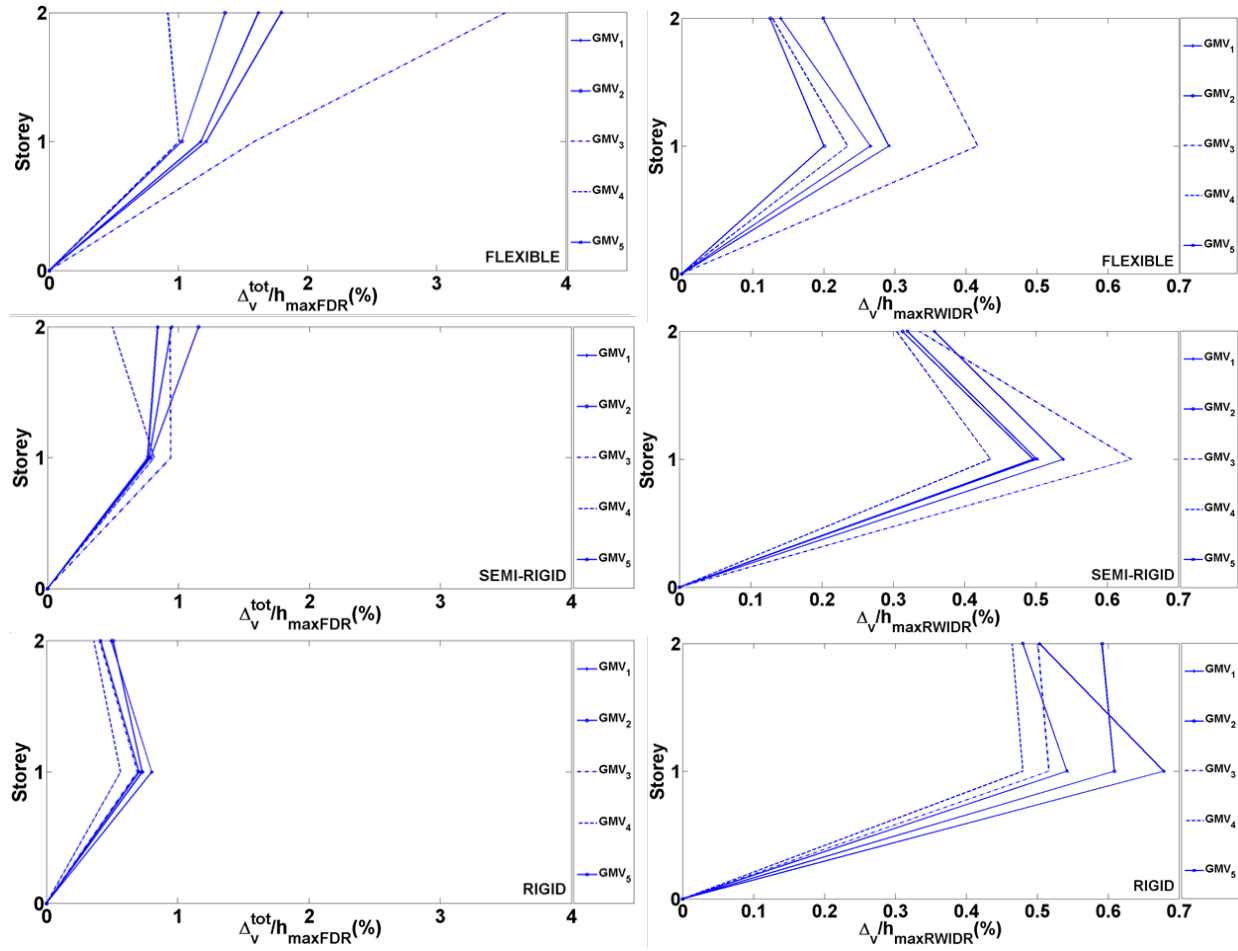


Figure E.8: Storey drift ratios at maxRWIDR and maxFDR time; Vancouver, site class D

